# A Broadband Laboratory Study of the Seismic Properties of Cracked and Fluid-saturated Synthetic Glass Materials

Yang Li

August 2016

A Thesis Submitted for the Degree of

Doctor of Philosophy

at the

Australian National University

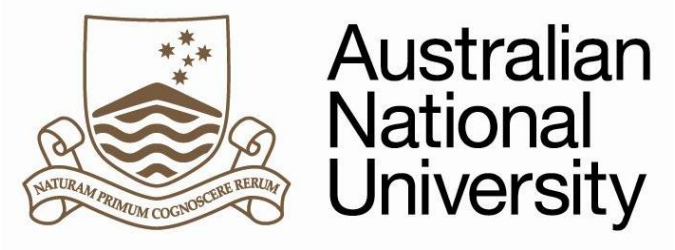

DECLARATION

The work in this thesis is my own original research except where otherwise acknowledged.

Yang Li

August 2016

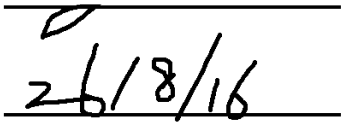

# Acknowledgements

First and foremost I would like to express my special and deep gratitude to my supervisor Prof. Ian Jackson who has led and guided me into the area of experimental rock physics and has been a tremendous mentor encouraging my work during the whole project. I have benefited a lot from the time working together with him on the attenuation apparatus, allowing me to understand not only the technical details of the high-pressure rock deformation apparatus, but also the way of scientific thinking, *i.e.*, proposing a scientific hypothesis and testing it against experiments in laboratory. His passion and enthusiasm in experiments was motivational for me and has a great influence on my decision for future career.

I really appreciate the chance provided by this project, allowing me to travel overseas among various prestigious rock physics laboratories to complete the broadband measurements, and meet fellow rock physicists on the other side of the Earth. I would like to express my sincere gratitude to my co-supervisor Prof. Douglas Schmitt for his generous support for my visits to the rock physics laboratory at the University of Alberta in 2013 and 2015. The kind help from Randy Kofman, Xiwei Chen, and Arif Rabbani is really appreciated in setting up the experiments for measuring ultrasonic wavespeeds. Discussions with Prof. Pratap Sahay and Dr. Joel Castro are also appreciated during my second visit to Edmonton.

I would like to thank Dr. Seiji Nakagawa for inviting me to visit the Lawrence Berkeley National Laboratory in 2013 and 2015, and generously providing access to the Split Hopkinson resonant bar. Dr. Tim Kneafsey is also thanked for his assistance in imaging the fluid-saturated glass samples by X-ray tomography in Berkeley.

I am also deeply indebted to Dr. Emmanuel David, whom I worked closely with at ANU during most of the project on interpreting the experiment results and performing effective medium modelling. The progress of this project has benefited a lot from the stimulating discussions with him. Prof. Stephen Cox, Prof. Tim Senden, Dr. Prame Chopra, and Dr. Eric Tenthorey, as the panel members of this Ph.D. project, are thanked for their suggestions and advices at different stages of this project. My sincere thanks also go to Harri Kokkonen, Hayden Miller, Andrew Latimore, Andrew Wilson for their generous technical support in the rock physics laboratory at ANU. I would also like to express my appreciation to my fellow labmates at ANU: Chris Cline, Richard Skelton, Kathryn Hayward.

Last but not least, personal thanks go to my beloved parents, for their love, understanding, encouragement, and support.

# Abstract

The presence and migration of fluids in Earth's upper crust is a topic of broad interest in geophysics, with applications ranging from imaging earthquake fault zones, through hydrocarbon and geothermal reservoir exploration, to the monitoring of sequestered supercritical carbon dioxide. The mechanical response of a fluid-saturated rock to an applied oscillatory stress depends on the scale of stress-induced pore-fluid flow within solid matrix, and hence is time (or frequency) dependent. Uncertainty, therefore, arises in applying ultrasonic measurements on elastic moduli/velocities of rocks at MHz frequencies, as the most commonly used technique in laboratory, to field data mainly acquired at frequencies of tens of Hz to a few kHz. A precise interpretation of the field data requires characterization of such frequency dependence or dispersion of seismic-wave velocities related to fluid flow, over the entire range of frequencies from mHz to MHz.

Broadband mechanical measurements were performed on a suite of synthetic media made either by sintering soda-lime-silica glass beads or from glass rods of similar composition with artificially controlled microstructures involving both equant pores and cracks. The goal was an improved understanding of the origin of wave-induced fluid flow and the influence of microstructure on fluid-flow related dispersion. Various fluid-flow regimes are accessed either by using pore fluids with contrasting viscosity or exciting fluid-saturated rocks at different oscillating frequencies. Synthetic samples, therefore, were measured under dry, argon- and water-saturated conditions in sequence, with a combined use of three techniques, namely, forced oscillation at mHz-Hz frequencies, resonant bar at kHz frequency, and ultrasonic wave transmission at MHz frequency, to cover a wide frequency range. Complementary measurements on permeability were also conducted on these synthetic glass samples with either argon or water.

Pressure dependent crack closure has been inferred for the cracked samples from the measured pressure dependence of the elastic and hydraulic properties. The microstructure of each cracked sample has been inferred from the measured pressure-dependent modulus deficit relative to the uncracked medium through a micromechanical model.

A water-saturated glass-rod specimen tested at mHz frequencies has a systematically higher shear modulus than its dry counterpart – evidence of the saturated isolated regime at seismic frequencies. Accordingly, the application of the Gassmann equation for the saturated isobaric regime, usually considered suitable for seismic frequencies, is inappropriate in this case. With argon and water saturation, a dispersion of shear modulus as high as ~ 10% has been observed over the frequency range from mHz to MHz on the cracked samples, and

various fluid flow regimes have been assigned based on the change in modulus due to fluid saturation and estimated characteristic frequencies. The observed dispersion indicates that conventional ultrasonic lab measurements of wavespeeds on cracked and fluid-saturated rocks cannot be directly applied in the interpretation of field data. Water with much greater viscosity than argon lowers the frequency for the squirt-flow transition on a cracked glass-rod specimen. The fluid-saturated samples with various equant porosities respond differently to the applied stress at the same frequency, indicating the influence of microstructure on the fluid-flow related dispersion.

# Contents

# Chapter 1 Introduction

## 1.1 Background and Motivation of Study

In exploration geophysics, seismic methods (both surface seismic survey and vertical seismic profiling) and sonic logging, among many other geophysical techniques, are most commonly used in the field in search of hydrocarbons or other underground geological structures of interest. The seismic methods are performed at frequencies of tens to hundreds of hertz and sonic logging works at a few kilohertz. To better understand the field data, cored samples are measured in laboratory for their elastic properties, *i.e.*, velocities or elastic moduli. The ultrasonic wavespeed measurement, involving the emission and reception of an elastic wave travelling through a studied sample, is widely used in laboratory. However, this method is performed at MHz frequencies. The marked difference in frequency between the laboratory and the field techniques may introduce uncertainties in explaining the field data based on the laboratory measurements if elastic properties are frequency dependent.

Assessment of the influence of fluids on the seismic properties of a rock involves two important aspects: 1) why the fluid saturation can change the overall elastic properties of a rock; and 2) why this change due to fluid saturation may depend on time (or frequency). For any given fluid, it has finite incompressibility. Considering a fluid-saturated rock, the solid matrix is deformed under stress, which could result in a net volumetric reduction of its voids. The net volume change is imposed upon the fluid contained within the voids. The incompressibility of fluid tends to resist the volume reduction of the solid, resulting in a higher stiffness of the fluid-saturated rock than its dry counterpart. The time dependency of the seismic properties arises from the rearrangement of the fluid within the void space. A viscous fluid takes a certain period of time to flow relative to the solid if its previous equilibrium is disturbed by the stress associated with a passing wave. The timescale for the fluid to reach the new pore-pressure equilibrium across an appropriate spatial scale, compared with the half cycle of the exciting wave, will determine the macroscopic mechanical response of the fluid-saturated rock.

In the field, the fluid saturated rocks are common, ranging from cracked crystalline rocks to hydrocarbon reservoirs, geothermal reservoirs, $CO_2$ sequestration site, *etc*. The precise interpretation of seismic data therefore needs a thorough understanding of the fluid-flow related dispersion of seismic properties. A family of studies concerning the influence of fluid saturation on the elastic properties of a rock (both the change in magnitude and frequency dependence), known as “fluid substitution problem”, is motivated.

The fluid substitution problem has been systematically considered by theorists over the last century, with models of two broad types: the poroelastic theory and the effective medium theory. These major theories will be reviewed in *Section 1.2* and summarised in a framework of fluid-flow regimes.

The validity of the proposed models needs to be tested against observations. In laboratory, most of measurements on fluid-saturated rocks have been done at ultrasonic and resonance frequencies. It is a more recent trend to perform low-frequency (Hz) measurements with forced oscillation method. The measurements have been done largely on fluid saturated natural crustal rocks, such as sandstones, carbonates, quartzites, *etc*. The past research also usually focused on the frequency provided by an individual technique or a combined use of the ultrasonic method and a single technique at lower frequencies, *i.e.*, resonant bar or forced oscillation. A survey of the experimental techniques and laboratory findings is given in *Section 1.3* and *Section 1.4*, respectively.

In order to highlight a certain physical mechanism from the complex mineralogical and microstructure background, synthetic samples have occasionally been previously used. Two major methods of fabricating synthetic samples analogous to natural sandstones have been developed separately, which will be reviewed in *Section 1.5*.

Based on the review, this chapter will end with a research outline and the aim of study in *Section 1.6*.

## 1.2 Theories of Dispersion in Fully Saturated Media

Numerous models have been developed since the 1950s to study how the fluid saturation influences the elastic behaviour of a cracked medium. The models are broadly categorised into two types: 1) the poroelastic theory proposed by Gassmann (1951) and Biot (1956 a & b); and 2) the effective medium theory with its roots in civil engineering and material sciences. After being tested by a large number of laboratory measurements and field data, these two types of theories are found to be valid only in specific frequency bands. The Biot-Gassmann theory is known to be mainly valid at seismic frequencies, and may or may not be applicable at kHz frequency. The laboratory ultrasonic measurements are commonly found to depart from the Biot-Gassmann prediction by an extra amount of stiffness. This discrepancy as considered in detail by Mavko and Nur (1975) and followers is attributed to (the inhibition of) squirt flow occurring at a grain scale. At ultrasonic frequency, when the communication of fluid between neighbouring inclusions is prohibited, the effective medium theory (or inclusion-based models) is thought to be more appropriate to capture the nature of the stiffening associated with fluid saturation.

The Biot-Gassmann theory and the effective medium theory are two extremes on the spectrum, and considerable efforts have been put into unifying these two theories into a single one to predict the dispersion at any given frequency associated with squirt flow. This requires the extension of either the Biot-Gassmann theory to higher frequencies considering the suppression of fluid flow, or the effective medium theory (inclusion-based models) to lower frequencies allowing the communication of fluid flow at a local scale to occur. The reconciliations with the Biot-Gassmann prediction at low frequency and the effective medium prediction at high frequency are considered as the strong constraints for the validity of a model (Thomsen, 1985; Chapman, 2002).

Besides the poroelastic, the effective medium theories and their extensions, another group of models, based on the seminal work by Murphy *et al.* (1984) using a grain contact model, also seems to be attractive. All these theories will be briefly reviewed in the remaining part of this section, followed by a summary of the various fluid-solid (physical) interactions (fluid-flow regimes) into a unified framework with theoretically predicted characteristic frequencies.

### 1.2.1 'Poroelastic' theory and the extensions

Gassmann (1951) developed the formalism for the bulk modulus and the shear modulus of a fluid-saturated medium based on its dry moduli, known as the Gassmann equation:

$$K_u = K_d + \frac{(1-\frac{K_d}{K_0})^2}{\frac{\phi}{K_{fl}}+\frac{1-\phi}{K_0}-\frac{K_d}{K_0^2}}, \tag{1.1}$$

$$G_u = G_d , \tag{1.2}$$

where $K_u$ is the bulk modulus of the undrained fluid-saturated rock, $K_d$ is the bulk modulus of the drained rock, $K_0$ is the bulk modulus of the mineral making up the rock, $\phi$ is the porosity, $K_{fl}$ is the fluid bulk modulus, $G_u$ is the shear modulus of the undrained fluid-saturated rock, and $G_d$ is the shear modulus of the drained rock. The drained moduli, in the absence of fluid-solid chemical interaction and using the effective pressure law with zero pore pressure, can be identified as the dry moduli.

The Gassmann equation predicts that the shear modulus is unaffected by fluid saturation, but that there is an increase in bulk modulus when the rock is saturated with pore fluid. The derivation of the Gassmann equation is based on a series of assumptions, the most important one among which is that the fluid needs to reach pore-pressure equilibrium over the entire medium. This fluid-rock status is termed the "saturated isobaric regime". The violation of this assumption is caused by two types of situations. A partial drainage of the

medium gives a fluid heterogeneity and leads to a patchy saturation problem, which is not described by the Gassmann equation. The complete drainage of fluid will reduce the fluid-saturated moduli to the dry moduli. Alternatively, pore-fluid pressure gradients may be incompletely relaxed by fluid flow. This leads to a higher shear modulus than the Gassmann prediction. But for bulk modulus, the unrelaxed fluid status may or may not result in a higher value than the Gassmann prediction, depending on the sample microstructure.

Biot (1956 a & b) extends the Gassmann equation to the full spectrum, and the low-frequency limit of the Biot formalism reduces to the Gassmann equation. The Biot formalism predicts a dispersion of P- and S-wave velocities between the high- and low-frequencies, associated with the competing viscous and inertial effects. The Biot's high- and low-frequency regimes are separated by a characteristic frequency $f_B$ given as:

$$f_B = \frac{\phi\eta}{2\pi\rho_f k}, \tag{1.3}$$

where $\phi$ is the porosity of a rock, $\eta$ is the fluid viscosity, $\rho_f$ is the fluid density, and $k$ is the permeability of a rock. The Biot characteristic frequency is found to be in the range of tens of MHz to GHz for rocks saturated with commonly seen fluids (Bourbié *et al.*, 1987), hence too high to be relevant even for ultrasonic measurements in laboratory.

The Biot theorem is a more complete form of the Gassmann equation, whereas the Biot-Gassmann theory still does not capture the entire nature of the fluid saturation as it is more based on a series of macroscopic parameters, such as porosity and moduli, ignoring the geometrical details of particular inclusions. However, the origin of squirt flow is directly linked to the inclusion geometry and associated spatial variation in compliance to an applied stress. This is the intrinsic limitation laid down by the assumptions of the Biot-Gassmann theory as a macroscopic treatment.

The Gassmann equation and the low-frequency limit of the Biot formalism were noticed to fail in predicting the measurements at ultrasonic frequency in laboratory. The discrepancy is not successfully explained by the Biot dynamic poroelastic theory. Experimental evidences (Jones & Nur, 1983; Batzle *et al.*, 2006) also clearly demonstrate that the characteristic frequency is proportional to the inverse of viscosity, inconsistent with the relation given by the Biot theory (Eq. 1.3). Mavko and Nur (1975) suggested the mechanism of squirt flow, which occurs at a much smaller grain scale between adjacent inclusions (compared with the global-scale flow for drainage). The suppression of squirt flow leads to unrelaxed fluid status termed "saturated isolated regime". This regime is predicted by the effective medium theory and has been proved to occur during the process of conventional ultrasonic wave propagation in laboratory.

Although the unrelaxed elastic moduli, with suppressed communication of fluid between neighbouring inclusions, can be calculated from the effective medium theory, it is still attractive to extend the poroelastic theory to a higher frequency to capture the extra stiffening associated with the suppression of squirt flow. In order to present such remaining fluid-saturation effect in the poroelastic framework, Mavko and Jizba (1991) introduced a new concept known as "wet-frame moduli" to replace the normal dry (or drained) moduli in the Biot-Gassmann formalism. The Mavko and Jizba method provides a one-step estimate for the unrelaxed high-frequency bulk modulus and shear modulus. Dvorkin *et al.* (1995) extended the Mavko and Jizba (1991) to any frequency at the cost of introducing an implicit parameter $Z$ associated with the frequency scale of dispersion.

The Biot-squirt (BISQ) model, proposed by Dvorkin and Nur (1993) and Dvorkin *et al.* (1994), is another attempt to unify the Biot dispersion and squirt dispersion in a single poroelastic model. As we have discussed earlier in this section, any valid model dealing with squirt dispersion needs to be consistent with the Biot-Gassmann theory at the low-frequency limit and with the effective medium theory at the high-frequency limit. However, the BISQ model fails to approach the Biot-Gassmann prediction at the low-frequency limit.

To sum up, the family of models based on the poroelastic theory starts with the low-frequency end member of the fluid substitution problem, either applicable to a uniform pore-fluid pressure only (*e.g.*, the Gassmann equation) or extending to higher frequencies (*e.g.*, the Mavko & Jizba model, the BISQ model). In any case, the derivation only involves the macroscopic parameters, such as porosity, permeability, *etc.*, ignoring the specific geometries of inclusions. In this sense, this family of models is more appropriate to describe the solid-fluid interaction at low frequency and at the sample scale, for which the particular geometry of pores and cracks may not play such an important role. The geometrical details of inclusions, related directly to the origin of squirt flow, are emphasised in the other group of models based on the effective medium theory, which will be introduced in the following section.

### 1.2.2 Effective medium theory and the extensions

The basic idea of the effective medium theory is to calculate the overall elastic properties of a composite from the elastic properties of its individual constituents. The constituent, *i.e.*, an inclusion, is embedded in the background medium. For this reason, the family of models based on the effective medium theory is also termed inclusion-based models.

Without specifying the geometries of the constituents, only the range in which the effective moduli of the composite could possibly fall can be determined from the moduli of the constituents and the corresponding volume fractions. The range of effective moduli is

demarcated by an upper and a lower bound. The bounds of the simplest form were given by Voigt (1928) and Reuss (1929). Later, Hashin and Shtrikman (1963) provided similar but narrower bounds.

The effective modulus of a composite can be more precisely predicted if the geometries of the constituent phases are specified. In the effective medium theory, the theoretical attempts to predict the effective moduli of the macroscopic rock from the microscopic geometries are also termed micromechanical models (Jaeger *et al.*, 2007). Inclusions, such as pores and cracks, in natural rocks are inevitably of irregular shape. However, in modelling, the inclusion is normally assumed to have an ellipsoidal shape (the lengths of the three semi-axes: $a_1$, $a_2$, and $a_3$), as it is amenable to three-dimension analytical treatment (Eshelby, 1957). In most cases, to achieve a simpler mathematical expression but keep the physical feature, a spheroid, which is an ellipsoid with two equal semi-axes ($a_1 = a_2$), is used to model an inclusion (Wu, 1966; Kuster & Toksöz, 1974). The other advantage of assuming the spheroidal shape of an inclusion is that the shape of the inclusion is simply governed by a parameter known as aspect ratio $\alpha = a_3 / a_1$. Three limiting cases, *i.e.*, a needle shape, a perfect sphere, and a penny (or disk) shape, can be achieved by allowing the aspect ratio $\alpha$ approaching infinity, 1, and 0, respectively. The perfect sphere is normally used to approximate a stiff pore, and the compliant crack is modelled as a flat spheroid. The hydrostatic and shear compliances of an individual inclusion with a specified geometry can be theoretically calculated (Eshelby, 1957; Berryman, 1995; David & Zimmerman, 2011).

In order to link the elastic properties of an individual inclusion to the effective elastic properties of the entire medium, various schemes have been developed. The simplest way is to assume non-interaction among the inclusions. But this is a poor model for a real porous medium, leading to overestimated effective moduli. Various attempts have been given to consider the interaction of inclusions, from low concentration to high concentration of inclusions. Kuster and Toksöz (1974) adopted the wave-scattering formalism to derive the expressions of the effective moduli of a composite from its constituents. This method is found to be limited to low concentrations of inclusions. The self-consistent method (Budiansky, 1965; Hill, 1965; Wu, 1966; O'Connell and Budiansky, 1974) and the differential effective medium (DEM) method (McLaughlin, 1977; Cleary *et al.*, 1980; Henyey & Pomphrey, 1982; Norris, 1985; Zimmerman, 1991b) are applicable to higher concentrations of inclusions. The expressions for both methods are given as a pair of coupled equations to be solved iteratively. In the self-consistent method, the interaction of inclusions is treated by substituting the background medium for the as-yet-unknown effective medium. In contrast, the DEM method follows a thought experiment by incrementally adding fractions of inclusion material into the host material until reaching the desired proportions.

The effective medium theory considers the specific geometries of inclusions, in contrast to the poroelastic theory, giving the potential to describe the physical origin of squirt flow. However, the fluid communication has not been taken into account in the schemes described above. The fluid is assumed to be trapped in each inclusion. As a result, the effective medium theory is more suitable for the saturated isolated regime when the fluid flow between adjacent inclusions is suppressed by high frequency. It has been argued that this method is most applicable to the ultrasonic measurements in laboratory.

In order to introduce the fluid communication between inclusions, an extension needs to be made from the conventional effective medium theory. O'Connell and Budiansky (1977) introduced frequency-dependent effective moduli of solids with assumed ellipsoidal shape cracks, based on the self-consistent method. A series of fluid-flow regimes has been proposed based on the predicted change in shear and bulk modulus and associated attenuation. The characteristic frequencies that separate these regimes are also provided by the model. The shape of inclusions is specified by their aspect ratio, but all inclusions are assumed to be of a uniform low aspect ratio (thin cracks). In such a medium, squirt flow can occur between connected thin cracks with different orientations relative to an imposed shear stress. However, such a medium allows no squirt flow under hydrostatic stress, since the same volumetric change in the connected identical thin cracks yields no pressure gradient. For the latter case, in order to capture the entire picture of the squirt-flow mechanism, connected inclusions with contrasting compliance need to be specified into the model. The spherical pores and thin cracks would be the two extremes in compliance to induce squirt flow.

Endres and Knight (1997) expanded the expressions based on O'Connell and Budiansky (1977) and Budiansky and O'Connell (1980), incorporating a bimodal microstructure, *i.e.*, spherical pores and compliant cracks. The total porosity is fixed while the fraction of the compliant cracks is varied. The model predicts the influence of microstructure on the bulk and shear dispersion as: 1) the maximum bulk dispersion is expected with a mixed spherical pores and compliant cracks; 2) zero bulk dispersion appears when all the inclusions are either the spherical pores or the compliant cracks; 3) both the bulk and the shear dispersion increase with reduced aspect ratio; and 4) shear dispersion is equal to zero when only spherical pores are present and monotonically increases with gradually increasing presence of cracks. The same relation is qualitatively recovered by Chapman *et al.* (2002) and Adelinet *et al.* (2010), who adopt a similar strategy of bimodal microstructure. Chapman *et al.* (2002) also clearly demonstrates the amount of dispersion and attenuation associated with squirt flow is reduced by increasing differential pressure. Unlike Endres and Knight (1997) and Chapman *et al.* (2002), Adelinet *et al.* (2010) uses the

Gassmann equation directly as the low-frequency limit instead of deriving it from its high-frequency effective medium theory.

Instead of a crack-pore squirt flow, Guéguen and Sarout (2011) focuses on the crack-crack squirt flow with three assumed types of arrangement of cracks: 1) identical cracks aligned in the same direction; 2) identical cracks with random orientations (isotropic distribution); and 3) cracks randomly distributed in zone with a given axis. With the combined use of the poroelastic theory at low frequency, both the anisotropy and dispersion are analyzed for the three cases, in which the second case is most analogous to a thermally cracked synthetic sample giving zero overall anisotropy but large dispersion.

In general, the inclusion-based models provide valuable insight into the mechanism of squirt flow with regard to the inclusion geometry. Its prediction at the high-frequency limit for the saturated isolated regime and the extensions to a lower frequency, in addition to the poroelastic treatment, gives another possibility to simulate squirt flow.

As shown in Adelinet *et al.* (2010), the combined use of the Biot-Gassmann theory at low frequency and the effective medium theory at high frequency is conveniently adopted in various theoretical studies. This method is illustrated in Fig. (1.1), with the amount of squirt-flow dispersion given as:

$$squirt - flow\ dispersion = \frac{M_{sat}^{HF} - M_{sat}^{LF}}{M_{sat}^{LF}}, \tag{1.4}$$

where $M_{sat}^{LF}$ is the Biot-Gassmann low-frequency modulus, and $M_{sat}^{HF}$ is the high-frequency unrelaxed modulus calculated by the effective medium theory.

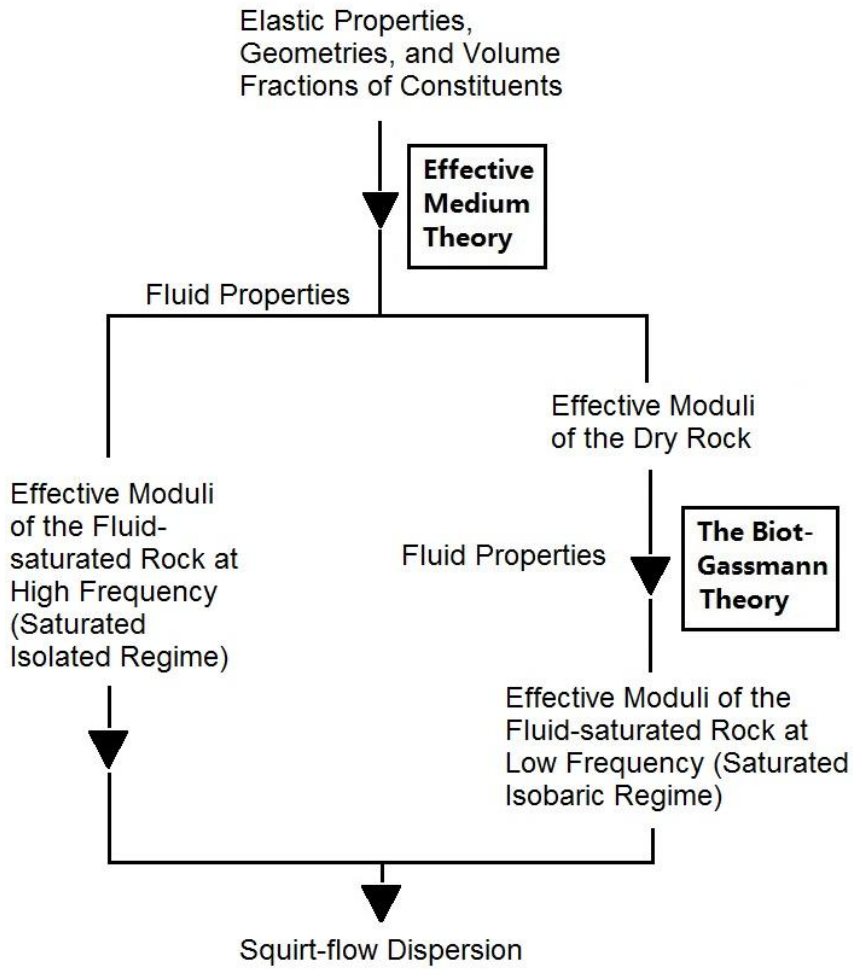


**Figure 1.1** Flow of computing the squirt-flow dispersion based on the combined use of the Biot-Gassmann theory and the effective medium theory adopted by for example Adelinet *et al.* (2010).

### 1.2.3 Grain contact models

Besides the models derived from the poroelastic theory and the effective medium theory, Murphy *et al.* (1984) is an alternative developed from the framework of Hertz-Mindlin grain-contact theory (Digby, 1981; Winkler, 1983). The model considers rigid grains and the compliance of a rock only comes from the weak grain contacts. Surface energy is taken into account for the dry solid-solid contact. For fluid saturation, squirt flow occurs between a fluid-filled thin gap between grains and a connected large stiff pore. This model predicts unrealistically high stiffness at high frequency, disagreeing with the prediction of the unrelaxed moduli by Mavko and Jizba (1991). This approach is recently adopted and further developed by Gurevich *et al.* (2010), which gives consistent results with the Biot-Gassmann theory at low frequency and the Mavko and Jizba prediction at high frequency.

### 1.2.4 Fluid flow regimes and characteristic frequencies

The review of the theories of the fluid substitution problem can be summarised into a framework of fluid flow regimes and associated characteristic frequencies. With increasing frequency, a fluid-saturated rock is expected to experience successively the drained, saturated isobaric, and saturated isolated regimes, separated by two characteristic frequencies $f_{dr}$ and $f_{sq}$ (O'Connell & Budiansky, 1977; Sarout, 2012).

The characteristic frequency $f_{dr}$ associated with the transition from the drained regime to saturated isobaric regime is given by Cleary (1978) as:

$$f_{dr} = \frac{kK_f}{\phi\eta l^2}, \tag{1.5}$$

where $k$ is the permeability of the sample, $K_f$ is the bulk modulus of the pore-fluid, $\phi$ is the porosity of the sample, $\eta$ is the viscosity of the fluid, and $l$ is the typical dimension of the sample.

The characteristic frequency $f_{sq}$ associated with the transition from the saturated isobaric regime to the saturated isolated regime is given by (O'Connell & Budiansky, 1977; Palmer & Traviolia, 1980) as:

$$f_{sq} = \frac{K_0\alpha^3}{\eta}, \tag{1.6}$$

where $K_0$ is the bulk modulus of the mineral material making up rock, $\alpha$ is the aspect ratio of a crack, and $\eta$ is the viscosity of pore fluid.

When the fluid-saturated rock is subject to an oscillating hydrostatic (or uniaxial) stress at a frequency lower than $f_{dr}$, the fluid has sufficient time to flow out of the pore space of the rock, allowing the rock to behave as if it were completely dry. At $f_{dr}$, a macroscopic fluid flow occurs between the rock and an external reservoir allowing drainage of the rock. A bulk attenuation peak is expected to be associated with the draining transition. If the excitation frequency is higher than $f_{dr}$ but lower than $f_{sq}$, the fluid-saturated rock is in the saturated isobaric regime with sample-wide pore pressure equilibrium (Fig. 1.2 & 1.3). The elastic moduli for this regime are predicted by the Biot-Gassmann low-frequency limit, which gives an increase in bulk modulus but an unchanged shear modulus with fluid saturation (Fig. 1.3). The second transition occurs at $f_{sq}$, beyond which frequency the fluid pressure equilibrium cannot be achieved over the entire sample. This transition to the saturated isolated regime is indicated by a shear attenuation peak and a possible bulk attenuation peak (for pore-crack arrangement only). At a frequency higher than $f_{sq}$, local-scale squirt flow is completely prohibited, and no fluid communication is allowed between neighbouring inclusions. The transition from saturated isobaric to saturated isolated regime gives an increase in shear

modulus and a possible increase in bulk modulus (for pore-crack arrangement only). The inclusion based models (or effective medium theory), considering embedding a second phase into a matrix without fluid communication, is thought to be applicable to this regime.

In the framework, the change in modulus between the saturated isobaric regime and the saturated isolated regime is defined as the squirt-flow related dispersion. Similarly, the change in modulus between the drained regime and the saturated isobaric regime is defined as the global-flow related dispersion.

The Biot dispersion, as its transition occurs at a frequency at tens of MHz to a few GHz, is not considered in the framework illustrated here.

According to viscoelastic theory, attenuation and dispersion are related to each other by causality through the Kramers-Kronig relation (Fig. 1.3). Attenuation is normally associated with dispersion in modulus or velocity.

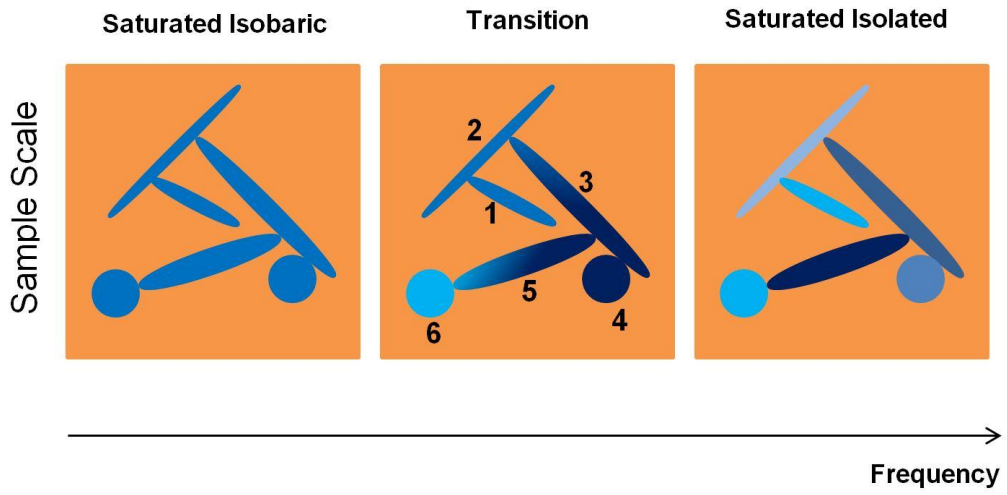


**Figure 1.2** A sketch of the spatial scales of fluid-flow regimes and the transition associated with squirt flow. The saturated isobaric regime involves fluid pressure equilibrium over the entire sample. An increasing frequency progressively limits the spatial scale of fluid pressure equilibrium, from a sample scale to the scale of neighbouring inclusions, before the fluid within each inclusion is completely isolated from its neighbours in the saturated isolated regime. In the transition, the fluid pressure gradient between adjacent inclusions is relaxed by squirt flow, and fluid pressure equilibrium can be achieved between some of the neighbouring inclusions (crack 1 & 2), but not all of them (inclusions 3-6) at the sample scale. The sketch is a schematic illustration of the scales of fluid equilibrium, and no particular mode of stress is considered.

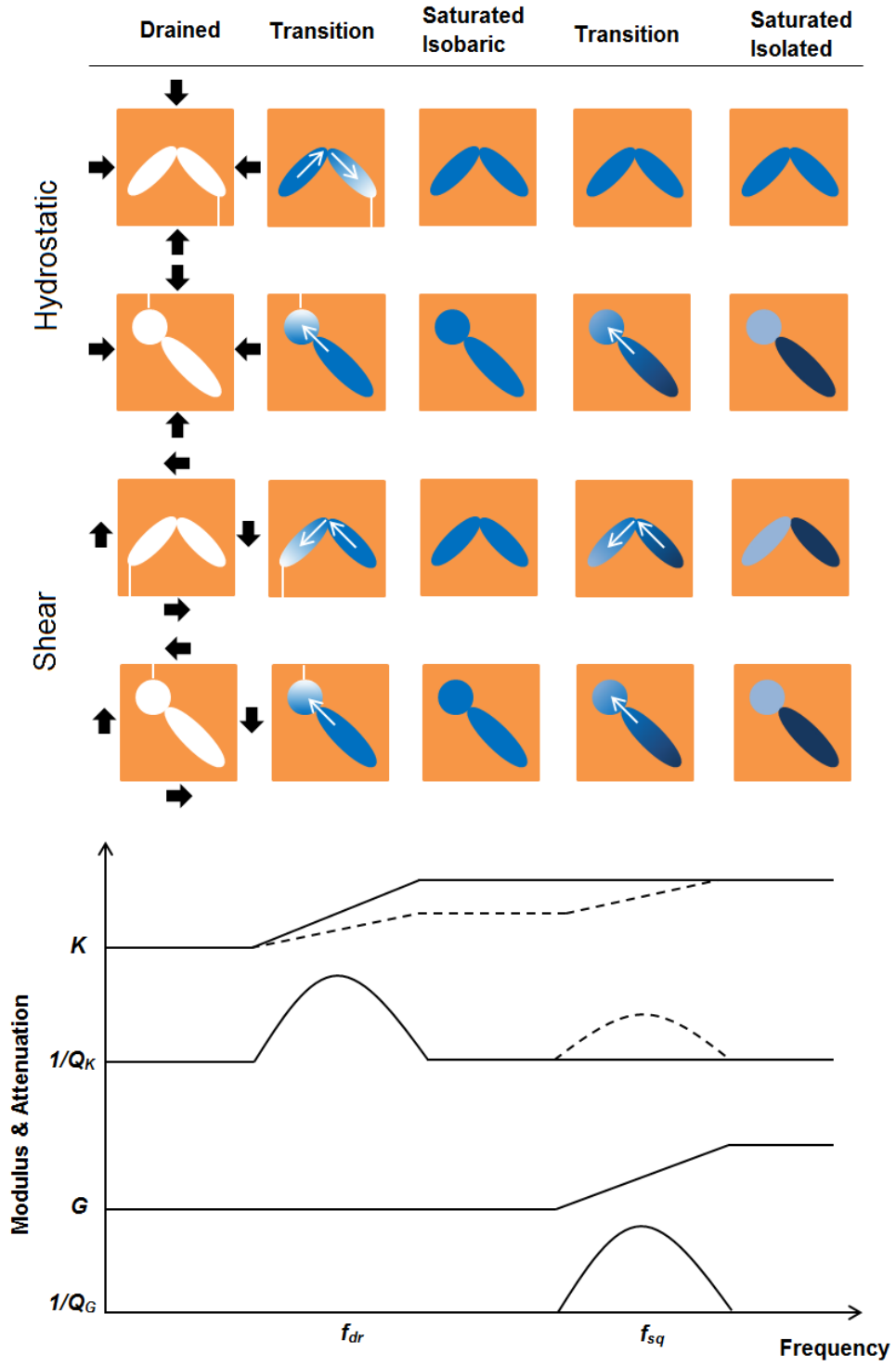


**Figure 1.3** Framework of fluid-flow regimes under either hydrostatic or shear stress, which consists of, with increasing frequency, the drained, saturated isobaric, and saturated isolated regimes. The framework has considered two types of inclusion arrangement: cracks only and a combination of cracks and pores. The darkness in colour in each inclusion indicates the magnitude of the pressure, and a darker colour corresponds to a higher pressure. Fluid flow and its direction during transition are indicated by arrows in the connected inclusions. The change in effective modulus and attenuation reflecting the transition of fluid-flow regimes on a fluid-saturated rock is also indicated (revised after Jackson, 1991, visualisation of the model given by O'Connell & Budiansky, 1977).

## 1.3 Experimental Techniques for Crustal Rock Deformation

In general, there are two broad categories of rock-deformation techniques in laboratory: 1) static rock deformation; and 2) dynamic rock deformation. They differ from each other in two major aspects: 1) frequency of applied stress: a constant force is applied to a sample in static rock-deformation experiments while a time-dependent stress is applied in dynamic deformation experiments; 2) strain amplitude: static deformation usually involves the strain amplitude of specimens up to $10^{-2}$, while mainly less than $10^{-6}$ for the dynamic deformation.

### 1.3.1 Static rock-deformation techniques

The triaxial apparatus for static deformation was pioneered by Von Kármán (1911). All the essential components of later triaxial machines can be found in this prototype. Thanks to major contributions especially from Griggs (1936) and Paterson (1970), the triaxial test has become a mature technique for static rock deformation in today's laboratory.

The design of a triaxial testing apparatus normally has a jacketed cylindrical rock sample exposed to confining pressure provided by either inert gas or hydraulic fluid. A superimposed uniaxial stress is applied by an axial actuator to one end of the sample. The shortening of sample is measured by a LVDT and the axial force is monitored by a load cell mounted together with the sample and the loading piston.

The static rock deformation in laboratory, determined by its physical mechanism, is more suitable to study the problems associated with the wellbore stability and in-situ stress field analysis rather than seismic interpretation.

### 1.3.2 Dynamic rock-deformation techniques

The dynamic modulus is reported different from the static one in laboratory due to the difference in strain amplitude and frequency. The dynamic measurement, in particular, the conventional ultrasonic wave-propagation method is the laboratory technique most analogous to the real seismic wave propagation in the field. The time-dependent fluid-solid interaction, which is crucial in seismic data interpretation, can only be studied by the dynamic techniques.

Boubié *et al.* (1987) have classified the dynamic techniques into three major types: 1) the travelling-wave method; 2) the standing-wave method; and 3) the forced-oscillation (or stress-strain) method.

The travelling-wave method, as indicated by the name, involves a pulse of elastic wave energy generated by a piezoelectric transducer at MHz frequency, travelling through the studied sample to a similar piezoelectric receiver, to determine the travel time of the pulse,

hence the P- and S-wave speeds. This technique is the dynamic method most widely used in laboratory. In contrast, resonance bar, as another important dynamic technique performed at kHz frequency, involves standing wave as the physical principle. The resonance frequency is directly detected in laboratory on a resonating sample, which can further yield wave speeds based on the relation between the resonance frequency, sample length, and wave speeds. The technical details of all these methods will be provided in *Chapter 3* in depth, while forced oscillation method at seismic frequency that readers may be less familiar with will be reviewed here in more detail.

Forced oscillation is needed in order to gain access to frequencies lower than kHz (*i.e.*, resonance frequencies in laboratory rock samples) to natural seismic frequency (mHz – 10 Hz). This method measures sample elastic properties in a much more straightforward way than the other two techniques described before by measuring stress and strain concurrently in situ to yield modulus as the ratio between them:

$$|M| = \frac{|\sigma|}{|\varepsilon|}, \tag{1.7}$$

where |M| is the magnitude of modulus, |σ| is the magnitude of stress, and |ε| is the magnitude of strain. The phases of the stress and strain are also measured, and the differential between them gives the phase lag between the applied stress and the resultant strain. The attenuation of the specimen in the form of the inverse of quality factor *Q* is estimated from the phase lag as:

$$\frac{1}{Q} = \tan(\Delta\,\varphi)\,, \tag{1.8}$$

where $\Delta\varphi$ is the phase lag between the applied stress and the sample strain.

Forced oscillation is simple in physical principle but difficult in laboratory implementation, especially under high pressure and temperature. Spencer (1981) constructed an instrument to measure the complex Young's modulus (*i.e.*, both the magnitude and the phase of Young's modulus) at seismic frequencies at ambient conditions. A similar design was used by Batzle *et al.* (1999), Mikhaltsevitch *et al.* (2011), and later Tisato and Madonna (2012). These Spencer-style machines may vary in some minor aspects, but in principle, all of them share the common feature of using an axial vibrator to apply forced oscillation at seismic frequencies on the end surface of a cylindrical specimen and the resultant longitudinal and circumferential strains are measured by transducers. Young's modulus and Poisson's ratio can be obtained from this technique.

In comparison, Jackson and Paterson (1993) and the ENS apparatus (Adelinet *et al.*, 2010) are exceptions. The former one applies torsional forced oscillation on a cylindrical sample to extract complex shear modulus, and recent improvement also allows it to perform

oscillating bending to obtain complex Young's modulus (Jackson *et al.*, 2011). The ENS apparatus involves an oscillating confining pressure, with the resultant volumetric change of a sample recorded, to yield complex bulk modulus.

All these forced-oscillation techniques share three essential components: 1) pressure system that provides independently varied confining and pore-fluid pressures; 2) dynamic system that apply a certain mode of forced oscillation to the tested sample; 3) measuring system that performs precision measurements of strain amplitudes of $10^{-6}$ or even less, providing access to the linear stress-strain regime for anelastic materials.

**The Spencer style apparatus**

The prototype of the Spencer apparatus (Spencer, 1981) is operated at ambient conditions. Independently varied confining and pore-fluid pressures are achieved by its followers (Batzle *et al.*, 1999; Mikhaltsevitch *et al.*, 2011; Tisato and Madonna, 2012; Madonna and Tisato, 2013). An actuator, either electromagnetic (Spencer, 1981; Batzle *et al.*, 1999) or piezoelectric (Mikhaltsevitch *et al.*, 2011; Tisato and Madonna, 2012; Madonna and Tisato, 2013), provides axial forced oscillation to a cylindrical sample at seismic frequencies. Stress is measured by either a commercial load cell (Spencer, 1981; Tisato and Madonna, 2012) or the elastic-standard method (Batzle *et al.*, 1999; Mikhaltsevitch *et al.*, 2011; Madonna and Tisato, 2013). The latter method involves connecting a specimen with an elastic standard of known moduli to determine the stress. The (longitudinal and/or circumferential) strain is measured by a series of different techniques, such as capacitive displacement transducers (Spencer, 1981), strain gauges (Batzle *et al.*, 1999; Mikhaltsevitch *et al.*), or LVDTs (Tisato and Madonna, 2012; Madonna and Tisato, 2013).

**The Jackson-Paterson style apparatus**

Two seismic-frequency torsion-mode apparatuses were developed separately at the Australian National University and Technical University Berlin (Jackson *et al.*, 1984; Jackson and Paterson, 1987; Jackson and Paterson, 1993; Paffenholz and Burkhardt, 1989). For torsion-mode forced oscillation, the studied specimen, similar to the Spencer type apparatus, is connected with an elastic standard in series. The differences lie in the direction of oscillation and resultant displacement. Instead of a longitudinal oscillating force applied by a shaker on the Spencer-type apparatus, a torque is provided by a pair of drivers working cooperatively at the end of the specimen-reference assembly. Tangential displacements of the specimen and the elastic reference are recorded in this case rather than the axial displacements on the Spencer-type apparatus.

Similar to the Spencer prototype, the Paffenholz and Burkhardt apparatus can only work at ambient conditions. In contrast, the Jackson and Paterson apparatus can reach confining pressure of up to 300 MPa and temperature of 1300 °C.

The Jackson and Paterson apparatus is equipped with a pair of electromagnetic drivers working at frequencies from ~1 mHz to ~1 Hz. A pair of piezoceremic drivers is installed on the Paffenholz and Burkhardt apparatus with nominal operating frequencies from 30 mHz to 100 Hz. But the equipment is reported to be subject to a supporting-frame resonance beyond 70 Hz, giving large uncertainties in measurement.

It is also necessary to mention that a further modification has been made on the Jackson-Paterson apparatus to incorporate the flexure-mode forced oscillation, yielding Young's modulus at seismic frequencies (Jackson *et al.*, 2011). This recent improvement provides an alternative, in addition to the Spencer style apparatuses, to measure Young's modulus at seismic frequencies. The use of the Jackson-Paterson apparatus forms an important part of this study, and the details of the arrangement and operation will be described in *Chapter 3*.

**The ENS style apparatus**

The apparatus located at the École Normale Supérieure, Paris is the only attempt so far for hydrostatic forced oscillation (Fortin *et al.*, 2005; Adelinet *et al.*, 2010; David *et al.*, 2013; Pimienta *et al.*, 2015). The apparatus is a commercial triaxial cell with independently controlled confining and pore-fluid pressure systems. The axial stress and confining pressure are separately servo-controlled by two hydraulic pumps (with an accuracy of 0.1 MPa) with the maximum pressures of 1 GPa and 300 MPa, respectively. The upstream and downstream pore-fluid pressures are servo-controlled by two precision volumetric pumps (with an accuracy of 0.01 MPa) with the maximum pressure of 100 MPa. The pore fluid is injected from one end of the specimen by the corresponding pump until the same fluid pressure is monitored on the other side of the specimen to ensure a thorough and uniform saturation of pore fluid within the specimen.

To implement the hydrostatic forced oscillation, with the axial piston idle, a small oscillating perturbation to the background confining pressure is applied by the servo-controlled pump. The pressure transducer for both confining-pressure monitoring and hydrostatic-stress measurements has an accuracy of 0.1 MPa. The axial and circumferential strains are measured by two strain gauges directly attached to the sample surface, working cooperatively to provide the volumetric strain of the sample through the relation:

$$\varepsilon_v = \varepsilon_a + 2\varepsilon_r \,, \tag{1.9}$$

where $\varepsilon_v$ is the volumetric strain of a specimen, $\varepsilon_a$ is the axial strain measured by the strain gauge attached longitudinally to the sample surface, and $\varepsilon_r$ is the radial strain (radial strain is equal to the circumferential strain) measured by the strain gauge attached circumferentially around the sample, perpendicular to the axial strain gauge.

At the end of the survey of the forced-oscillation techniques, it is also necessary to point out the common features in terms of the data acquisition and processing. For all apparatuses discussed above, the very small strain amplitude (normally less than $10^{-6}$), regardless of the type of transducer used, needs to be resolved by an electrical bridge, after signal amplification and analogue-to-digit conversion, and is finally recorded as a time series of stress and strain in a sinusoidal form. A Fast Fourier Transform (FFT) is then performed on the time series of stress and strain to extract the amplitudes and phases of the stress and the strain at the driving frequencies. The elastic modulus and attenuation are determinable by using Eq. (1.7) and (1.8).

## 1.4 Experimental Findings

Techniques of measuring modulus/wavespeed at various frequencies need to be combined in order to quantitatively study the dispersion and the attenuation related to the stress induced fluid flow in cracked media. Historically, the ultrasonic wave propagation is the first laboratory technique to provide reliable wavespeed measurements at MHz frequencies and still the most widely used method today. The development of resonant bar expands the frequency at which data are collected from MHz to kHz. This laboratory technique is of great interest for exploration geophysicists as it operates at a similar frequency as that for sonic logging in the field. The development of forced oscillation is a more recent story, which lowers the frequency range used in laboratory down to mHz to hundreds of Hz. The results yielded by forced oscillation are better correlated with the passive or active seismic data in the field. The Biot-Gassmann equation was commonly used in early studies to predict the elastic properties in saturated isobaric regime from dry ultrasonic wavespeed data.

### 1.4.1 Combined use of the ultrasonic measurement and the Biot-Gassmann theory

This is the most commonly used method in studying the fluid-flow related dispersion. It is a mix of theoretical prediction and laboratory measurement. The differential between the Biot-Gassmann prediction from the dry ultrasonic wavespeed and the fluid-saturated ultrasonic wavespeed provides the wanted dispersion. The Biot-Gassmann theory is assumed to capture the nature of the saturated isobaric regime, while the ultrasonic measurements are thought to provide the elasticity in the saturated isolated regime.

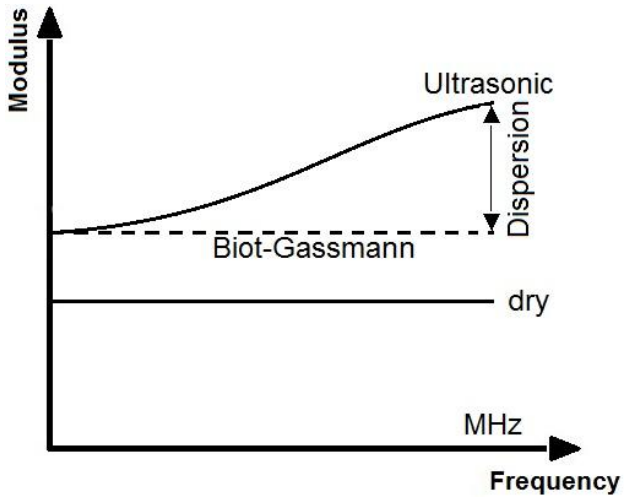


**Figure 1.4** A sketch of the semi-experimental method to estimate the dispersion of elastic properties on a cracked medium caused by stress induced fluid flow. In theory, the laboratory measurement (solid) and the Biot-Gassmann prediction (dashed) should converge at the low-frequency limit. The difference between them at high frequency gives the dispersion of modulus (after Winkler, 1986).

The validity of this method relies on no dispersion of elastic properties under dry conditions. Then it allows the use of the dry ultrasonic data as the input for the Biot-Gassmann theory to predict in the saturated isobaric regime. This assumption should always be true as long as the strain amplitude in measurement is less than $10^{-6}$ and no frictional energy loss at grain boundaries is activated (Winkler *et al.*, 1979).

Winkler (1985) used this method to study the dispersion in fused glass beads (not thermally cracked) and Berea sandstones. The former material with only spherical pores present is thought to be free of local fluid flow. The ultrasonic velocities for both fused glass beads and Berea sandstones were measured under dry, brine- and oil-saturated conditions. The Biot-Gassmann low-frequency velocities and the Biot high-frequency velocities are calculated based on the dry ultrasonic data. The Biot dispersion, which is defined as the difference between the low- and high-frequency velocities predicted by the Biot theory, has well explained the "apparent dispersion", defined as the difference between the predicted Biot-Gassmann low-frequency velocity and the measured ultrasonic velocity at high frequency, observed on the fused glass beads. It means that the measured dispersion on fused glass beads is solely caused by the Biot dispersion mechanism. But on Berea sandstones, the apparent dispersion is much larger than the predicted Biot dispersion. This may indicate the existence of another fluid-flow related relaxation mechanism besides the Biot mechanism, and the author interpreted this as an evidence for squirt flow on the grain scale.

In a later paper, Winkler (1986) standardised this method and applied it to more datasets in literature, *e.g.*, kerosene saturated Berea and Boise sandstones in King (1966),

water saturated Travis peak, Bandera, Berea, Gulf coast and Boise sandstones in Gregory (1976), *etc.*, to calculate the "total velocity dispersion" (TVD) which is equivalent to the "apparent dispersion" in the previous article. It shows that TVD for both P- and S-wave velocities can reach as high as 25% at low differential pressures, and this value may vary with different rock types and saturation conditions. TVDs on all the studied rocks are observed to decrease with elevated differential pressure, perhaps caused by the expulsion of fluid by crack closure at higher pressure. These universally observed TVDs are thought to be evidences for the local-flow (squirt) dispersion mechanism. This work provides bounds to the dispersion that can be expected in the commonly studied sandstones.

King *et al.* (2000) and King and Marsden (2002) employed a similar method to do an ultrasonic study on 44 sandstone samples cored from hydrocarbon reservoirs. P- and S-wave ultrasonic velocities were measured under dry and brine saturated conditions. The dry velocities are corrected for the matrix weakening caused by the absorption of moisture and then used as the input for the Biot-Gassmann low-frequency prediction. The ultrasonic velocity measured under brine-saturated condition is compared with the Biot-Gassmann prediction, and the difference between them (dispersion) is interpreted as the local-flow (squirt) effects. The crack-closure pressure for a spheroidal crack of aspect ratio $\alpha$ is given by Walsh (1965) as:

$$P = \frac{E_0 \pi \alpha}{4(1-\nu_0^2)} \approx E_0 \alpha \,, \tag{1.10}$$

where $E_0$ and $\nu_0$ are the Young's modulus and the Poisson's ratio of the material making up the matrix, respectively; and $\alpha$ is the aspect ratio of the crack. For microcracks with aspect ratio of about $10^{-3}$, the author estimates that the crack-closure pressure is ~ 40 MPa. Most of the increase in ultrasonic P-wave velocity with brine saturation is predictable by the Biot-Gassmann theory beyond 40 MPa, whereas a significant higher ultrasonic velocity is observed below 40 MPa, explained as the presence of brine in the open microcracks.

### 1.4.2 Resonant bar measurement at intermediate frequency

Resonant bar measures the wavespeeds on a cylindrical specimen at kHz frequency. Various frequencies around kHz can be achieved by either varying the length of the bar or using higher order of harmonics besides the fundamental mode of resonance.

In the late 1970s and early 1980s, a major question to answer associated with the attenuation mechanism in the upper part of the earth's crust is which mechanism, frictional sliding at grain boundaries or viscous pore-fluid flow, is dominant? To address this, the

resonance method was extensively used by the research group at Stanford University to conduct a series of studies on both natural sandstones and synthetic samples.

Winkler *et al.* (1979), Winkler and Nur (1982), Murphy (1982) clearly demonstrated that frictional loss at grain boundaries is not the dominant mechanism when strain amplitude is lower than $10^{-6}$. This claim is supported by the finding that the measured attenuation ($1/Q$) and the velocity on Berea sandstones are independent of strain amplitude below $10^{-6}$, but strain amplitude higher than the threshold significantly increases the attenuation and decreases the velocity.

To further confirm the viscous fluid flow as the dominant attenuation mechanism, Winkler and Nur (1982) measured extensional and shear velocities ($V_E$ and $V_S$) and corresponding attenuation ($1/Q_E$ and $1/Q_S$) at frequencies from 0.5 to 9 kHz on Berea, Massilon sandstones and Vycor porous glass with partial or full water saturation at room temperature, with pressure of up to 300 bars. With water saturation, the density effect on velocities and the influence of fluid-flow on attenuation have been observed. An attenuation peak is discovered at about 5 kHz on the water-saturated Berea sandstone, but no such feature noticed under dry condition. The observed attenuation in this study was noticed to be higher than that can be explained by the Biot dispersion. Therefore, the authors infer a second fluid-flow attenuation mechanism, *i.e.*, intra- or inter-crack fluid flow, from this departure. The shear attenuation ($1/Q_S$) of Vycor porous glass shows less sensitivity to the degree of water saturation. Vycor porous glass consists of spherical grains of ~ 50 nm in diameter and relatively noncompliant pores of ~ 4 nm in diameter. Such a structure has much less response to the applied stress, and weaker local fluid flow is induced by the oscillating stress.

Murphy (1982) studied Massilon sandstones and synthetic Vycor porous glass using a similar method at room temperature but ambient pressure. The measurements were conducted under both dry and water saturation conditions, and the percentage of saturation varied from "very dry" without absorption of moisture, "dry" with absorption of small amount of moisture, partial saturation, to full saturation. The frequencies of measurements cover a relatively broad range from 14 kHz to 300 Hz, with a complementary torsional pendulum method to extend the frequency to 25 Hz. Massilon sandstones and Vycor porous glass are found to be sensitive to both water saturation and frequency.

Fluid related mechanisms were adopted by the author to explain the change of velocities and attenuation with saturation and frequency: 1) surface, capillary film of moisture at grain contacts to explain the observed significant amount of reduction in velocity and associated attenuation peak during the initial absorption of moisture on the extremely dry granular samples. The free surface energy at grain contacts is thought to be significantly reduced due to the absorption of moisture. This mechanism is applicable to the saturation

degree of less than 1%. 2) viscous "squirt" flow to explain the extensional and shear attenuation peaks at ~2 kHz for Massilon sandstones and ~7 kHz for Vycor porous glass with a saturation degree of 2 to 100%. The value of attenuation *1/Q* of the Vycor porous glass is found to be only a tenth of that for Massilon sandstones, explained by the higher aspect ratio pores, hence less stress induced fluid flow in Vycor porous glass.

The influence of elevated temperature and pressure on velocity and attenuation on Berea sandstones was studied by Jones and Nur (1983). The fluid viscosity can be altered by temperature, which further changes the timescale of fluid flow. With the resonance method, the attenuation peak shifts from 2 kHz at room temperature to 8 kHz at 120 °C on the water saturated Berea sandstones. The characteristic frequency associated with the transition between the saturated isobaric and the saturated isolated regime is inversely proportional to fluid viscosity, *i.e.*, lower water viscosity at higher temperature raises the characteristic frequency to a higher level. The reconciliation between the theory and the observation again confirms that the local fluid flow as the dominant attenuation mechanism.

The work of Jones and Nur (1983) was extended by O'Hara (1985, 1989) to more non-dipole fluids, in contrast to brine as a dipole fluid, to study the fluid-matrix chemical reaction. The measured attenuation systematically increases with the product of frequency and viscosity, consistent with the finding reported by Jones and Nur (1983). However, the author preferred the fluid-matrix chemistry as the dominant attenuation mechanism, supported by two aspects of his findings. First, an air dried Berea sandstone was measured by resonance bar with a concurrent vacuum drying for a few days. A continuous reduction in attenuation was observed for the first 4 days before reaching a relatively stable attenuation level. This confirms the significant role of the fluid-matrix chemistry in attenuation (Clark *et al.*, 1980; Tittmann *et al.*, 1980). Second, at a given value of the product of frequency and viscosity, the attenuation for brine (dipole fluid) is about twice that for non-dipole fluid, indicating the role of fluid – matrix chemical interaction in attenuation mechanism.

Besides the sedimentary rocks, Murphy (1984) also performed resonance measurements on micro-cracked Sierra White granite under different water saturation conditions at 1-2 kHz. Similar to water-saturated Massilon sandstones and Vycor porous glass, Sierra White granite also shows strong dependence on frequency and degree of water saturation. The results demonstrate that the local-flow mechanism exists not only in sedimentary but also crystalline rocks as long as the contrast in microstructural compliance is present.

### 1.4.3 Combined use of resonance and ultrasonic methods

The frequencies used by resonance bar and the ultrasonic method usually differ by 2-3 orders of magnitude. The comparison of the wavespeeds collected by the two methods is expected to provide dispersion between kHz and MHz.

Jones and Nur (1983) not only performed measurement on Berea sandstones at kHz frequency with resonance bar but also introduced the ultrasonic method at MHz at high temperature. The amount of dispersion between kHz and MHz is much higher than the prediction based on the local fluid flow. It is suggested that a non-dispersive temperature softening of the shear modulus may exist, to account for the extra part of dispersion that is not explained by the fluid-flow relaxation.

Cadoret *et al.* (1995) also combined the two techniques in the study of partially saturated limestone, focusing on the influence of frequency and fluid distribution at ambient conditions. Limestones from eight quarries in France were cored with widely varying porosity (18 – 41%) and permeability ($8 – 4067 \times 10^{-15}$ m$^2$). At a given degree of saturation, P-wave velocity increases with frequency. Comparing the observation with theories, the Mavko-Jizba model associated with the squirt dispersion gives a better explanation than the Biot dispersion on most of the samples. But the dispersion on some of the samples is still significantly underestimated by the local-flow model. The discrepancy is interpreted as the "fast path dispersion" caused by the heterogeneity of water patches within the sample. The deformed wave front by the sample heterogeneity gives biased arrival time (smaller than the arrival time of the real wave front).

### 1.4.4 Forced-oscillation measurement at low frequency

Spencer (1981) performed a systematic measurement on various crustal rocks with fluid saturation in extensional forced oscillation at frequencies between 4 and 400 Hz. The measurements were conducted at contrasting temperatures to study whether the dispersion of Young's modulus and extensional attenuation is thermally activated. The samples were also saturated with different fluids (water, Ethonal, and *n*-decane).

Dispersion in Young's modulus and the related attenuation peak was observed on water-saturated Navajo sandstone, Oklahoma granite, and Spergen limestone. The attenuation peak shifts to higher frequency with elevated temperature. The Young's modulus is systematically reduced with fluid saturation, and the amount of modulus reduction is independent of the amount of fluid involved, *i.e.*, a tiny amount of water reduces the modulus as much as full saturation does. Water, Ethonal, and *n*-decane have similar densities and viscosities, but give different amounts of attenuation. Based on the findings,

the author argues that the Young's modulus dispersion and attenuation is not explained by the fluid mechanical mechanisms (the Biot dispersion or squirt flow), but rather a thermally activated mechanism and a chemical interaction between the fluid and the solid in changing surface free energy.

The seminal work by Spencer (1981) demonstrated the feasibility of performing forced oscillation measurement on fluid-saturated crustal rocks, and inspired the later studies. But some aspects of the method and the interpretation of results as a non-fluid-mechanical mechanism were questioned. White (1986) pointed out the attenuation peaks observed on the Navajo sandstone in Spencer (1981) could be a laboratory artefact simply caused by the open boundary of samples. White (1986) argues that global fluid flow could occur either at the open boundary of a sample or from the compressional side of the sample to the dilatational side in a bending test. The temperature dependency of the attenuation peak on the Navajo sandstone is also explained as a dependence on fluid viscosity rather than the initial explanation of thermally activated mechanism. Dunn (1986) developed formalism concerning the open bound condition and was later proved by laboratory measurements (Dunn, 1987). In his formalism, the drainage related frequency is proportional to the sample permeability, and inversely proportional to the fluid viscosity and the square of the sample radius. This recovers part of the expression of the characteristic frequency between the drained and the saturated isobaric regimes (Eq. 1.5). Dunn (1987) noticed the presence of the global flow associated with open boundary at ambient conditions even when the sample was properly sealed by aluminium metal jacket. The author claims that high pressure is needed to completely eliminate the global flow at the open sample boundary.

The open boundary problem has received careful treatment in later studies performed at low frequency. Samples are well jacketed and confined by pressure, allowing them to be free of global flow at radial directions. The top and bottom ends of a cylindrical sample are, in most designs, sealed with valves to isolate the sample from external reservoirs (Batzle *et al.*, 1999 & 2006; Adelinet *et al.*, 2010).

Mikhaltsevitch *et al.* (2014) measured complex Young's modulus and Poisson's ratio on sandstones with contrasting permeabilities at frequencies between 0.1 and 120 Hz. The sample of high permeability shows a good agreement with the Biot-Gassmann theory with water saturation at seismic frequency. For the samples of low permeability, dispersion of bulk modulus and associated extensional attenuation peaks are observed with water saturation and the Gassmann equation underestimates the bulk modulus when the fluid is beyond the transition. On one of the low-permeability samples, the attenuation peak shifts to higher frequency with increasing differential pressure, whereas the attenuation peak on another low-permeability sample is fixed at 0.8 Hz when the differential pressure is raised from 2.5 MPa to 15 MPa. The finding on both low-permeability samples disagrees with the

notion that lower crack aspect ratio, achieved by higher differential pressure, decreases the characteristic frequency between the saturated isobaric regime and the saturated isolated regime.

Delle Piane *et al.* (2014) performed low-frequency measurements ($10^{-2}$ – $10^{2}$ Hz) on shales with Spencer type apparatus described by Madonna & Tisato (2013). Preserved shale samples were cored with different orientation with respect to the bedding. The samples were tested both before and after dehydration. The compression/extension attenuation was observed to be significant in the direction perpendicular to the macroscopic bedding in both the preserved and dehydrated samples. In contrast to preserved samples, dispersion was noticed on the dehydrated (therefore partially saturated) samples at ~ 40 Hz when the stress perturbation was provided normal to the direction of bedding.

### 1.4.5 Combined use of forced-oscillation and ultrasonic methods

The development of the high-pressure forced-oscillation apparatuses makes it possible to compare the elastic properties of fluid saturated medium at frequencies below 1 kHz with those obtained at MHz frequency by the conventional ultrasonic method.

Batzle *et al.* (2006) realized that the way that a fluid-saturated rock responds to applied stress is decided by the status of fluid within the rock, *i.e.*, whether an equilibrium of fluid can be achieved and the spatial scale of fluid equilibrium within a half wave cycle. The authors therefore believe that the mobility of fluid is the key parameter to describe the time-dependent behaviour of fluid-saturated rocks. The capability of fluid moving in a rock is decided by not only the permeability of the rock (a property of the solid phase) but also the viscosity of fluid (a property of the fluid phase). Consequently, fluid mobility M is defined as the combination of the both factors:

$$M = \frac{k}{\eta}, \tag{1.11}$$

where $k$ is the permeability of a rock and $\eta$ is the fluid viscosity. It should also be noticed that the defined mobility is actually the coefficient of one-dimension Darcy's law (1856). Low fluid mobility is expected to give unrelaxed status (higher modulus of fluid-saturated rock) and high mobility would result in relaxed status of pore fluids (lower overall modulus) at a given frequency.

Batzle and co-workers used both the extension-mode forced oscillation and the ultrasonic wave propagation technique to measure moduli/velocities at 1-2500 Hz and 0.8 MHz, respectively. The permeability of a clay-rich rock and the viscosity of glycerine were varied in situ. Either higher permeability or lower fluid viscosity is found to increase the transition frequency that separates the relaxed and unrelaxed modulus.

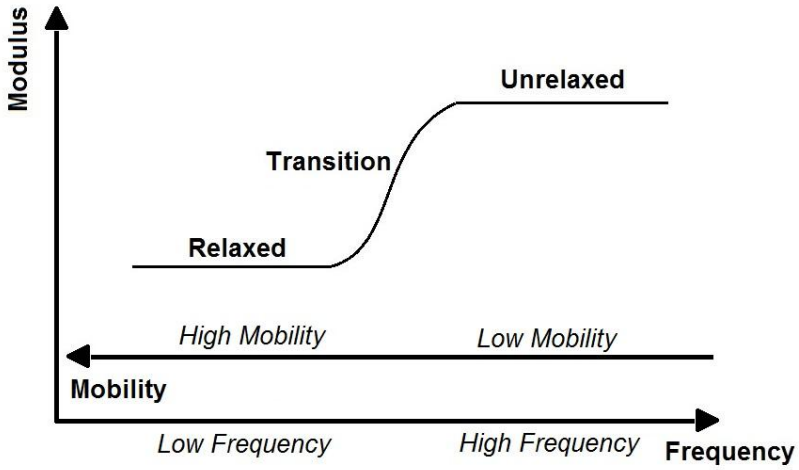


**Figure 1.5** Relation between modulus and fluid mobility (modified after Batzle *et al.*, 2006). The transition from the relaxed regime to the unrelaxed regime can be achieved by either an increase in frequency or a decrease in fluid mobility. An important implication from this framework is that stiffening due to unrelaxed fluid pressure could occur even at seismic frequency as long as the fluid mobility is low.

The experiments have proven, at least qualitatively, the relationship between modulus and fluid mobility. The framework based on the concept of fluid mobility has an important implication that a fluid saturated medium can become unrelaxed and contribute to the stiffening of the overall sample even at seismic frequencies for low-mobility rock-fluid combinations, *i.e.*, shales, tight sandstones and carbonates, heavy oil sands, *etc*. To this end, it means that the unchanged shear modulus with fluid saturation predicted by the Biot-Gassmann could become invalid even at very low frequency. Mikhaltsevitch *et al.* (2014) confirms this idea on low permeability sandstones with water saturation at frequencies between 0.1 and 120 Hz, with extensional attenuation peaks observed at a few Hz.

Adam *et al.* (2006, 2009) and Adam and Batzle (2008) report measurements on carbonates, as many of today's major oil and gas reservoirs are in carbonates. The combined use of extensional forced oscillation and ultrasonic method allows the access to frequencies of 3-3000 Hz and 0.8 MHz. The carbonate samples were saturated with light hydrocarbon (butane) and brine in sequence. The samples show little change in shear modulus with butane saturation as a non-polar fluid. With brine saturation, a systematic reduction in shear modulus has been noticed, explained as 1) a surface energy reduction due to chemical reaction between the polar fluid and the solid; and/or 2) subcritical crack-growth mechanism. The brine-saturated shear modulus increases with frequency, explained by the authors as 1) a fluid-mechanical mechanism associated with fluid flow (global- or squirt-flow); and/or 2) path-dependent overestimation in ultrasonic method as a wave preferentially propagates through the stiffest region of an heterogeneous sample, which gives an overestimated ultrasonic wavespeed. The Gassmann equation is found to work better for the bulk modulus

of brine saturated carbonates with less compressible microstructure (round pores or vugs) at higher differential pressure (~ 30 MPa) and seismic frequency.

Adam *et al.* (2009) reported the attenuation on various carbonate samples. The bulk dispersion $1/Q_K$ is systematically higher than the shear dispersion $1/Q_S$, consistent with the argument by Johnston *et al.* (1979) for connected crack-pore microstructure. This is explained as brine as a polar-fluid interacts with the solid matrix to open new grain contacts and soften certain parts of the rock. The increasing contrast in compliance in the sample creates higher pressure gradient, subsequently inducing more differential movement between the fluid and the solid. Second, the attenuation on most of the carbonate samples is frequency independent at seismic frequency, except one sample with the largest permeability which demonstrates a partial attenuation peak at seismic frequency. Third, by replacing non-polar fluid butane with polar brine, the bulk attenuation $1/Q_K$ increases by 250%, compared with only 7% change in $V_P$. It is argued that the bulk attenuation instead of the compressional wavespeed would be a better time-lapse indicator for reservoir flooding in the field.

The first attempt of performing hydrostatic forced oscillation on rock samples was reported by Adelinet *et al.* (2010) at ENS Paris. The bulk modulus of Icelandic basalt was obtained at 0.01 Hz, combined with an ultrasonic measurement conducted under the same pressure condition. The porosity of the basalt sample, determined by mercury injection, comprises both flat cracks (~ 1% crack porosity) and equant pores (~ 7% equant porosity) of ~ 0.1 μm and ~ 100 μm in pore entry diameter, respectively. The sample was fully saturated with water and the fluid pressure was maintained at 10 MPa throughout the measurement. With an increase in confining pressure from 10 MPa to 200 MPa, the bulk modulus at 0.01 Hz and P- and S-wavespeeds at 1 MHz were measured. Two major findings obtained: 1) the bulk modulus under drained condition is systematically lower than the dry modulus. The poroelastic theory predicts that the dry bulk modulus should be equal to the bulk modulus under drained condition. This departure is then explained as the rock-fluid physico-chemical interaction at grain boundaries and crack surfaces to reduce the surface energy, hence stiffness of the total rock. 2) The measured ultrasonic velocities are substantially higher than those predicted by the Gassmann equation by ~ 20%. This discrepancy is attributed to the squirt flow between connected equant pores and flat cracks. The characteristic frequency estimated for pore-fluid drainage is 25 Hz, significantly higher than 0.01 Hz at which the hydrostatic forced oscillation was performed. This again confirms that the bulk modulus measured at 0.01 Hz with water saturation is in the drained regime. The measured bulk dispersion on the Icelandic basalt is fitted by the model reported by Adelinet *et al.* (2011). The model considers bimodal microstructure, *i.e.*, equant pores and cracks. The squirt flow occurs between the two types of inclusions. The model relates the bulk and shear dispersion

between the saturated isobaric regime and the saturated isolated regime to the sample microstructure (crack aspect ratio) and the volumetric ratio between the two types of inclusions.

David *et al.* (2013) followed the same experimental strategy and performed measurements at mHz and MHz on two Fontainebleau sandstones with contrasting (total) porosities (4% and 13%). A thermal treatment (cooling the sample directly from 500 °C to room temperature) was performed on the 4% porosity sample to increase its crack porosity. Bimodal microstructure (with 0.4 μm and 7 μm in pore entry diameter) is detected by mercury injection porosimetry. Without thermal treatment on the sample of 13% porosity, a single pore entry diameter of 30 μm is detected. A static hydrostatic loading was performed on both samples to obtain pressure – volumetric strain curves. From the assumption of closable cracks and non-closable equant pores, any departure of the curve from linearity provides porosity of closable cracks. In such a way, crack porosities of 0.06% and 0.01% are estimated for the 13% and 4% (total) porosity samples, respectively. In general, both Fontainebleau sandstones are proven to consist of both non-closable pores and more compliant microcracks to induce squirt flow during periodic hydrostatic loading and unloading.

With forced oscillation, no bulk modulus stiffening is observed on either sample with either water or glycerine saturation at 0.02 Hz. This is explained as the oscillation frequency, *i.e.*, 0.02 Hz, is lower than the draining frequency. The theoretical prediction of this frequency is 2 kHz and 4 Hz respectively for 13% and 4% porosity samples with water saturation and 4 Hz and 0.01 Hz with glycerine saturation. The oscillation frequency is significantly lower than the estimated characteristic frequencies (except the glycerine saturated 4% porosity sample). The theoretical prediction confirms that the forced-oscillation experiments on both fluid-saturated Fontainebleau sandstones probe the drained regime. The bulk modulus with equilibrated pore fluid is predicted by the Biot-Gassmann equation from the dry modulus, the value of which is ~ 20% lower than that measured by the ultrasonic method, indicating the local-flow related dispersion of ~ 20%.

The results from the Icelandic basalt and Fontainebleau sandstones measured at ENS Paris are further summarised by Fortin *et al.* (2014). The Icelandic basalt and Fontainebleau sandstones share common feature in microstructure: with both spherical pores and compliant cracks present in favour of squirt flow between the two types of inclusion under hydrostatic forced oscillation. The findings in common are listed below: (1) The oscillation frequencies used, *i.e.*, 0.01 Hz for basalt and 0.02 Hz for sandstones, are lower than the draining frequency, giving no observable stiffening in bulk modulus at seismic frequency. The relation shown below is true on both basalt and sandstone:

$$K_{dry}^{HF} = K_{dry}^{LF} = K_{sat}^{LF} , \tag{1.12}$$

where $K_{dry}^{HF}$ is the bulk modulus calculated from the measured P- and S-wavespeeds at ultrasonic frequency, $K_{dry}^{LF}$ and $K_{sat}^{LF}$ are the measured dry and fluid-saturated bulk modulus at seismic frequency, respectively. (2) The local-flow related dispersion is estimated by the difference between the Biot-Gassmann prediction and the ultrasonic measurement. On average, this dispersion of bulk modulus is ~ 20% for both types of rocks. (3) The local-flow related dispersion is pressure dependent and decreases with elevated differential pressure. Cracks are gradually closed by increasing pressure, expelling fluid from the sample, hence progressively reducing the influence of fluid on the mechanical properties of the overall rock.

The maximum oscillation frequency of hydrostatic pressure is limited to sub-Hz, due to the capability of the servo-controlled hydraulic pump. This gives difficulty in detecting the saturated isobaric regime. From Eq. (1.5) (Cleary, 1978), the characteristic frequency can be effectively lowered by saturating a sample of lower permeability with fluid of higher viscosity.

Pimienta *et al.* (2015) performed similar measurements on two Fontainebleau sandstones, of ~7% and ~9% in total porosity, respectively. Unlike David *et al.* (2013), no extra thermal cracks is introduced into these sandstones. The experimental protocol, same as those used by Adelinet *et al.* (2010) and David *et al.* (2013), involves the combined use of hydrostatic forced oscillation at seismic frequency (0.004 – 0.4 Hz) and ultrasonic wavespeed measurement at 0.5 MHz.

No dispersion is found with water saturation, but gradual stiffening in bulk modulus with increasing frequency and associated attenuation peaks are noticed on both samples with glycerine saturation within the oscillation frequency band. The observed variation in bulk modulus and attenuation is explained as the transition from the drained regime to the saturated isobaric regime, supported by: (1) The oscillation frequency matches the cut-off frequency given by Cleary (1978) with glycerine saturation on the 7% porosity sample. (2) The Gassmann prediction well matches the measured bulk modulus at the highest frequency at 0.4 Hz on the 7% porosity sample, the value of which, in turn, is lower than the ultrasonic measurement at 0.5 MHz. (3) The measured pseudo-Skempton coefficient *B**, at sufficiently low frequencies, provides direct evidence for the pore fluid exchange between the pore space of the specimen and the external reservoir. The coefficient *B** is defined as:

$$B^* = \frac{\Delta P_f^*}{\Delta P_c} , \tag{1.13}$$

where $\Delta P_c$ is the change in confining pressure, and $\Delta P_f^*$ is the change in fluid pressure, induced by the change in confining pressure, measured at the outlet of pore-fluid lines. For a

given change in confining pressure, more fluid drained from a sample, hence more pressure build-up in fluid lines results in a higher pseudo-Skempton coefficient $B^*$, and vice versa. The measured $B^*$ decreases monotonically with frequency from 0.8 at 0.004 Hz to almost zero near 0.4 Hz at differential pressure of 1 MPa on the 7% porosity sample. It is consistent with the notion that the drainage of fluid is suppressed by higher frequency. The glycerin-saturated sample eventually approaches the undrained saturated isobaric condition at the highest oscillation frequency of 0.4 Hz, indicated by the near zero value of $B^*$.

### 1.4.6 Combined use of laboratory measurement and field observation

In some cases, the ultrasonic wavespeeds obtained in laboratory are directly compared with the field data collected by vertical seismic profiling (VSP) or sonic log at tens of Hz to a few kHz.

Moos and Zoback (1983) noticed a 20% velocity differential between the field data by VSP and the ultrasonic wavespeeds obtained in laboratory. Murphy (1984) performed ultrasonic measurements on micro-cracked granite in laboratory and compared the results with the field data by VSP. "Intrinsic dispersion" is defined in a similar way to Winkler (1985, 1986) as the difference between the Biot-Gassmann low-frequency prediction and the ultrasonic measurement. It is found that the dispersion between the VSP data and the ultrasonic wavespeeds is at least a factor of four greater than the intrinsic dispersion. The intrinsic dispersion is related to the local fluid flow, and the extra part of dispersion is explained as an issue about sampling resolution. The sonic log data are acquired on the entire rock mass probably containing macroscopic fractures, whereas the geometry of the cored sample is limited and possibly free of macroscopic fractures. The missing fractures in the cored sample may explain the extra amount of dispersion beyond the intrinsic dispersion. On the other hand, the extra dispersion observed between the sonic log data and the ultrasonic wavespeeds in laboratory may work as an indicator for the presence of macroscopic fractures in the field.

Sams *et al.* (1997) is the first attempt to make measurements of velocities and attenuation over the entire range of frequencies from seismic to ultrasonic on sedimentary rocks. In contrast to the broadband measurements conducted in laboratory only, the authors compared the ultrasonic measurements in laboratory with in-situ data collected at a borehole test site in northeastern England. Four different techniques operating at different frequencies were used in this study: VSP within the frequency range 30-280 Hz, cross-hole surveys at 0.2-23 kHz, sonic logging at 8-24 kHz, and laboratory measurements at 300-900 kHz. Similarly, the sampling issues have also been encountered in this research: 1) bias due to the disintegration of soft mudstones during coring; 2) bias because of the presence of a

macroscopic fault with a 10 m throw in the field, the information of which is not reflected in the cored samples. A series of corrections and averaging has been done to account for the influence of coring on velocity and attenuation before comparing the laboratory ultrasonic data and the field measurements. A systematic increase in velocity (both P- and S-wave) from seismic to ultrasonic frequencies (dispersion) has been observed. The attenuation is found to maximise at about 10 kHz. The dispersion and attenuation are assumed to be associated with local viscous flow and therefore fitted by the models suggested by Jones (1986) and Mavko and Jizba (1991), which predict the influence of local fluid flow on velocity and attenuation. This study, although uncertainties still present in the collection and the correction of the field data, confirms qualitatively the local flow induced dispersion and attenuation.

## 1.5 Synthetic Samples

Most of the past research has been conducted on natural rocks cored from the field. However, the mineralogical and microstructural complexity of natural rocks makes it difficult to isolate a single physical mechanism of interest from the others. In this context, synthetic samples are attractive for their simpler mineral composition and microstructure. In the study of porous medium, especially the influence of microstructure and fluid saturation on mechanical properties, it is highly desirable to control the quantity and shape of pores and cracks in a synthetic sample.

The first type of method (Rathore *et al.*, 1994; Tillotson *et al.*, 2012; Amalokwu *et al.*, 2014; Ding *et al.*, 2014) involves the preparation of a solid matrix from loose sand grains and cement materials (either epoxy or sodium silicate), which has aluminium discs embedded inside. The aluminium discs are leached out by acid to leave penny-shaped voids in the solid matrix. In this way, well aligned layers of penny-shaped cracks are fabricated within cemented sands. The orientations of crack embedded layers are well managed, making it ideal to test the shear-wave anisotropy on these synthetic sandstones.

Another popular method involves the use of spherical glass beads, either loose or sintered. Soda-lime-silica glass is the most commonly used glass in daily life, *e.g.*, window and container glass. Sodium carbonate (soda) is added into silicon dioxide (silica) to lower its melting point from ~1700 ℃ to 500-600 ℃. Calcium carbonate (lime) is also added into the molten mixture to make it water insoluble. Soda-lime-silica glass, therefore, is mainly composed of $SiO_2$ (~75% by weight), $Na_2O$ (~15%), and CaO (~10%). Natural sandstone has a very high percentage of silica ($SiO_2$). If the "sedimentary differentiation" process is strong enough, sandstones composed of even 100% quartz can be obtained (Guéguen and

Palciauskas, 1994). Therefore, the high percentage of silica of soda-lime-silica glass makes it an ideal analogue to natural sandstones in the mineralogical sense.

In laboratory studies, loose glass beads are commonly used to simulate the unconsolidated porous sand reservoirs (Wyllie *et al.*, 1956; Domenico, 1977) and unconsolidated marine sediments (Richardson *et al.*, 2002), or to verify various theoretical models, taking the advantage of the well-characterised geometry (Plona, 1980; Johnson & Plona, 1982; Palciauskas, 1992; Bouzidi and Schmitt, 2009). The lowest porosity that can be achieved by compacted but unfused spherical glass beads of uniform diameter is ~ 38% (Guéguen and Palciauskas, 1994). This implies that sintering is needed to reach a porosity of less than 38%. In terms of the mechanical measurement, loose glass beads can be placed in a holder, subject to an ultrasonic pulse transmission, but are not well suited to measurements by resonance or forced-oscillation methods due to the lack of overall mechanical integrity.

In sintering, glass beads of a uniform size are held in a heat-resistant mould, heated to a temperature between 650 ℃ and 800 ℃, above the glass transition temperature (520 – 600 ℃). Lower porosity can be achieved by lengthening the duration of heating. A progressive cooling with controlled rate is required to prevent thermal cracks. The strategies of fusing glass beads are similar in the previous studies (Sen *et al.*, 1981; Johnson & Plona, 1982; Berge *et al.*, 1995). A minimum porosity of ~1% by sintering is reported by Berge *et al.* (1995).

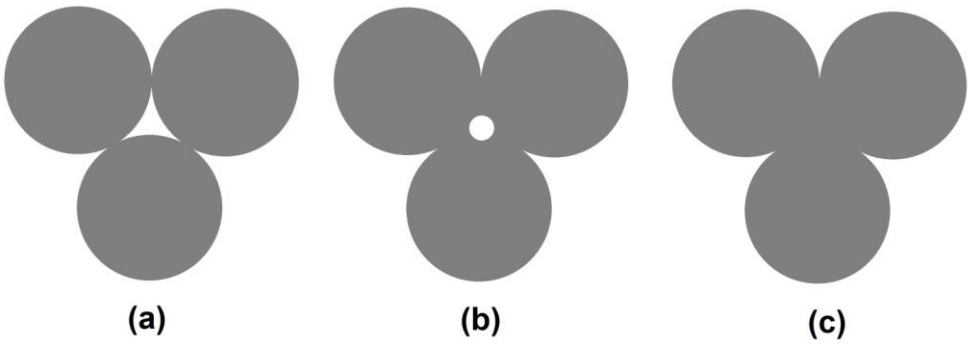


**Figure 1.6** Degree of fusion for glass beads can be controlled by varying the temperature and duration of heating. With increasing temperature or/and duration of heating, an aggregate of glass beads with (a) fusion at contact points only to form a consolidated frame; (b) spherical pores; (c) fully-dense status can be achieved progressively.

A main interest in fabricating synthetic specimens is to have controllable microstructure, *i.e.*, the quantity and shape of pores and cracks. The equant porosity can be varied by changing conditions of sintering. The inter-granular pore shape also depends on the temperature and the timescale of sintering. A spherical or quasi-spherical pore (Fig. 1.6b) can be achieved by an appropriate temperature and time length of sintering before glass beads are completed fused together (Fig. 1.6c). Besides equant pores, cracks are also

achievable in laboratory. Thermal cracks can be introduced to an intact specimen, given sufficient thermal expansivity to create necessary thermal stresses, by a rapid decrease in temperature, *i.e.*, quenching. This strategy has proved to be able to create cracks with uniformly low aspect ratio (~$10^{-4}$), but less manageable in terms of the randomness of orientation and the precise quantity of cracks if compared with the first crack-making method (embedded aluminium disks and chemical dissolution).

## 1.6 Research Outline and Aim of Study

To sum up the review, on the theoretical side, a framework of fluid-flow regimes has been proposed with the explicitly expressed characteristic frequencies. The importance of squirt flow at the grain scale in explaining the dispersion between the saturated isobaric regime and the saturated isolated regime has been emphasized. The theory indicates the crucial roles of inclusion geometry and fluid viscosity in squirt flow. Among the experiments attempting to test the framework, few of them had access to the entire frequency band from mHz, kHz, to MHz frequencies, and most of them mainly focused on the natural crustal rocks with relatively complex mineralogical composition and microstructure. Based on the theoretical and experimental considerations, a new study is proposed, in which we are aiming for:

1) Fabricating and measuring on synthetic soda-lime-silica glass samples with the presence of well characterised bimodal microstructure (equant pores and cracks) well-suited to squirt flow;
2) Saturating the synthetic samples with fluids of contrasting viscosity, *i.e.*, argon and water differing in viscosity by ~ 30 times (at the fluid pressure of 10 MPa and room temperature) to vary the timescale of fluid flow;
3) Performing a genuine broadband measurement from mHz, kHz, to MHz frequencies, by the combined use of forced oscillation, resonance bar, and ultrasonic wave transmission;
4) Measurements on a series of samples with various equant porosities to study the influence of crack-pore microstructure on the fluid-flow related dispersion;
5) Quantitatively determine the amount of dispersion between mHz and MHz.

In this study, only the physical interaction between the fluid phase and the solid phase is focused on. The study also only considers the full saturation problem. Therefore, the chemical interaction between the fluid and the solid, the phase transformation of the matrix, mineral melting, preferred orientation of cracks, and partial saturation are all beyond the consideration in designing the experiment, although some of them might be taken into account in interpreting the results.

In this dissertation, the synthetic sample preparation and characterisation are described in *Chapter 2*. The broadband techniques, including forced oscillation, resonant bar, and ultrasonic wave propagation, and in-situ permeability measurement are introduced in *Chapter 3*. From *Chapter 4* to *7*, the results of the permeability, the moduli at low frequency, high frequency, and intermediate frequency are presented in sequence. In *Chapter 8*, the results are assimilated, interpreted and modelled. The study concludes in *Chapter 9* with the major findings and the direction in which this study could be extended in future.

# Chapter 2 Sample Preparation and Characterisation

## 2.1 Synthetic Samples

The occurrence of stress-induced squirt flow of pore fluid requires the spatial variation in compressibility of the void space in a solid. A local fluid pressure gradient, as the driving force for squirt flow, is generated between more compliant regions (*e.g.*, cracks) and less compliant regions (*e.g.*, equant pores) within the solid when a stress is applied appropriately. It is natural, therefore, to design an experiment to test a series of synthetic samples with varying crack-pore microstructure, in order to characterise squirt flow and the influence of inclusions on squirt flow in a more controlled and quantitative way.

To this end, this study involves the fabrication of and measurements on three sets of synthetic samples, categorised by the presence of equant pores and cracks, in different concentrations. In general, all these synthetic samples are made of soda-lime-silica glass, starting from either a fully dense glass rod or an aggregate of glass beads of a uniform size.

The first type of material starts as a fully dense soda-lime-silica glass rod with no equant pores present. Subsequent thermal cracking yields a limiting case of microstructure, *i.e.*, a specimen with cracks only (schematically illustrated in Fig. 2.1 a). The other materials contain both equant pores and cracks. Sintering of soda-lime-silica glass beads provides specimens with low equant porosities near 2% (Fig. 2.1 b) and 5% (Fig. 2.1 c).

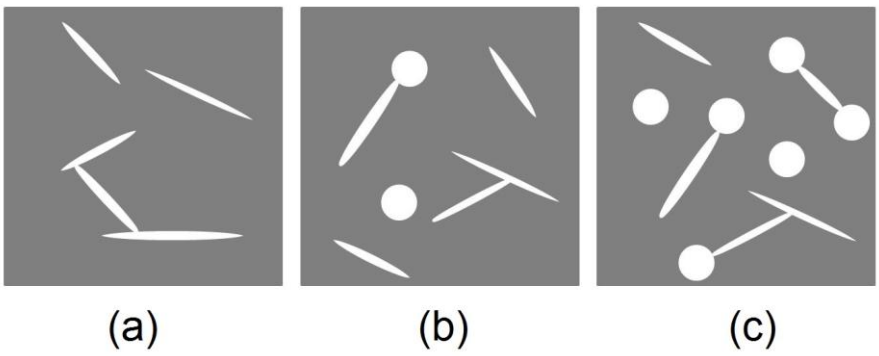


**Figure 2.1** A cartoon to illustrate the three types of soda-lime-silica glass samples involved in the project. (a) A thermally cracked glass-rod sample containing no pores; (b) A sintered glass-bead sample with both cracks and a relatively low concentration (~ 2%) of equant pores; (c) A sintered glass-bead sample with both cracks and a relatively high concentration (~ 5%) of equant pores.

## 2.2 Sample Preparation

### 2.2.1 Soda-lime-silica glass-rod specimen

2.2.1.1 Soda-lime-silica glass rods

A batch of soda-lime-silica glass rods was supplied by Nadège Desgenétez of the Glass Workshop, School of Art, Australian National University. The glass rods, as the raw material for the preparation of pore-free samples, are visually transparent. Minor internal flow structures are found in parts of these glass rods, and specimens were prepared from the more uniform segments to ensure isotropic properties. The chemical composition of the glass rods is determined by an Electron Microprobe (EMP) analysis and listed in Table 2.1.


**Figure 2.2** The raw soda-lime-silica glass rods with a diameter of either ~ 20 mm (upper) or ~ 40 mm (lower), which were later precision ground into cylindrical specimens for measurements.

Glass rods of ~ 20 mm diameter (Fig. 2.2, upper) were precision ground and tested in ultrasonic wave transmission and forced oscillation experiments, whereas rods of ~ 40 mm diameter (Fig. 2.2 lower) were precision ground and measured by the resonance technique.

The specimen to be tested with the ultrasonic wave transmission method requires a length of 50 mm and a diameter of 15 mm (Fig. 2.3 a). A sample with larger dimension, 76.2 mm (3 inches) in length, and 38.1 mm (1.5 inches) in diameter, is needed for the resonant bar test (Fig. 2.3 b). The forced oscillation method needs a specimen of 150 mm in length and 15 mm in diameter (Fig. 2.3 c).

Table 2.1 Major Chemical Components of Raw Glass Materials

| Material | Chemical Composition (weight%) of Major Components | | | | | |
|---|---|---|---|---|---|---|
| | $SiO_2$ | $Na_2O$ | CaO | $Al_2O_3$ | $K_2O$ | MgO |
| Glass rod* | 79.6 ± 1.5 | 12.1 ± 4.3 | 4.9 ± 0.2 | 1.1 ± 0.1 | 0.9 ± 0.1 | 0.0 ± 0.0 |
| Glass beads** (300 – 350 μm) | 71.8 | 12.8 | 7.7 | 2.8 | 0.5 | 2.3 |
| Glass beads* (180 – 211 μm) | 75.4 ± 1.5 | 10 ± 2 | 9 ± 3 | 2.7 ± 1.1 | 0.6 ± 0.3 | 0.5 ± 0.6 |

*Chemical compositions determined by electron microprobe (EMP).
**Chemical composition determined by scanning electron microscope (SEM) (Olin, 2011).

2.2.1.2 Thermal cracking

To introduce cracks into the precision ground cylindrical samples, a process of quenching from high temperature was performed on these uncracked samples. The strategy of thermal cracking is applicable to both glass-rod and glass-bead specimens. An uncracked specimen is firstly heated at 500 °C (*cf.* 330 ℃ used for borosilicate glass by Ougier-Simonin *et al.*, 2011) in a furnace for 2 hours, followed by removal from the furnace and plunging into liquid water at room temperature. Thermal stresses occur within the specimen due to the temperature gradient created between the centre of the specimen remaining at 500 °C and the outer surface of the specimen, in contact with water, at room temperature. Cracks, caused by such thermal stresses, develop throughout the specimen at the moment of quenching, but mechanical integrity is maintained.

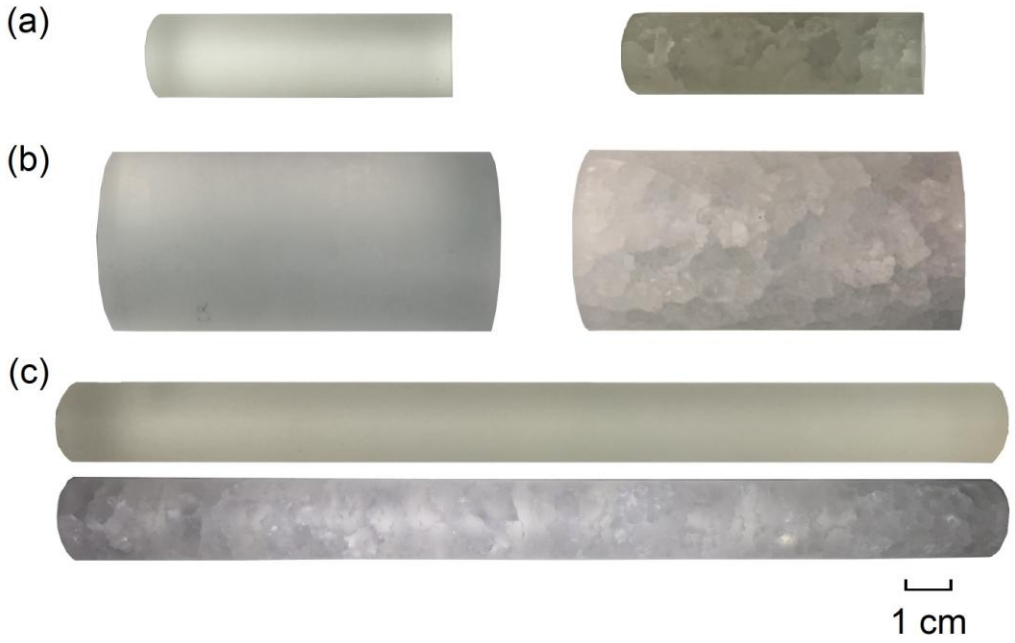


**Figure 2.3** Soda-lime-silica glass-rod samples, with different dimensions, mechanically tested before and after thermal cracking. A specimen for (a) ultrasonic wave transmission tests of 50 mm in length and 15 mm in diameter; (b) resonant bar tests of 76.2 mm (3 inches) in length and 38.1 mm (1.5 inches) in diameter; (c) forced oscillation tests of 150 mm in length and 15 mm in diameter.

A specimen dilates due to the presence of newly introduced thermal cracks. By comparing the volume of specimen determined by mensuration before and after thermal cracking, the fractional increase in the specimen volume, contributed by the newly developed thermal cracks, is determinable. This fractional increase in the volume of a sample is the crack porosity $\phi_c$ of the sample.

$$\phi_c = \frac{V_c - V_u}{V_u}, \tag{2.1}$$

where $V_u$ and $V_c$ are the volumes of the specimen before and after thermal cracking, respectively.

### 2.2.2 Low-porosity soda-lime-silica glass-bead specimen

2.2.2.1 Glass beads

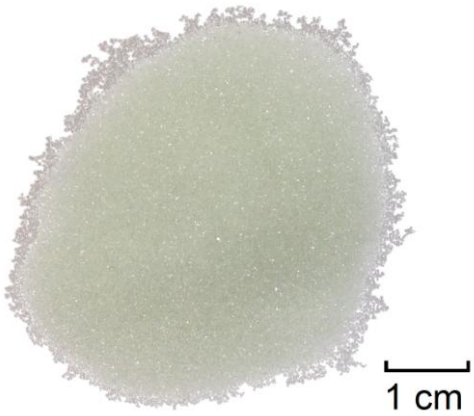


**Figure 2.4** Soda-lime-silica glass beads used in this project, which will undergo the process of sintering to achieve consolidation.

The glass beads (Fig. 2.4) used in the project are commercial products used for sand blasting and supplied by the Engineering Workshop, Research School of Earth Sciences, Australian National University. The chemical composition of the glass beads is determined by a Scanning Electron Microscope (SEM) analysis (Olin, 2011) and listed in Table 2.1. Metallic contaminants are also seen in some of the raw glass beads, most of which are removed with a magnet before sintering.

2.2.2.2 Glass bead sintering

For unconsolidated glass beads of a uniform size, the lowest achievable porosity is ~ 38%. Sintering can assist in lowering the porosity of glass beads to a level below this limit.

The glass beads for sand blasting vary widely in diameter, and only those with diameters between 300 and 350 μm are sieved for sample fabrication. A cylindrical mould accommodates the glass beads during sintering (Fig. 2.5). A glass tube serving as the mould has a height of 100 mm and an inner diameter of 22 mm. The glass tube is held vertically by an alumina ring, further supported on an alumina pedestal. The tube is lined with an aluminium foil to separate the glass beads from the glass tube to avoid sintered contact during heating. Once the glass tube is filled with glass beads, the entire sintering jig is subjected to vibration to compact the glass beads before being placed in a furnace. The compaction of glass beads minimizes the possible porosity gradient along the axis allowing homogeneity of the sintered sample.

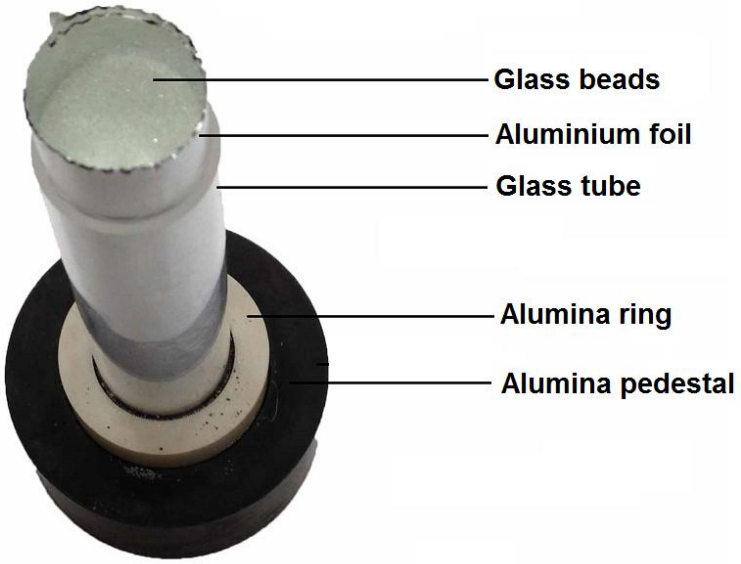


**Figure 2.5** The sieved glass beads are loaded into a cylindrical mould for sintering. The glass beads are sintered by following a carefully designed protocol for the periods of heating and cooling.

Sintering is done near the soda-lime-silica glass transition temperature of 500 – 600℃, so that the surface energy of an individual glass bead is reduced, causing coalescence of adjacent beads. But the transition temperature of the glass beads inferred from this experiment seems to depart slightly from the reported values. Prior tests show the beads begin to soften appreciably at 680℃, soften slowly and controllably at 690℃, and soften readily at 700℃ (Olin, 2011).

Porosities are found to be not only related to the temperature of sintering but also the duration of sintering, with lower porosities achieved by lengthening the sintering time (Sen *et al.*, 1981). Olin (2011) found that glass beads sintered for up to 6 hours retain high porosities up to 15%, but 2 – 3% residual porosity is achieved by lengthening the sintering time to longer than 24 hours.

| Process | | Temperature, ℃ | Duration |
|---|---|---|---|
| Heating | I - Ramp up | 300 | 1.5 h |
| | | 400 | 1 h |
| | | 500 | 1 h |
| | | 600 | 1 h |
| | | 650 | 0.5 h |
| | II - Dwell | 700 | 18 h |
| Cooling | III - Ramp down (Controlled) | 680 | 20 min |
| | | 660 | 20 min |
| | | 640 | 20 min |
| | | 620 | 20 min |
| | | 600 | 20 min |
| | | 580 | 20 min |
| | | 560 | 20 min |
| | | 540 | 20 min |
| | | 520 | 20 min |
| | IV - Natural cooling | 500 – room temperature | 3-4 h |

**Table 2.2** The protocol for sintering soda-lime silica glass beads. The temperature is increased from room temperature to 700 ℃ progressively. Sintering occurs during the temperature dwell at 700 ℃ for 18 hours before a controlled cooling allowing the temperature to decrease to 500 ℃. After that, the furnace is turned off and a natural cooling takes place until reaching room temperature.

In order to maintain the mechanical integrity of the sample and avoid thermal cracks after sintering, a thermal protocol of gradual and slow cooling needs to be followed (Table 2.2 & Fig. 2.6). The temperature is progressively increased from room temperature to 700 ℃ with an 18 hour dwell before temperature is decreased stepwise to 500 ℃, followed by a natural cooling to room temperature.

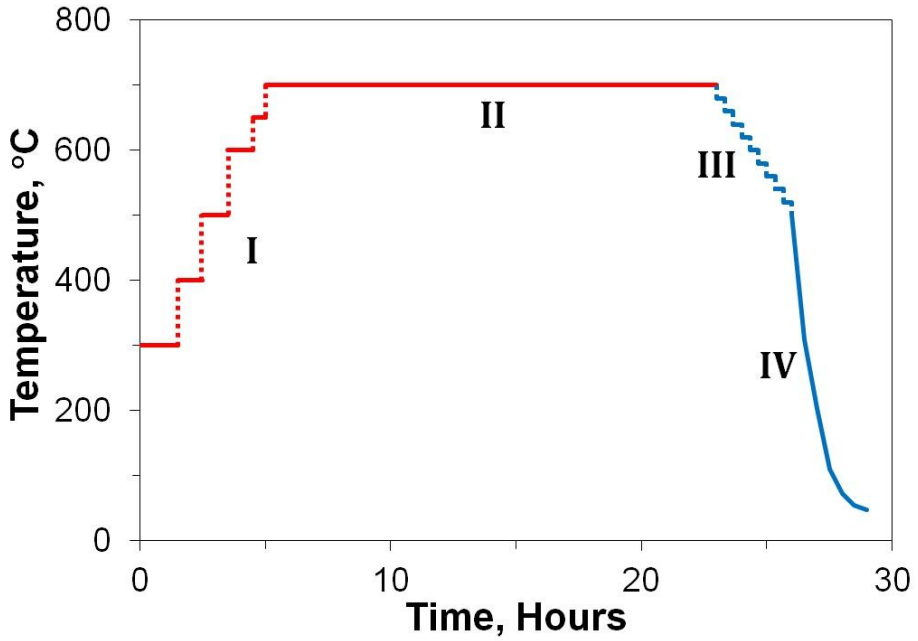


**Figure 2.6** A graphical illustration of the thermal history for glass-bead sintering. The process of heating (red) consists of a progressive increase in temperature from room temperature to 700 ℃ (Stage I) followed by a dwell (Stage II). The controlled cooling (Stage III) takes the temperature down to 500 ℃, followed by a natural cooling until reaching room temperature (Stage IV).

The aggregate of sintered glass beads (Fig. 2.7 a) is retrieved from the glass mould. After that, the sintered glass-bead aggregate is precision ground into a cylindrical shape with a length of 50 mm and a diameter of 15 mm (Fig. 2.7 b) to allow the measurements with either forced oscillation or ultrasonic wave transmission. In order to obtain a better coupling between the specimen and the other components of a testing machine, especially the apparatus for forced oscillation, both ends of the specimen are lapped with diamond paste (1 μm or 3 μm) to optical flatness. Due to the limited dimension of the furnace for sintering, a cylindrical specimen can be fabricated with the maximum length of 50 mm.

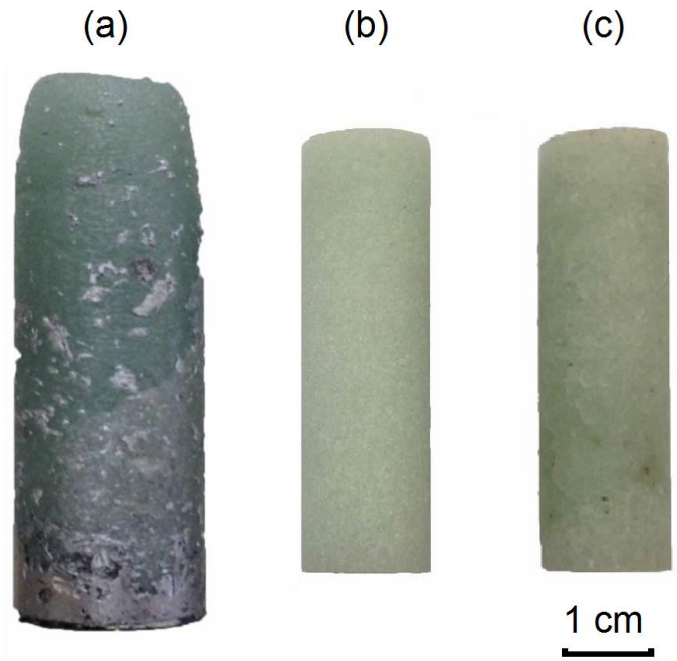


**Figure 2.7** (a) The aggregate of sintered glass beads, recovered from the mould, has a rough cylindrical shape. The grey material attached to the sample surface is the remaining aluminium foil melted during the sintering. (b) The glass-bead sample, after being precision ground, has a length of 50 mm and a diameter of 15 mm. (c) The same glass-bead specimen after thermal cracking with an observable crack network throughout the entire specimen.

2.2.2.3 Thermal cracking

The thermal cracking performed on the glass-bead samples follows the same strategy as for the glass-rod samples, *i.e.*, quenching the specimen, after being heated at 500 ℃ for 2 hours, into liquid water at room temperature to introduce thermal cracks (Fig. 2.7 c). In contrast to the glass-rod specimens, equant pores already exist in the glass-bead specimens before cracking. The equant pores present in the uncracked glass-bead specimens are largely isolated. The process of quenching introduces cracks which create partial connectivity of the previously isolated pores.

### 2.2.3 High-porosity soda-lime-silica glass-bead specimen

The high-porosity (~5%) samples were sintered from a second batch of glass beads of smaller diameter. The chemical composition of such glass beads was determined by electron microprobe (EMP) and listed in Table 2.1. Following the same procedure as that described for the low-porosity glass-bead specimens, the glass beads were sieved to 180 μm to 211 μm and sintered (Fig. 2.8 a & b). The thermal protocol used for the first batch of glass beads was found to provide higher equant porosity of ~ 5% for the second batch of finer glass beads. Following a precision grinding, the aggregate of sintered glass beads was re-shaped into a

cylinder of 50 mm in length and 15 mm in diameter (Fig. 2.8 c). The same strategy for thermal cracking was applied to the high-porosity glass-bead specimen (Fig. 2.8 d).

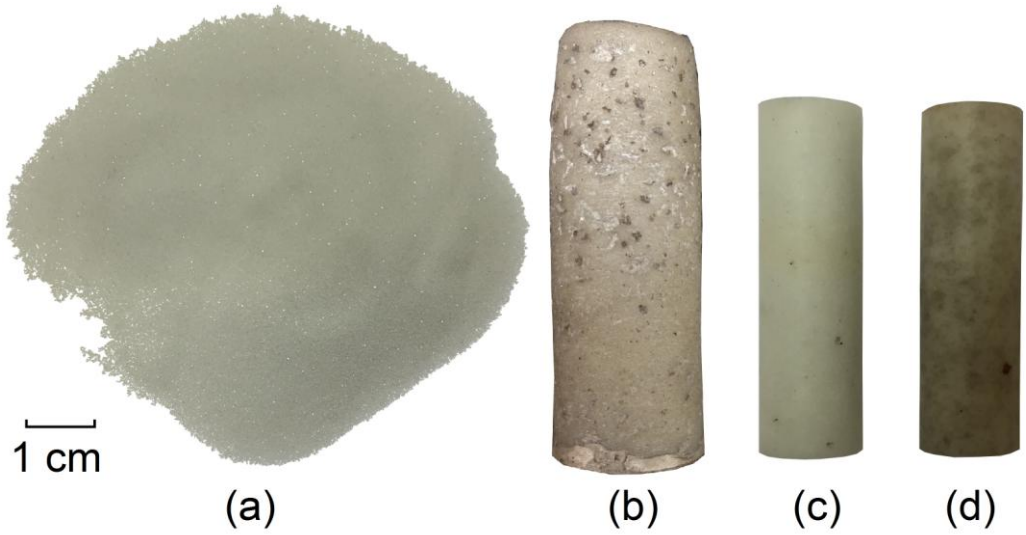


**Figure 2.8** (a) Finer glass beads used to fabricate soda-lime-silica glass-bead samples with higher equant porosity (~5%); (b) The sintered glass beads recovered from the furnace with residual aluminium foil left on the outer surface; (c) The sintered glass beads were precision ground into a cylindrical shape with a length of 50 mm and a diameter of 15 mm; (d) Thermal cracks were introduced by quenching the specimen heated at 500 °C into tap water at room temperature.

A few large pores intersecting the sample surface (Fig. 2.8 c & d) could cause a puncture of the copper jacket under pressure during forced-oscillation experiments. A tiny amount of 5-min epoxy was placed into these exposed pores before jacketing to prepare a pit-free surface of the specimen.

## 2.3 Sample Characterisation

### 2.3.1 Sample geometry and crack porosity

The crack porosities determined by mensuration are all below 1% (Table 2.3). The specimens with a diameter of 15 mm have crack porosities less than 0.5%, whereas higher crack porosities, ranging from 0.7% to 0.9%, are observed on the specimens with a larger diameter of 38.1 mm.

### 2.3.2 Optical estimation of porosity

A few different techniques have been used, attempting to determine the equant porosity of a glass-bead specimen. Olin (2011) performed optical, density, and imbibition methods on a glass-bead specimen sintered with a similar thermal protocol. Similar estimates were obtained from the optical and density methods. In contrast, the imbibition method gave a much lower porosity, indicating that most of the equant pores are isolated from the outer surface of the specimen.

The density and optical methods are thus expected to yield robust estimates of total equant porosity, whereas the imbibition and gas expansion methods only provide the connected porosity. The use of density method needs a prescribed literature value for the density of a glass bead. The estimation of porosity depends heavily on the chosen value of the density of a glass bead. To this end, the optical method is another commonly used alternative (Guéguen & Palciauskas, 1994; Dullien, 1992), which links the areal porosity on a thin section of a specimen to the volumetric porosity of the specimen. For a porous medium, in a statistical sense, the volumetric porosity can always be properly approximated by the areal porosity of a thin section taken from the medium as long as the distribution of pores is random. For a synthetic glass-bead specimen, the specimen is isotropic and equant pores are expected to distribute randomly. In this sense, the optical method is applicable to the sintered glass-bead samples.

In this method, thin sections were prepared from each end of a glass-bead specimen, and mounted in epoxy resin. The thin sections were examined under an optical microscope and the area of interest was imaged and recorded by a digital camera installed on the microscope (Fig. 2.9). The pores in a selected area are traced by the image-processing software *ImageJ*. The pores are easily distinguished from the background as they have lower light reflection, hence darker in intensity. The threshold of intensity, converting the raw image into a black-and-white mode, needs to be carefully assigned to find the optimal value to allow a maximum automatic selection of pores. Some pores are filled with epoxy resin when the polished blocks were made and appear lighter in intensity. *ImageJ* may overlook the presence of the epoxy-filled pores, and a manual selection is needed in this case to complement the auto selection.

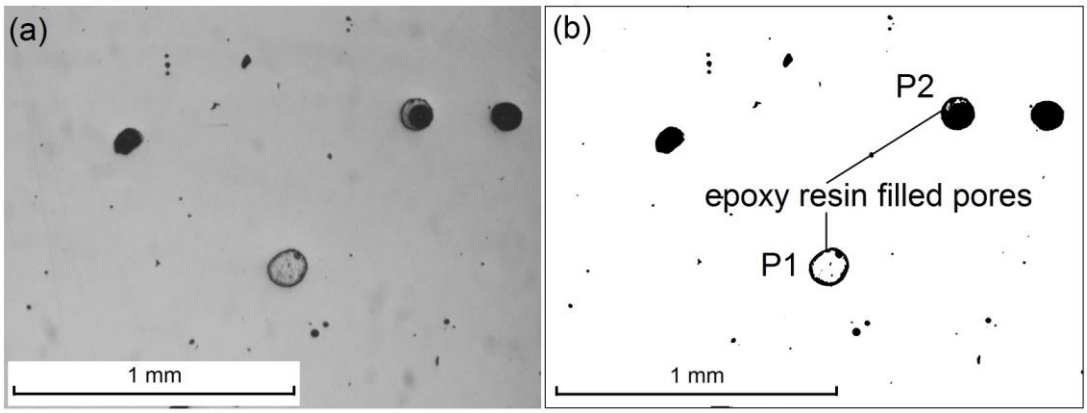


**Figure 2.9** Images (a) before and (b) after the application of an intensity threshold. Pores and non-pore area are distinguished by the intensity threshold. The pores almost completely (P1) and very partially (P2) filled with epoxy resin, overlooked by *ImageJ*, need to be manually selected, contributing to the total areal porosity of the thin section.

Both the total pore area and the total area of the microscopic image are estimated in pixels, and the ratio between them provides an optical estimation of the total porosity of a sample:

$$\phi_v = \phi_a = \frac{A_{pore}}{A_{total}}, \tag{2.2}$$

where $\phi_v$ is the volumetric porosity of a specimen, $\phi_a$ is the areal porosity of a specimen, $A_{pore}$ is the total pore area (in pixels) determined by *ImageJ* in an examined microscopic image, including both the automatically and manually selected pore areas, and $A_{total}$ is the total area (in pixels) of the microscopic image under examination.

To achieve statistical significance, multiple microscopic images need to be taken from a thin section. Olin (2011) took eight images from a polished block to obtain the average porosity of a specimen. In this project, 16 images were taken from each sample and averaged to provide a more representative value of porosity. The optical porosity varies among the different areas of the sample, indicated by the standard deviation (Table 2.3). Thin sections have been taken from both ends of the sintered glass beads and no obvious trend has been found between the porosities at the top and bottom of the specimen.

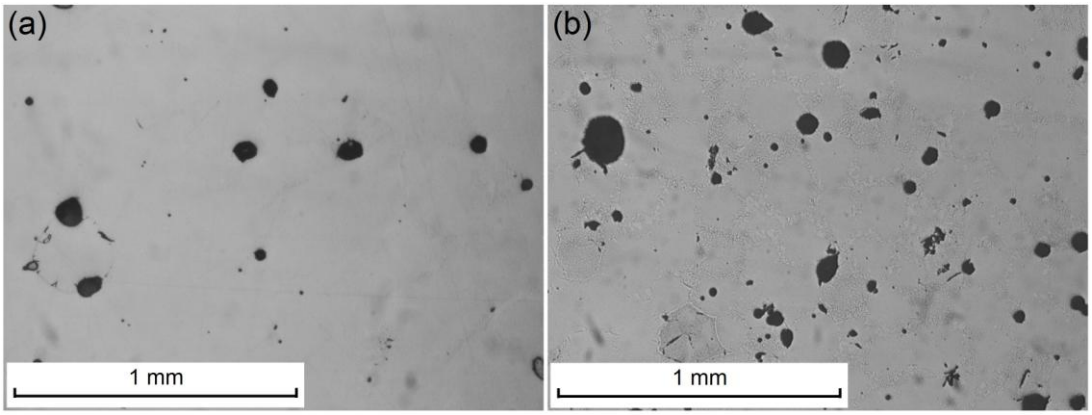


**Figure 2.10** Representative images of (a) a low-porosity (~2%) glass-bead specimen and (b) a high-porosity (~5%) glass-bead specimen determined by optical microscopy. Equant and quasi-equant pores formed at the boundaries of glass beads during sintering. Most of the equant pores are isolated from each other. The images were taken from the as-sintered specimens and no thermal cracks are present.

### 2.3.3. Helium pycnometry – grain volume and connected porosity

The connected pore space open to the outside of a specimen can be probed by a wetting fluid or gas. The former method with wetting fluid is termed imbibition and the latter involving the use of gas will be described in this section as helium pycnometry.

Regardless of the types of inclusions, *e.g.*, equant pores, cracks, *etc.*, the volume of the solid is determined. The volume of solid determined by this method is different from the actual grain volume by the presence of inaccessible pores, allowing an overestimation of solid volume and an underestimation of total porosity. The porosity determined by either imbibition or helium pycnometry is the connected porosity, as part of the total sample porosity, limited by the connectivity of inclusions within a sample.

#### 2.3.3.1 Theory of helium pycnometry

'Pycnometry' derives from the ancient Greek word 'puknos' which means 'dense'. Two physical principles are involved in the idea of pycnometry: the first one is using fluid displacement to measure volume; the second one is Boyle's law for ideal gas which relates the change of pressure to the change of volume of an ideal gas.

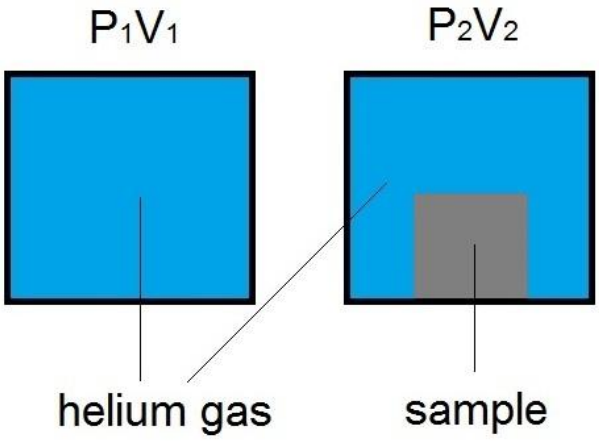


**Figure 2.11** A schematic illustration of the principle involved in the helium pycnometry.

A chamber with known volume $V_1$ is filled with gas, and the pressure within the chamber is measured as $P_1$. After placing a sample into the chamber, the volume of the helium gas is reduced as part of the space is occupied by the solid matrix of the sample. The pressure, with the sample placed in the chamber, is measured as $P_2$. From Boyle's law,

$$P_1V_1 = P_2V_2 = P_2(V_1 - V_P)\,, \tag{2.3}$$

the volume of the solid particles of the sample $V_P$ is determined.

There are two reasons to use helium as the gas medium: 1) helium has small atomic dimension and is able to penetrate the finest pores (1 Angstrom or 0.1 nm) to assure the maximum accuracy; 2) helium closely approaches the behaviour of an ideal gas.

2.3.3.2 Pycnometer and experiment procedure

A *MVP-D160-E* type helium pycnometer manufactured by *Quantachrome Instruments* at the University of Alberta was used in this experiment.

The pycnometer needs to be calibrated against a sphere with known volume before starting a measurement with an unknown specimen. The process of calibration is performed repeatedly to iteratively refine the current values of the volumes of the sample cell and the reference (Fig. 2.12 a) until the measured volume of the standard sphere matches the specified value of 56.5592 $cm^3$ within the error range $\pm$ 0.0023 $cm^3$. The determined volumes of the sample cell and the reference in calibration are later used in the measurements of the volume of a specimen.

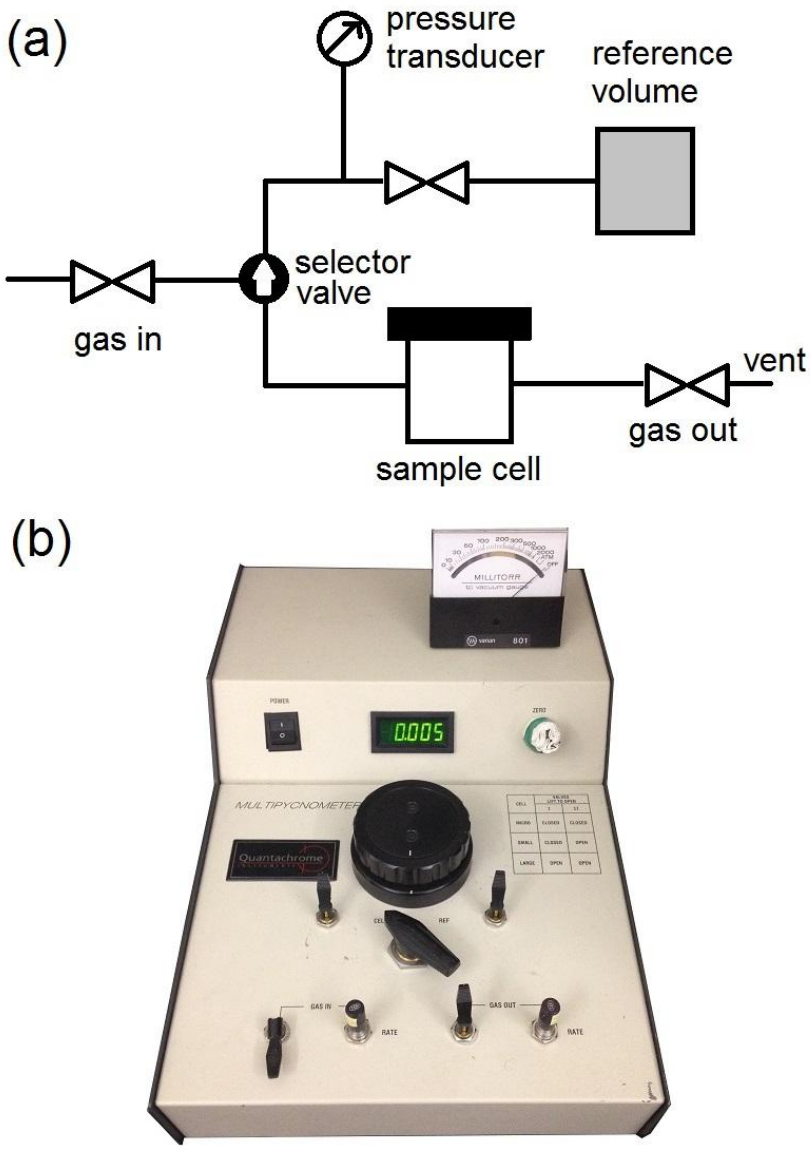


**Figure 2.12** a) The arrangements of the MVP-D160-E type helium pycnometer. b) A photograph of the helium pycnometer in the Rock Physics Laboratory at the University of Alberta.

Generally, three steps are involved in a helium pycnometry measurement. First, the sample is carefully loaded into the sample cell. The selector valve is switched to connect the sample cell with reference volume. Following a thorough evacuation to reach a residual air pressure of less than 150 mTorr, helium gas is allowed to flow through the sample cell and the reference volume chamber to purge the entire system. The gas in and gas out valves are toggled off once the process of purging is finished. The system is still filled with residual helium after purging giving a non-zero reading on the pressure gauge. The current helium pressure throughout the system is set as the background by re-zeroing the pressure gauge. Any increase in helium pressure with respect to the background pressure is measured by the pressure gauge. The current status is expressed through the ideal gas law as:

$$P_a(V_c - V_P) = n_a RT_a \,, \tag{2.4}$$

$$P_a V_R = n_b RT_a \,, \tag{2.5}$$

where $P_a$ and $T_a$ are absolute ambient pressure and temperature, respectively; $n_a$ is the number of moles of the gas occupying the sample cell and $n_b$ is the number of moles of the gas in the reference cell; $V_c$, $V_P$, and $V_R$ are the volumes of the sample cell, the sample particles, and the reference cell, respectively; $R$ is the ideal gas constant.

The sample cell and the reference cell remain connected so far. In the second step, the selector valve is switched to the reference cell to connect the reference cell to the gas inlet with the sample cell disconnected. The reference cell is then pressurised with helium gas flowing in from the reservoir to reach a reading $P_1$ of ~ 17 psi (~ 0.12 MPa). This pressure reading $P_1$ is not the absolute value of helium pressure but the relative pressure with respect to the ambient helium pressure $P_a$. The new status of the helium gas within the reference cell is expressed as:

$$(P_a + P_1)V_R = n_1 RT_a \,, \tag{2.6}$$

$$n_1 = n_b + \Delta n \,, \tag{2.7}$$

where $P_1$ is the current pressure reading, $n_1$ is the total number of moles of the helium gas in the reference cell which is the sum of the previously introduced helium in the reference cell $n_b$ and the newly supplied helium $\Delta n$, and $T_a$ is the ambient temperature.

The last step requires that the selector valve be switched to the sample cell, allowing the helium gas within the reference cell to expand to the sample cell. The stable reading after the switching of the selector valve is taken as $P_2$. This gives:

$$(P_a + P_2)(V_R + V_c - V_P) = n_2 RT_a \,, \tag{2.8}$$

$$n_2 = n_1 + n_a = n_a + n_b + \Delta n \,. \tag{2.9}$$

Substituting equation (2.4), (2.6) and (2.9) into (2.8), gives:

$$(P_a + P_2)(V_R + V_c - V_P) = (P_a + P_1)V_R + P_a(V_c - V_P) \,. \tag{2.10}$$

Notice that the ambient pressure reading $P_a$ has been zeroed initially, then the equation above can be rewritten as:

$$P_2(V_R + V_c - V_P) = P_1 V_R \,, \tag{2.11}$$

and re-arrange it to give:

$$V_P = \left(1 - \frac{P_1}{P_2}\right) V_R + V_c \,, \tag{2.12}$$

which is the working equation for the helium pycnometer.

With the particle volume (or grain volume) $V_P$ determined by Eq. (2.12), the connected porosity of a sample with a bulk volume of $V_b$ is given as:

$$\phi_{conn} = \frac{V_b - V_P}{V_b} \,. \tag{2.13}$$

The measurement on each specimen is repeated six times. The first measurement allows the pycnometer to achieve a stable performance after the loading of a new specimen, and is usually noticed significantly different from the following five measurements. Therefore, only the subsequent five measurements are taken into account to give the averaged connected porosity of a specimen. Variation in particle volume among the five repeated measurements is indicated by the standard deviation (Table 2.3).

#### 2.3.3.3 Crack porosity, equant porosity and connected porosity

The connected porosity of a specimen $\phi_{conn}$ (or $\phi_{He}$ in Table 2.3) determined by helium porosimetry, due to the presence of isolated pores, is systematically lower than the total porosity of the specimen $\phi_{total}$ which consists of both equant porosity $\phi_{eq}$ (or $\phi_{op}$ in Table 2.3) and crack porosity $\phi_{cr}$. The relationship is expressed as:

$$\phi_{conn} < \phi_{total} = \phi_{eq} + \phi_{cr} \,. \tag{2.14}$$

The optical method and geometrical change before and after thermal cracking provide good estimates for the equant porosity and crack porosity, respectively. To characterise the relaxation of pore fluid between equant pores and cracks as the mechanism of interest, the fraction of connected pores and cracks, where fluid flow takes place, needs to be estimated as the connected porosity of a specimen.

### 2.3.4 Mercury porosimetry – pore-entry diameter distribution

The previous attempts mainly aim for determination of the bulk volume of a certain family of inclusions with respect to the total volume of a specimen. The geometry of inclusions, such as pore size, is not characterised. Mercury porosimetry, introduced in this section, is capable of probing each individual connected pore with pressurised mercury liquid to infer the pore size distribution of a specimen.

2.3.4.1 Principle

The mercury injection porosimetry was used to infer the pore-size distribution of the low-porosity (~2%) glass-bead samples. This technique can resolve pores with sizes ranging from 3.5 nm to 500 μm (Giesche, 2006). Intrusion porosimetry relies on the simple principle that a higher pressure is needed for an intruding fluid to penetrate pores with smaller pore throats. Conversely, the pore-throat size can be inferred from the in-situ fluid pressure that is needed to penetrate such a pore throat.

Mercury is almost exclusively used in this type of liquid intrusion technique as its non-wetting nature. A wetting liquid can enter a capillary by itself, but a non-wetting liquid normally does not enter a capillary until external forces applied onto it. The non-wetting behaviour is desirable in the liquid intrusion technique as it can provide a stable and reliable pressure value for a liquid entering a studied capillary.

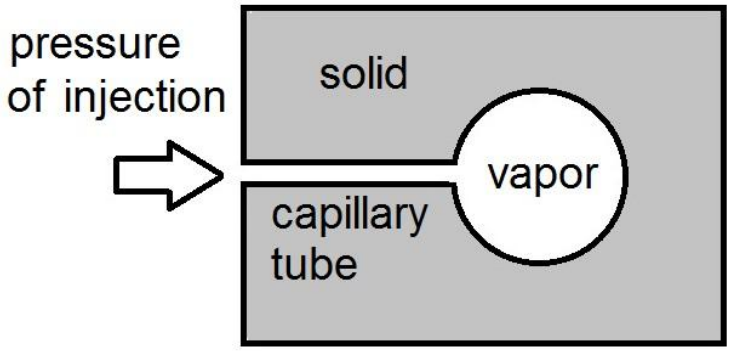


**Figure 2.13** The liquid-solid-vapour boundary during the intrusion of a liquid into a capillary tube. The triple-boundary equilibrium model is described mathematically by the Washburn equation.

The relationship between the injection pressure and the pore-throat size described above can be modelled as a liquid-solid-vapour triple-boundary equilibrium issue during a liquid intrusion into a capillary tube with a perfectly cylindrical shape (Fig. 2.13) and quantitatively expressed as the modified Young-Laplace equation or the Washburn equation (Washburn, 1921) as:

$$D_{pore} = -\frac{4\gamma cos\theta}{P}, \tag{2.15}$$

where $D_{pore}$ is the diameter of the pore throat; $\gamma$ is the surface tension of mercury which is 0.485 $Nm^{-1}$ at 25 °C; $\theta$ is the contact angle of mercury ranging from 130 °to 150°; and $P$ is the pressure applied to force mercury into the pore space.

To obtain a better understanding of the Washburn equation, it needs emphasis that $D_{pore}$ in the equation is the pore-throat size rather than the actual pore size. The pore-throat

is the idealised tube-shape entrance connected to the studied pore, and the diameter of the pore throat is normally smaller than the real size of the pore.

2.3.4.2 Mercury porosimeter

Samples need to be fragmented (Fig. 2.14 b) before being loaded into the sample cup of a penetrometer to its maximum capacity. Then the cup is sealed at the top with a cap. The penetrometer is then loaded into the low-pressure system of the mercury porosimeter. The maximum pressure that can be reached for the low-pressure system is 30 psi. Within this range of pressure, mercury is only expected to fill the space among the sample pieces without any intrusion into the sample pores. After depressurisation from 30 psi, the penetrometer is then loaded into the high-pressure system of the porosimeter to achieve a maximum pressure of ~ 414 MPa (60,000 psi).

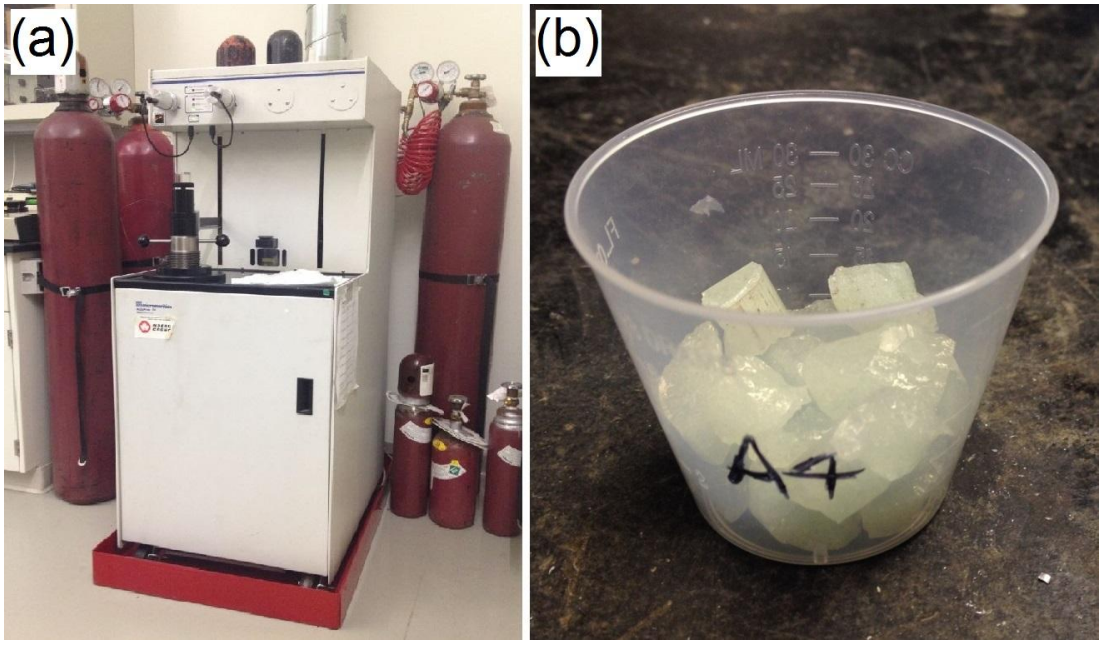


**Figure 2.14** a) The mercury porosimeter, Autopore IV 9500 manufactured by Micrometritics, located in the Rock Physics Laboratory at the University of Alberta; b) The specimen pieces prepared from a low-porosity (~2%) soda-lime glass-bead specimen by mechanical breaking before being loaded into the sample cup of the penetrometer.

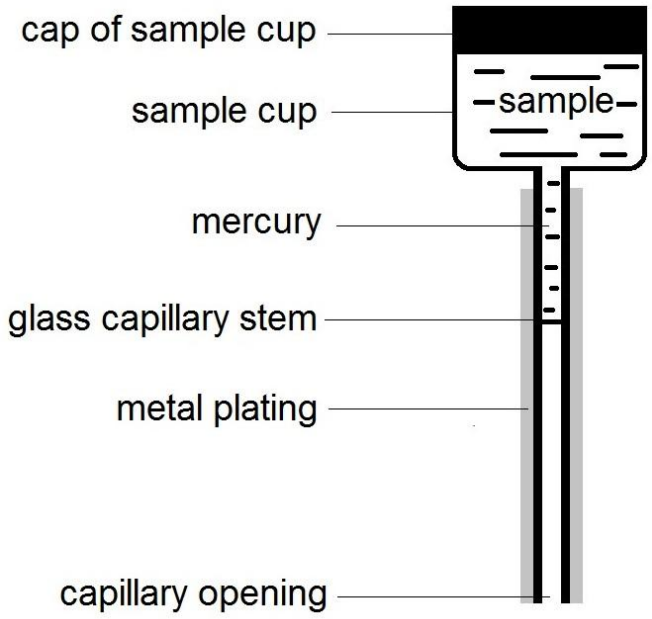


**Figure 2.15** The arrangement of a penetrometer. The fractured sample is loaded into the sample cup sealed at the top with a cap. Pressurised mercury is injected into the sample cup from the glass capillary stem, with the pressure applied from the capillary opening.

The amount of mercury intruding into a sample can be measured by the loss of mercury in volume within the glass stem of the penetrometer. The concentric metal plating outside the glass stem and mercury (electrical conductors) are separated by the glass stem (an electrical insulator), constructing a basic capacitor. The change in mercury volume within the stem, therefore, is reflected by the change in capacitance of the capacitor (Fig. 2.15).

2.3.4.3 Pore-size distribution of low-porosity glass-bead samples

The mercury porosimeter (*Autopore IV* 9500, *Micrometritics*) needs a relatively high consumption of mercury in the glass capillary stem of the penetrometer to provide a reliable result. The accuracy of measurement is optimised if 60 – 70% of the mercury within the stem is injected into a sample. This means samples with larger dimensions and higher porosities are desirable for a reliable measurement. However, in our case, each glass-bead specimen tested has a small size and low porosity of ~2%, resulting in the percentage use of mercury within the stem less than 15%.

A series of low-porosity (~ 2%) glass-bead specimens has been measured with mercury porosimetry, yielding widely varying results. For instance, the modal pore-entry diameters are 45.3 μm and 0.18-0.43 μm for specimens Y-2 and Y-4, respectively, differing by two orders of magnitude (Fig. 2.16). The synthetic samples tested have similar microstructure, indicating that the large variation in pore-entry-diameter distribution is most probably caused by the uncertainty of the mercury porosimeter itself.

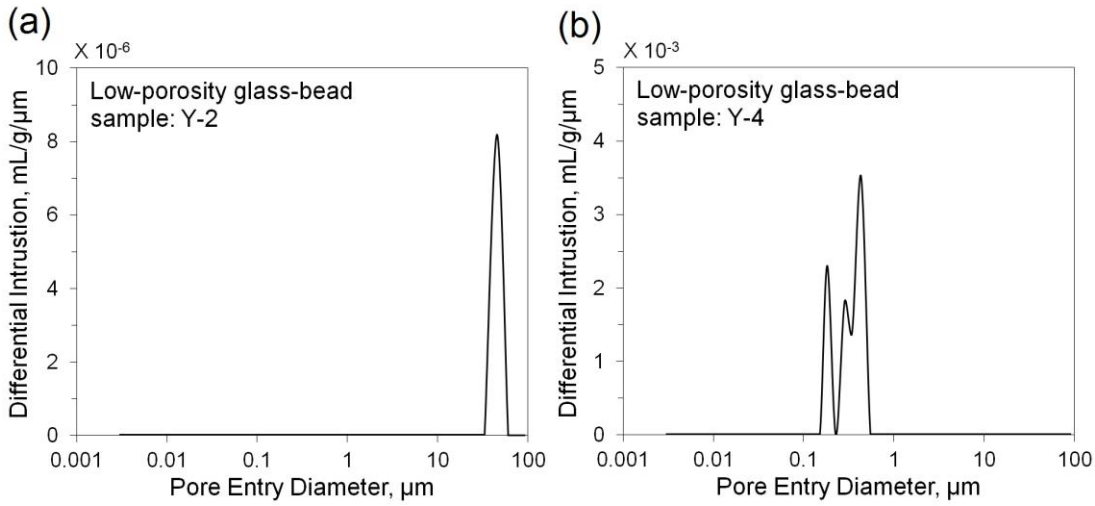


**Figure 2.16** Pore-entry diameter distributions determined by mercury injection porosimetry for low-porosity (~2%) glass-bead samples (a) Y-2 and (b) Y-4. The modal pore entry diameters determined are 45.3 µm and 0.18-0.43 µm for Y-2 and Y-4, respectively, differing by two orders of magnitude.

From geometrical considerations (Fig. 2.17), the largest equant pore that can be accommodated in plane among adjacent spherical glass beads has a radius $r = \frac{2\sqrt{3}-3}{3}R$. The glass beads used for sintering these specimens have diameters between 300 and 350 µm, giving the maximum radius of equant pores between 46.4 and 54.1 µm. The modal pore-entry diameters determined on both samples (Fig. 2.16) are less than this limit. But the extremely large variation in pore-entry diameter distribution still makes the results questionable. This indicates that the mercury porosimetry is perhaps not an ideal technique to characterise the pore-entry diameter distribution of samples with such low porosities.

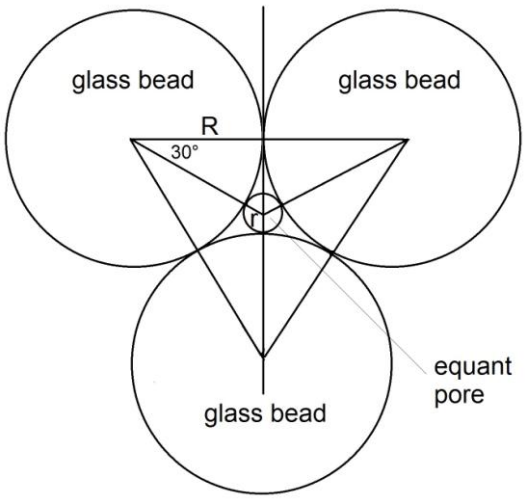


**Figure 2.17** Radius of the largest equant pore *r*, accommodated in plane among adjacent spherical glass beads, is related to the radius of glass bead R as $r = \frac{2\sqrt{3}-3}{3}R$.

### 2.3.5 Crack network, crack aspect ratio, and crack density

Thermal cracks develop instantaneously on a specimen when it is plunged into liquid water at room temperature. A crack is presumably nucleated at an existing weak point on the outer surface of the specimen in contact with liquid water. Cooling of the outer surface of the specimen from 500 °C to room temperature creates tensile stress responsible for nucleation and propagation of the crack (Fig. 2.18 a). The cracks created so far have relatively short lengths and mainly concentrate near the outer surface of the specimen. During the second stage, with the cooling gradually reaching the core of the specimen, longer cracks develop through the entire sample volume (Fig. 2.18 b), which tends to connect the short cracks created at the first stage. But not all of the short cracks develop into long cracks during the second stage, with some of them remaining isolated from the others. As a result, two families of cracks, *i.e.*, short cracks near the outer surface of a specimen and interconnected long cracks going across the entire sample, are commonly observed.

The tensile stress to create a crack is primarily controlled by thermal expansivity of the material and temperature differential. The diameter of a specimen is a secondary factor that influences the cooling time of the quenched specimen. A specimen with small diameter is expected to develop more long cracks that penetrate the centre of the specimen. This is confirmed by the observation that a small-dimension sample with a diameter of 15 mm is dominated by long cracks (Fig. 2.20) and a large-dimension sample with a diameter of 38.1 mm has nearly equivalent amount of short cracks near the outer surface and long cracks penetrating the centre of the specimen (Fig. 2.21).

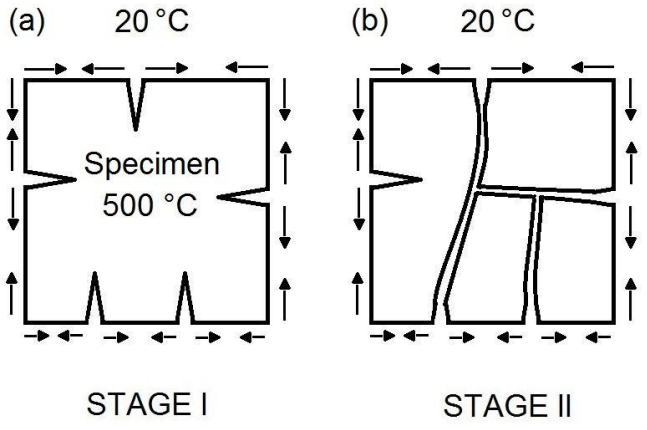


**Figure 2.18** The process of thermal cracking on a specimen: (a) short cracks are created by tensile stress when the specimen at 500 ℃ is quenched into liquid water at 20 ℃; (b) longer cracks develop with progressive cooling from the outer surface to the core of the specimen, connecting some of the previously isolated short cracks.

The mechanism of thermal cracking illustrated in Fig. 2.18 is applicable to all types of cracks. Depending on the location of a crack and the orientation of the crack plane on a

cylindrical sample, the cracks could be categorised into three types. The first type of crack is created by axial tensile stress with its plane parallel to the end surface of the sample. A cross-section along the longitudinal axis of a cylindrical sample provides for the examination of such cracks (Fig. 2.19 a). The second type of crack is created by circumferential tensile stress with its plane containing both the longitudinal and radial axes of the sample. A transverse cross-section parallel to the end surface of a cylindrical sample allows its observation (Fig. 2.19 b). The third type of crack is termed ring crack, propagating axially inwards from the ends of the specimen, results from radial tensile stresses acting on the ends of the specimen (Fig. 2.19 c). In reality, the crack network is much more complicated, and the three types of cracks could be interconnected (Fig. 2.20). The observation shows that the distribution of crack orientations is probably less isotropic, instead reflecting the cylindrical symmetry of the thermal stress field.

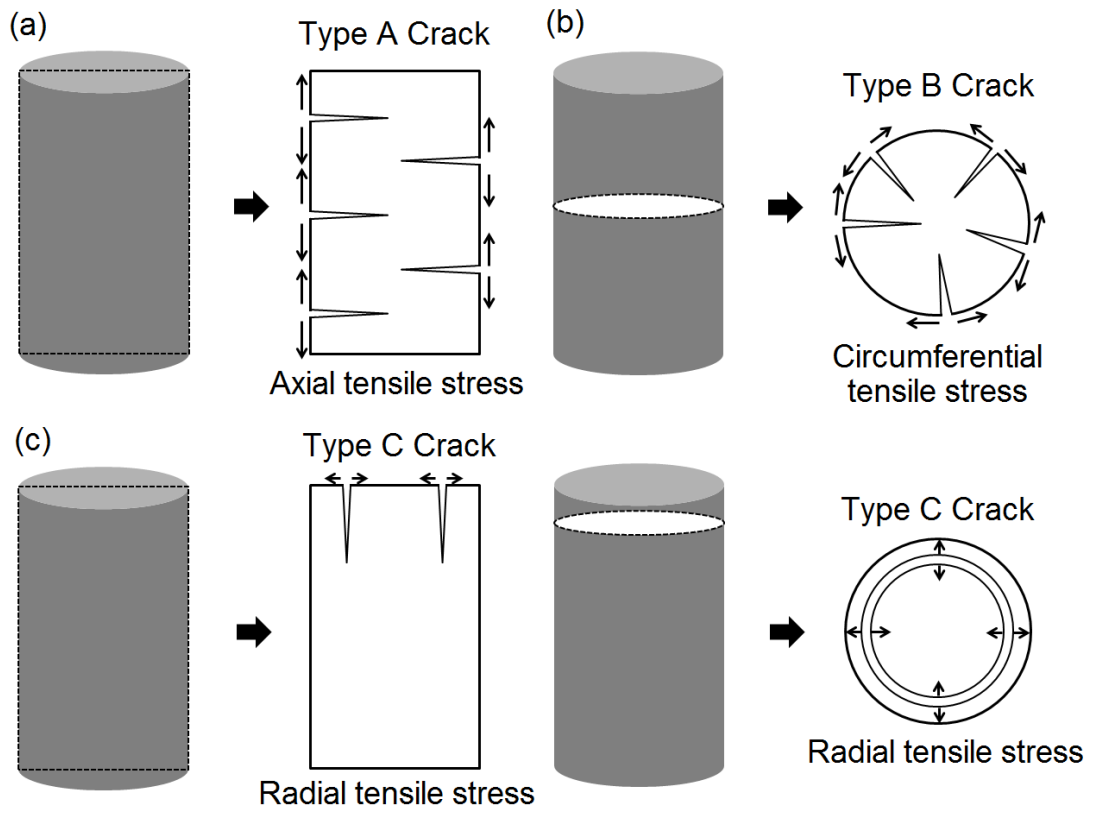


**Figure 2.19** An illustration of (a) Type-A cracks observed on a longitudinal cross-section; (b) Type-B cracks observed on a cross-section parallel to the end surfaces of a cylinder; and (c) Type-C (ring) cracks observed on both longitudinal and radial cross-sections.

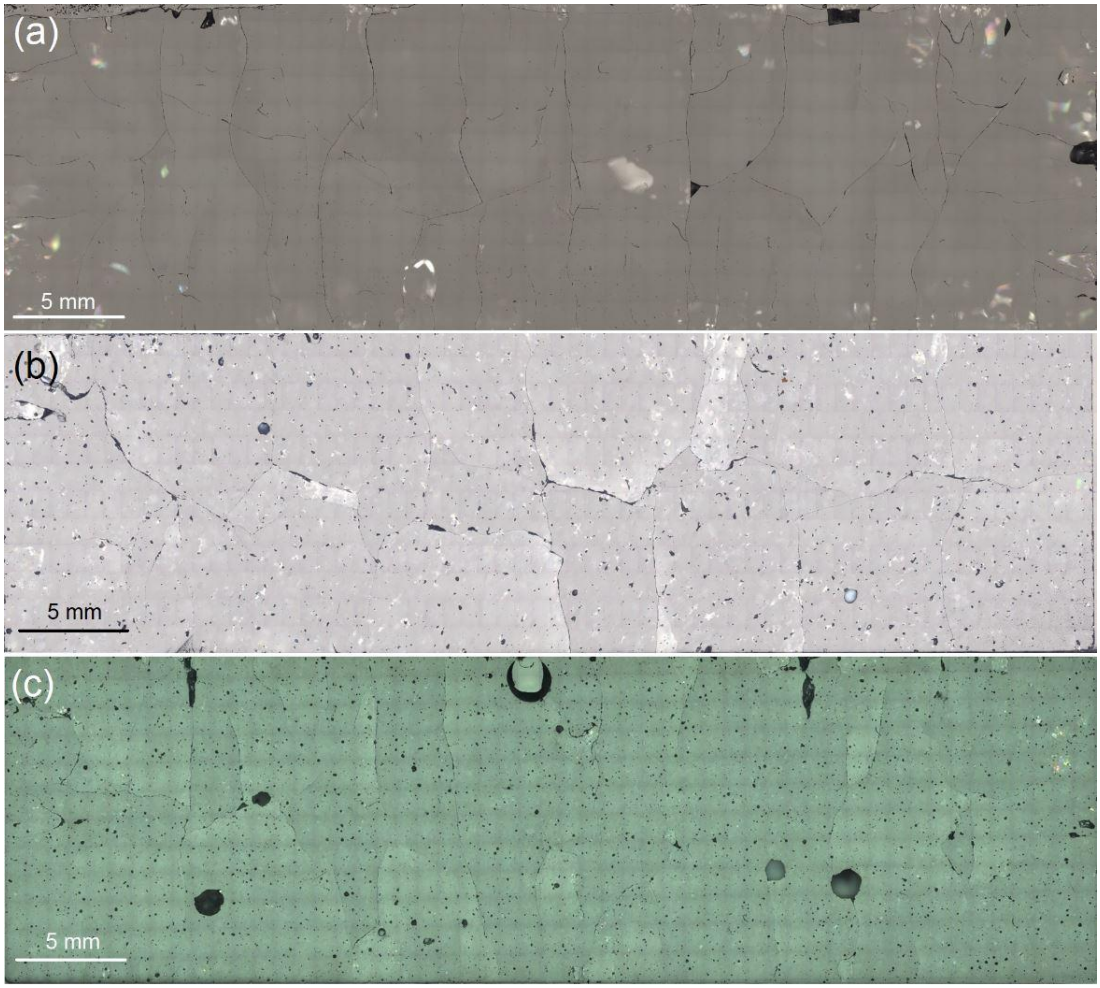


**Figure 2.20** Crack network visible on the longitudinal cross-sections of (a) a glass-rod specimen (FDS-2); (b) a low-porosity glass-bead specimen (A-3); (c) a high-porosity glass-bead specimen (YF-1). Each of these samples has a 15 mm diameter. Typical crack lengths are estimated from these images.

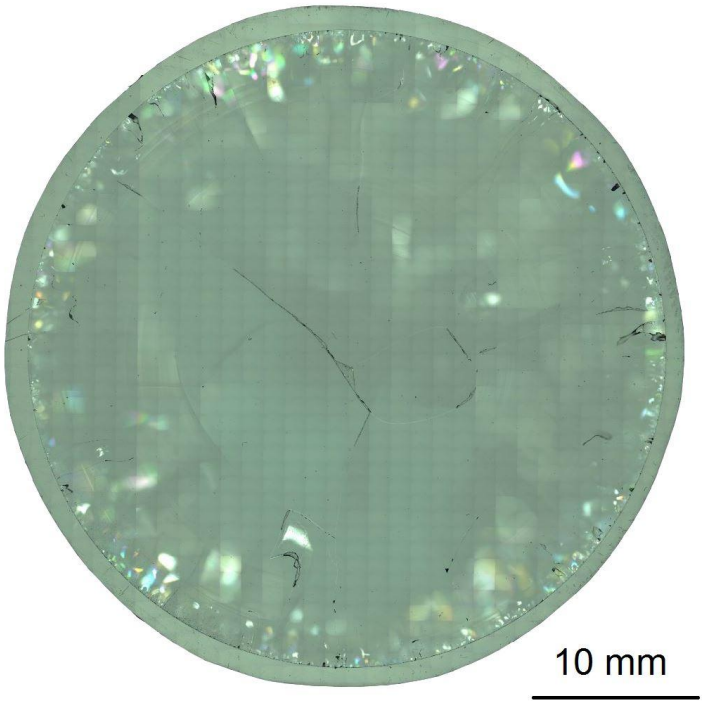


**Figure 2.21** The crack network observed on the cross-section of a glass-rod specimen (FDL-3) with a diameter of 38.1 mm. Besides the long cracks going through the centre of the specimen, many isolated short cracks are also noticed near the circumference of the cross-section. The thin outer rim is the epoxy resin used to hold the cracked sample.

Crack aspect ratio $\alpha$ is defined as the ratio between the aperture and the length of a crack. Compared with equant pores, thermal cracks are much less controllable as they form instantaneously during the process of quenching and it is therefore not feasible to manipulate either the length or aperture of cracks. The cracks made on all the synthetic samples have universally low aspect ratio. This suits the purpose of this experiment because cracks with high aspect ratio favour drainage of fluid and thus pose difficulties in detecting the other undrained regimes, *i.e.*, saturated isobaric and saturated isolated regimes. The lengths and apertures of cracks can be estimated from the images taken by optical microscopy. A conventional optical microscope provides a good resolution and estimation of the crack aperture (Fig. 2.22, 2.23, 2.24). However, the field of view on a conventional optical microscope is heavily limited, and the image at the edge of the field of view is distorted. Instead, a mosaic optical microscope was used to image the entire cross-sectional area with no distortion and even illumination (Fig. 2.20). Finally, the ratio between the mean aperture and the mean length of cracks on a cross-section gives the average crack aspect ratio of a specimen (Table 2.4).

Each crack is idealised as a spheroid, which is ellipsoid having two equal axes (Walsh, 1965). If $a_1 = a_2$ and $a_3$ are the lengths of the equal and unequal axes, respectively, the aspect ratio is defined as $\alpha = a_3 / a_1$.

Crack density $\Gamma$ is a dimensionless parameter defined as:

$$\Gamma = \frac{N{a_1}^3}{V_b}, \tag{2.16}$$

where $N$ is the number of cracks within a bulk volume $V_b$. It is noticed that the (crack) porosity of the specimen $\phi_{cr}$ with bulk volume $V_b$ is:

$$\phi_{cr} = \frac{N(\frac{4}{3}\pi a_1^2 a_3)}{V_b}, \tag{2.17}$$

Combining Eq. (2.16) and (2.17), it gives:

$$\Gamma = \frac{3\phi_{cr}}{4\pi\alpha}, \tag{2.18}$$

This parameter involves the ratio of crack porosity $\phi_{cr}$ to crack aspect ratio $\alpha$, which plays an important role in theories for the physical (*e.g.*, elastic, hydraulic, *etc.*) properties of cracked media. The determined crack densities of all types of samples are listed in Table 2.4. The glass-bead specimens, regardless of equant porosity, have similar average crack aspect ratios of $9.5 \times 10^{-4}$, close to what has been found in Olin (2011) of $7 \times 10^{-4}$. However, the crack aspect ratios of glass-rod specimens are 2 ~ 4 times those of glass-bead specimens. It is argued that the microstructural parameters determined by 3D method could be slightly different from those provided by 2D images. For instance, the 2D mean aspect ratios of thermally treated Carrara marbles determined by SEM are noticed to be larger than those obtained by 3D micro-CT in Delle Piane *et al.* (2015). The materials and temperature of thermal treatment in this study are different from those reported in Delle Piane *et al.* (2015) and it is therefore hard to apply the finding to this study.

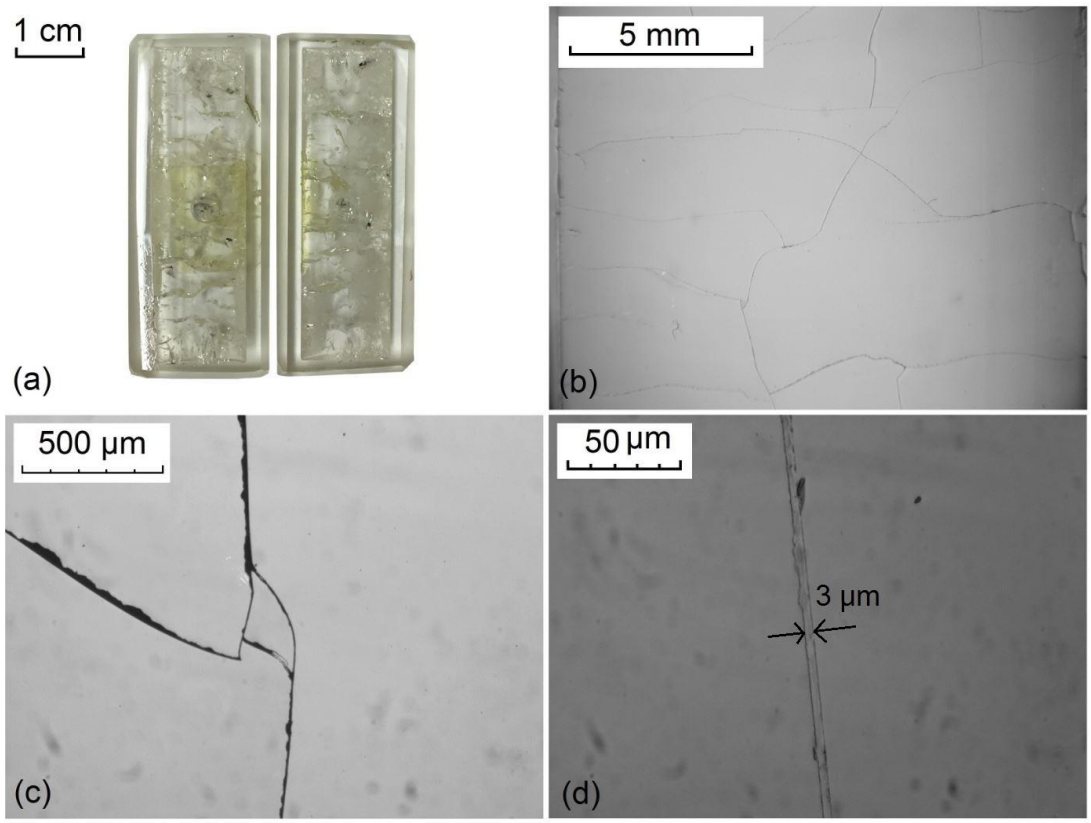


**Figure 2.22** (a) The longitudinal cross-section of a glass-rod specimen (FDS-2) and the crack network (b-d) imaged by optical microscopy with progressively increasing magnification.

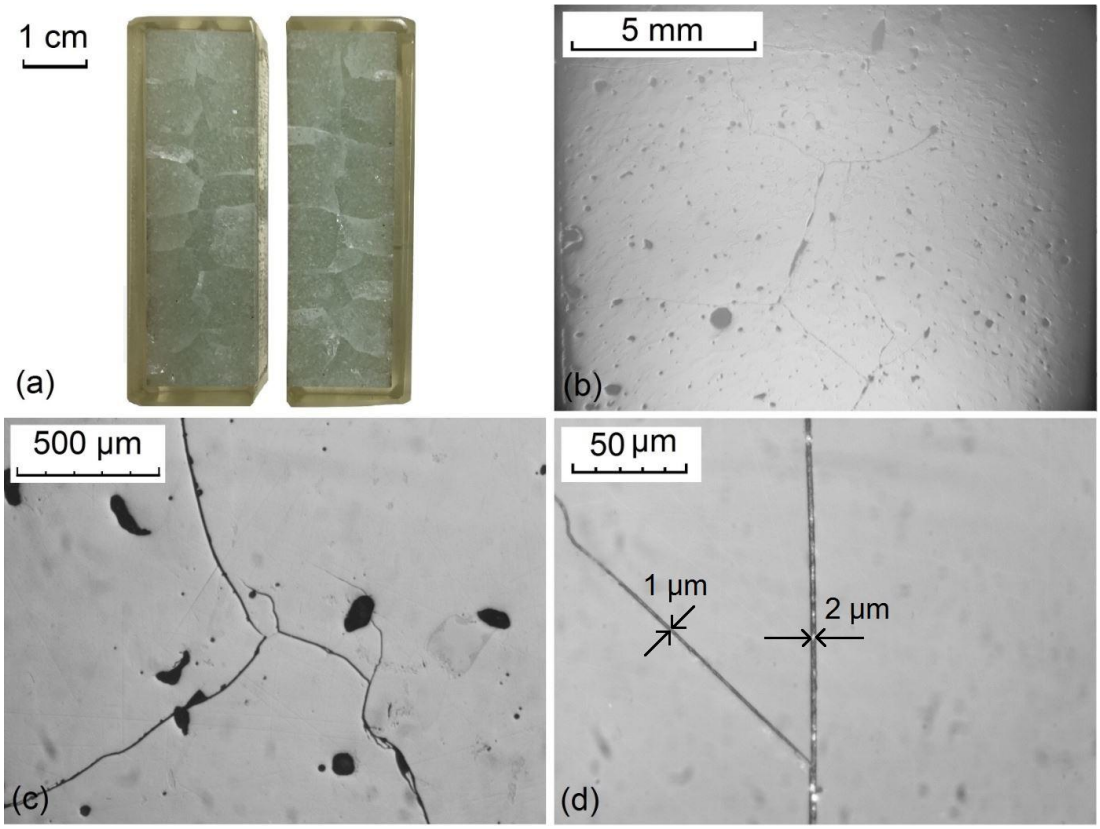


**Figure 2.23** (a) The longitudinal cross-section of a low-porosity glass-bead specimen (A-3) and the crack network (b-d) imaged by optical microscopy with progressively increasing magnification.

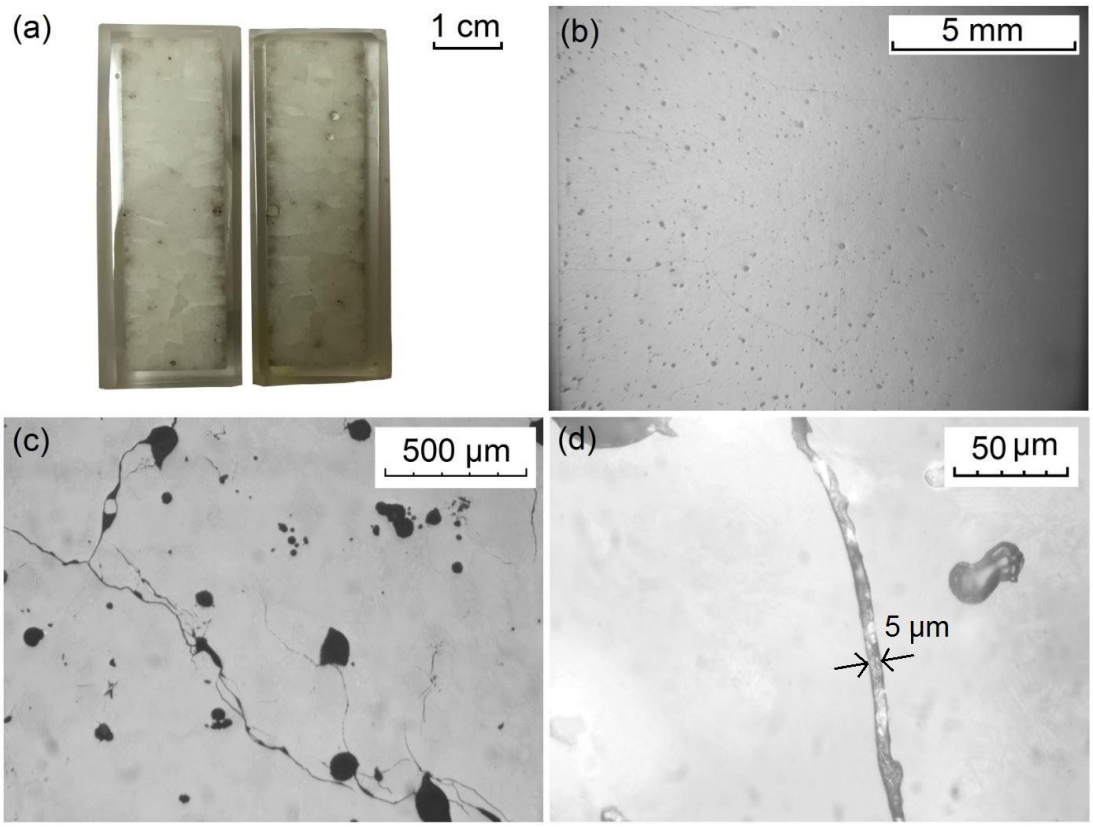


**Figure 2.24** (a) The longitudinal cross-section of a high-porosity glass-bead specimen (YF-1) and the crack network (b-d) imaged by optical microscopy with progressively increasing magnification.

Table 2.3 Sample Information

| Specimen Type | Specimen Name | $L_0$, mm +/- 0.001 | $D_0$, mm +/- 0.001 | $V_0$, mm$^3$ +/- 0.7 | $L_1$, mm +/- 0.001 | $D_1$, mm +/- 0.001 | $V_1$, mm$^3$ +/- 0.7 | $\phi_{cr}$, % +/- 0.02% | $\phi_{op}$, % | $\Phi_{He}$, % | Mass, g | $\rho$, kg/m$^3$ |
|---|---|---|---|---|---|---|---|---|---|---|---|---|
| Glass-rod specimen | FDSL-1 | 150.010 | 14.980 | 26,438.3 | 150.220 | 14.992 | 26,517.8 | 0.30 | - | - | 66.45994 ±0.00001 | 2506.24 ±0.07 |
| | FDL-1 | 76.20 | 38.10 | 86,875.0 | - | - | - | - | - | - | 218.541 ±0.001 | 2515.58 ±0.02 |
| | FDL-2 | 76.20 | 38.10 | 86,875.0 | 76.40 | 38.19 | 87,515.0 | 0.74 | - | - | 218.665 ±0.001 | 2498.60 ±0.02 |
| | FDL-3 | 76.20 | 38.10 | 86,875.0 | 76.43 | 38.20 | 87,595.2 | 0.83 | - | - | - | - |
| | FDS-1 | 49.997 | 15.006 | 8,842.3 | 50.080 | 15.028 | 8,882.9 | 0.46 | - | 0.4 ±0.3 | 22.21946 ±0.00004 | 2501.4 ±0.2 |
| | FDS-2 | 50.001 | 15.006 | 8,843.0 | 50.071 | 15.022 | 8,874.3 | 0.35 | - | 0.5 ±0.1 | 22.22253 ±0.00002 | 2504.1 ±0.2 |
| | FDS-3 | 49.985 | 15.008 | 8,842.5 | - | - | - | - | - | 0.3 ±0.4 | 22.22789 ±0.00003 | 2513.8 ±0.2 |

Table 2.3 (Continued) Sample Information

| Specimen Type | Specimen Name | $L_0$, mm +/- 0.001 | $D_0$, mm +/- 0.001 | $V_0$, mm$^3$ +/- 0.7 | $L_1$, mm +/- 0.001 | $D_1$, mm +/- 0.001 | $V_1$, mm$^3$ +/- 0.7 | $\phi_{cr}$, % +/- 0.02% | $\phi_{op}$, % | $\Phi_{He}$, % | Mass, g | $\rho$, kg/m$^3$ |
|---|---|---|---|---|---|---|---|---|---|---|---|---|
| Low-porosity glass-bead specimen | A-3 | 49.989 | 14.992 | 8,824.4 | 50.036 | 14.997 | 8,838.6 | 0.16 | 2.0 ±1.0 | - | - | - |
| | A-4 | 49.995 | 14.994 | 8,827.8 | 50.040 | 15.002 | 8,845.2 | 0.20 | 2.0 ±0.7 | 1.0 ±0.1 | 21.64 ±0.01 | 2447 ±1 |
| | A-5 | 50.009 | 14.996 | 8,832.6 | 50.049 | 14.996 | 8,839.7 | 0.08 | 1.8 ±0.7 | 0.5 ±0.1 | 21.64 ±0.01 | 2448 ±1 |
| | Y-2 | 49.984 | 14.971 | 8,798.8 | - | - | - | - | 3.2 ±1.5 | 0.1 ±0.1 | 21.47 ±0.01 | 2440 ±1 |
| | Y-4 | 49.969 | 14.966 | 8,790.3 | 50.021 | 14.980 | 8,815.9 | 0.29 | 3.0 ±1.3 | 0.9 | 21.57 ±0.01 | 2447 ±1 |

Table 2.3 (Continued) Sample Information

| Specimen Type | Specimen Name | $L_0$, mm +/- 0.001 | $D_0$, mm +/- 0.001 | $V_0$, mm$^3$ +/- 0.7 | $L_1$, mm +/- 0.001 | $D_1$, mm +/- 0.001 | $V_1$, mm$^3$ +/- 0.7 | $\phi_{cr}$*, % +/- 0.02% | $\phi_{op}$, % | $\phi_{He}$, % | $W$, g | $\rho$, kg/m$^3$ |
|---|---|---|---|---|---|---|---|---|---|---|---|---|
| High-porosity glass-bead specimen | YF-1 | 49.965 | 14.991 | 8,819.0 | 50.002 | 14.996 | 8,831.4 | 0.14 | 5.4 ±1.5 | 2.5 ±0.2 | 21.32081 ±0.00003 | 2414.2 ±0.2 |
| | YF-2 | 49.971 | 14.991 | 8,820.0 | 50.015 | 15.001 | 8,839.6 | 0.22 | 6.0 ±0.8 | 3.4 ±0.1 | 21.30352 ±0.00002 | 2410.0 ±0.2 |
| | YF-3 | 49.984 | 14.996 | 8,828.2 | 50.035 | 15.009 | 8,852.5 | 0.28 | 5.9 ±0.8 | 2.9 ±0.1 | 21.34247 ±0.00000 | 2410.9 ±0.2 |
| | YF-4 | 49.995 | 15.001 | 8,836.0 | - | - | - | - | 4.6 ±1.2 | 0.6 ±0.2 | 21.44219 ±0.00003 | 2426.7 ±0.2 |

$L_0$: sample length before cracking; $D_0$: sample diameter before cracking; $V_0$: sample volume before cracking; $L_1$: sample length after cracking; $D_1$: sample diameter after cracking; $V_1$: sample volume after cracking; $\phi_{cr}$: crack porosity calculated as the dimensional change of a cylindrical sample after thermal cracking; $\phi_{op}$: total equant porosity determined by optical microscopy; $\phi_{He}$: connected porosity determined by helium pycnometry; $W$: weight of sample; $\rho$: bulk density of sample.

*Details of the determination of crack porosity, optical porosity, and helium porosity are given in *Section 2.3*.

Table 2.4 Crack Network, Crack Aspect Ratio, and Crack Density

| Sample | Sample Name | Crack Network | Mean Crack Length, mm | Mean Crack Aperture, μm | Mean Aspect Ratio | Crack Porosity, % ±0.02% | Crack Density |
|---|---|---|---|---|---|---|---|
| Small-dimension glass-rod specimen | FDS-2 | Type A, B, & C, dominated by long cracks | 3.9 | 7.5 | $1.9 \times 10^{-3}$ | 0.35 | 0.43 |
| Large-dimension glass-rod specimen | FDL-3 | Type A, B, & C, both long and short cracks | 6.4 | 21.3 | $3.3\times 10^{-3}$ | 0.83 | 0.60 |
| Small-dimension low-porosity glass-bead specimen | A-3 | Type A, B, & C, dominated by long cracks | 4.6 | 4.4 | $9.5 \times 10^{-4}$ | 0.16 | 0.40 |
| Small-dimension high-porosity glass-bead specimen | YF-1 | Type A, B, & C, dominated by long cracks | 4.6 | 4.4 | $9.5 \times 10^{-4}$ | 0.14 | 0.35 |

# Chapter 3 Experimental Methodology

The first two chapters have outlined the target of this research, *i.e.*, exploring the fluid flow related dispersion in crustal rocks, and the procedure of making synthetic samples with simple crack-pore microstructure. Then the mechanical properties of theses synthetic samples saturated with fluids are systematically studied with techniques over a wide range of frequencies, from sub-Hz to MHz frequencies. This broadband measurement includes, with increasing frequency, forced oscillation technique (mHz-Hz), resonant bar (kHz), and ultrasonic wave propagation method (MHz). The ultrasonic interferometry and strain gauge measurement are also included to complement the three major techniques and provide additional information on the mechanical properties of samples. The details of techniques mentioned above will be described in the first part of this chapter. The hydraulic data are also crucial alongside the mechanical measurements to better characterise the solid-fluid interaction. A simple method directly based on Darcy's Law with water pore fluid and a transient flow method with argon pore fluid were used to obtain permeability of samples, which will be detailed in the second part of this chapter.

## 3.1 Forced Oscillation Method

In the first chapter, all mechanical techniques involved in the past research have been reviewed. It is worth recalling that Bourbié *et al.* (1987) categorised the measurements of velocity and attenuation on rock specimens into three types: (i) travelling wave or ultrasonic method, which involves a process of wave propagation similar to seismic exploration, but different in frequency: tens of Hz to a few kHz for seismic exploration in the field whereas ~ 1 MHz for ultrasonic method in laboratory; (ii) resonance method at a few kHz, which can be further divided into two types: pendulums (*e.g.*, Peselnick and Outerbridge, 1961) and resonant bar (*e.g.*, Winkler *et al.*, 1979; Vo-Thanh, 1990; McCann *et al.*, 2009); (iii) forced oscillation method (or subresonance method) at mHz to Hz, which is implemented under both ambient (*e.g.*, Spencer, 1981; Paffenholz and Burkhardt, 1989) and high-temperature, high-pressure conditions (Jackson and Paterson, 1993). In this section, the forced-oscillation method realised on the Jackson-Paterson Attenuation Apparatus will be introduced.

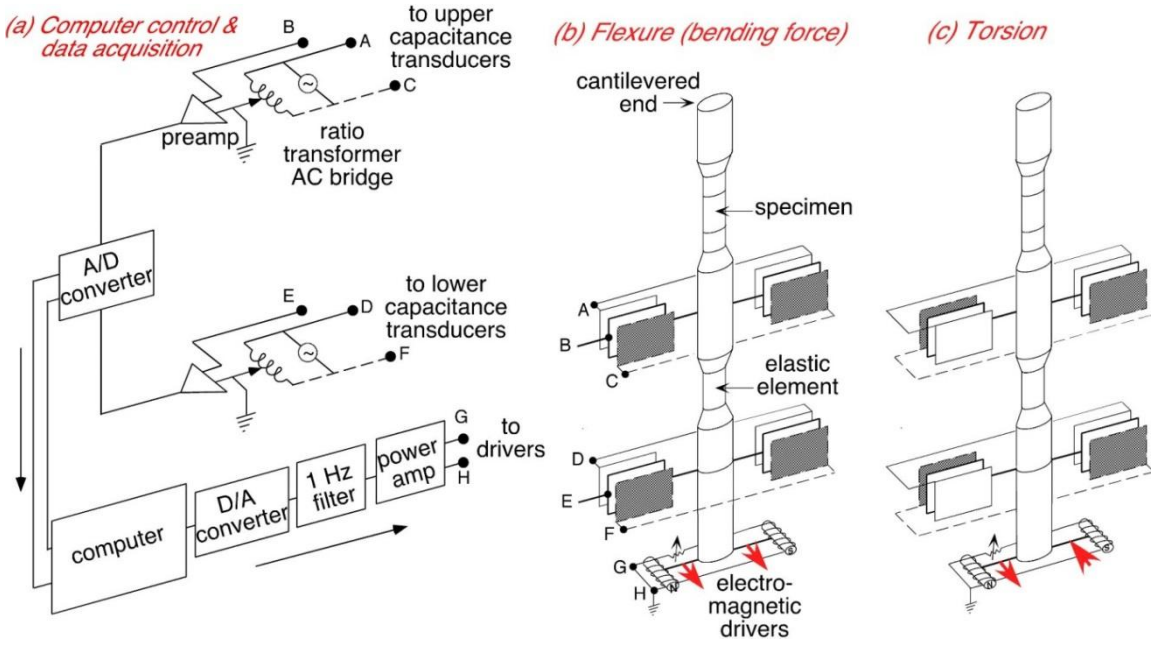


**Figure 3.1** Experimental arrangements for (a) computer control and data acquisition system and forced oscillations in (b) flexure (bending force) and (c) torsion modes with alternative configurations of electromagnetic drivers and displacement transducers (after Jackson *et al.*, 2011).

In the context of increasing interest in low-frequency mechanical measurements with high pressure and temperature, the Jackson – Paterson Attenuation Apparatus (Figure 3.1) has been developed since the late 1970s. The apparatus, which is located at the Research School of Earth Sciences at the Australian National University, is an instrument for the measurement of viscoelastic and anelastic response of a rock specimen to applied torque or bending force. The viscoelastic and anelastic behaviours depart from the elastic behaviour by a phase difference between the applied stress and the resulting strain. However, the definition of anelasticity requires complete strain recoverability once the applied stress is removed, the requirement of which is relaxed for the viscoelastic behaviour. Basically, the design of this facility has addressed two challenges: the high pressure sealing for gas medium (argon), and the high precision required for the measurement of displacement.

Over three decades of development, the Jackson – Paterson Attenuation Apparatus has become a versatile facility for performing both forced oscillation (torsion and flexure) and pore-fluid re-equilibration experiments. From 2012 to 2013, the electronic system for data acquisition on the Attenuation Apparatus was upgraded. Commissioning and thorough testing of the new arrangements for computer control and data acquisition forms a significant part of this Ph.D. project. The general description of the methods used on the Attenuation Apparatus is given in *Section 3.1.1* with description of the upgrade of the system in *3.1.2*.

### 3.1.1 General description of method

3.1.1.1 Principle of torsional forced oscillation on the Attenuation Apparatus

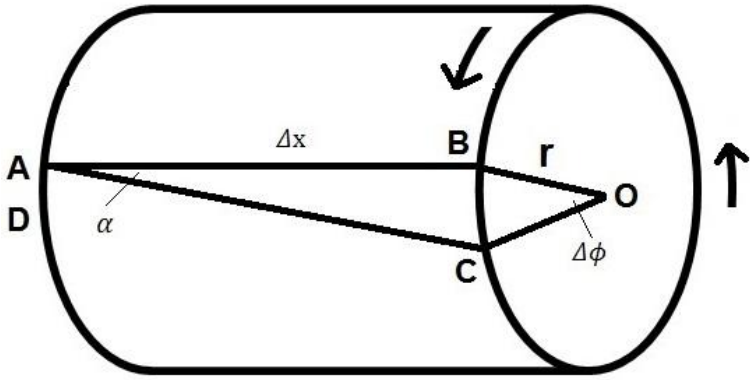


**Figure 3.2** A schematic illustration of a rod subject to a torque.

Before introducing the principle of the torsional forced oscillation experiments, it is worth recalling some basic definitions and relationships for torsional deformation on a rod. Imagine a rod with one end fixed is subject to a torque and a torsional deformation is caused. An arbitrary point B on the twisted end moves to its new position C after deformation by a twist angle of $\Delta\phi$. Points B and C are both away from the centre of the circular end surface by the radius r. Segment AB is parallel to the longitudinal axis of the rod and the distance between point A and B is $\Delta x$. D is another point on the circumference of the fixed end which is infinitesimally close to Point A. Before applying the torque, ∠DAB is a right angle. After deformation, new angle DAC is smaller than the original right angle DAB by $\alpha$ (angle CAB). According to the definition of shear strain, *i.e.*, the change in angle between two originally perpendicular line segments that intersect at point A, $\alpha$ should be the shear strain $\varepsilon$ at point A. In the right triangle ABC, $\alpha$ is infinitesimal small, and then we have:

$$\alpha = \tan\alpha = \frac{\overline{BC}}{\overline{AB}} = \frac{\overline{BC}}{\Delta x}, \tag{3.1}$$

and notice that:

$$\overline{BC} = \Delta\phi \cdot r, \tag{3.2}$$

we get strain at point A as:

$$\varepsilon = \lim_{\Delta x \to 0} \frac{\Delta\phi \cdot r}{\Delta x} = r\frac{d\phi}{dx}. \tag{3.3}$$

In a uniform rod, shear strain is thus a function only of distance *r* from the axis of rod. Then the relationship between torque and shear strain needs to be determined. For an infinitesimal area $dA$ near point B, shear force $dF$ is related to shear stress $\sigma$ as:

$$dF = \sigma \cdot dA \ . \tag{3.4}$$

The moment associated with the force *dF* exerted on the area $dA$ is:

$$dM = r \cdot dF = r \cdot \sigma \cdot dA \ , \tag{3.5}$$

and notice shear stress $\sigma$ and strain $\varepsilon$ are related by shear modulus *G*:

$$G = \frac{\sigma}{\varepsilon} \ . \tag{3.6}$$

Combine Eq. (3.3), (3.5) and (3.6), we get:

$$dM = rG\varepsilon \, dA = r^2 G \frac{d\phi}{dx} dA \ , \tag{3.7}$$

and torque *T* as: $$T = \int_A \ dM = \int_A \ r^2 G \frac{d\phi}{dx} dA = G \frac{d\phi}{dx} \int_A \ r^2 \, dA \ , \tag{3.8}$$

in which polar moment of inertia *J* is defined as:

$$J = \int_A \ r^2 \, dA \ . \tag{3.9}$$

If Eq. (3.3), (3.8) and (3.9) are combined, torque *T* and shear strain $\varepsilon$ are linked as:

$$T = \frac{GJ}{r} \varepsilon \ , \tag{3.10}$$

or rearrange it to express shear strain $\varepsilon$ as a function of torque *T* as:

$$\varepsilon = \frac{r}{GJ} T \ . \tag{3.11}$$

Torque *T* in the expression above is a steady one, and can be modified to a sinusoidal torque $T_0 sin\omega t$ as below:

$$\varepsilon = \frac{r}{GJ} T_0 sin\omega t \ . \tag{3.12}$$

So far we have just focused on the purely elastic material for which an instantaneous or in-phase response is expected to the applied torque. But for anelastic or viscoelastic materials, a phase lag $\delta$ is expected in its response to the applied torque. In this case, the resultant shear strain can be expressed as:

$$\varepsilon = \frac{r}{GJ} T_0 \sin(\omega t - \delta) \,. \tag{3.13}$$

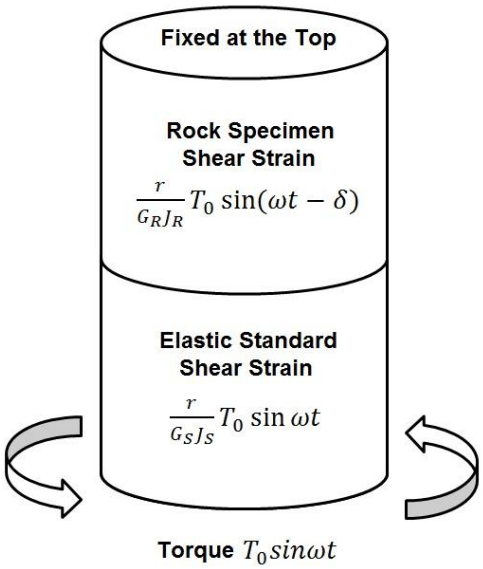


**Figure 3.3** A schematic diagram to illustrate the principle underlying the torsional forced oscillation experiments. At sufficiently low amplitudes, the constitutive relationship between stress and strain, and their time derivatives are linear. $G_R$ and $G_S$ are the shear modulus of the rock specimen and elastic standard, respectively; $J_R$ and $J_S$ are the polar moments of inertia of the cylindrical rock sample and standard, respectively; and $r$ is the distance from the torsional axis (after Jackson & Paterson, 1993).

In practice, shear modulus of an unknown rock specimen can be determined if the torque $T_0 \sin(\omega t)$ and the resulting shear strain $\varepsilon$ are measured (Eq. 3.13). The measurement of shear strain can be realised by a strain gauge or a capacitance transducer. But it seems much more difficult to precisely measure the associated torque. To overcome this issue, a commonly used strategy in the stress-strain method is to mechanically connect the unknown specimen to an elastic standard with known shear modulus $G_S$. At sufficiently low frequencies, both specimen and standard are subject to the same torque $T_0 sin\omega t$, the value of which can be determined from the shear strain of the elastic standard. By comparing the sinusoidal shear strains of the unknown specimen and the elastic standard, the phase lag $\delta$ is obtained. As a result, the shear modulus of the unknown rock specimen $G_R$ and attenuation $Q^{-1}$ (= tan $\delta$) are determined (Jackson & Paterson, 1993).

### 3.1.1.2 Three-plate capacitance transducer and electrical bridge

The sub-resonant method (or forced oscillation method) is simple in principle but difficult in implementation. From the principle of measurement introduced in the last section, it is obvious that the high-precision measurement of strain is the most important part of this low-

frequency technique. The development of 'capacitance micrometry' (Stacey *et al.*, 1969) made it possible to precisely measure strain amplitudes down to $10^{-8}$. This technique relies on the combined use of 1) a parallel-plate capacitor, relating the displacement between two plates to the capacitance of the capacitor, and 2) an electrical bridge with capacitive and inductive arms to resolve small changes in electrical signal, and hence eventually achieve high-precision measurements of displacement (Brennan and Stacey, 1977; Brennan, 1981). This technique was later incorporated into the Jackson – Paterson Attenuation Apparatus to perform strain measurements.

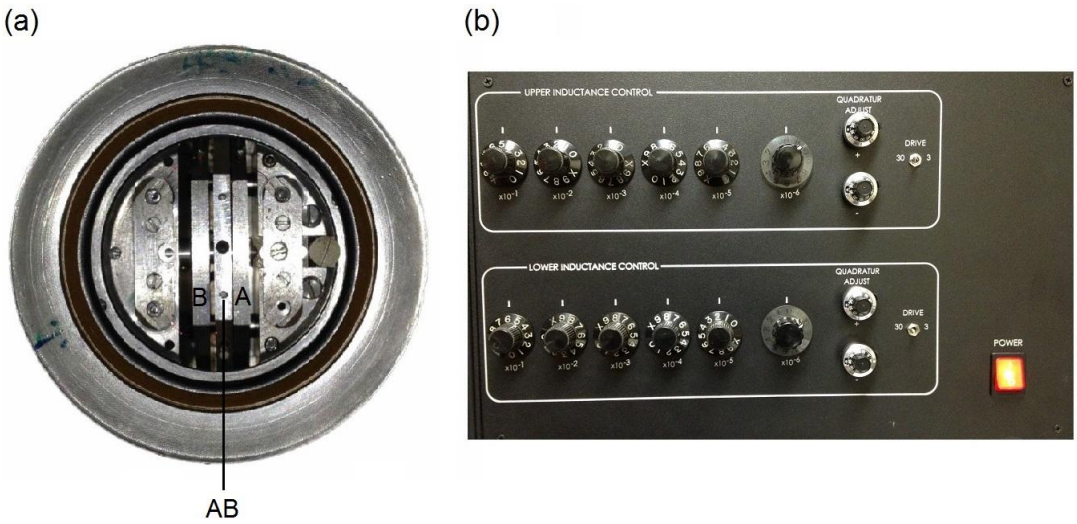


**Figure 3.4** (a) A three-plate capacitance transducer; (b) the 6-digit ratio transformers.

The linearity between displacement and capacitive impedance is discussed below. First, each single transducer has three individual plates to construct two parallel-plate capacitors. The three plates are denoted from right to left as plate A, plate AB, and plate B. Two outer plates A and B are rigidly bolted together with a fixed spacing (for instance, the current value is 1.95 mm as shown in Fig. 3.4).

Recall the electrical relationships for AC circuitry:

$$Z = R + iX \,, \tag{3.14}$$

where $Z$ is impedance, $R$ is resistance, and $X$ is reactance. Reactance $X$ has different forms for capacitance and inductance. For capacitive reactance,

$$X_C = \frac{1}{\omega C} \,. \tag{3.15}$$

For inductive reactance,

$$X_L = \omega L \,, \tag{3.16}$$

where $\omega$ is angular frequency, $C$ is capacitance, and $L$ is inductance. For a parallel-plate capacitor, the capacitance $C$ is related to the distance $d$ between two plates as:

$$C = \frac{\varepsilon A}{d}, \tag{3.17}$$

where $\varepsilon$ is the dielectric constant, $A$ is the overlap area of plates, and $d$ is the spacing between the two parallel plates. By combining equations (3.15) and (3.17), we have:

$$X_C = \frac{d}{\omega \varepsilon A}, \tag{3.18}$$

which indicates the linear relationship between the capacitive reactance $X_C$ and the plate spacing $d$. This is the essential relationship to convert displacement, a physical quantity, into an electrical quantity to measure.

A bridge, including both inductive and capacitive arms, is constructed in order to provide a more precise measurement of the small change of an electrical quantity (Fig. 3.5). For the inductive part of the bridge, the ratio $r$ of inductive reactance between the lower coil $X_{L1}$ to the total $X_L$ is adjustable by switching the six knobs, corresponding to the first six decimal digits, on the ratio transformer (Fig. 3.4 b). For the capacitive arm of the bridge, by convention, the capacitive reactance ratio $r'$ is always expressed as the proportion of reactance for the left-hand side pair of plates to the total. The bridge is balanced if the potential difference across the bridge from left to right is zero. Under such a condition, the capacitive reactance ratio between plates B-AB and plates A-B $r'$ is equal to the inductive reactance ratio $r$ which is readable from the 6-digit ratio transformer (Fig. 3.5). For a parallel-plate capacitor, remember its capacitive reactance is proportional to the distance between the plates (Eq. 3.18). The expression below is obtained:

$$r = \frac{X_{L1}}{X_L} = \frac{X_{C,B-AB}}{X_{C,A-B}} = \frac{d_{B-AB}}{d_{A-B}} = \frac{d_{B-AB}}{1.95\ mm}. \tag{3.19}$$

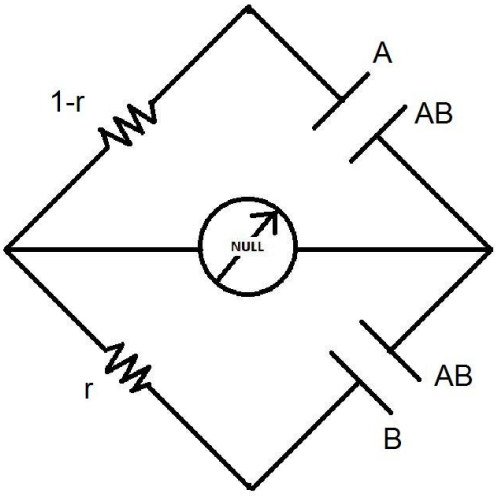


**Figure 3.5** AC bridge circuitry for an individual three-plate capacitance transducer. The displacement of either the rock specimen or the elastic standard can be directly converted to an electrical quantity, *i.e.*, the out-of-balance voltage of the bridge. Notice that plate AB is physically a single plate, but drawn separately for clearer illustration.

In practice, the central plate AB is movable relative to the two fixed outer plates A and B. The relationship derived above gives the exact position of the central moving plate AB relative to the fixed outer plates A and B. The bridge (Fig. 3.5) is excited at 10 kHz with synchronous detection at 20 kHz on the Jackson – Paterson Attenuation Apparatus.

3.1.1.3 Torsional and flexural discrimination and sensitivities

Another technical challenge in measuring the torsional displacement is to isolate the torsional response from a mixture of torsional and flexure deformations, resulting, for example, from any imbalance between the forces applied by the two driver units.

To address this, the idea of using a pair of three-plate capacitance transducers and connecting them diagonally in parallel (Fig. 3.6 a) was adopted (Brennan, 1981). In this way, any flexural displacement is discriminated against, leaving torsional displacement only. In Fig.3.6 a, consider that the first three-plate capacitance transducer is denoted as A-AB-B and the second transducer of the same arrangement is denoted as C-CD-D. Each three-plate capacitance transducer can be split into a pair of two-plate capacitance transducers. For example, transducer A-AB-B can be separated into two-plate transducer A-AB and AB-B. The same is true for transducer C-CD-D. The diagonal connection requires the two-plate capacitance transducer A-AB is connected in parallel with the two-plate transducer CD-D instead of its counterpart of C-CD. Similarly, two-plate transducer AB-B is connected in parallel with transducer C-CD (Fig. 3.5 b). Then transducer pair A-AB and CD-D is

connected with the other transducer pair AB-B and C-CD in series to form the capacitive arm of the bridge. Among all these six plates, plate A, B, C, D are outer plates and the positions of which are always fixed during the forced-oscillation experiments, whereas plate AB and CD are central plates which are mechanically connected with the axial specimen assembly and can move along with it if any deformation takes place.

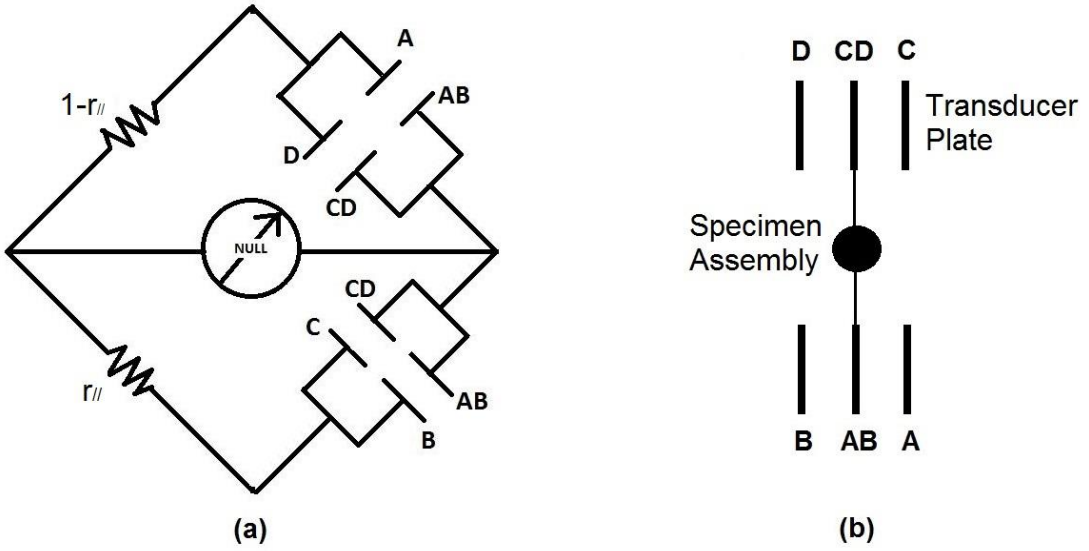


**Figure 3.6** Two three-plate transducer A-AB-B and C-CD-D are connected together to form the capacitive arm of an AC bridge. (a) The two-plate capacitor A-AB is diagonally connected with D-CD, and the two-plate capacitor AB-B is connected with C-CD to discriminate against any flexural mode displacement following the design by Brennan (1981). (b) The plan view of transducer plates on the Jackson–Paterson Attenuation Apparatus.

Grounding one of the pair of three-plate capacitance transducers will reduce the circuitry to that for a single three-plate capacitance transducer introduced in *Section 3.1.1.2*. In this case, the individual transducer ratios $r_1$ and $r_2$ are readable, corresponding to the capacitive reactance ratios between plates B-AB and plates A-B, and the ratio between plates C-CD and plates C-D, respectively. If both three-plate transducers are connected in the bridge, the inductance ratio read from the 6-digit ratio transformer is denoted as $r_{/\!/}$. The explicit expressions of the torsional sensitivity $A_T$ and the flexural sensitivity $A_F$ are given in Jackson and Paterson (1993), and the detailed derivation can be found in *Appendix A*:

$$A_T = \frac{\partial r_{/\!/}}{\partial r_1} + \frac{\partial r_{/\!/}}{\partial r_2} = 1 + \frac{(r_1 - r_2)^2[(1-r_1)(1-r_2)+r_1 r_2]}{[r_1(1-r_1)+r_2(1-r_2)]^2}, \tag{3.20}$$

$$A_F = \frac{\partial r_{/\!/}}{\partial r_1} - \frac{\partial r_{/\!/}}{\partial r_2} = \frac{(r_2^2 - r_1^2)(1-r_1-r_2)(2-r_1-r_2)}{[r_1(1-r_1)+r_2(1-r_2)]^2}. \tag{3.21}$$

The ideal situation is $A_T = 1$ and $A_F = 0$, which means there is only sensitivity to torsional mode. From the expression above, it is concluded that this ideal condition can only be

achieved when $r_1 = r_2$. In practice, the procedure of transducer alignment is routinely needed so as to achieve or approach this ideal condition of $r_1 = r_2 = 0.5$.

The existence of pressure dependent distortions on the transducer plates, the pressure vessel, and the specimen assembly at certain pressure level disturb the ratio from the original value of 0.5 set at ambient conditions. But fortunately, this pressure-induced distortion proves to be reproducible, which implies that the ideal ratios at a certain pressure level still can be achieved once appropriate corrections are applied to the transducers in advance at ambient conditions. The corrections are predetermined from the most recent run at the desired pressure.

Practical transducer alignment first involves choice of a pressure level as the ideal working condition, which is usually half of the maximum pressure involved in the experiment. For instance, 50 MPa is normally selected as the ideal pressure level for experiments conducted below 100 MPa. The individual transducer ratios are measured and corresponding corrections are determined at this target working pressure. The corrections are subsequently applied to transducers at ambient conditions. If the alignment is appropriately performed, the individual transducer ratios will be found to be within +/- 0.03 of 0.5 once the chosen pressure level is reached again – so that the parallel transducer sensitivities $A_F$ and $A_T$ deviate from their ideal values by no more than +/- 0.01.

#### 3.1.1.4 Calibration

There are two crucial aspects from the previous discussion: 1) the bridge balance ratio for an individual three-plate capacitance transducer can provide us with the position of the central moving plate which is further mechanically connected with the specimen assembly; 2) the balance of bridge for a pair of three-plate transducer is disturbed by any displacement of the central moving plate, giving an out-of-balance electrical quantity, *i.e.*, voltage in our case. Then the question becomes how to determine the factor that converts between the displacement of the central moving plate and the out-of-balance voltage. A calibration is needed in order to obtain the answer.

It is obvious that the accuracy of measurement of displacement is directly decided by the quality of the calibration factor. There are two dimensions to characterise such quality: representativeness and uncertainty. It is desirable that the total range of out-of-balance voltage created in forced oscillations should be covered as closely as possible in calibration. The representativeness of calibration should also take into account any time dependent changes in pressure which can result in drift of transducer ratios and sensitivities. For a forced-oscillation experiment with duration of about 1 hour, calibrations are needed both prior to and after the forced oscillation tests, in order to represent the entire duration of

experiments. The calibrations are required to be conducted right before the start and immediately after the end of forced oscillations. In such a way, calibrations are expected to well simulate and represent the environment of the real forced oscillations in the sense of both voltage amplitude and time.

Minor difference in calibration factors collected before and after forced oscillations is expected and related to the change of pressure and other environmental conditions. This difference gives the uncertainty in calibration factor, eventually propagating into the displacement of specimen. In order to minimize this uncertainty, a stable working condition is highly desirable for the entire duration of forced oscillations, *i.e.*, normally about 1 hour. Any leak of confining-pressure gas contributes to a variation in the calibration factor and thus uncertainty in the converted displacement.

Before describing the operational process of calibration, it is worth emphasising that the central moving plate of a transducer remains fixed during the whole process of calibration. If we recall the electrical circuitry shown in Fig. 3.6 (a) and (b), the same out-of-balance voltage $\delta V$ can be achieved by either the displacement of the central moving plate with the inductive arm of the circuitry unchanged or by an intentional change of the ratio on the inductive arm by switching on the 6-digit ratio transformer with the central moving plate undisturbed. The process of calibration involves the latter method to simulate and recover the same out-of-balance voltage created by the former method.

In calibration, practically, a 10 min-duration data record is logged with the sampling density of one sample per 0.1 s. Totally, 6000 samples are taken and equally divided into three segments with 200s duration for each (Fig. 3.7). Symmetrical out-of-balance voltages $\delta V$ are created by a manual switching of the transformer ratio through a known increment $\delta r_{/\!/}$ in the absence of an applied torque.

Similar to the single transducer described in Eq. (3.19), the parallel mode of a pair of transducers also has the relationship as:

$$\delta d = D \cdot \delta r_{/\!/} \,, \tag{3.22}$$

where $D$ is the fixed spacing between two outer plates with the current setting of 1.95 mm. Physically, this can be interpreted as the bridge out-of-balance voltage caused by the increment of the ratio for parallel combination of transducers $\delta r_{/\!/}$ is of the same amount as that would be created by the displacement of the central moving plate $\delta d$. This expression directly provides the displacement that corresponds to the known ratio increments applied in calibration. The conversion factor, naturally, comes as the ratio between the out-of-balance voltage $\delta V$ and the displacement $\delta d$ after the increment $\delta r_{/\!/}$ performed on the ratio transformer.

However, the bridge out-of-balance voltage for the parallel combination of transducers $\delta V$ during forced oscillation comprises both torsional and minor flexural mode displacement, which are distinguished by the sensitivities $A_T$ and $A_F$. The calibration factor, finally, is therefore given:

$$f = \frac{A_T \cdot \delta V}{\delta d} = \frac{A_T \cdot \delta V}{D \cdot \delta r_{/\!/}} . \tag{3.23}$$

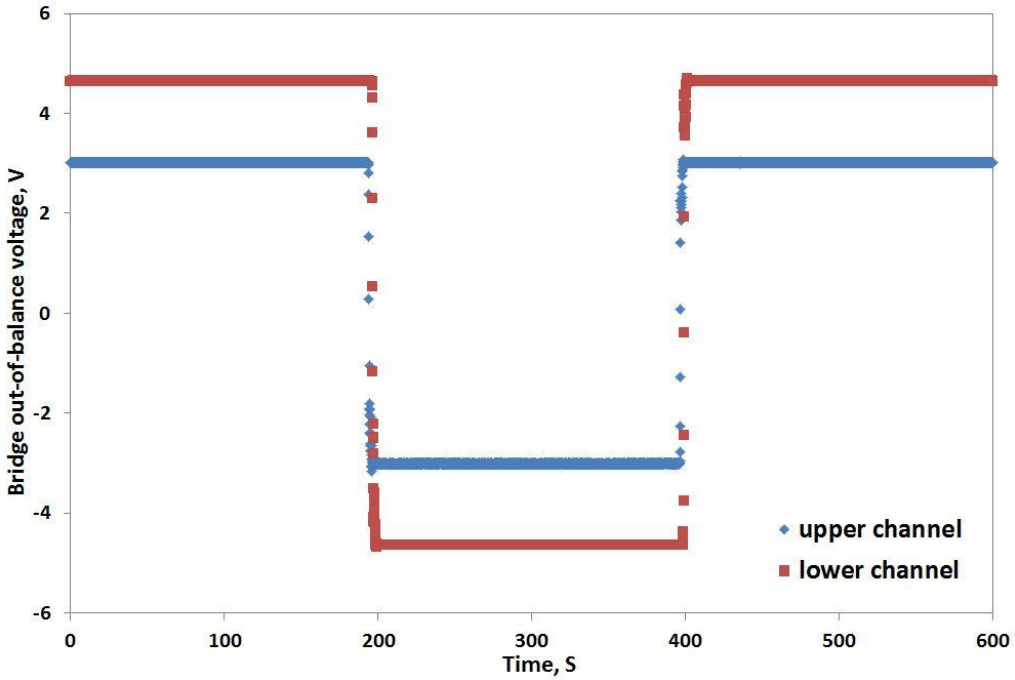


**Figure 3.7** A representative calibration record associated with symmetrical switching of transformer ratios for both upper and lower channels. The calibration factor of either the upper or the lower channel is further calculated from such a record with known increment of inductance ratio $\delta r_{/\!/}$ and recorded out-of-balance voltage δV.

Two calibration factors are obtained from the prior and subsequent calibration processes, respectively. The arithmetic mean of these two calibration factors is then calculated and applied to the forced oscillation record to convert the out-of-balance voltage (V) into displacement (μm).

Uncertainties in calibrations are reflected in any difference between the prior and subsequent calibration factors, and the standard deviation $\sigma(C)$ between them provides an estimate of the error of calibration $\frac{\sigma(C)}{C}$.

Generally speaking, $\frac{\sigma(C)}{C}$ is determined by two factors. The first aspect is the stability of the measuring condition: better pressure sealing and constant temperature can lower calibration uncertainties. On the other hand, $\frac{\sigma(C)}{C}$ is also determined by the quantisation error associated with the analog-to-digital conversion. The data acquisition system of the

attenuation apparatus has benefited from an upgrade of the previous 12-bit A/D converter to 18-bit. This has systematically lowered calibration uncertainties by an order of magnitude.

3.1.1.5 Specimen assembly for forced oscillation


**Figure 3.8** Cracked low-porosity (~2%) glass-bead cylinders (labelled as A3, A4, and A5) and two alumina rods, all of which need to be inserted into an annealed copper jacket to form a specimen assembly.

The specimen assembly loaded into the Attenuation Apparatus comprises a sometimes compound specimen of total length 150 mm and diameter 15 mm, between a pair of connecting rods as spacers (Fig. 3.8). The components of a specimen assembly are enclosed within an annealed copper jacket. The purpose of the copper jacket is to accommodate all specimens and connecting rods in place and also separate the pore fluid within the jacket from the confining gas medium outside the jacket. The details of the preparation of a specimen assembly will be described below.

Two types of connecting rods were used in this study: alumina and steel rods, requiring outer diameters of 15 mm in each case. The pair of alumina rods is made of 99.7% Degussa Duramic. The lengths of the upper and lower alumina rods are 96.9 mm and 92.0 mm, respectively. This pair of alumina connecting rods was used in the measurements of compound low-porosity glass-bead specimen A3-5. The presence of microcracks in alumina rods, after many pressure-temperature cycles, causes difficulty in the precise determination of their modulus. Instead, for the other samples, a pair of newly machined steel rods was used, of 94.56 mm and 94.17 mm in length, respectively. Both alumina and steel connecting rods contain axial pore-fluid channels of diameter 2 mm, to allow a pore-fluid flow from reservoirs to the crack network of a specimen. The end surfaces of connecting rods in

contact with specimens are grooved in order to facilitate a more uniform distribution of fluid at interfaces (Fig. 3.9b).

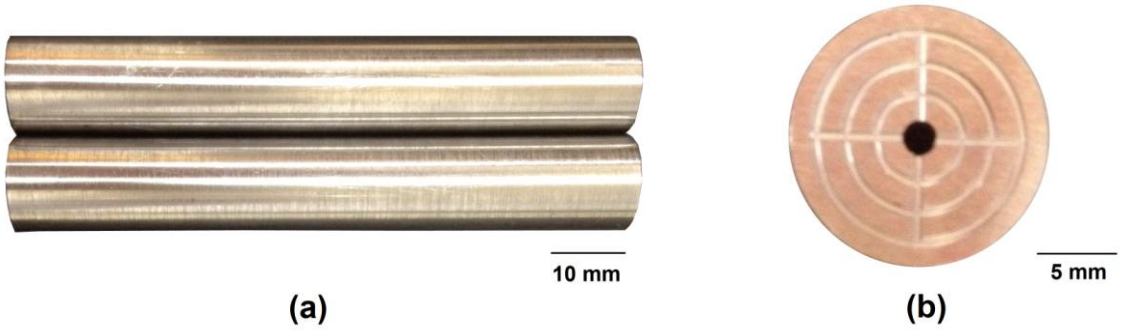


**Figure 3.9** (a) A pair of steel connecting rods was used to replace the microcracked alumina ones; (b) the end of each steel rod in contact with a specimen is machined into concentric grooves connected with radial ones to achieve an even distribution of pore fluid at steel rod – sample interfaces.

The end surfaces of all components are lapped with diamond paste on a polishing jig to achieve optical flatness (checked by a Mitutoyo® optical flat), in order to achieve optimal coupling at interfaces within the specimen assembly. Specimens and connecting rods are thoroughly cleaned with an ultrasonic cleaner while being immersed in tap water, ethanol, and acetone in sequence. After that, both specimens and connecting rods are dried in an oven at 110℃ overnight to remove moisture.

A copper jacket of 15 mm inner diameter and 386 mm in length is prepared on a lathe. Annealing is needed to improve the softness of the jacket by heating at 600 °C surrounded by argon for 30 mins. After annealing, an intimate contact between the jacket and the specimen can be achieved under pressure to minimise any short-circuit flow at the interface between the jacket and specimen, the presence of which may result in an overestimation of permeability.

After a thorough cleaning and drying, the copper jacket is ready to encapsulate all components of the specimen assembly, *i.e.*, specimens and connecting rods. These components are slid into the jacket from either end. A three-way seal O-ring at the top and double nitrile O-rings at the bottom of the jacket assist in sealing the pore-fluid system against the confining pressure system. The loading of specimens and connecting rods may leave scratches on the sealing surfaces for these O-rings. A careful manual polishing is needed then to remove any noticeable scratches to minimise the possibility of a leak.

#### 3.1.1.6 Pressure medium

Either gas or oil can be used as the pressure medium in high-pressure experiments. But the maximum temperature that can be achieved is limited by the boiling point of oil on oil-

medium apparatuses. The Attenuation Apparatus was initially designed for high-temperature work, and noble gas, argon more specifically, was chosen consequently as the confining medium.

At the beginning of each experiment, the pressure vessel of the Attenuation Apparatus is purged with argon gas to drive remaining air out. Three stages are needed to pressurise to the maximum level, *i.e.*, 150 MPa employed in this study: 1) a pressure, normally less than 13 MPa, is reached by simply introducing argon from the commercially supplied gas cylinder; 2) a gas booster is then used to raise the pressure to a level higher than the bottle pressure but no more than 100 MPa; 3) an oil-driven intensifier is needed to increase the pressure beyond 100 MPa. The oil piston of the intensifier, which is advanced by oil pressure generated by an oil pump driven by compressed air, is ~ 6.5 times larger in cross-sectional area than the mechanically connected gas piston (giving the compression ratio of ~ 6.5). The gas pressure is therefore always ~ 6.5 times higher than the oil pressure within the oil chamber of the intensifier.

Besides the medium for confining pressure, argon is also used as a pore-fluid medium in experiments to contrast with water in fluid properties. This will be discussed in *Section 3.1.1.14*.

#### 3.1.1.7 Coupling of specimen assembly components

From previous discussion, all components of the specimen assembly and steel pistons need to be well coupled to form an integral beam. Excessive interfacial compliance will lead to an unsuccessful experiment.

The initial pressurisation to 150 MPa after sample loading deforms the annealed copper jacket into longitudinal and tangential grooves on the steel members of the specimen assembly. All components of the specimen assembly, the steel elastic standard, and the inner top nut of the pressure vessel are frictionally coupled through a normal stress equal to the confining pressure. In this way, the applied torque is transmitted from the driver units to the full cross-section of the entire integral beam.

3.1.1.8 Electromagnetic drivers and forced-oscillation protocol

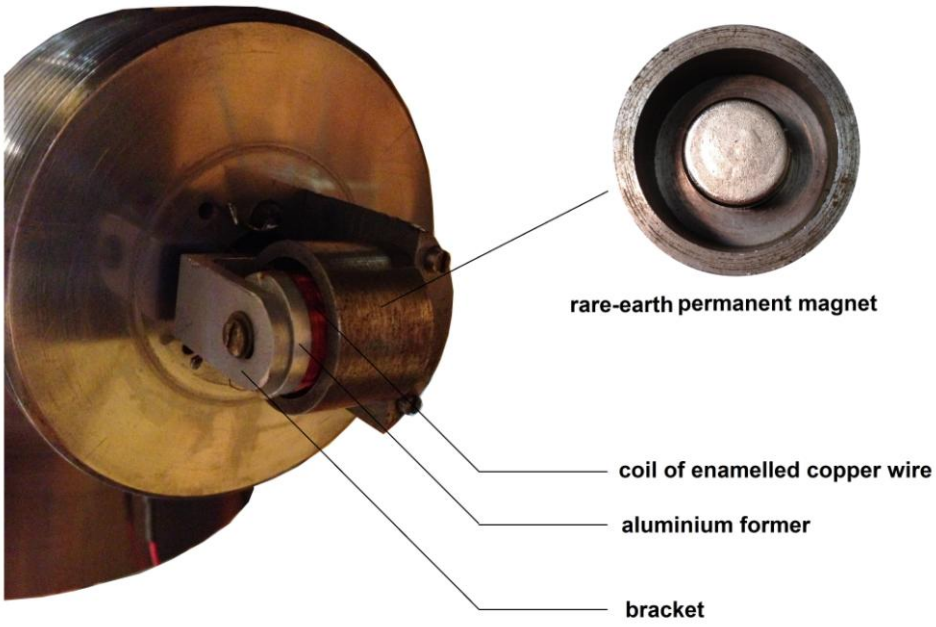


**Figure 3.10** Arrangements of an electromagnetic driver. The $Nd_2Fe_{14}B$ permanent magnet remains stationary all the time with a coaxial soft-iron cup to shape the magnetic field. The aluminium former with a coil of wound copper wire is mounted on a bracket, forming a mechanically integral unit with the steel elastic standard and specimen assembly. An oscillating magnetic field generated by a current through the coil allows relative motion of the former with respect to the stationary permanent magnet.

The previous sections have discussed each major component of the design for forced oscillations. The forced oscillation is realised by putting all these components together: a specimen assembly is mechanically and frictionally coupled with the steel elastic standard, lever arms and moving central transducer plates under pressure. A balanced pair of electromagnetic drivers works cooperatively at the lower end of the steel elastic standard to generate a torque at a prescribed oscillation period (Fig. 3.10). The torque is transmitted through the elastic standard to the specimen to allow it torsionally deformed. The deformation associated with the specimen and elastic standard are monitored by pairs of three-plate capacitive transducers at each of the upper and lower stations.

The oscillation periods at which the torque is generated need to be carefully designed. Each forced oscillation experiment involves successive measurement of the response at 8 different forced oscillation periods: 0.64s, 1.28s, 3.84s, 6.40s, 11.52s, 21.76s, 47.36s and 101.12s. 16 consecutive cycles of forced oscillation are collected for each oscillation period, and 128 samples are collected in each cycle. Totally, $128 \times 16 = 2{,}048$ samples are acquired for each oscillation period. At each particular oscillation period, several

preliminary cycles are needed to achieve a steady status for the formal data acquisition. The preliminary oscillations are not recorded. An extra cycle is needed at the end of each oscillation period in case of incomplete data record caused by the mechanical distortion at the end of each oscillation period.

This forced oscillation protocol is designed based on the considerations listed below:

(i) Having an exact integer number $N$ of samples per oscillation period $T_0$ to avoid energy spreading between adjacent frequencies in the Fourier transform;

(ii) Setting $N = 2^n$ to allow the use of the Fast Fourier Transform algorithm;

As a result, $N = 2^7 = 128$ samples are collected for each sinusoidal cycle. Another constraint is:

(iii) The 50 Hz mains-frequency noise is aliased with the signal. The cleanest separation between the noise and signal is to choose the forced oscillation period $T_0$ and the sampling frequency $f_s$ so that any 50 Hz noise appears at the Nyquist (folding) frequency $f_N = \frac{f_s}{2}$. Physically, the Nyquist frequency represents the highest frequency of a signal that can be reconstructed from the given sampling frequency $f_s$. Express this idea mathematically:

$$50\ Hz = (2n+1)f_N = (2n+1)\frac{f_s}{2} \quad n = 0, 1, 2, 3 \dots . \tag{3.24}$$

Notice that the sampling frequency $f_s = \frac{128}{T_0}$, then substitute into the expression above:

$$50\ Hz = (2n+1)\frac{128}{2T_0} = (2n+1)\frac{64}{T_0} \quad n = 0, 1, 2, 3 \dots , \tag{3.25}$$

$$T_0 = 1.28(2n+1) \quad n = 0, 1, 2, 3 \dots . \tag{3.26}$$

Hence the optimal oscillation periods are 1.28s ($n$ = 0), 3.84s ($n$ = 1), 6.40s ($n$ = 2), 11.52s ($n$ = 4), 21.76s ($n$ = 8), 47.36s ($n$ = 18), and 101.12s ($n$ = 39) (Table 3.1) – these values of $n$ being chosen for approximately even logarithmic spacing of the oscillation periods. An additional oscillation period of 0.64s is also included in the latest protocol after the upgrade of the data acquisition system to test at a relatively high frequency.

| Oscillation period, s | Oscillation sampling interval, s | Oscillation sampling frequency, Hz | Samples to read | Number of pre-generation cycles | Number of cycles for formal data acquisition | Total number of cycles |
|---|---|---|---|---|---|---|
| 0.64 | 0.005 | 200 | 100 | 188 | 17 | 205 |
| 1.28 | 0.01 | 100 | 200 | 94 | 17 | 111 |
| 3.84 | 0.03 | 33.3 | 600 | 31 | 17 | 48 |
| 6.40 | 0.05 | 20 | 1000 | 19 | 17 | 36 |
| 11.52 | 0.09 | 11.11 | 1800 | 10 | 17 | 27 |
| 21.76 | 0.17 | 5.88 | 3400 | 6 | 17 | 23 |
| 47.36 | 0.37 | 2.703 | 7400 | 3 | 17 | 20 |
| 101.12 | 0.79 | 1.266 | 15800 | 1 | 17 | 18 |

**Table 3.1** Protocol of forced oscillation experiments based on the criteria described in the text. Bridge sampling frequency is fixed at 20 kHz for the 10 kHz bridge excitation frequency. For each prescribed oscillation period, oscillation sampling interval is adjusted so as to collect and record 128 samples for every single oscillation cycle. The reciprocal of oscillation sampling interval gives oscillation sampling frequency, which is related to the 20 kHz bridge sampling frequency through a parameter known as "samples to read". This parameter is the number of successive samples collected with the 20 kHz bridge sampling frequency for average and recording, which gives that the product of oscillation sampling frequency and samples to read is always equal to 20 kHz bridge sampling frequency. The total number of oscillation cycles is determined by the pre-generated cycles (2 minutes or single period whichever is greater), 16 data-acquisition cycles, and one additional incomplete cycle at the end of oscillations at each period.

3.1.1.9 Complex normalised torsional compliance

Because of non-linearity in the conversion of electric current into torque by electromagnetic drivers, and interference at the mains frequency of 50 Hz (Jackson & Paterson, 1993), the response at the driving frequency needs to be extracted from the background noise by using discrete Fourier analysis.

With the collected 2048 samples, the lowest resolvable integer frequency $v = 1$ corresponds to a single complete period contained in the entire time series. For a record containing 16 oscillation periods, the signal appears in the Fourier transform at $v = 16$ (Fig. 3.11). The highest resolvable (Nyquist) frequency is associated with consecutive samples of opposite sign with $v = 1024$. The smooth curve at integer frequencies higher than 50 (Fig. 3.11) shows the benefit of the newly installed low-pass digital filter, which excludes any noise with frequency higher than three times the oscillation frequency. The signal-to-noise

ratio estimated always remains at $10^2$ to $10^4$ throughout the experiments after the upgrade of the data acquisition system, which means clear and reliable signals can be distinguished from the background noise.

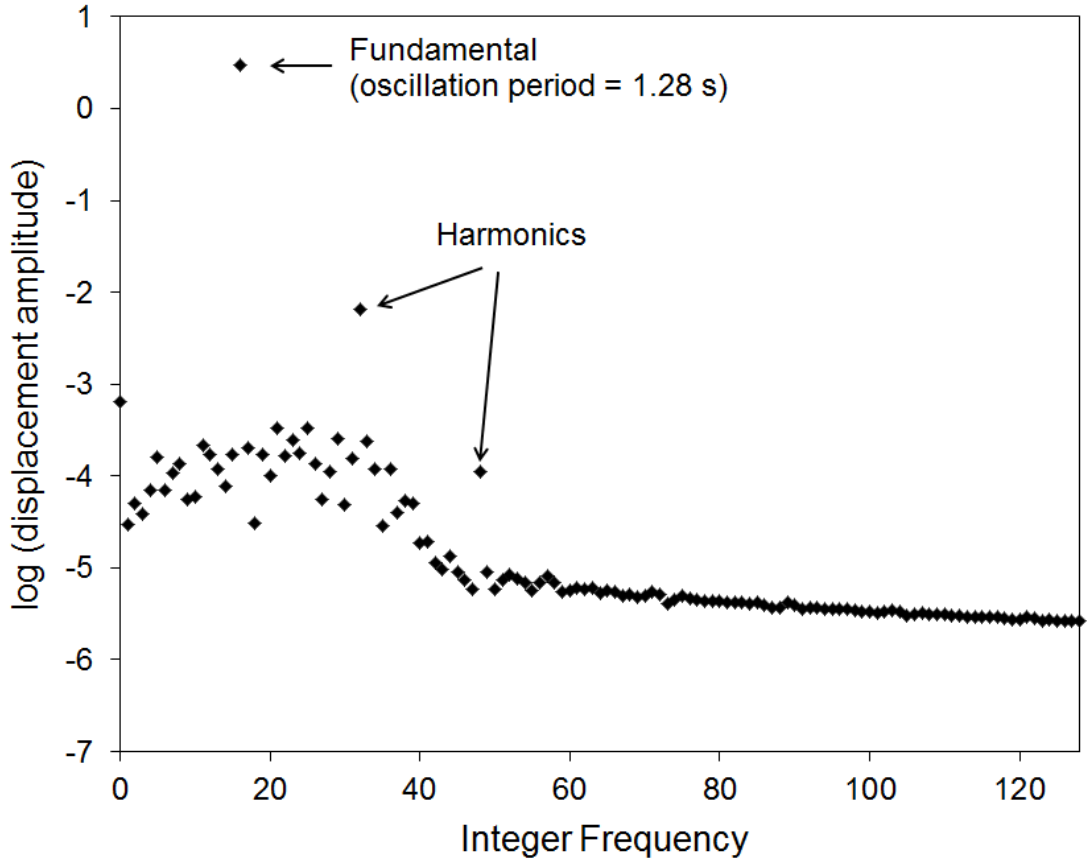


**Figure 3.11** Fourier transformed displacement (part of spectrum) of the upper channel. Harmonic distortion arises from the non-linearity in conversion of electric current into torque in the electromagnetic drivers. It shows a signal-to-noise ratio of $10^3$ to $10^4$ at the fundamental driving frequency (integer frequency $v$ = 16). This FFT result is taken from the measurements on a compound low-porosity glass-bead specimen (A3-5) with water saturation.

With the assistance of discrete Fourier analysis, both the amplitude and phase of the original sinusoidal out-of-balance voltage are obtained for each of the upper and lower channels, *i.e.*, $A_1 e^{i\phi_1}$ and $A_2 e^{i\phi_2}$ (Fig. 3.12 a). After applying the calibration factors (Eq. 3.23, unit: V/μm) to the time series of voltage of each channel, the displacements (unit: μm) measured at the upper and lower stations are obtained (Fig. 3.12 b) as $d_1 e^{i\phi_1}$ and $d_2 e^{i\phi_2}$. Notice that the response measured at the upper station $d_1 e^{i\phi_1}$ is the displacement associated with distortion of the specimen assembly (inclusive of jacket and connecting rods), whereas the differential response between the two stations is the displacement associated with distortion of the elastic standard $d_{12} e^{i\phi_{12}}$ (Fig. 3.12 c).

$$d_{12} e^{i\phi_{12}} = d_2 e^{i\phi_2} - d_1 e^{i\phi_1} \tag{3.27}$$

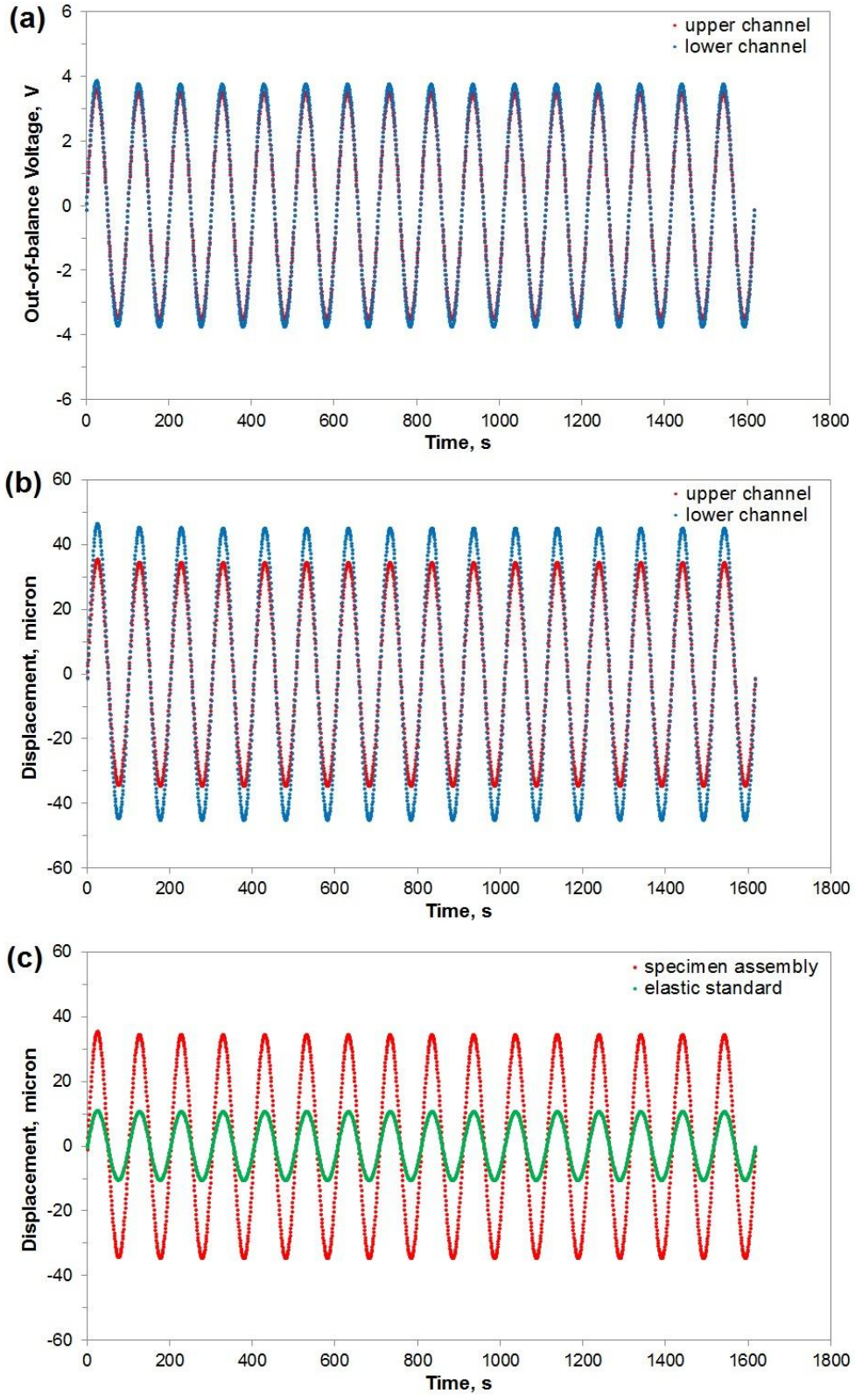


**Figure 3.12** An illustration of extracting (c) the torsional displacement time series of both the specimen and elastic standard from (a) the raw out-of-balance voltages measured at the upper and lower stations, through (b) the conversion from voltage into displacement by applying calibration factors. These representative results are obtained from a fully-dense glass sample (uncracked) under the confining pressure of 60 MPa and at 101.12 s oscillation period. 16 consecutive cycles are recorded by the *LabVIEW* program.

The torsional stiffness *k* is defined as:

$$k = \frac{T}{\Delta\phi}, \tag{3.28}$$

where $T$ is the applied torque and $\Delta\phi$ is the twist angle. The reciprocal of the torsional stiffness *k* is called the torsional compliance *S* (rad/Nm):

$$S = \frac{1}{k} = \frac{\Delta\phi}{T}. \tag{3.29}$$

Fig. 3.13 illustrates the way that the twist angle $\Delta\phi$ relates to the measured displacement *d*. Assuming this is the case of the upper station, the measured displacement and twist angle are directly related to the specimen assembly. The geometry gives:

$$d_1 = \Delta\phi_1 \cdot R, \tag{3.30}$$

where $d_1$ is the measured displacement amplitude of the specimen at the upper station; $\Delta\phi_1$ is the associated angle of twist at the upper station; and *R* is the distance from the centre of the specimen-elastic standard assembly to the centre of the active part of the transducer central moving plate.

Similarly, we have an equivalent expression for the lower station:

$$d_2 = \Delta\phi_2 \cdot R, \tag{3.31}$$

where $d_2$ is the measured displacement amplitude at the lower station; $\Delta\phi_2$ is the associated angle of twist at the lower station.

The displacement of the elastic standard is:

$$d_{12} = \Delta\phi_{12} \cdot R, \tag{3.32}$$

where $d_{12}$ is the displacement amplitude of the elastic standard; $\Delta\phi_{12}$ is the associated angle of twist of the elastic standard.

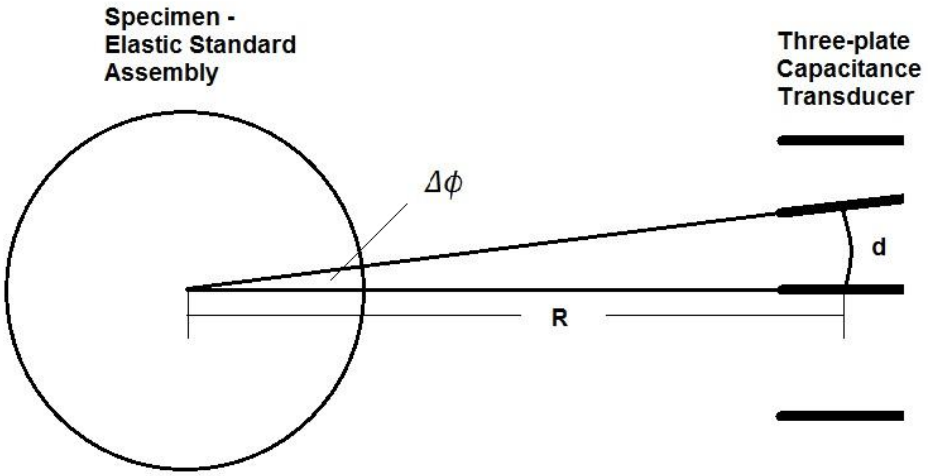


**Figure 3.13** A schematic illustration of the geometry of the specimen-elastic standard assembly, the twist angle, and the capacitance transducer.

By combining Eq. (3.29) and (3.30) or (3.32), the torsional compliances of the specimen assembly and elastic standard are given as:

$$S_1 = \frac{d_1}{RT_1}, \tag{3.33}$$

$$S_{12} = \frac{d_{12}}{RT_{12}}. \tag{3.34}$$

If the torsional compliance of the specimen is normalised to that of the elastic standard, and notice that both the specimen and elastic standard share the same torque ($T_1 = T_{12}$), the complex normalised torsional compliance $S_N^*$ is obtained as:

$$S_N^* = \frac{S_1 e^{i\phi_1}}{S_{12} e^{i\phi_{12}}} = \frac{d_1}{d_{12}} e^{i(\phi_1 - \phi_{12})}, \tag{3.35}$$

with its magnitude $S_N = |S_N^*| = d_1/d_{12}$. Cracked materials have higher $S_N$ at lower differential pressures (confining pressure – pore pressure) because the specimen becomes more compliant with open cracks. $S_N$ is routinely calculated during experiments, and further processed to shear modulus $G$ by comparing with a elastic reference of known modulus. In the meantime, the phase lag between the specimen assembly and elastic standard is converted to attenuation $1/Q$. The purpose of the comparison with an elastic reference assembly will be described in the next section.

3.1.1.10 Extraneous sources of apparent anelasticity

There are several ways that can introduce extraneous anelasticity to the system under test besides the mechanical behaviour of the specimen itself.

(i) Interface

Interfacial issue between the tested specimen and apparatus is universal in almost all techniques for mechanical tests, *e.g.*, ultrasonic wave propagation, resonant bar, forced oscillation, *etc*. A good specimen – machine coupling can minimize this interfacial issue. More specifically, on the Attenuation Apparatus, interfaces between different members within the specimen assembly (specimen - specimen, specimen - connecting rod, connecting rod - steel piston) introduce uncertainties due to relative sliding under low pressures. So, interfacial compliance is minimised by normal loading on the interfaces resulting from the application of confining pressure. This effect was generally found to be negligible beyond 50 MPa (Jackson & Paterson, 1993; Lu, 1996).

Contaminants at interfaces or uneven contacting surfaces can introduce uncertainties. If a thin film of annealed copper jacket intrudes at interfaces between different assembly members, a relatively high normalised compliance $S_N$ is expected. A suspiciously high value of $S_N$ can be viewed as an indicator for a possible jacket intrusion.

(ii) Connecting rods and annealed copper jacket

The imperfect connecting rods, for instance, alumina rods with microcracks, and the annealed copper jacket are found to contribute extra anelasticity to the overall compliance of the assembly.

A parallel experiment is needed with a purely elastic control specimen of known moduli, *e.g.*, fused silica (Fig. 3.14), uncracked soda-lime glass, *etc.*, in the same arrangement as that for the unknown specimen. The elastic properties of the purely elastic reference can be determined by either referring to published values or wave speeds measured by ultrasonic method. By comparing the results of the reference and specimen assemblies, extraneous contributions of anelasticity from sources (i) and (ii) are both minimised, leaving the anelasticity contributed from the specimen only (Jackson & Paterson, 1993).

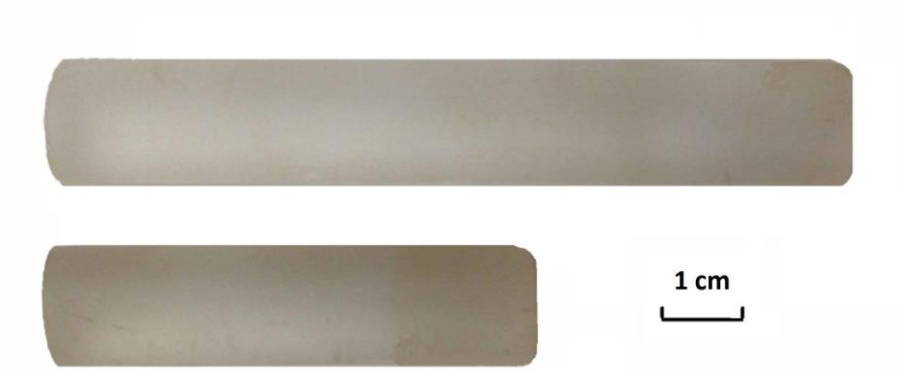


**Figure 3.14** Two cylinders of fused silica of 15 mm in diameter, and 92.46 mm and 57.60 mm in length, respectively. Together they have a total length of 150 mm as the elastic control specimen in a parallel experiment.

(iii) Interaction with the (gas) pressure medium

The central moving plate of each transducer, as discussed in previous sections, is mechanically connected to a lever arm, forming an integral unit with the specimen assembly. The twist resulting from the torque generated by a pair of electromagnetic drivers is reflected in the motion of the central moving plate, resulting in an oscillatory motion of the central plate with respect to the fixed outer plates. This periodic motion of the central plate induces argon gas flow between the closely spaced plates. The argon gas displaced by plate motion exerts a force on the central plate resulting in an additional torque with impact on the position of the central moving plate. Compensation for this effect related to pressure medium is applied routinely during data processing. The argon correction is normally performed before obtaining the interim normalised torsional compliance. This effect is more significant at short oscillation periods (0.64 s and 1.28 s periods) as the argon between the transducer plates has less time for the necessary radial flow, and becomes negligible at longer periods.

3.1.1.11 Extracting shear modulus of the unknown

From the description in the previous sections, the raw data of the time series of displacement (in Volts) yield the amplitudes and phases of angular distortions of the specimen and the elastic standard of known compliance. The complex normalised compliance $S_N^* = \frac{d_1}{d_{12}} e^{i(\phi_1 - \phi_{12})}$ of the entire specimen assembly inclusive of specimen, jacket and connecting rods provides an interim measure of the anelastic response of the specimen assembly pending calculation of the absolute compliance and thus the shear modulus of the specimen.

The measured (complex) torsional compliance consists of the intrinsic response from the specimen itself and many other sources, including the steel members of the assembly, the connecting rods, interfacial compliances, and the copper jacket. A parallel experiment with a control specimen (reference) of known compliance is therefore conducted. Subtraction of the complex compliance of the reference assembly from that of the specimen assembly yields the difference in compliance between the jacketed specimen and the jacketed control specimen (Fig. 3.15).

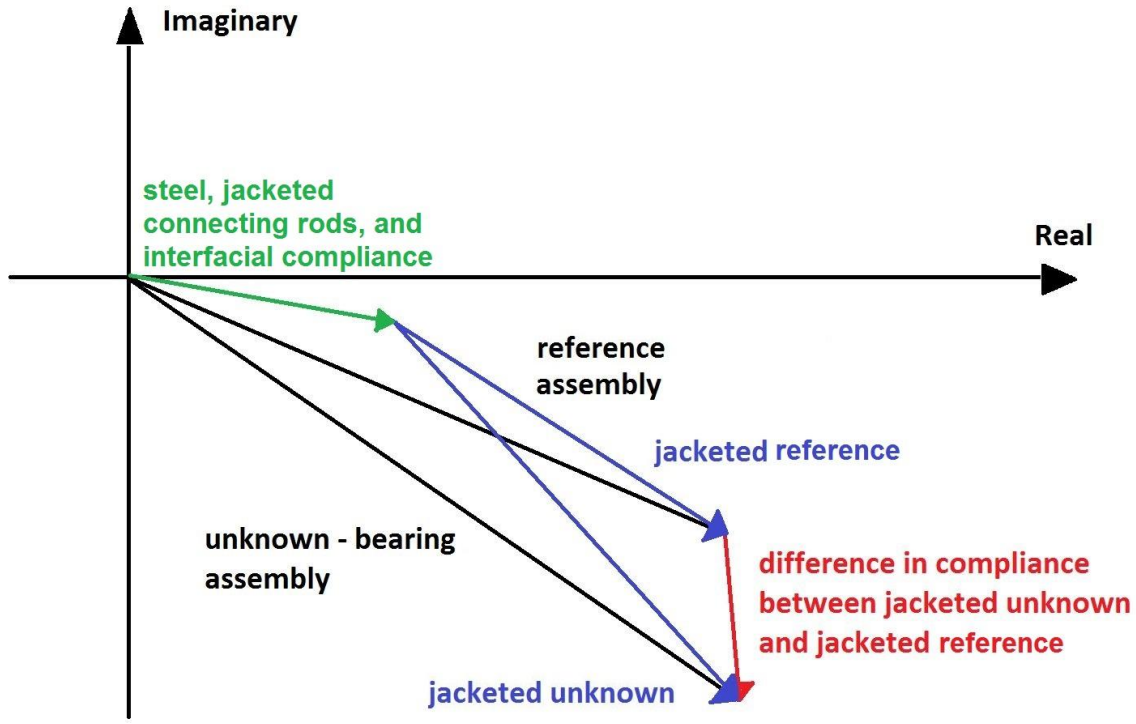


**Figure 3.15** An illustration of different contributions to the measured (complex) torsional compliance of both reference assembly and unknown specimen assembly (Revised after Jackson and Paterson, 1993).

The measured (complex) normalised compliance of the reference assembly $S^*_{N,Ref}$ (upper black) consists of two components: the compliance contributed from (i) the steel, jacketed connecting rods, and interfacial compliance $S^*_{N,0}$ (green); (ii) the jacketed control specimen $S^*_{N,jref}$ (upper blue). It is expressed as:

$$S^*_{N,Ref} = S^*_{N,0} + S^*_{N,jref} \ . \tag{3.36}$$

For the normalised torsional compliance for the unknown-bearing assembly $S^*_{N,Un}$ (lower black), it also consists of the compliances contributed from (i) the steel, jacketed connecting rods, and interfacial compliance $S^*_{N,0}$ (green); (ii) the jacketed unknown $S^*_{N,jun}$ (lower blue). This is expressed as:

$$S^*_{N,Un} = S^*_{N,0} + S^*_{N,jun} \,. \tag{3.37}$$

Notice the common term $S^*_{N,0}$ in both equations, because the setups for both experiments are identical except for the specimen, and combine them to get:

$$S^*_{N,jun} = (S^*_{N,Un} - S^*_{N,Ref}) + S^*_{N,jref} \,. \tag{3.38}$$

It is the compliance of the jacketed unknown $S^*_{N,jun}$ that is of interest. The compliances of the unknown-bearing assembly and reference assembly $S^*_{N,Un}$ and $S^*_{N,Ref}$ are from the measurements, and thus the difference between them $(S^*_{N,Un} - S^*_{N,Ref})$, indicated as the red line in Fig. 3.15, is a known quantity. Remember that the torsional compliance of the elastic reference is known and the compliance of the jacketed reference specimen $S^*_{N,jref}$ thus can be theoretically calculated. The torsional compliance of the jacketed unknown $S^*_{N,jun}$, as a result, is determined by the measurements.

The processing, so far, works with the normalised compliance instead of the absolute compliance itself. To convert the normalised compliance of the jacketed unknown $S^*_{N,jun}$ back to the absolute compliance $S^*_{jun}$, it is necessary to multiply by the known compliance of the steel elastic standard $S^*_{12}$:

$$S^*_{jun} = S^*_{N,jun} \cdot S^*_{12} \,. \tag{3.39}$$

The stiffness of the jacketed unknown $k^*_{jun}$ is the reciprocal of the compliance of the jacketed unknown $S^*_{jun}$:

$$k^*_{jun} = \frac{1}{S^*_{jun}} \,. \tag{3.40}$$

The jacket is treated as elastic and a jacket correction is performed to subtract the amount of stiffness contributed by the copper jacket $k^*_j$ to leave the stiffness of the unknown only:

$$k^*_{un} = k^*_{jun} - k^*_j \,. \tag{3.41}$$

Combining Eq. (3.3) and (3.10) and rearranging, the explicit expression of the angle of twist is:

$$d\theta = \frac{T}{GJ} dx. \tag{3.42}$$

If the length of the beam is *L* and the torque *T*, shear modulus *G*, and the polar moment of inertia *J* is independent of the distance from the origin of the beam, it can be integrated to give:

$$\theta = \int_0^L \frac{T}{GJ} dx = \frac{T}{GJ} \int_0^L dx = \frac{TL}{GJ} . \quad (3.43)$$

Combined with Eq. (3.28), the definition of torsional stiffness, we have:

$$k = \frac{T}{\theta} = \frac{GJ}{L} . \quad (3.44)$$

Rearrange to get:

$$G = \frac{Lk}{J} . \quad (3.45)$$

The complex shear modulus of the unknown specimen $G^*_{un}$, finally, is extracted from the corrected torsional stiffness $k^*_{un}$ with the equation given above. As $G^*_{un}$ is a complex number, the absolute value of $G^*_{un}$ gives the shear modulus of the unknown and the phase of $G^*_{un}$ relative to an elastic standard provides the attenuation of the unknown (defined as the tangent of the relative phase). The maximum shear strain at the periphery of the specimen $\varepsilon_{max}$ is obtained by combing Eq. (3.11) and (3.34) as:

$$\varepsilon_{max} = \frac{r}{GJR} \frac{d_{12}}{S_{12}} . \quad (3.46)$$

where $r$ is the radius of the specimen; $R$ is the distance from the centre of the specimen-elastic standard assembly to the centre of the active part of the transducer central moving plate; $G$ is the shear modulus of the specimen; $J$ is the polar moment of inertia; $d_{12}$ is the displacement of the elastic standard; $S_{12}$ is the torsional compliance of the elastic standard.

#### 3.1.1.12 Flexure-mode forced oscillation

Two different elastic moduli are required to fully characterise the elastic properties of a material. To better understand the fluid-flow regimes, *e.g.*, as predicted by O'Connell & Budiansky (1977), and distinguish between the saturated isobaric regime and the specimen-wide global flow, it is highly desirable to measure both the bulk and shear moduli.

From the review in *Chapter 1* on the dynamic techniques for mechanical measurement, the behaviour of the bulk modulus of a specimen is accessible either directly or indirectly through Young's modulus with forced oscillation method at seismic frequencies. Alternative techniques involve (i) oscillating confining pressure (the ENS type); (ii) alternating uniaxial compression and extension (the Spencer type); or (iii) flexure (Jackson *et al.*, 2011).

The Jackson-Paterson attenuation apparatus was recently modified to incorporate flexure-mode forced oscillation (Jackson *et al.*, 2011). The electromagnetic drivers, used to provide torque in torsion-mode forced oscillation, were operated in the alternative axial orientation to provide a bending moment near the lower end of the specimen-standard beam

(Fig. 3.16 a). However, the early tests with the arrangements of bending moment showed considerable inconvenience, as the orientations of both drivers and capacitance transducer plates need to be changed each time between horizontal and vertical polarisations. Bending force, as a more convenient alternative, was used since then (Fig. 3.16 b). The alternating polarisations of a pair of electromagnetic drivers near the bottom of the assembly bend the integral assembly periodically.

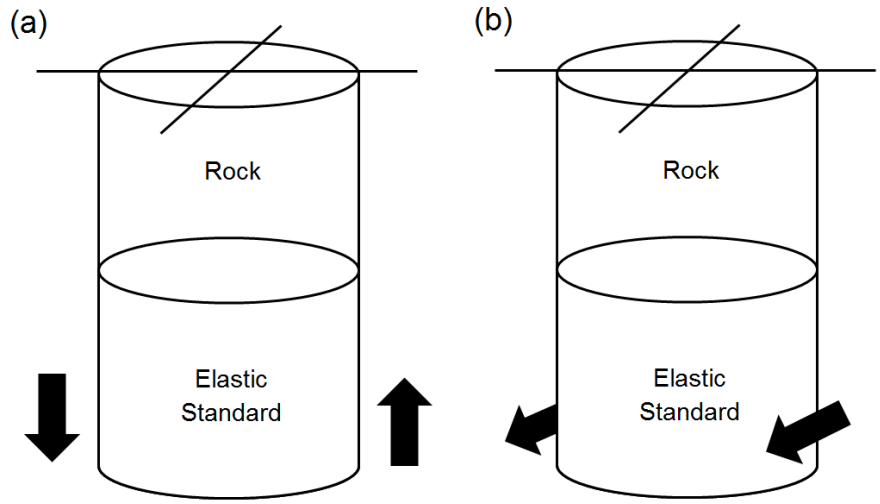


**Figure 3.16** A sketch of the arrangements for flexure-mode forced oscillation method with (a) bending moment and (b) bending force. See Fig. 3.1 for more technical details.

In addition, the two-plate capacitors within the three-plate capacitance transducers need to be connected differently (Fig. 3.17), in order to now discriminate against any torsional component of deformation.

The new arrangement for the bridge circuitry makes the expressions of Eq. (A-3) to Eq. (A-6) change to:

$$X_{A-AB} = X_0 \cdot (1 - r_1) \,, \tag{3.47}$$

$$X_{AB-B} = X_0 \cdot r_1 \,, \tag{3.48}$$

$$X_{C-CD} = X_0 \cdot (1 - r_2) \,, \tag{3.49}$$

$$X_{CD-D} = X_0 \cdot r_2 \,. \tag{3.50}$$

This means, for the individual three-plate capacitance transducer A-AB-B, the ratio *r* read on the 6-digit transformer still reflects the ratio of the B-AB plate separation to that of B-A, as for the torsion mode. However, for the transducer C-CD-D, the ratio *r* becomes the ratio of the D-CD and D-C separations, instead of the ratio between C-CD and C-D for torsion. The consequence is the ratio of individual transducer remains unchanged for the transducer A-AB-B but changes from $r_{2,T}$ to $r_{2,F}$ for the transducer C-CD-D. It is obvious that:

$$r_{2,T} + r_{2,F} = 1\,, \tag{3.51}$$

where $r_{2,T}$ is the ratio of the individual three-plate transducer C-CD-D in torsion and $r_{2,F}$ is the counterpart in flexure. This rule is routinely used in experiments to check the connection of circuitry when the mode is switched from torsion to flexure.

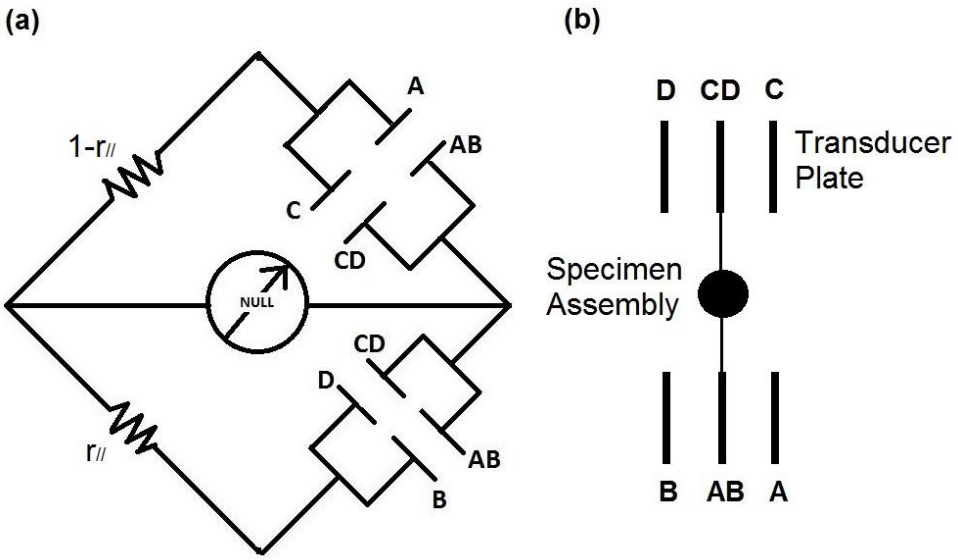


**Figure 3.17** (a) Two three-plate transducers A-AB-B and C-CD-D are connected together to form the capacitive arm of the bridge for flexure-mode forced oscillation; and (b) Plan view.

When both three-plate capacitance transducer A-AB-B and C-CD-D are connected in circuitry, two-plate capacitor AB-B and CD-D are connected in parallel and the equivalent reactance is:

$$\mathrm{X}_{B-D} = \frac{X_{AB-B}X_{CD-D}}{X_{AB-B}+X_{CD-D}} = \frac{X_0 \cdot r_1 \cdot X_0 \cdot r_2}{X_0 \cdot r_1 + X_0 \cdot r_2} = \frac{X_0 \cdot r_1 \cdot r_2}{r_1 + r_2}\,. \tag{3.52}$$

Similarly, the equivalent reactance of A-AB and C-CD connected in parallel is:

$$\mathrm{X}_{A-C} = \frac{X_{A-AB}X_{C-CD}}{X_{A-AB}+X_{C-CD}} = \frac{X_0 \cdot (1-r_1) \cdot X_0 \cdot (1-r_2)}{X_0 \cdot (1-r_1) + X_0 \cdot (1-r_2)} = \frac{X_0 \cdot (1-r_1) \cdot (1-r_2)}{2-r_1-r_2}\,. \tag{3.53}$$

The parallel ratio $r_{/\!/}$ in flexure expressed as:

$$r_{/\!/} = \frac{X_{B-D}}{X_{B-D}+X_{A-C}} = \frac{\frac{X_0 \cdot r_1 \cdot r_2}{r_1+r_2}}{\frac{X_0 \cdot r_1 \cdot r_2}{r_1+r_2} + \frac{X_0 \cdot (1-r_1) \cdot (1-r_2)}{2-r_1-r_2}} = \frac{r_1 \cdot r_2 \cdot (2-r_1-r_2)}{r_1(1-r_1)+r_2(1-r_2)}\,. \tag{3.54}$$

Compared with Eq. (A-9), the expressions of $r_{/\!/}$ in torsion and flexure are identical but involve different values as $r_2$ is for torsion and flexure (Eq. 3.51), unless $r_{2,T} = r_{2,F} = 0.5$, *i.e.*, the central moving plate CD of transducer C-CD-D exactly located in the middle of the two fixed outer plates C and D.

The bridge imbalance $\delta r_{/\!/}$ in flexure has the same expression as that in torsion. However, $\frac{\delta r_1+\delta r_2}{2}$ is now the flexural rather than the torsional component of the bridge imbalance $\delta r_{/\!/}$ in the flexure-mode circuitry. Its coefficient is defined as flexural sensitivity $A_F$ and has the same expression as that given in Eq. (3.20). Similarly, $\frac{\delta r_1-\delta r_2}{2}$ becomes the torsional component of the bridge imbalance $\delta r_{/\!/}$ and has its coefficient defined as torsional sensitivity $A_T$ with the form given in Eq. (3.21).

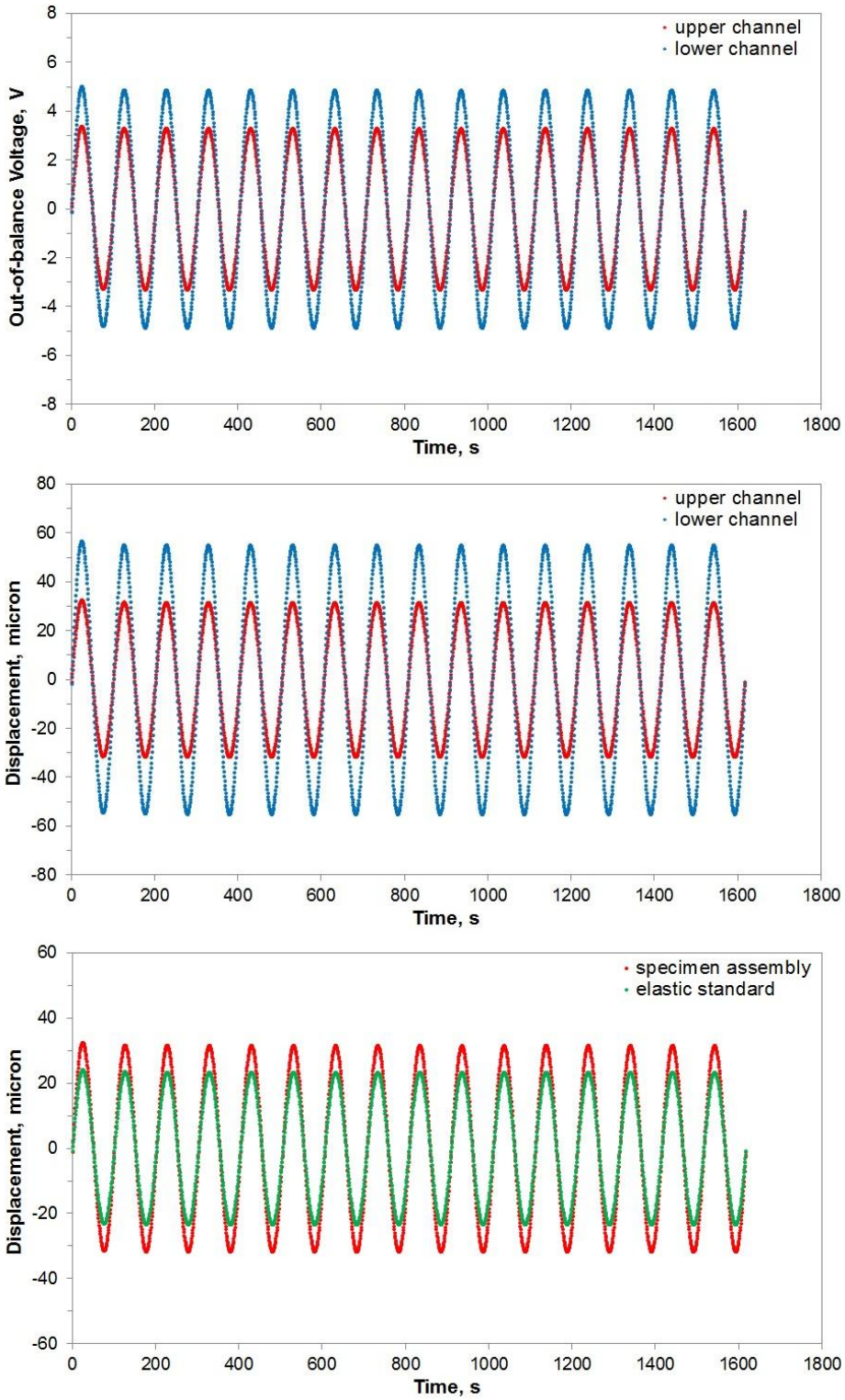


**Figure 3.18** An illustration of extracting (c) the flexural displacements of both the specimen assembly and elastic standard from (a) the raw out-of-balance voltages measured at the upper and lower stations, through (b) the conversion from voltage into displacement by applying calibration factors. These representative results are obtained from a cracked high-porosity glass-bead sample with a confining pressure of 97 MPa and water pore-fluid pressure of 16 MPa at 101.12 s oscillation period. 16 consecutive cycles are recorded by a *LabVIEW* program.

Similar to torsional forced oscillation, an interim quantity called normalised flexural 'modulus' $S_{NF}$ is defined as:

$$S_{NF} = \left|\frac{d_1}{d_{12}}\right|, \tag{3.55}$$

where $d_1$ is a measure of the flexure of the specimen assembly and $d_{12}$ is a measure of the flexure of the elastic standard. Compared with normalised torsional compliance, normalised flexural 'modulus' $S_{NF}$ depends in a more complicated way upon the geometry and material properties of the beam. This observed quantity is later simulated in a filament elongation model for the flexural mode distortion of the beam, described in the next section, to extract the Young's modulus $E$ of the unknown. The loss angle $\delta$ (rad) is the phase lag of $d_1$ relative to $d_{12}$, representing any strain energy dissipation associated with viscoelastic or anelastic behaviour of a specimen.

3.1.1.13 Extracting Young's modulus by iterative forward modelling

Young's modulus of the unknown cannot be directly determined from flexure-mode forced oscillation. In parallel with the experimental work, numerical modelling is needed to further extract the Young's modulus $E$ of the specimen from the observed $S_{NF}$. The response of a long, thin beam to a bending force is treated with the filament elongation model in which the shortening of filament is controlled by the Young's modulus but the influence of shear stresses acting between adjacent filaments is neglected. The appropriateness of this approximation was demonstrated in Jackson *et al.* (2011) by similar results from filament elongation and finite element modelling. The specimen is assigned different values of Young's modulus until the modelled normalised flexural 'modulus' $S_{NF,mod}$ is equal to the observed normalised flexural 'modulus' $S_{NF,obs}$. To achieve this, the flexural displacement of the beam axis of a given position along the beam, with a bending force (or moment) applied, needs to be determined first. This is given by the moment-curvature equation of Bernoulli – Euler beam theory:

$$E(x)I(x)\frac{\partial^2 v}{\partial x^2} = M(x), \tag{3.56}$$

where $E$ is the Young's modulus; $I$ is the diametral moment of inertia of the beam cross-section; $M$ is the local bending moment; and $v(x)$ is the deflection of the beam at a distance $x$ from the anchored end of the beam. The product $EI$ is called the flexural rigidity of the beam. The details of derivation of this equation are given in *Appendix B*.

The beam strongly propped was previously subject to a tight lateral constraint (Jackson *et al.*, 2011) at the lower end. Subsequently, however, the radial clearance has been

increased to 1.5 mm to allow substantial deflection from its axial position by a locally applied bending force rather than bending moment. The lower end of the beam still does not have complete freedom as it is connected to the enclosing pressure vessel by a thin spiral steel vent tube which provides access to the specimen for pore fluid from an external reservoir. Accordingly, the boundary condition $v = 0$ and the associated lateral reaction force $R_L$ are applied where the vent tube meets the lower closure plug of the pressure vessel at $x = L$ (Fig. 3.19).

In order to apply this equation to the compound beam that consists of both the specimen assembly and steel elastic standard in flexural forced oscillation on the Attenuation Apparatus, a free-body diagram (FBD) analysis is required.

With an applied bending force by the pair of electromagnetic drivers at $x=l_3$ and geometry of weakly propped lower end of the beam, depending on the location of $x_i$, the moment of interest $M(x_i)$ can be expressed as:

$$M_i = F(l_3 - x_i) + R_L(L - x_i)\ , \qquad \text{for } 0 \leq x_i < l_3 \tag{3.57}$$

$$M_i = R_L(L - x_i)\ , \qquad \text{for } l_3 \leq x_i \leq L \tag{3.58}$$

where $F$ is the bending force applied at $x = l_3$ by a pair of electromagnetic drivers, $M_i$ is the reactive moment of interest at position $x_i$, and $R_L$ is the lateral reactive force exerted by the lower vent tube connected to the lower end of the beam.

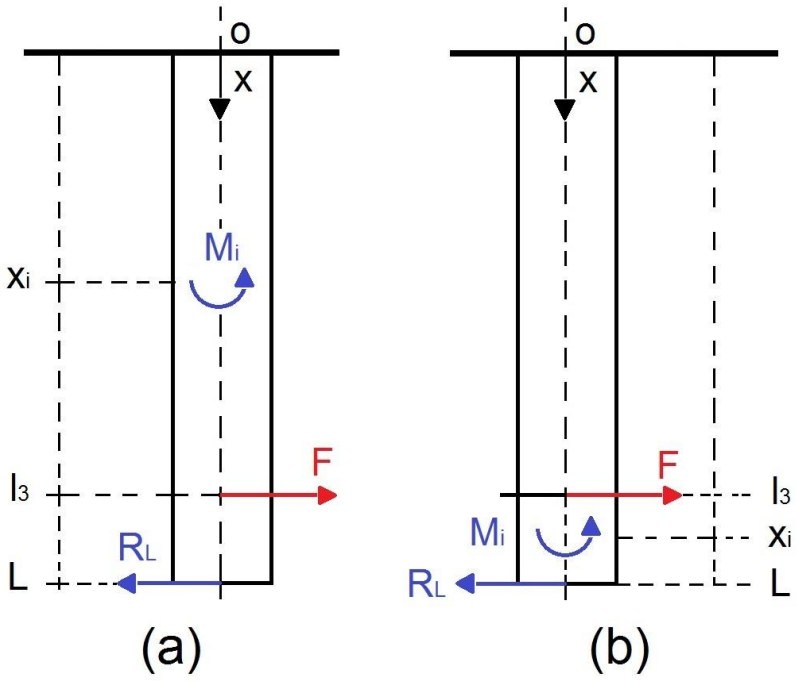


**Figure 3.19** Free-body diagram of the compound beam that consists of both the specimen assembly and stainless steel elastic standard in flexural forced oscillation on the Attenuation Apparatus. The analysis depends on the location of $x_i$, and divided into two cases: (a) $0 \leq x_i < l_3$; and (b) $l_3 \leq x_i \leq L$.

With a finite difference approximation, involving $N$ segments each of length $L/N$, Eq. (3.56), (3.57) and (3.58) are transformed into a system of $N$ linear equations with $N$ unknowns, which are solved for the deflection $v(x_i)$, $I$ = 1, … , *N-1* and the terminal reaction force $R_L$ (Jackson *et al.*, 2011; or *Appendix C*). Of particular interest for comparison with experimental observations are the deflections at $x = l_1$ and $x = l_2$ corresponding to the upper and lower transducer stations, respectively (Fig. 3.20). Then the modelled normalised flexural 'modulus' is expressed as:

$$S_{NF,\ mod} = \left| \frac{v(l_1)}{v(l_2) - v(l_1)} \right| . \tag{3.59}$$

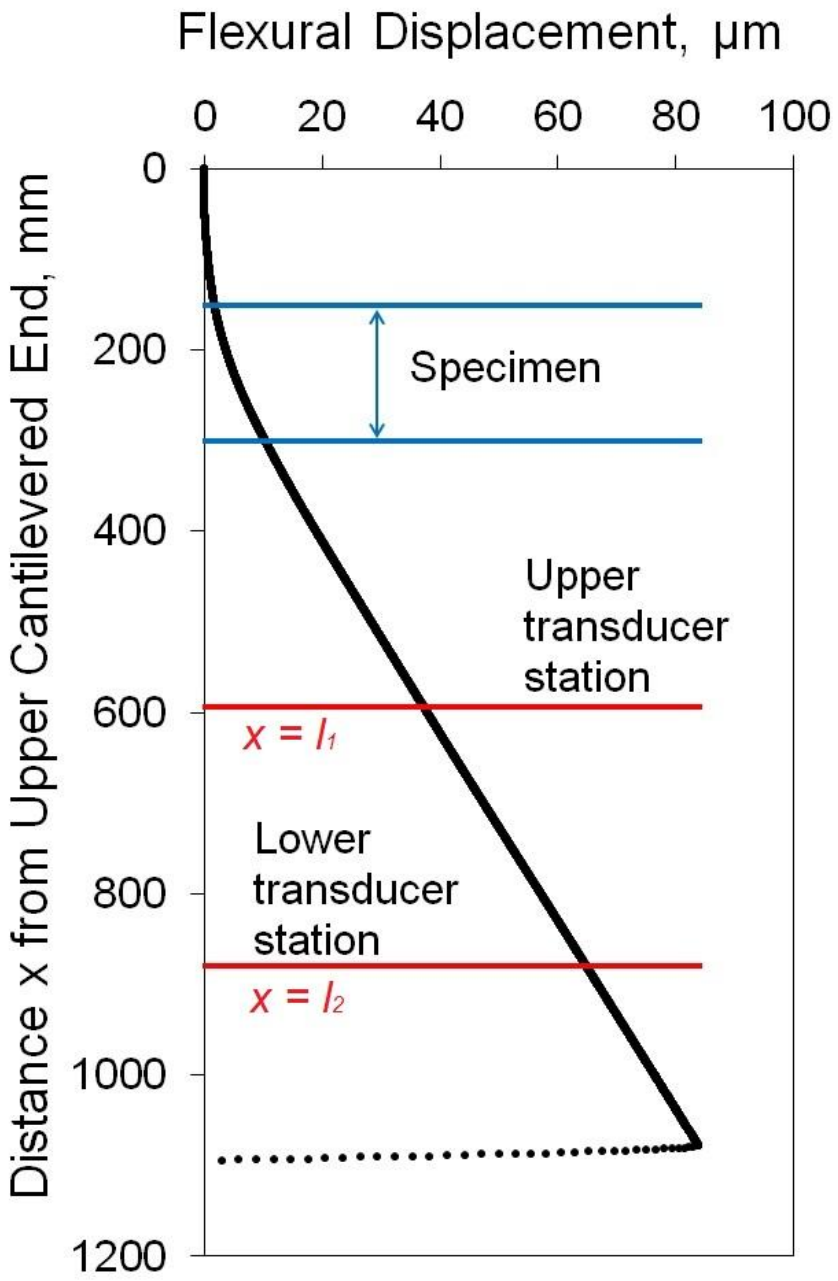


**Figure 3.20** Representative results of the modelled flexural displacement *v(x)* along the beam, which is cantilevered at the top end. The upper and lower stations are located at 592.82 mm and 878.62 mm from the origin (red), respectively. The material properties are those appropriate for a high-porosity glass-bead specimen at 11 MPa, with the outer diameter of the lower vent tube fixed at 1.10 mm and the Young's modulus of the specimen assigned as 72.69 GPa. The intervals occupied by the compliant specimen provide the greatest curvature (blue). The deflection returns to zero at the lower end of the beam due to a weak prop by a spiral vent tube.

The basic idea of the forward modelling is simple: allocating trial values for the Young's modulus of the specimen until the modelled normalised flexural 'modulus' $S_{NF,\ mod}$ matches the observed normalised flexural 'modulus' $S_{NF,\ obs}$ by forced oscillation experiments (Fig. 3.21).

There are two important preparatory steps involved with the modelling. First, the irregular geometry of the steel vent tube connected to the lower end of the elastic standard introduces uncertainties into the modelling. In order to constrain the parameter of the vent tube, *i.e.*, the effective outer diameter of a straight rather than spiral tube, a parallel experiment with a control specimen with known Young's modulus needs to be conducted (Fig. 3.21). In some cases, the dry Young's modulus determined at the highest pressure, *e.g.*, 100 MPa, on the specimen by ultrasonic wave propagation can also be used as a constraint. During the first step, the effective outer diameter of the lower vent tube is inferred from the normalised flexural modulus measured at the highest pressure, and the known Young's modulus of the control specimen, and its value then remains fixed throughout the following forward modelling.

It needs to be emphasised that the raw data of the normalised flexural 'modulus' obtained in forced oscillation comprise both the interfacial effect between components of the beam and the real effects caused by the cracks and pore fluids in specimen. To this end, the second preparatory step involves use of the pressure dependence of the normalised flexural modulus measured on the reference assembly to correct for interfacial compliance in the specimen assembly (Fig. 3.21). The resulting (adjusted) normalised flexural 'modulus' at pressure $P$ $S_{NF,adj}(P)$ can be expressed mathematically as:

$$S_{NF,adj}(P) = S_{NF,spec}(P) - [S_{NF,ref}(P) - S_{NF,ref}^{HP}] \,, \tag{3.60}$$

where $S_{NF,spec}(P)$ is the measured normalised flexural 'modulus' of the specimen assembly at pressure $P$; $S_{NF,ref}(P)$ is the measured normalised flexural 'modulus' of the reference assembly at pressure $P$; and $S_{NF,ref}^{HP}$ is the measured normalised flexural 'modulus' of the reference assembly at the highest pressure and deemed to be free of interfacial issue (around 100 MPa in this study).

With the inferred effective outer diameter of the lower vent tube and trial value of Young's modulus of the specimen as inputs, the normalised flexural 'modulus' yielded by the filament-elongation model $S_{NF,mod}(P)$ is compared with $S_{NF,adj}(P)$ at pressure $P$ (Fig. 3.21). This process is conducted iteratively until a good match between $S_{NF,mod}(P)$ and $S_{NF,adj}(P)$ is achieved, indicating the real Young's modulus of the specimen is well approximated by the Young's modulus assigned in the model.

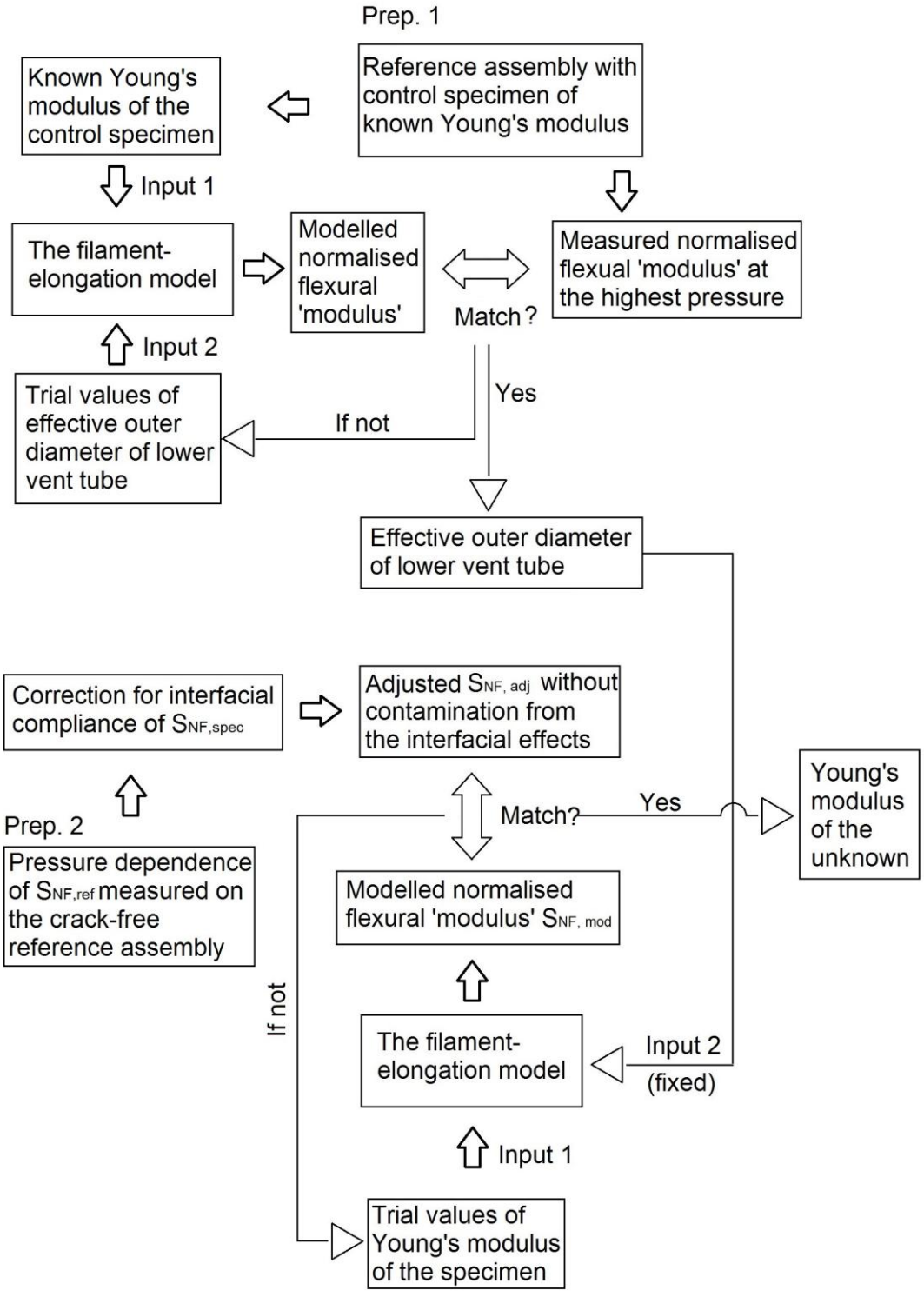


**Figure 3.21** Workflow of the flexure-mode modelling to extract the Young's modulus of the specimen.

3.1.1.14 Pore-fluid pressure system

The argon confining pressure and pore fluid pressure systems are independently controlled on the attenuation apparatus. In general, the pore-fluid pressure system consists of both pore-

fluid reservoirs and a pore-fluid channel between them formed by hollow (steel and/or alumina) rods and cracked specimens (Fig. 3.22).

The unknown specimen is sandwiched between two connecting rods, all of which are encapsulated in an annealed copper jacket with a wall thickness of ~0.25 mm. The copper jacket and rubber O-rings sealing at either end of the jacketed assembly work together to exclude the argon confining medium from the pore-fluid pressure system.

Argon, besides its role as confining medium, is also used as pore fluid as it is chemically inert, therefore, effects such as adsorption of molecules and polar fluids can be ignored (Lu and Jackson, 2006). Water, as a more viscous and polar pore fluid, is also used on the attenuation apparatus. Rust inhibitor is added into water pore fluid to prevent potential corrosion of the steel part of the attenuation apparatus. The rust inhibitor, containing 0-50% water, 10-30% petroleum oil, 10-30% unknown proprietary additives, 0-10% amine and amine esters, 0-1% methyl benzotriazole, and 0-0.2% iodo-butyl-carbamate, was mixed with deionised water (volume ratio 1:20) and used for the low-porosity glass-bead specimen. Alternative water-soluble rust inhibitor, 0.02 wt.% sodium dichromate ($Na_2Cr_2O_7$) and 0.003 wt.% sodium hydroxide (NaOH) mixed with distilled water, was used for the high-porosity glass-bead specimen and glass-rod specimen.

For experiments with pore fluids, the confining pressure is always maintained at least 10 MPa higher than pore-fluid pressure, because bloating of the copper jacket will occur if the pore-fluid pressure even transiently exceeds the confining pressure. The control of pore-fluid pressure becomes even more difficult with water as pore fluid, due to its much greater incompressibility compared with that of argon. Each stroke of the water intensifier gives ~ 20 MPa increase in water pore-fluid pressure. In practice, when a relatively low differential pressure is desired, the safest approach to achieve this is to first increase the confining pressure much higher than the target water pressure by at least 30 MPa to create a buffer for adjusting the water pressure. Once the target water pressure is achieved, the confining pressure is then carefully reduced to give the desired differential pressure.

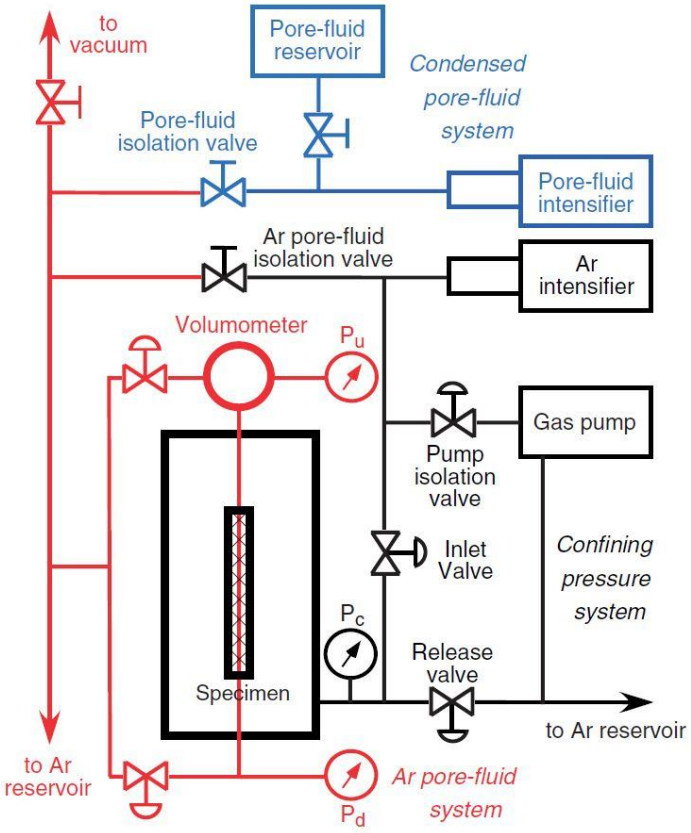


**Figure 3.22** Arrangements for independently controlled argon confining pressure and pore-fluid pressure systems (after Jackson *et al.*, 2011).

The upstream reservoir consists of a volumometer, the steel piston of which is driven by a DC motor forward and backward to allow the measurement of the storage capacity and hence volume of the upstream reservoir through the covariation of the fluid pressure and the position of the piston (Zhang *et al.*, 1994). The upstream reservoir also has an air-operated isolation valve and a steel connecting pipe between the volumometer and the copper-jacketed compound specimen assembly.

The downstream reservoir consists of the space within the hollow lower connecting rod, the elastic standard, the driver and transducer lever arms, lower vent tube and an air-operated isolation valve. A filter is installed at the interface between the elastic standard and the lower vent tube to prevent any possible blockage by the solid contaminants within the pore fluid system.

Both upstream and downstream reservoirs are monitored by high-pressure transducers (Precise Sensors, model 114) with a resolution of 0.1 mV/10 V (equivalent to 0.05/500 MPa) (Lu, 1996). The pressure transducers have been calibrated against a Heise pressure gauge.

The position of the steel piston within the volumometer is measured by a DC-LVDT (Linear Variable Differential Transformer, model 500 HR-DC, Schaevitz Engineering).

From a bench test, the calibration factor for this DC-LVDT is determined as 2.99±0.01 mm/V (Lu, 1996).

The details of the piston traversing and pore-pressure equilibration experiments will be given in *Section 3.5.1* and *3.5.2*.

### 3.1.2 Upgrade of data acquisition system

It has been mentioned elsewhere that the data acquisition system of the Attenuation Apparatus underwent a major upgrade during this project. The upgrade and post-upgrade tests lasted for ~ 10 months from early July of 2012 to late April of 2013 before reliable performance was re-established. The author was heavily involved in the post-upgrade tests. The data reported in this thesis were all collected after the upgrade, allowing close comparison of the results. The upgraded data acquisition system has several prominent new features, and the following summary was developed in collaboration with Mr. Andrew Latimore and Prof. Ian Jackson:

(1) A *LabVIEW* (Version 11.0) system for computer control and data acquisition performed in *Windows* environment has been developed to replace the previous *DOS*-based program, making the process of data acquisition more user-friendly.

(2) The new *LabVIEW* system employs an 18-bit DAQ card (High-accuracy M series Multifunction NI 6281, National Instruments®) to replace the previous 12-bit analog-to-digital converter, in order to minimize the quantisation error and hence improve the signal-to-noise ratio.

(3) The signal responsible for driving the forced oscillation of the experimental assembly is digitally synthesised in the *LabVIEW* system from a look-up table, subjected to digital/analog conversion, low-pass filtering, and power amplification, before being applied to the electromagnetic driver units.

(4) In terms of the excitation of the AC bridge (Fig. 3.6 & 3.17), a square wave of precisely 10 kHz frequency is synthesised in the *LabVIEW* system, low-pass filtered to retrieve the fundamental 10 kHz sinusoidal signal, digital/analog converted, and amplified to provide optional 3 V/30 V excitation. The bridge out-of-balance signal at 10 kHz is filtered and pre-amplified before being synchronously sampled at 20 kHz for the amplitudes of peaks and troughs of the signal.

(5) To implement improved low-pass filtering of the displacement-time series, the cut-off frequency is adaptively varied with imposed oscillation frequency.

(6) The higher signal-to-noise ratio makes it possible, after upgrade, to replace multiple calibrations of short duration (~3 minutes) in the former experiment protocol with a

single one of longer duration (10 minutes) conducted both before and after a series of forced oscillation tests.

(7) The switch between the torsional and flexural forced oscillations was previously achieved by reversing the leads of transducers manually. In the upgraded system, appropriate electrical lead connection within the transducers is achieved by activating relays within *LabVIEW*. In addition, the direction of current flow through one of the electromagnetic driver coils is reversed by remote switching to replace an oscillating torque by an oscillating bending force, and vice versa.

(8) The format of raw data recorded by the *LabVIEW* program is different from that generated by the previous *DOS* program. A new *FORTRAN* program was developed to re-format the raw data and include key information concerning environmental conditions and data acquisition in the way that is readable by the processing programs.

(9) Signals transmitted from the panel meters associated with the Manganin resistance gauge for measuring confining pressure and the thermocouple for measuring temperature, and from the LVDT responsible for measuring the displacement of the volumometer piston, require analog-to-digital conversion by the DAQ card. The meters associated with measurement of pore pressure provide digitised signals for acquisition within *LabVIEW*.

## 3.2 Resonant Bar

### 3.2.1 Principle of conventional resonant bar tests

A typical, conventional resonant bar test involves vibrating a slender specimen at its resonant frequencies by either forced oscillation or free oscillation. A mechanical system can be subjected to forced oscillation at any frequency. However, such oscillation will be largest in amplitude at particular resonance frequency. Free oscillation refers to the persistence of such oscillation at the resonance frequency following removal of the exciting force. In this study, a rock specimen is subjected to forced oscillation over a range of imposed frequencies, resonances being identified by maxima in the response. The velocities of extensional and shear waves travelling in the specimen are determined from the measured length of the specimen $L$ and resonance frequencies $nf$ (where $f$ is the fundamental mode resonance frequency and integer $n$ is the resonance order). This can be expressed as:

$$V = \frac{2Lf}{n}. \tag{3.61}$$

The resonance order $n$ = 1 indicates the fundamental mode of resonance frequency, and the equation above is reduced to:

$$V = 2Lf\ . \tag{3.62}$$

The extensional velocity $V_E$ and shear velocity $V_S$ are further linked to Young's modulus and shear modulus as:

$$V_E = \sqrt{\frac{E}{\rho}}, \tag{3.63}$$

and

$$V_S = \sqrt{\frac{G}{\rho}}, \tag{3.64}$$

where $\rho$ is the density of the sample. The amplitude spectrum of resonance peak provides attenuation. A sharp resonance peak indicates nearly elastic behaviour with low energy dissipation, and a broad resonance peak corresponds to higher attenuation.

### 3.2.2 Specimen-bar assembly for Split Hopkinson Resonant Bar

The conventional resonant bar involves the measurement of velocities on a specimen of about 1 m in length at a few kHz. But the requirement for such specimen length is usually difficult to satisfy as most available specimens obtained from the field are of lengths less

than 10 cm. From Eq. (3.61) and (3.62), the resonance frequency, for a given velocity, is increased to a few hundred kHz for a specimen with a length of ~10 cm.

In order to i) measure specimens of more readily available length (< 10 cm), and ii) keep resonance frequencies as low as possible within the range of hundreds of Hz to a few kHz, extension bars are needed to create additional length for the resonance system. To differentiate from the conventional resonant bar, this technique is called "split Hopkinson resonant bar (SHRB)" (Xia, 2009; Chen *et al.*, 2009; Nakagawa, 2011; Nakagawa *et al.*, 2013).

In the current setup, cylindrical specimen of 38.1 mm in diameter and a few centimeters in length is sandwiched between a pair of stainless steel bars of the same diameter but each 406.4 mm in length, forming a specimen-bar assembly for SHRB tests. The details of the assembly preparation will be described below.

A cylindrical specimen, after being appropriately lapped on both end surfaces and oven dried, is jacketed with a thin (150 – 500 μm in thickness), PVC heat-shrink tube. The jacket is properly heat-treated to ensure an intimate contact with the specimen without observable trapped air bubbles. The PVC jacket needs to be trimmed, leaving about 13 mm as the extra length at each side of the specimen in order to couple with the steel extension bars.

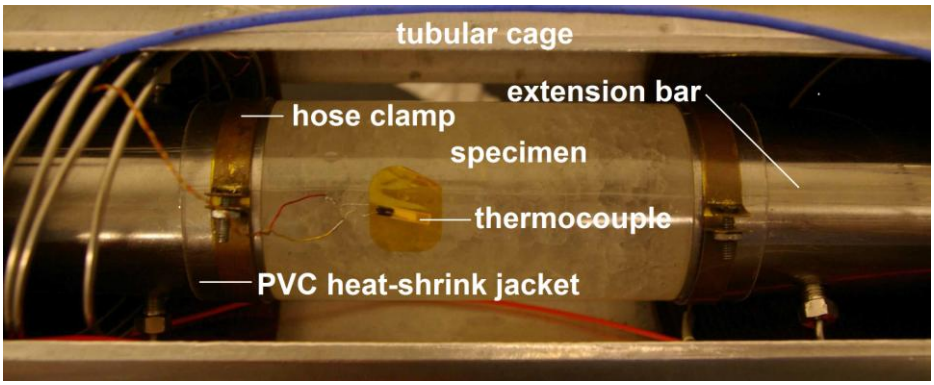


**Figure 3.23** Specimen-bar assembly for Split Hopkinson Resonant Bar (SHRB) tests. A cracked glass-rod specimen (FDL-2) is jacketed with a PVC heat-shrink tube, and sandwiched between a pair of stainless steel extension bars.

Thin lead foils (~50 μm in thickness) are placed at the interfaces between the specimen and extension bars in order to achieve a better mechanical coupling at interfaces between the specimen and extension bars. Any interfacial gap behaves as a compliant crack in a fractured medium and provides a continuous pressure-dependent increase in inferred modulus with increasing pressure. This interfacial artefact may be more significant for hard and consolidated samples. The circular lead foils are cut with intervening cross-shaped cut-out to channel the flow of pore fluid. Each remaining sector of the foil is temporarily attached to

the end surface of extension bars with tiny amount of isopropanol before the specimen and extension bars are held together by the jacket. Excessive amount of isopropanol may introduce extraneous attenuation.

A Viton® O-ring is located in the groove at the near end of each extension bar, coupled with the PVC heat-shrink tube and clamped by a hose clamp. The positions of O-rings are close to the specimen-bar interfaces, and excessive O-ring grease could be squeezed and flow consequently into interfaces and introduce artificial attenuation.

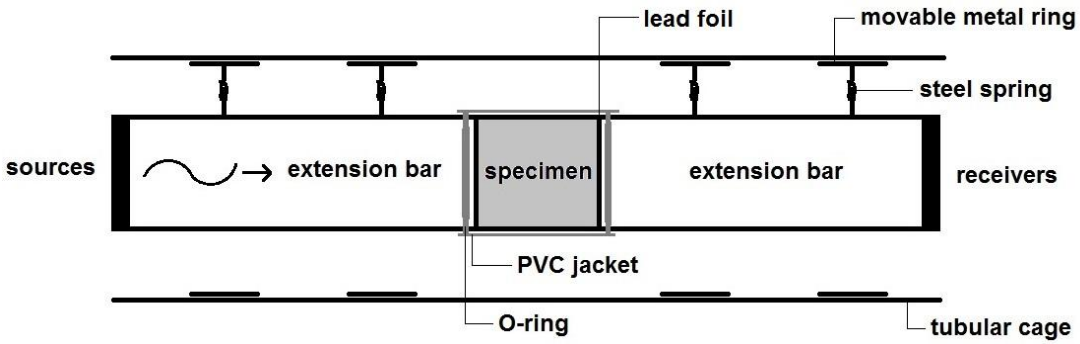


**Figure 3.24** An illustration of the arrangement of the specimen-bar assembly for the Split Hopkinson Resonant Bar (SHRB) tests. The assembly is enclosed within a pressure vessel to provide confining and pore-fluid pressures.

In the case of SHRB technique, the specimen-bar assembly is suspended by four steel springs each with one end mounted on a movable metal ring, located within an aluminium tubular cage.

Extension/compression- and torsion-mode sources and receivers are mounted on the far ends of the extension bars. The source unit consists of mode-specific piezoelectric ceramics (Channel Industries C5500). The receiver unit consists of an axial accelerometer and a pair of torsional accelerometers to measure longitudinal and shear motions, respectively (Endevco 27AM1-100, 258A-100).

### 3.2.3 Confining and pore-fluid pressure systems

The specimen-bar assembly, suspended by steel springs within a tubular cage, is prepared on the bench. Then the assembly is loaded into a pressure vessel with independently controlled confining and pore-fluid pressure systems.

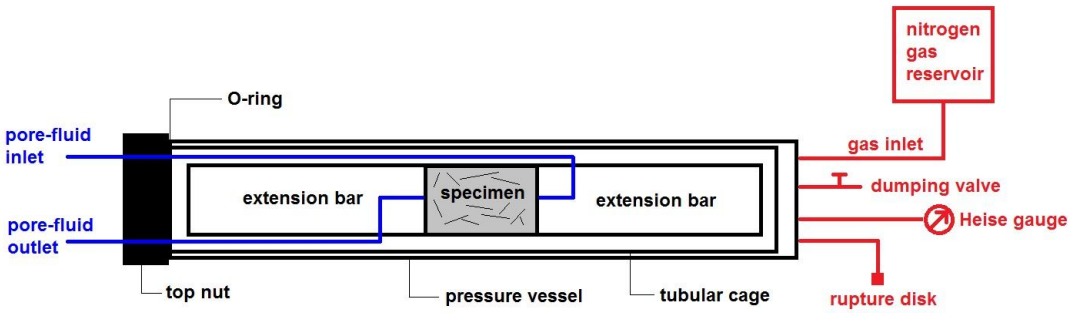


**Figure 3.25** Arrangements of the confining (red) and the pore-fluid (blue) pressure systems on the Split Hopkinson Resonant Bar (SHRB).

Nitrogen is used as the confining medium. In the absence of a pump on the apparatus, the maximum confining pressure in the pressure vessel is determined by the maximum bottle pressure. The highest confining pressure reached in this set of measurements was ~ 30 MPa. All confining pressure lines are arranged at the far end of the pressure vessel (far from the top nut) with rupture disks installed for safety purpose.

Two types of pore fluid (Nitrogen and tap water) are used in this study. Nitrogen pore fluid is introduced from the gas reservoir directly until reaching the target pore-fluid pressure. A servo-controlled fluid pump with adjustable injection rate is used for water pore fluid. Both pore-fluid inlet and outlet lines are fed through the top nut of the pressure vessel and reach, through the extension bars, both ends of the specimen, allowing the circulation of pore fluid through the specimen.

### 3.2.4 Measurements of resonance frequency and attenuation

Regarding the measurement of resonance frequency, input signals (either chirp or random signals with desired range of frequencies) are generated by an FFT analyser (ONO SOKKI CF-6400), and after amplification, excite the piezoelectric ceramics, allowing the forced vibration of the specimen-bar assembly. The signal detected by the accelerometers mounted on the other end of the specimen-bar assembly, after proper conditioning and amplification, is received by the same FFT analyser. The central frequency and width of the resonance peak provide the resonance frequency and attenuation, respectively.

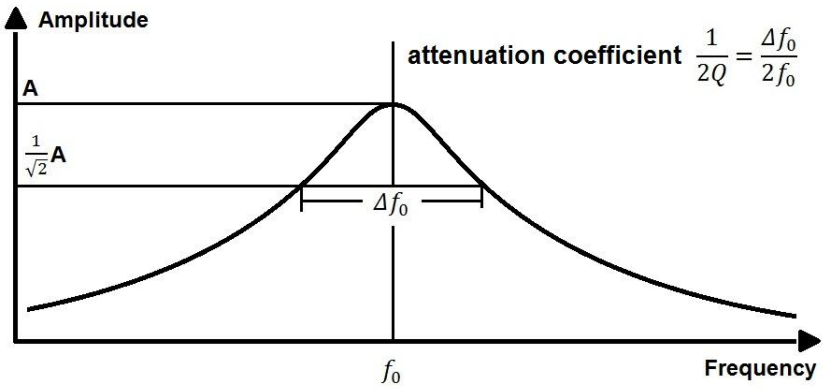


**Figure 3.26** Extracting the resonance frequency $f_0$ and attenuation *1/2Q* from a fundamental mode resonance peak.

If the full power associated with the resonance peak is $S_{max}$, the attenuation is determined by the half-power method, *i.e.*, the width of power spectrum at $\frac{S_{max}}{2}$ with respect to the total range of resonance-peak frequency $2f_0$. As $S \propto A^2$, half the maximum power $\frac{S_{max}}{2}$ corresponds to $\frac{1}{\sqrt{2}}$ times the maximum signal amplitude *A*. Notice that the quality factory *Q* is equal to $f_0/\Delta f_0$. The attenuation is then given as:

$$attenuation\ coefficient\ \frac{1}{2Q} = \frac{\Delta f_0}{2f_0}. \tag{3.65}$$

where $\Delta f_0$ is the width of the resonance peak at $\frac{A}{\sqrt{2}}$ in hertz, and $f_0$ is the fundamental mode resonance frequency.

### 3.2.5 Numerical modelling and inversion

The use of extension bars makes it possible to perform resonance measurements on samples with considerably shorter length (< 10 cm), compared with the conventional resonance bar technique, but at the cost of more complexity in determining velocities from the measured resonance frequencies. In the case of wavelength that is short compared to the diameter of the bar, the Poisson's effect cannot be neglected and a three-dimension wave propagation model is needed. However, the wavelength in SHRB tests is much longer than the bar diameter, so that the radial effect becomes negligible and a one-dimension wave propagation model is valid.

In the one-dimension model, an excitation is introduced to the system by either a point, directional force source in extensional mode or a point torque in torsional mode. The source and the receiver are modelled as point mass in extension and angular mass in torsion. Alongside the assumption of continuity of displacement and stress in different segments of

the bar, the displacement at the receiver can be determined as a function of frequency. Starting from an assumed complex elastic modulus of the specimen, the resonance frequency and attenuation of the entire system is computed by the 1-D wave propagation model. The modulus is updated iteratively until a good match between the computed quantities and the observation.

The numerically inverted complex shear and Young's moduli, however, are still different from the real values by the 3-D effects induced by the PVC heat-shrink jacket and interfaces between the specimen and extension bars. The jacket and interfacial effects need to be corrected correspondingly before the real shear and Young's moduli of the specimen are obtained. The details of the corrections are described in Nakagawa (2011).

## 3.3 Ultrasonic Wave-speed Measurement

Ultrasonic wave-speed measurement is the most mature one of the three techniques used in this study for determining the mechanical/acoustic properties of a specimen. Depending on the arrangement of the receiver, ultrasonic wave-speed measurements can be broadly categorised into 1) pulse transmission methods; or 2) pulse-echo methods. For the first case, the ultrasonic pulse emitted by a piezoelectric crystal is allowed to propagate through a specimen and is later received by another piezoelectric crystal on the other end of the specimen. In contrast, for the pulse-echo method, a single transducer is used as both source and receiver, *i.e.*, the ultrasonic pulse generated by a piezoelectric crystal travels through a specimen and, after being reflected at the sample-air interface, returns to be received by the same piezoelectric crystal. The frequency of the pulse used in ultrasonic wave-speed measurement is in the range of hundreds of kilohertz to a few megahertz, much higher than those frequencies used in the stress-strain and resonance methods.

### 3.3.1 Pulse Transmission Method

3.3.1.1 Principle

In this method, it is required that a specimen be placed between a pair of piezoelectric ceramic transducers. The transmitting transducer is first excited by application of a rapid rise-time voltage step to generate an elastic wave that propagates through the specimen to be received by the second receiving piezoelectric transducer mounted on the opposite side of the specimen. The differential time between the emission and reception of the pulse is equal to the travel time of the elastic wave through the specimen. As a result, the velocity of the wave propagating through the specimen can be determined as the ratio between the sample length and the wave travel time. Note that the velocity determined is not strictly speaking the

phase velocity, but approaches it to a very good approximation (Bourbié *et al.*, 1987; Molyneux & Schmitt, 2000).

#### 3.3.1.2 Piezoelectric transducer

The dual-mode transducer consists of an aluminium buffer cap and P- and S-wave piezoelectric ceramics. These components are electrically connected and properly sealed. Details of the arrangement are given below.

The end surface of a cylindrical aluminium buffer cap needs to be carefully lapped to achieve flatness before test. An uneven end surface of a buffer cap could cause bad coupling with hard, consolidated specimens, such as sintered glass-bead and glass-rod samples.

Piezoelectric ceramics, converting between electrical potential and strain, are used as transducers. P-wave is generated if the piezoelectric ceramic is longitudinally polarised. S-wave is generated if the piezoelectric ceramic is laterally polarised. As the piezoelectric effect is reversible, the pulser and the receiver are interchangeable.

P-wave, S-wave piezoelectric ceramics and aluminium buffer caps are assembled in a stacked configuration such that S-wave ceramic is directly attached to the upper surface of the buffer cap and the P-wave ceramic is then attached to the top surface of the S-wave ceramic (Fig. 3.27). These components are glued together by conductive silver epoxy. Before stacking the P-wave and S-wave ceramics together, a thin copper foil is placed between them and glued by the conductive silver epoxy as a common electrode. A second piece of copper foil is attached to the top surface of the P-wave ceramic by the silver epoxy to serve as another electrode. The electrical circuitry for piezoelectric ceramic transducers is illustrated in Fig. 3.27. In the case of a buffer cap with a pore-fluid tube, the stainless steel tube is mechanically connected to the grounded steel pressure vessel and there is no need to introduce a separate ground lead to the buffer cap.

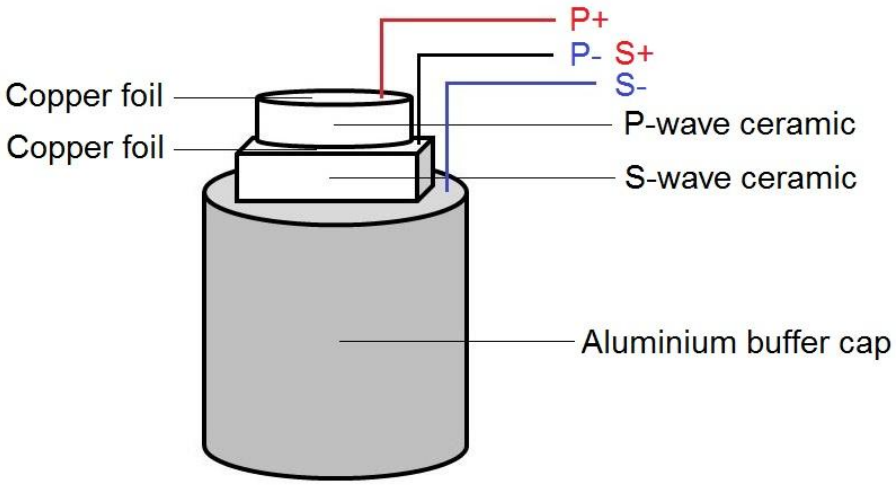


**Figure 3.27** Arrangement of P- and S-wave piezoelectric ceramics and the aluminium buffer cap. Either P- or S-wave ceramic is selectively excited to generate corresponding elastic waves. Similarly, either P- or S-wave ceramic can also be selectively connected to receive corresponding elastic waves on the other end of a specimen.

Electrical leads for P- and S-wave transducers are soldered onto the copper electrodes. Flexane® liquid 80 is used to coat the ceramic components for isolation from the hydraulic oil in the pressure vessel. Flexane needs seven days to cure to its full strength and 5-minute epoxy needs to be placed on the outer surface of the cured Flexane® to improve sealing.

#### 3.3.1.3 Calibration assembly

The measured travel time is the total travel time through both the specimen and the pair of buffer caps for a pulse. In order to extract the actual travel time of the pulse in the specimen, calibration is needed to determine the traveltime for the pair of buffer caps (Fig. 3.28).

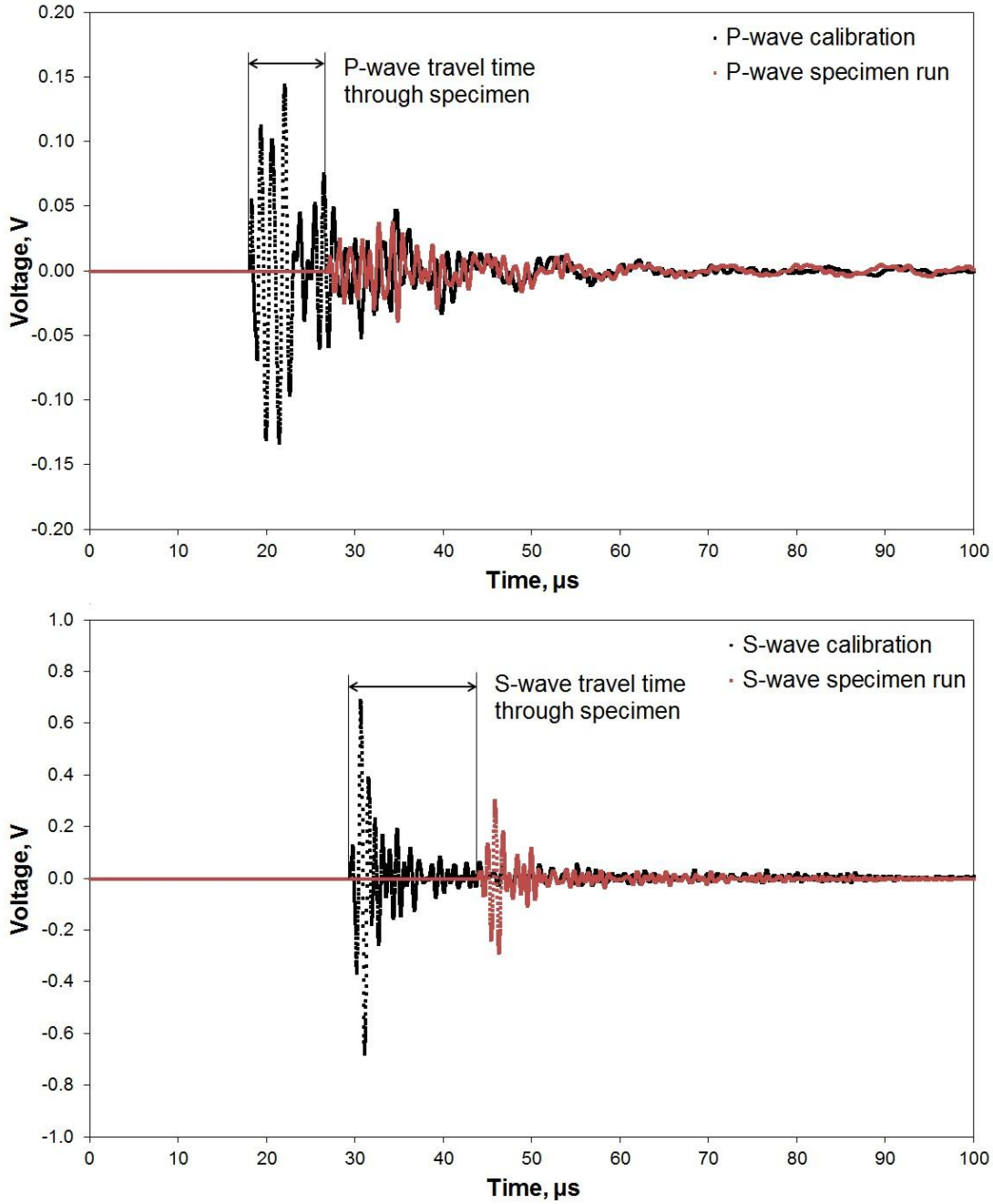


**Figure 3.28** Travel time of either P- or S-wave through the specimen is extracted by comparing the travel times measured in a calibration (black) and a specimen run (red). The pulse was sent at the moment $t$ =0. The example is taken from an uncracked high-porosity glass-bead specimen (YF-4) at a confining pressure of 100 MPa. To provide a clearer illustration, noise prior to the first arrival of each record has been removed.

In a calibration run, no specimen is involved in the experiment assembly. The pulser and receiver are aligned in both axial and azimuthal directions (Fig. 3.29). A pair of nitrile O-rings is placed in the grooves on the contacting end of the aluminium buffer cap, together with a PVC jacket, to seal against the hydraulic oil within the pressure vessel. The Nalgene® PVC jacket is of ~ 50 mm in length, 15 mm in inner diameter and ~ 20 mm in outer diameter.

Before sliding onto the buffer caps, the PVC jacket needs to be gently pre-heated with a heat gun in order to i) straighten the initially curved jacket; and ii) slightly increase the inner diameter of the jacket to allow a frictionless sliding. Small amount of grease on O-rings is also helpful for a smooth jacketing.

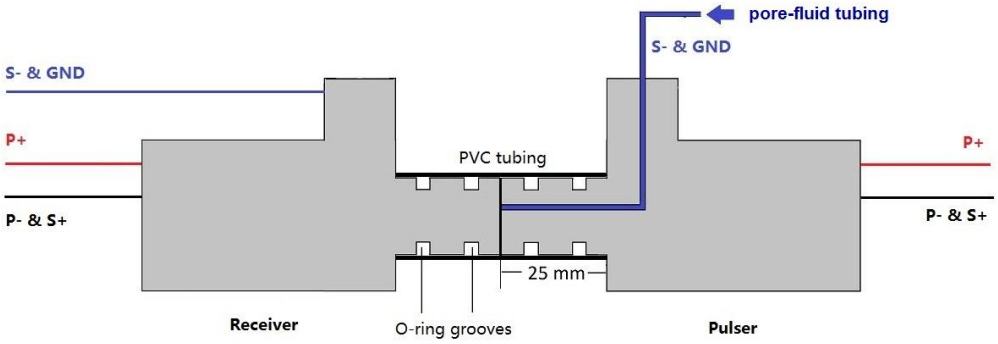


**Figure 3.29** Arrangement of a calibration assembly, consisting of a pair of buffer caps with intimate contact between them and sealed by a PVC jacket and two pairs of nitrile O-rings.

Four metal hose clamps need to be positioned around the PVC jacket and right above O-rings. A thin iron foil is normally placed between the jacket and hose clamps to i) allow even tightening over the O-rings by hose clamps; ii) prevent potential damage to the PVC jacket during clamping.

Before fully tightening the hose clamp, one needs to check: i) for close contact between two end caps at ambient conditions. An intimate physical contact between two end caps, allowing wave transmission, is normally established at ~ 5 MPa for calibration runs and ~ 10 MPa for sample runs. ii) for alignment of the shear-mode transducer polarisation. In practice, the pore-fluid inlet port on one of the pair of transducers is selected as the reference and the pore-fluid inlet port on the other transducer needs to be aligned with it. Once the two transducers are well positioned in both longitudinal and azimuthal directions, metal hose clamps are fully tightened.

### 3.3.1.4 Specimen assembly

A specimen assembly differs from a calibration assembly in that a specimen is sandwiched between the pulser and receiver. Before assembling, the specimen is dried in a vacuum oven at 70 ℃ for more than 24 hours before being moved to a desiccator jar to cool to room temperature.

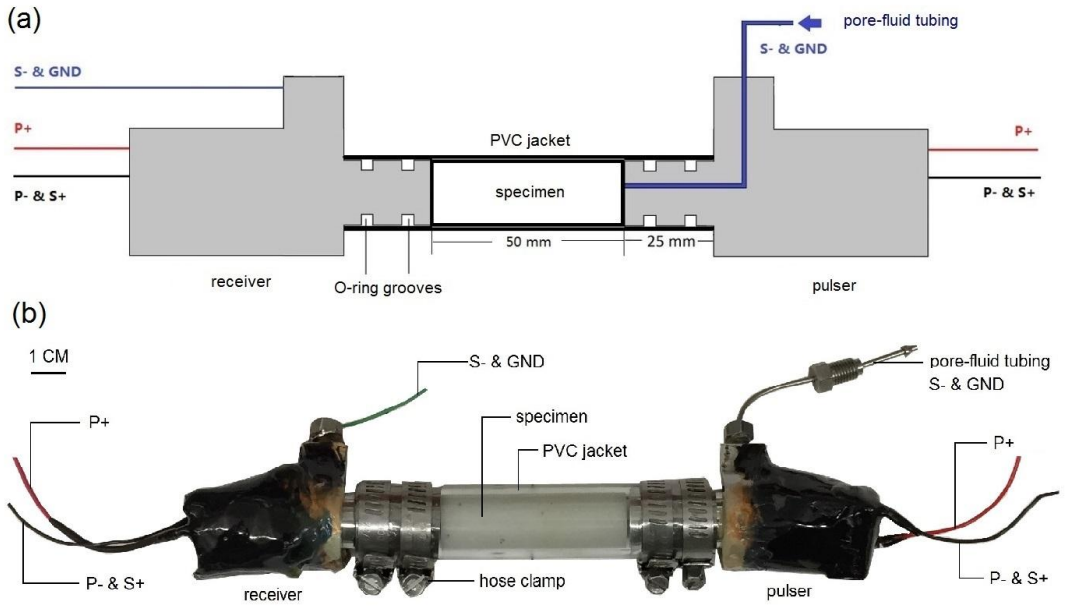


**Figure 3.30** (a) A sketch and (b) a photographic illustration of the arrangement of a specimen assembly, consisting of a specimen sandwiched between a pulser and a receiver. The specimen and the end caps of the pulser and the receiver are sealed by a PVC jacket of 100 mm in length.

The specimen, after drying and cooling, is loaded into a PVC jacket of 100 mm in length and sandwiched between two buffer caps (Fig. 3.30). Once the specimen assembly is prepared on the bench, the whole assembly is suspended below the top nut of the pressure vessel by the stainless steel pore-fluid tube. The connection between the pore-fluid tube and the top nut of the pressure vessel 1) allows the assembly to be relatively stable within the pressure vessel during pressurisation; 2) provides a passage for pore fluid; and 3) serves as the ground lead of the pulser.

Electrical leads between the specimen assembly and feedthroughs on the top nut are connected and checked for their electrical continuity before closing the top nut of the pressure vessel. A nitrile O-ring seals between the top nut and pressure vessel itself.

### 3.3.1.5 Confining and pore-fluid pressure systems

In contrast to the gas confining medium used in the forced oscillation and resonant bar techniques, hydraulic oil is used as the confining medium for the ultrasonic wave-speed measurements. Hydraulic oil due to its much lower compressibility allows for faster pressurisation and depressurisation. Compared with gas confining medium, however, oil requires a much longer period of time to achieve thermal equilibrium after each adjustment of pressure. This is caused by 1) more significant adiabatic heating and cooling effects due to faster change of pressure; and 2) much higher viscosity of oil, that retards thermal

equilibration by effective convection. On the other hand, it is much easier to seal a specimen against the more viscous oil as confining medium as compared with gas. There are also substantial reductions in safety hazards as a breach of tubing or connectors by the pressurised oil is easily contained whereas release of high-pressure gas can be explosive.

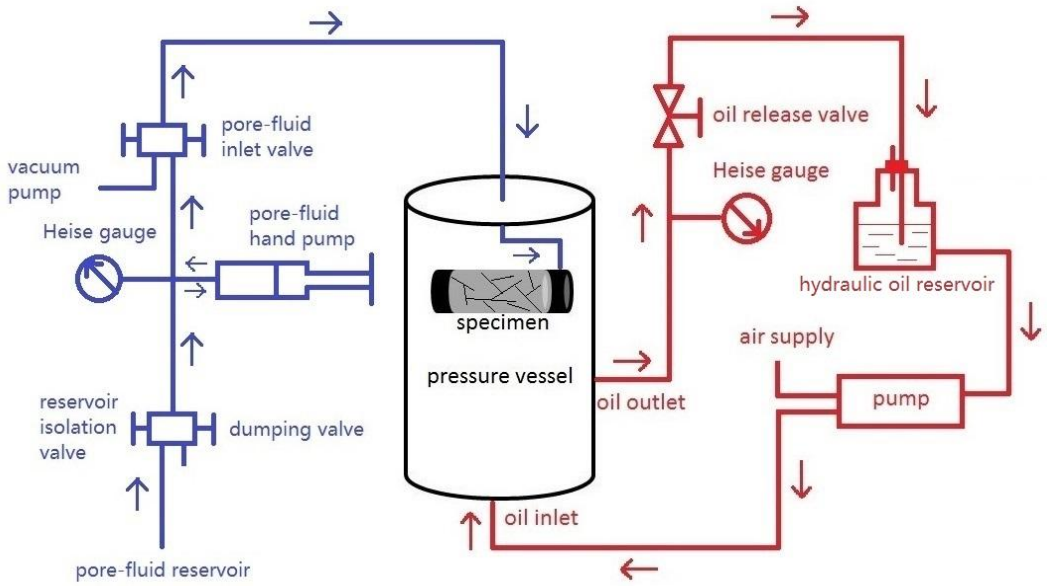


**Figure 3.31** The arrangements of the confining and pore-fluid pressure systems. The confining pressure (red) is provided by hydraulic oil and raised up by a pneumatic liquid pump to a maximum pressure of 100 MPa. The pore-fluid pressure system (blue) involves either argon or water as pore fluid, and a hand pump is used to raise the pore-fluid pressure. Both confining and pore-fluid pressures are independently monitored by separate Heise gauges.

A pneumatic liquid pump is used to raise the confining pressure to 100 MPa. The confining pressure within the pressure vessel is monitored in-situ by a Heise gauge with a resolution of 0.5 MPa. During depressurisation, the release valve needs to be gently opened to allow the pressurised oil to flow slowly back to the reservoir.

The pore-fluid system is independently controlled and monitored. The pore-fluid system is thoroughly vacuumed before introducing pore fluid from the reservoir. The pressurisation of pore fluid is realised by a manual pressure generator (HiP®, model 37-6-30) with 11 ml capacity per stroke. By revolving the handles of the pressure generator, the piston within the pore-fluid chamber is slowly advanced to raise the pore-fluid pressure. After the initial charge with argon at the bottle pressure $P_0$, the reservoir isolation valve needs to be closed before operating the pressure generator. The first full stroke of the pressure generator raises the pore-fluid pressure from bottle pressure $P_0$ to a higher pressure $P_1$, at which the pore-fluid inlet valve is closed. To raise the pore-fluid pressure higher than $P_1$, the pressure generator needs to be re-stroked, admitting more argon gas from the reservoir. Following re-stroking, with the reservoir isolation valve closed again, advance the piston of the pressure

generator and open the pore-fluid inlet valve once $P_1$ is reached during pressurisation. With the newly supplied argon gas, the remaining travel of the piston within the chamber of the pressure generator is expected to increase the argon pore-fluid pressure to a pressure level higher than $P_1$. In theory, repetition of this procedure can increase the argon pore-fluid pressure to any pressure level. The high compressibility of gas, however, makes it difficult to achieve pressures higher than 20 MPa and thus the highest pore pressure in the experiments is 20 MPa for argon pore fluid. The pressurised pore fluid is delivered to one end of the cracked specimen through the stainless steel tube which is mechanically connected to the end cap of the specimen assembly.

In contrast to argon, the charge and pressurisation of water as used as a pore fluid is slightly different in two aspects. First, argon is initially stored in a steel bottle with bottle pressure of ~ 12 MPa, and the pore-fluid system can be automatically charged by the pressure gradient between the bottle and the vacuumed pore-fluid system. But in the case of water pore fluid, the pore-fluid system needs to be vacuumed for several hours before being charged with water by atmospheric pressure. For the current arrangement, a full saturation of the pore-fluid system requires ~ 50 ml water. Second, the much lower compressibility of water allows its pressure to be easily raised to 50 MPa with a single stroke of the pressure generator and no continuous supply of pore fluid is needed.

#### 3.3.1.6 Data acquisition system

The computer-controlled measuring system consists of a *LabView* program, an 8-bit A/D converter, an ultrasonic wave generator including amplifiers and filters, a switch box remotely controlled by the *LabView* program, and electrical leads fed through the pressure vessel from the top nut and connected with piezoelectric ceramic transducers (Fig. 3.32). The *LabView* program determines the timing of the wave generator, a "JSR-PR35 type Pulser and Receiver", to excite the piezoelectric transducer. The received signal, after travelling through the specimen and end caps, is re-converted to the electrical signal by the receiver. After amplification with a gain of 32 dB and band-pass filtering between 0.3 and 15 MHz, the electrical signals are digitised and displayed in the *LabView* program. The switch box is remotely controlled to combine selective connectors to switch automatically between P- and S-wave mode measurements. The sampling interval is 10 ns and a set of 10,000 continuous samples is collected and displayed in the *LabView* program, which means a waveform of 100 μs is windowed. To minimize the high-frequency noise, a stack of over 300 waveforms is collected and averaged. The stacked waveform is then recorded for further analysis.

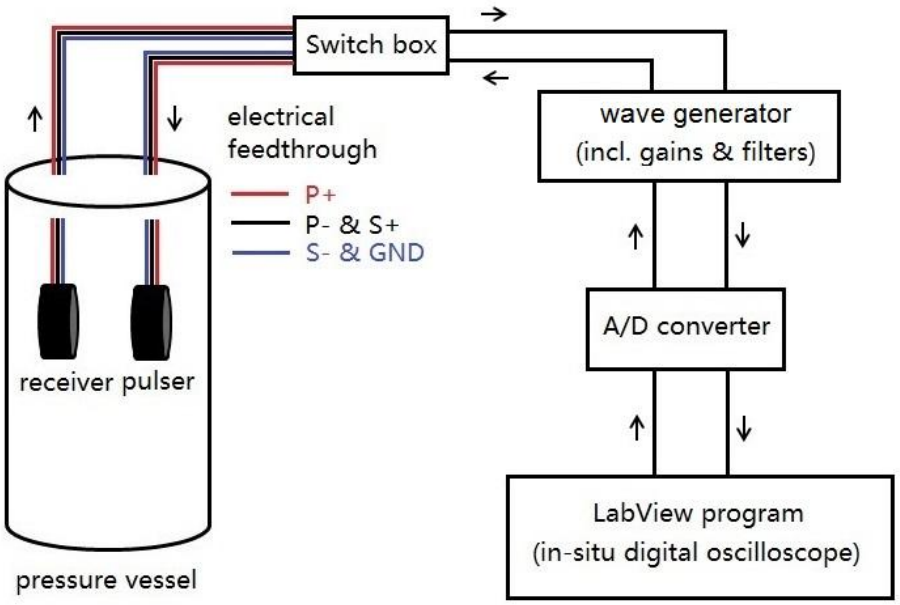


**Figure 3.32** Arrangement of the data acquisition system for ultrasonic wave propagation measurements.

3.3.1.7 P- and S-wave velocities

From the previous discussion, P- and S-wave travel times through the specimen are determined by the time delay of the first arrivals between the specimen run and the calibration run. However, the first positive arrival is sometimes difficult to identify due to its relatively small amplitude and distorted waveform. The second positive arrival, therefore, is selected as the reference to determine the travel time of ultrasonic waves through the specimen (Fig. 3.33).

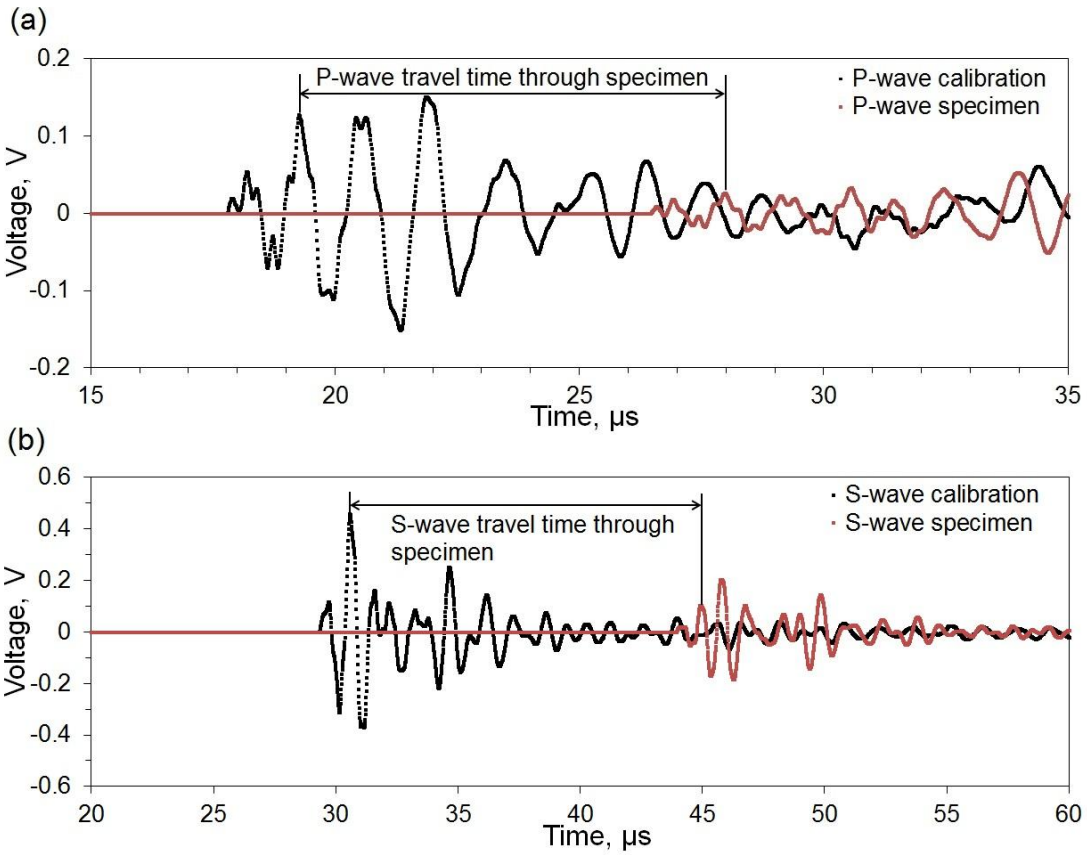


**Figure 3.33** A comparison of the waveforms of calibration and specimen runs to determine the travel time of ultrasonic waves through the specimen for either (a) P-wave or (b) S-wave. The second positive arrival is selected as the reference for both P- and S-waves, taking advantage of its relatively large amplitude and less distorted waveform. Noise prior to the first breaks of both calibration and specimen runs has been removed from the plot to give a clearer illustration.

The difficulty is commonly reported in identifying the correct phase in the received waveform, as a consequence of distortion in waveform and low signal-to-noise ratio. Cross correlation is a mathematical solution for this. For two time series $X(t)$ and $Y(t)$ with similar waveforms delayed by a time interval $\tau$, $\tau$ can be determined by calculating the cross-correlation coefficient $r(\tau)$. The coefficient is defined as the ratio between the covariance of $X(t)$ and $Y(t+\tau)$ and the product of individual standard deviation of each time series, mathematically expressed as:

$$r(\tau) = \frac{COV[X(t),Y(t+\tau)]}{\sigma_{X(t)} \cdot \sigma_{Y(t+\tau)}}, \tag{3.66}$$

in which

$$COV[X(t),Y(t+\tau)] = E[XY] - E[X]E[Y], \tag{3.67}$$

$$\sigma_{X(t)} = \sqrt{E[X^2] - (E[X])^2}, \tag{3.68}$$

$$\sigma_{Y(t+\tau)} = \sqrt{E[Y^2] - (E[Y])^2}, \tag{3.69}$$

where *E(X)* and *E(Y)* are the expected values of *X* and *Y*, respectively. Notice the cross-correlation coefficient $r(\tau)$ is different from the Pearson product moment correlation coefficient by introducing a time delay $\tau$. The cross-correlation coefficient $r(\tau)$ has a value between -1 and 1. $X(t)$ and $Y(t+\tau)$ are perfectly correlated if $r(\tau) = 1$; $X(t)$ and $Y(t+\tau)$ are anti-correlated if $r(\tau) = -1$; and there is no relationship between $X(t)$ and $Y(t+\tau)$ if $r(\tau) = 0$.

The time delay $\tau$ giving the maximum cross-correlation coefficient $r(\tau)$ should be a robust estimate of travel time of ultrasonic waves through the specimen. The travel time calculated by the cross-correlation method generally matches the manually picked arrival times with difference of only 0.01 – 0.02 μs. However, the cross-correlation coefficient is sometimes biased by the presence of high-level noise, creating ambiguity. The selection of second positive arrivals is therefore still preferred to routinely determine the travel time, crosschecked by the complementary cross-correlation method.

Velocities of P- and S-waves travelling through a specimen are calculated as the ratios between the length of sample and the measured P- and S-wave travel times, respectively. A source of uncertainty in velocity measurement arises from the pressure-dependent geometric change of specimen. Sample shortening is expected to occur under pressure, so that the velocities will be overestimated if they are calculated with the length of sample measured at ambient conditions. This uncertainty can be estimated by in-situ measurements under pressure with strain gauge, the details of which will be described in a later section. The sample shortening can also be estimated by simple theoretical considerations of isotropic elasticity. For an isotropic specimen, under hydrostatic pressure:

$$\varepsilon_a = \frac{P}{3K}, \tag{3.70}$$

where *K* is the bulk modulus, *P* is the hydrostatic pressure, and $\varepsilon_a$ is the axial strain. The maximum confining pressure involved in ultrasonic measurements is 100 MPa, and the average bulk modulus of the glass samples is ~ 40 GPa, giving the axial strain, *i.e.*, shortening of the sample length, is less than 0.1%.

Finally, the elastic moduli are related to the measured P- and S-wave velocities as:

$$K = \rho({V_P}^2 - \frac{4}{3}{V_S}^2), \tag{3.71}$$

$$G = \rho {V_S}^2, \tag{3.72}$$

$$E = \frac{9KG}{3K+G}, \tag{3.73}$$

where $K$, $G$, and $E$ are the bulk, shear, and Young's moduli, respectively; $V_P$ and $V_S$ are P- and S-wave velocities, respectively; $\rho$ is the bulk density.

#### 3.3.1.8 (Differential) attenuation coefficient

Spectral ratio is the conventional method in determining attenuation for the ultrasonic wave transmission measurements (Toksöz *et al.*, 1979; Bourbié *et al.*, 1987). The low signal-to-noise ratio caused difficulty in applying this method to the acquired waveforms. The less robust results of attenuation will not be presented in the main text. But the details of the spectral ratio method can be found in *Appendix D*.

#### 3.3.1.9 Strain Gauge Measurement

The dimensions of the sample change both axially and radially under hydrostatic pressure. As discussed previously, the sample shortening in the axial direction affects the estimation of wave velocity. A theoretical computation given by Eq. (3.70) can provide a rough estimate for the axial shortening. To more precisely determine the change in length in situ, a strain gauge measurement is needed. An ideal ultrasonic-wave speed measurement requires obtaining both velocities and axial strain at the same time and under the same pressure condition. However, the strain measurement requires feeding of the electrical leads of strain gauges through the PVC jacket - a process involving cutting and resealing the jacket. This significantly increases the chance of a hydraulic oil leak. A compromise requires the strain gauge measurement to be performed separately from the wavespeed measurement but following the same protocol in terms of pressure variation. Assuming a negligible hysteresis, the axial strain obtained in the separate strain measurement is applicable to that in the wavespeed measurement. Details of the strain measurement will be provided below.

Omega® SGD-10/350-LY41 linear strain gauges are used in experiments. The principle of strain gauge relies on that the electrical resistance of an electrical conductor varies proportionally with strain. Strain affects resistance through changes of length and cross-sectional area of conductor. It needs to be emphasised that neither stretching nor compression should exceed the elasticity limits of the conductor. The strain, as a mechanical quantity, is then converted into measurable electrical signals. The zig-zag pattern of metallic foil (conductor) multiplies the change in resistance in the direction parallel to the foil lines, allowing an easier detection of a small strain (Fig. 3.34).

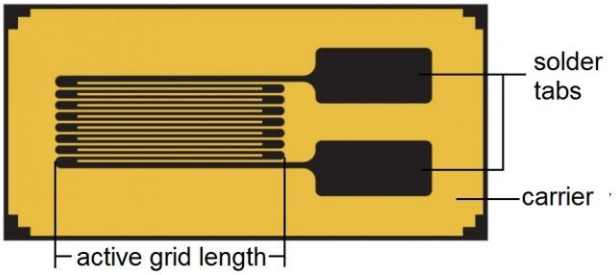


**Figure 3.34** Arrangement of a strain gauge. Metallic foil is arranged in a grid pattern. Electrical leads are soldered on the tabs to connect the strain gauge into an electrical circuit. The metallic foil and solder tabs are mounted on a carrier to allow an easy attachment to a specimen.

A Wheatstone bridge is required to measure the unknown electrical resistance of a strain gauge. The details of constructing the Wheatstone bridge can be found in *Appendix E*. The working equation that converts the measured bridge voltages to the strain of a sample is expressed as:

$$\varepsilon = \frac{-4\Delta U_r}{(2\Delta U_r + 1)GF}, \tag{3.74}$$

$$\Delta U_r = \frac{U_0}{U_{ex,0}} - \frac{U_1}{U_{ex,1}}, \tag{3.75}$$

where $\varepsilon$ is the strain of a sample; $\Delta U_r$ is the change in voltage ratio; $GF$ is the gauge factor; $U_0$ and $U_{ex,0}$ are the bridge voltage and the excitation voltage at ambient conditions, respectively; $U_1$ and $U_{ex,1}$ are the bridge voltage and the excitation voltage at a pressure higher than the ambient pressure.

In practice, before the attachment of strain gauges, a smooth area on the outer surface of a cylindrical sample needs to be sanded and cleaned with acetone. A combined use of a longitudinal and a tangential strain gauge provides strains in both axial and tangential directions. Both strain gauges are attached to the sample surface by M-Bond® 300 adhesive. Any air bubble trapped between the strain gauges and sample surface needs to be driven out by firmly pressing the strain gauges on the top surface, in order to achieve an intimate contact between the gauges and the specimen. The specimen with the strain gauges glued is jacketed with PVC tubing. The area for electrical feedthroughs on the PVC tubing needs to be pre-determined and cut before jacketing. Once the specimen slides into the correct longitudinal position within the PVC jacket, indicated by a complete exposure of solder tabs of the strain gauges, electrical leads need to be connected with the strain gauges. Flexane® 80 liquid, the same sealing material as that used in the construction of the pulser and receiver, is prepared and performs the sealing for the electrical feedthroughs. The specimen assembly

is then prepared with the specimen sandwiched between the pulser and the receiver in the same way as for the wavespeed measurements.

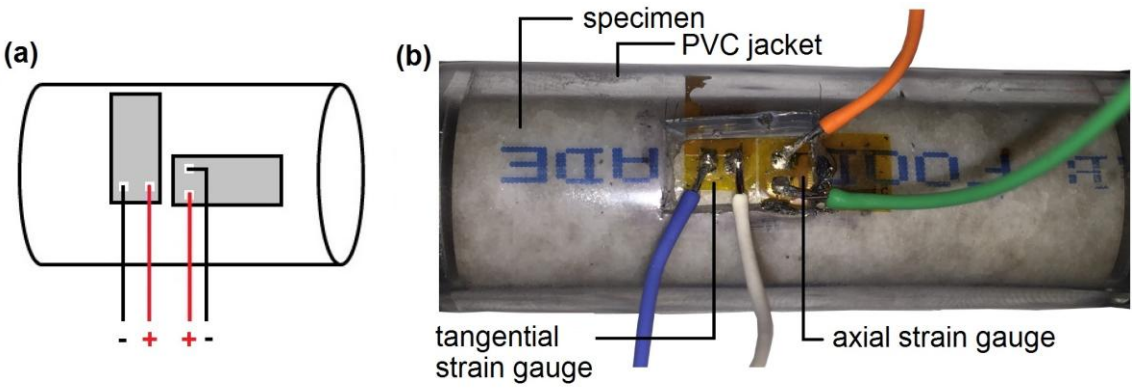


**Figure 3.35** (a) A sketch and (b) a photographic illustration of the arrangements of an axial strain gauge and a tangential strain gauge. The strain gauges need to be directly attached to the surface of a specimen before jacketing. The PVC jacket is cut through to expose the solder tabs of the strain gauges to allow connection to electrical leads. The cut jacket requires a resealing with Flexane® before pressurisation.

The bridge excitation voltage is kept constant at 2.5 V through the entire measurement. The gauge factor of the strain gauges used on the glass-rod specimen and the high-porosity glass-bead specimen is 2.14, but the gauge factor is 2.13 of the strain gauges used on the low-porosity glass-bead specimen. The bridge voltage needs to be measured at ambient conditions and a desired level of pressure, alongside the known bridge excitation voltage and gauge factor, to yield the local axial and tangential strains. By assuming homogeneity of a sample, the volumetric strain of the sample can be estimated from the local strain.

### 3.3.2 Ultrasonic Interferometry

As discussed in *Section 3.1.1.10*, in order to extract shear and Young's moduli by forced oscillations at mHz-Hz frequencies, the elastic properties of an elastic reference specimen need to be pre-determined by either referring to literature values or ultrasonic method. For the latter case, ultrasonic interferometry is normally used in the laboratory at the Australian National University. This technique is performed on a locally designed and built ultrasonic interferometer.

Broadly speaking, ultrasonic interferometry is a pulse-echo method. Compared with the ultrasonic wave-transmission method involving a pulser and a receiver separately, a piezoelectric transducer bonded on the surface of a specimen serves as both the pulser and the receiver in ultrasonic interferometry. An ultrasonic pulse emitted by the piezoelectric transducer travels through the studied specimen until being reflected at the far end of the

specimen and received again by the same piezoelectric transducer as an echo. The time-of-flight is the two-way travel time of the ultrasonic pulse through the specimen, which is determined by the time delay between either the applied pulse and the first received echo or any two successively received echoes.

Taking the advantage of the single-transducer arrangement, two waveforms, either pulse and echo or echo and echo, can be superimposed on each other to create interference, refining the measurement of travel times. Interference maximum (minimum) occurs when two waveforms with the same frequency are separated by an integral (half-integral) number of wavelengths of the elastic wave, termed constructive (destructive) interference (Fig. 3.36). In other words, the round-trip travel time of the elastic wave should also contain the same integral (half-integral) number of the known wave periods which is the physical basis for the determination of travel time by ultrasonic interferometry. In this way, the measurement of travel time is improved in precision from $10^{-2}$ μs in ultrasonic wave transmission method to $10^{-4}$ μs in ultrasonic interferometry.

High-frequency (10-100 MHz) ultrasonic interferometry works well in uncracked samples, either crystalline or amorphous. But difficulties in interference may arise from the wave scattering at crack interfaces, so that the method is not suitable for cracked samples. Therefore, ultrasonic interferometry is involved in this experiment to determine the P- and S-wave travel times in an uncracked glass-rod specimen at ambient conditions.

In practice, lithium niobate compressional (36 °rotated Y-cut) and shear (41 °rotated X-cut) mode transducers with 0.25-inch diameter are bonded to a steel buffer rod by 1:1 (molar) mixture of glycerine and phthalic anhydride. An uncracked glass-rod specimen is bonded on the other end of the steel buffer rod (Fig. 3.36a). To achieve a reproducible thin layer of bond, the transducer-buffer-specimen assembly is evenly clamped and heated with controlled temperature for 10 to 20 minutes for bond thinning. After cooling and stiffening of the thinned bond, the transducer-buffer-specimen assembly is loaded on the ultrasonic interferometer.

Each set of source signals consists of a pair of coherent sinusoidal signals separated by a time delay $t_d$ (Fig. 3.36b red and blue source signals). The time interval between successive two pairs of source signals is termed recycle time $t_r$. The oscilloscope used for displaying source signals and echoes is triggered at the same recycle frequency to give a stable display of echoes. The first incident pulse (Fig. 3.36b red) travels through the buffer rod until being partly reflected at the buffer-sample interface as the first buffer echo, later received by the transducer (Fig. 3.36c - i). Part of the first incident pulse continues travelling until being reflected at the far end of the sample. The second pulse is applied with a time delay $t_d$. Choice of $t_d \sim t_s$ allows a superposition between the first sample echo from the first applied pulse and the first buffer echo from the second applied pulse. Under such a condition,

the interference between the two indicated echoes is established. By tuning the source signal frequency, interference maxima (constructive) and minima (destructive) are achieved alternately, corresponding to integral and half-integral numbers of wavelengths (or wave periods) within the sample, respectively. For the case of an interference maximum with the source frequency $f$, the round-trip travel time within the specimen $t_s$ is expected to contain an integral number *p* of wavelengths (or wave periods), determined as:

$$t_s = \frac{p}{f}. \tag{3.76}$$

A minor effect due to the transducer-bond phase shift needs to be corrected before obtaining the final travel time of an ultrasonic wave in a sample. The details of this correction are provided by Jackson *et al.* (1981).

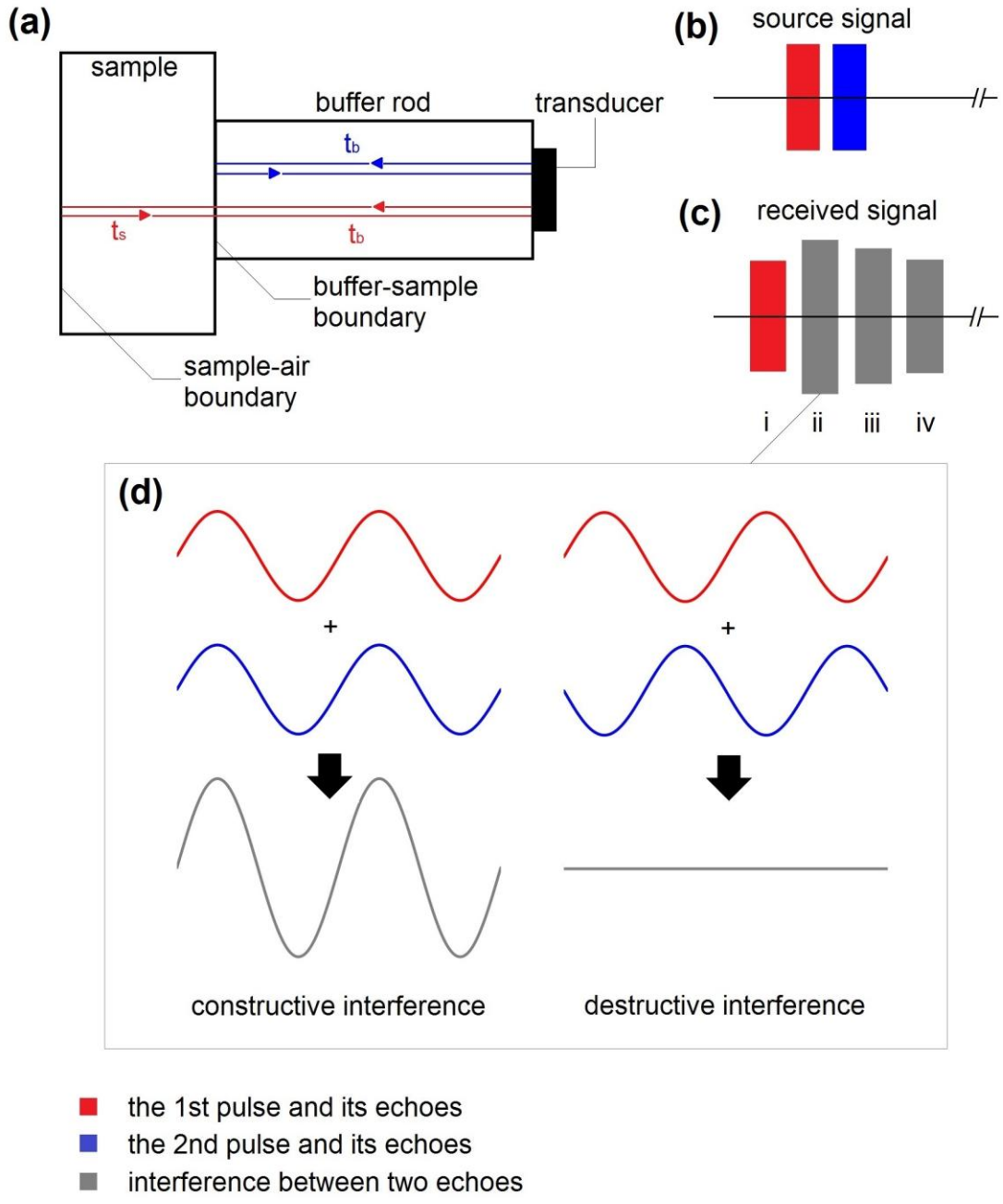


**Figure 3.36** A schematic illustration of the arrangement and mechanism of ultrasonic interferometry. (a) A transducer-buffer-sample assembly has two interfaces to reflect an ultrasonic incident wave; (b) A pair of source pulses applied by the transducer, separated by a time delay of $t_d$; (c) With $t_s = t_d$, the first sample echo from the first applied pulse interferes with the first buffer echo from the second applied pulse shown in (ii), except the first buffer echo from the first pulse is free of interference shown in (i). The following echoes from the two applied pulses in (iii) and (iv) may be free of interference or interfered with each other, depending on the relation between $t_s$ and $t_b$; (d) The superposition between the first buffer echo from the second pulse and the first sample echo from the first pulse in (ii) achieves either a constructive or a destructive interference by tuning the source frequency.

**Hydraulic Measurements – Permeability**

Besides the mechanical properties, *i.e.*, velocities or elastic moduli, permeability, as a measure of how easily fluid flows through a rock, is the other physical parameter of most interest in this study. It is an important parameter in modelling the mechanical response of a fluid-saturated rock and its pressure dependence provides evidence for crack closure. Two commonly used methods in laboratory in determining permeability are introduced below.

## 3.4 Permeability Measurement with Steady Flow

Darcy's law states that, for a laminar flow with constant pore-fluid pressure gradient applied, the flux $q$ is proportional to the pore-fluid pressure gradient $\frac{dP_f}{dx}$ and inversely proportional to the fluid viscosity $\eta$. It is expressed mathematically as:

$$q = -\frac{k}{\eta}\frac{dP_f}{dx}, \tag{3.77}$$

where the coefficient $k$ is defined as the permeability of a specimen. From Darcy's law, permeability is determinable as long as a steady flow is established.

This method was applied to a glass-rod sample on the apparatus set up for resonance measurements (Fig. 3.25). A constant water pressure gradient was maintained across the sample, with the water pressure on one end of the sample always kept at 500 psi (3.45 MPa) by a servo-controlled water pump whereas the other end was open to the atmosphere (14.7 psi) through a piece of rubber tubing. The advance of the water front within the tubing is monitored as a measure of the flux. The permeability of the sample, from Darcy's law, is then calculated.

Darcy's law is only applicable when a flow is stable. For a highly permeable sample with gas as pore fluids, the Reynolds number $R_e \gg 1$, indicating a turbulent flow and thus invalidity of Darcy's law. For a low-permeability sample saturated with highly viscous fluid, it becomes impractical to apply Darcy's law since an extremely long time is required to establish a steady flow. In the latter case, for samples with extremely low permeability, a more practical method based on the measurement of the evolution of pore-fluid pressure is employed, which is introduced in the following section.

## 3.5 Permeability Measurement with Transient Flow

In contrast to the steady-flow method directly based on Darcy's law, Brace *et al.* (1968) developed a more flexible method for low-permeability samples, in which a steady flow is no longer required during measurements. Instead of a constant pressure gradient that drives a steady fluid flow, a time-varying pressure gradient is allowed in this method. The time-dependent decay of an imposed pore pressure differential, instead of the flux in the steady-flow method, is measured to yield the permeability of a specimen. This method is termed a transient-flow or a pressure-decay measurement of permeability.

The transient-flow method is performed on the Jackson-Paterson Attenuation Apparatus with argon as pore fluid before each forced oscillation experiment. In such a pore-pressure equilibration experiment, an initial equilibrium between the two pore-fluid reservoirs is perturbed by introducing a small pressure increment/decrement to either the upstream or downstream reservoir. The return of the pore-fluid pressure to equilibrium is monitored until a common pore-fluid pressure is re-established between two reservoirs. As a prelude to forced-oscillation testing, this procedure ensures a uniform pore-fluid pressure through the specimen, along with an estimate of permeability from the record of the decaying pore-pressure increment.

The success of performing a permeability measurement requires that the pore fluid travels nowhere but through the specimen. A major concern of the permeability measurement is the possibility of a short-circuit flow between two reservoirs at the jacket-specimen interface. As a result, an intimate contact between the jacket and the specimen is highly desirable. For a soft PVC jacket, a good contact with the specimen can be easily achieved under pressure. For a copper jacket, annealing is normally needed to soften the jacket in order for intimate contact with the outer surface of the specimen to be established.

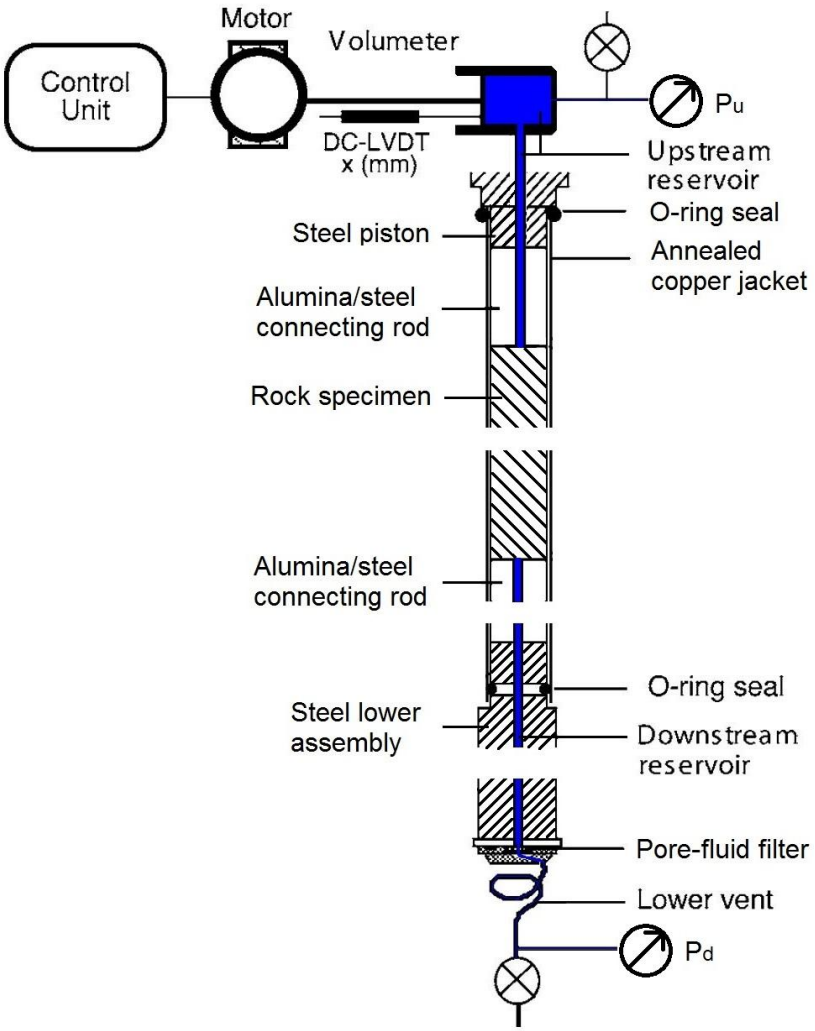


**Figure 3.37** The arrangement of the motor-controlled volumometer and the upstream and downstream pore-fluid reservoirs on the Attenuation Apparatus (modified after Lu & Jackson, 2006). The space occupied by pore fluid (blue) is physically located either above the rock specimen (upstream reservoir) or below the rock specimen (downstream reservoir). The entire pore-fluid system is separated from confining argon gas by an annealed copper jacket and O-rings.

### 3.5.1 Piston traversing experiment and upstream reservoir volume

For either the steady-flow or the transient-flow method, two separate reservoirs are needed on either side of the specimen to give a pressure difference to drive a fluid flow through the specimen. In the former method, it is not necessary to estimate the volumes of both reservoirs, which, however, are key parameters required in the transient-flow method.

The volume of the downstream reservoir is directly calculated from its geometry as $40{,}000 \pm 200$ mm$^3$ (Lu, 1996), but the volume of the upstream reservoir is more difficult to estimate from its complex geometry. Instead, a procedure involving advancing and retracting the piston of the volumometer in the upstream reservoir is developed to allow the estimation

of the volume of the upstream reservoir. By relating the change in pore-fluid pressure in the upstream reservoir to the displacement of the volumometer piston, the volume of the upstream reservoir is determined.

To perform the piston traversing experiment, only the upstream reservoir is assumed to be involved and the downstream reservoir needs to be completely disconnected from the pore-fluid system by being blocked with an impermeable specimen (Zhang *et al.*, 1994). In the present study, a low-porosity glass-bead specimen with no thermal cracks was used for this purpose.

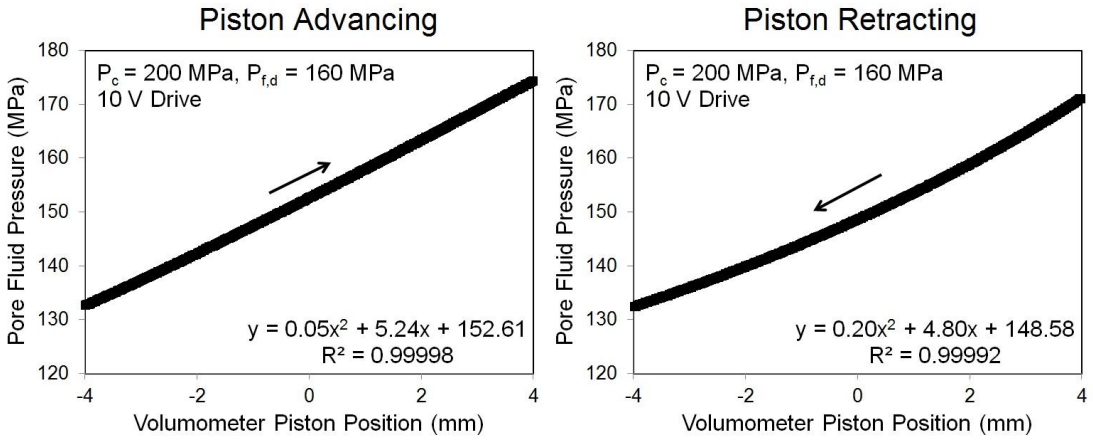


**Figure 3.38** The pore-fluid pressure in the upstream reservoir varies with the position of the volumometer piston during either advancing (left) or retracting (right) the piston. The confining pressure and the pore-fluid pressure in the isolated downstream reservoir were fixed at 200 MPa and 160 MPa, respectively, during the traversing of the volumometer piston. The parameter $dP_{f,u}/dx$ is estimated at $x = 0$ with a quadratic fit. The arrows indicate the directions of movement for the volumometer piston.

The expression for the upstream-reservoir volume is given by Zhang *et al.* (1994) and Lu and Jackson (2006) as:

$$V_u = \frac{A_v K_f}{(dP_{f,u}/dx)}, \tag{3.78}$$

where $A_v$ is the cross-sectional area of the volumometer piston equal to 17.833 mm$^2$ (Lu, 1996); $K_f$ is the bulk modulus of the pore fluid, *i.e.*, argon in this experiment; $dP_{f,u}/dx$ is determined from the piston traversing experiment.

During a piston traversing experiment, the steel piston within the volumometer is driven by a DC motor to allow a movement (either advancing or retracting) within the range of ± 4 mm. The pore-fluid pressure in the upstream reservoir (MPa) co-varies with the position of the volumometer piston (mm) (Fig. 3.38). The value of $dP_{f,u}/dx$ at $x = 0$ is determined from a quadratic fit, allowing the upstream reservoir volume $V_u$ to be calculated through Eq. (3.78).

### 3.5.2 Permeability measurement

As the volume of the downstream reservoir is ~ 25 times larger than that of the upstream reservoir, the pore-fluid pressure in the downstream reservoir changes almost imperceptibly during the entire pore-pressure equilibration. Therefore, it is more practical to monitor the evolution of the pore-fluid pressure in the upstream reservoir regardless of which reservoir is perturbed by a small pressure increment/decrement. If an increment of pressure is given to the downstream reservoir or a decrement of pressure to the upstream reservoir, the fluid pressure in the upstream reservoir is expected to grow exponentially. Conversely, if a decrement of pressure is given to the downstream reservoir or an increment of pressure to the upstream reservoir, the fluid pressure in the upstream reservoir is expected to decay exponentially. To simplify the analysis, the derivation given below focuses on the case of an increment in fluid pressure introduced to the upstream reservoir, but the solution is applicable to all the other cases.

Hsieh *et al.* (1981), assuming the limiting case of a negligible storage capacity of the specimen, provides an analytical solution for a dimensionless hydraulic head in the upstream reservoir after being perturbed by an increase in hydraulic head in the upstream reservoir as:

$$\frac{p(t)-p_0}{\Delta p} = \frac{S_u+S_d \exp(-At)}{S_u+S_d}, \tag{3.79}$$

$$A = \left(\frac{k\gamma_w A_s}{\eta L_s S_u}\right)\left(1+\frac{S_u}{S_d}\right), \tag{3.80}$$

where $p(t)$ is the pressure in the upstream reservoir at time $t$; $p_0$ is the initial equilibrium pressure which is perturbed by a small pressure change $\Delta p$ (Fig. 3.39 left); $[p(t)-p_0]$ is the hydraulic head (assuming the initial equilibrium pressure $p_0$ as the reference) in the upstream reservoir at time $t$ after a perturbation $\Delta p$ to the upstream-reservoir hydraulic head; $S_u$ and $S_d$ are the storage capacities for the upstream and downstream reservoirs, respectively; $A$ is called the rate constant, which is the inverse of the time constant, and experimentally determinable by a pore-pressure equilibration experiment; $k$ is the permeability of a sample; $\gamma_w$ is the specific weight of the fluid; $L_s$ and $A_s$ are the length and the cross-sectional area of a sample, respectively; $\eta$ is the pore-fluid viscosity.

Assuming a parameter $R(t) = \frac{p(t)-p_\infty}{\Delta p}$, we have:

$$R(t) = \frac{p(t)-p_\infty}{\Delta p} = \frac{[p(t)-p_0]-(p_\infty-p_0)}{\Delta p}, \tag{3.81}$$

where $p_\infty$ is the pore-fluid pressure when the equilibrium is reached again throughout the specimen and the two reservoirs (Fig. 3.39 left). In theory, the re-established equilibrium

pressure $p_\infty$ should be higher than initial equilibrium pressure $p_0$ before perturbation as extra argon has been introduced into the overall pore-fluid system. However, the volume of the downstream reservoir is much larger than that of the upstream reservoir, giving $p_\infty \approx p_0$ in practice. Then,

$$R(t) = \frac{p(t)-p_\infty}{\Delta p} = \frac{p(t)-p_\infty}{p(t=0)-p_0} \approx \frac{p(t)-p_\infty}{p(t=0)-p_\infty} \ . \tag{3.82}$$

The parameter $R(t)$, therefore, is a measure of how far the process of equilibration is from the final equilibrium between the upstream and downstream reservoirs. And notice:

$$\frac{p_\infty-p_0}{\Delta p} = \lim_{t\to\infty} \frac{p(t)-p_0}{\Delta p} = \lim_{t\to\infty} \frac{S_u+S_d \exp(-At)}{S_u+S_d} = \frac{S_u}{S_u+S_d} \ , \tag{3.83}$$

hence,

$$R(t) = \frac{S_u+S_d \exp(-At)}{S_u+S_d} - \frac{S_u}{S_u+S_d} = \frac{S_d \exp(-At)}{S_u+S_d} = bexp(-At) \ , \tag{3.84}$$

where $b = \frac{S_d}{S_u+S_d}$. Taking natural logarithm of both sides of the equation, we have:

$$\ln[R(t)] = \ln\left[\frac{p(t)-p_\infty}{\Delta p}\right] = \ln[bexp(-At)] = -At + lnb \ , \tag{3.85}$$

where $-A$ is the slope of $lnR(t)$ versus time curve, determined by a pore-pressure equilibration experiment (Fig. 3.39 right).

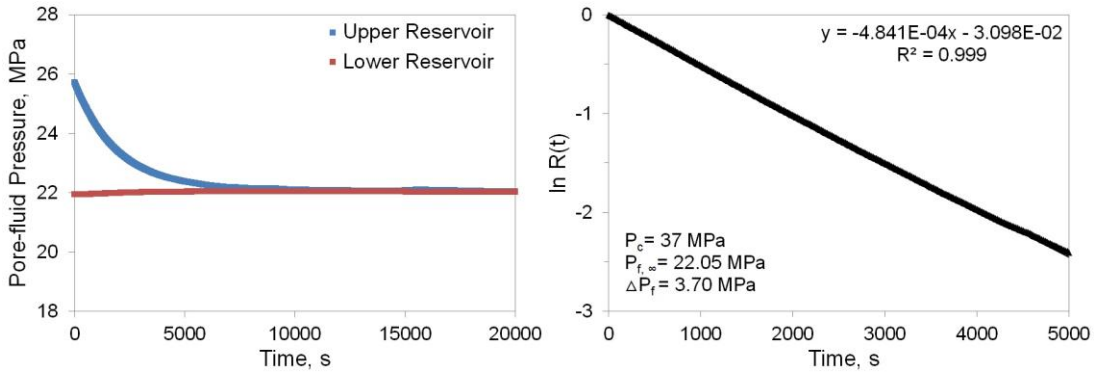


**Figure 3.39** An example of the fluid-pressure evolution in both reservoirs (left) and the extraction of the rate constant *A* from the pressure decay in the upstream reservoir (right) in a pore-pressure equilibration experiment. The representative measurements were taken from a cracked glass-rod sample with constant confining pressure of 37 MPa. An instantaneous increment of 3.70 MPa in fluid pressure was introduced to the upstream reservoir before a common fluid pressure of 22.05 MPa was reached between both reservoirs.

Re-arranging Eq. (3.80), we have the expression for permeability as:

$$k = \frac{A\eta L_s S_u}{(1+\frac{S_u}{S_d})A_s\gamma_w} = \frac{A\eta L_s}{(\frac{1}{S_u}+\frac{1}{S_d})A_s\gamma_w}, \tag{3.86}$$

and notice the relation between the storage capacity $S$ and the volume of a reservoir $V_f$ :

$$S = \frac{V_f\gamma_w}{K_f}, \tag{3.87}$$

where $\gamma_w$ is the specific weight of pore fluid; $K_f$ is the bulk modulus of pore fluid. Substitute equation (3.87) into (3.86), we have:

$$k = \frac{A\eta L_s}{(\frac{1}{V_u}+\frac{1}{V_d})K_f A_s}. \tag{3.88}$$

It needs emphasis that any variation associated with fluid properties with changing pressure is neglected in deriving the expression above. For the assumption of constant fluid properties to be valid, it is required that $\Delta p$ be less than 5 MPa and also that $\frac{\Delta p}{p_0} \ll 1$.

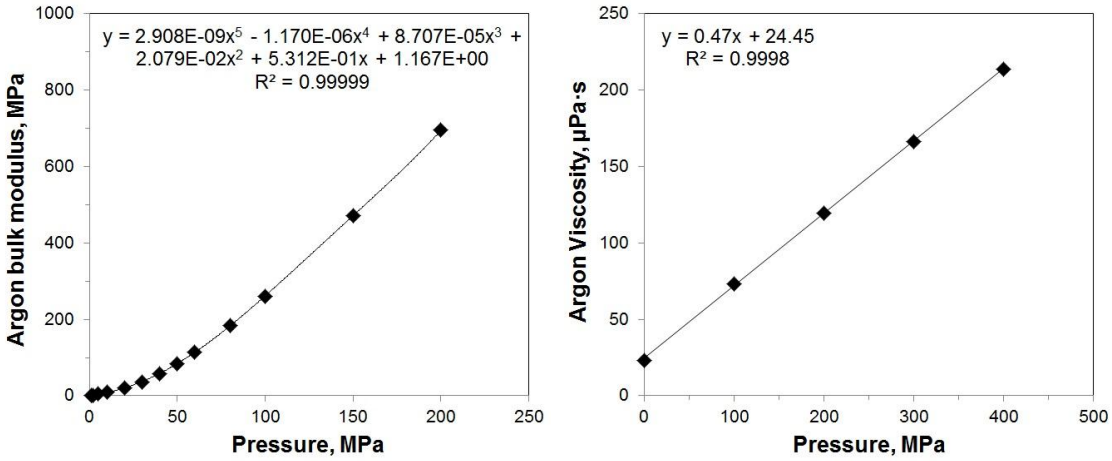


**Figure 3.40** Argon bulk modulus and viscosity at different fluid pressures. The data of the argon bulk modulus (left) and the viscosity (right) are taken from Stewart & Jacobsen (1989) and Vidal *et al.* (1979), respectively, allowing an estimate of the argon bulk modulus and viscosity at any given pressure through polynomial and linear fits.

In more detail, to perform a pore-pressure equilibration experiment with argon, both the upstream and downstream reservoirs, which have the same fluid pressure, are first isolated from the pore fluid delivery lines. Before perturbing the fluid pressure in the reservoir, an appropriate period of waiting time is needed to allow a uniform pore-fluid pressure to be established in both the specimen and reservoirs. Then a fluid-pressure perturbation is introduced to either the upstream or the downstream reservoir. The perturbation is achieved

by re-connecting the target reservoir to the pore-fluid delivery line to make an essentially instantaneous pressure adjustment, *i.e.*, a pressure increment or decrement of less than 5 MPa, before isolating the reservoir again from the delivery line. A pressure gradient is thus created between the two reservoirs. The argon pore fluid is driven by this pressure gradient from one reservoir to the other through the specimen. The evolution of the pore-fluid pressure in the upstream reservoir is logged at the rate of 1 datum per 10 seconds in a *LabVIEW* program, from which the time series of $ln\,[R(t)]$ is determined and later subject to a linear fit to yield the rate constant $A$ (Fig. 3.39 right). The pressure-dependent bulk modulus and viscosity of argon are taken from Stewart & Jacobsen (1989) and Vidal *et al.* (1979), respectively (Fig. 3.40). With the known geometry of a sample and volumes of both reservoirs, the permeability of the sample is determinable by Eq. (3.88).

# Chapter 4 Hydraulic Properties

Permeabilities of the synthetic specimens have been measured with either argon or water as pore fluid. In principle, the permeability of a specimen should be independent of the type of pore fluid used in measurements. However, gas permeability is sometimes found to be several times to one order of magnitude higher than water permeability due to the Klinkenberg effect (Tanikawa & Shimamoto, 2009) when pore-fluid pressure is lower than 1 MPa. The velocity of water in contact with the solid wall of the fluid passageway is reduced to zero, whereas a gas still has a finite velocity at the contacting surface, which is called gas slippage at the walls or the Klinkenberg effect. At low pressure, the mean free path of gas molecules is large and the gas slippage is more significant. With increasing pressure, the gas slippage is gradually suppressed by high chance for molecular collisions and the velocity of gas molecule is reduced from the velocity of free motion to that of water. This effect is negligible in our measurements as the argon pore-fluid pressure used was always significantly higher than 1 MPa. Argon permeability of all three types of synthetic samples was measured on the Jackson-Paterson Attenuation Apparatus at the Australian National University and water permeability of a large-dimension glass-rod specimen was measured on the apparatus for resonance tests in the Lawrence Berkeley National Laboratory. Both sets of permeability data are presented in this chapter.

## 4.1 Argon Permeability

The permeability of synthetic samples was measured on the Attenuation Apparatus with argon as pore-fluid medium before each forced-oscillation test as described in *Section 3.5*.

### 4.1.1 Upstream reservoir volume

The upstream reservoir volume on the Attenuation Apparatus is estimated by piston traversing experiment as described in *Section 3.5.1*. The success of the piston traversing experiment requires the upstream reservoir is completely isolated from the downstream reservoir, which is achieved by the use of an impermeable specimen sandwiched in between. The results reported here were obtained with an uncracked low-porosity glass-bead specimen present. The confining pressure was kept at 200 MPa with varying argon pore-fluid pressure in the upstream reservoir. The minimum differential pressure (confining pressure – pore-fluid pressure) was ~ 50 MPa throughout the piston traversing experiments. The relatively high differential pressure was chosen to achieve an intimate contact between

the annealed copper jacket and the specimen to prevent any communication of argon pore fluid between two reservoirs. The typical timescale for pore-pressure equilibration between two reservoirs is on the order of tens of hours on this uncracked low-porosity glass-bead specimen, whereas the piston traversing experiment was normally completed within 15 minutes. The contrast in timescales indicates that any fluid flow from the upstream to the downstream reservoir due to the presence of ~2% background equant porosity would be negligible in these measurements.

At each differential pressure, the volumometer piston was driven forward and backward within the range of +4/-4 mm around its origin, corresponding to about $\pm 70$ mm$^3$ change in upstream reservoir volume. The motor was driven by DC voltages of 5 V and 10 V to perform the piston traversing at different rates. The co-varying displacement of piston and pore-fluid pressure in the upstream reservoir were recorded and fitted to a quadratic function $P_f(x)$ to yield the argon pore-fluid pressure in the upstream reservoir and the value of derivative $dP_{f,u}/dx$ when the piston was at the origin ($x$ = 0 mm). The response of the pore-fluid pressure in the upstream reservoir differs slightly during piston advancing and retracting (*Appendix F*). This was probably caused by frictional effects between the steel piston and O-ring during piston advance and retreat. The pore-fluid pressure values when the piston was at the origin shown in Table 4.1 are the mean values of both piston advance and retreat at a given differential pressure. Argon bulk modulus at a given pore-fluid pressure was estimated by using the literature values given in Stewart and Jacobsen (1989) (Fig. 3.40). The volume of the upstream reservoir was then calculated through Eq. (3.78) at each given argon pore-fluid pressure (Table 4.1). Taking into account the variation of the values estimated at pore-fluid pressures from 19.47 MPa to 150.60 MPa, the volume of the upstream reservoir is $1548 \pm 98$ mm$^3$. The highest values of the upstream reservoir volume are determined at the highest pore-fluid pressure of 145 MPa – 150 MPa, which is probably explained as the elastic expansion of stainless steel pipe which forms part of the upstream reservoir (Fig. 3.37). The upstream reservoir volume was determined with the presence of old alumina connecting rods, which were later replaced with new steel connecting rods. The slight change in geometry for the new rods introduces a reduction in volume of 7.4 mm$^3$ for the upstream reservoir, which is taken into account in the uncertainty.

**Table 4.1** Piston Traversing Experiment and Upstream Reservoir Volume

| $P_c$, MPa | $P_{f,u}$ at $x$ = 0 mm, MPa | Drive Voltage, V | $K_f$, MPa | $dP_{f,u}/dx$ at $x$ = 0 mm, MPa/mm | $A_v$, mm$^2$ | $V_u$, mm$^3$ |
|---|---|---|---|---|---|---|
| 200 | 19.47 | 5 | 20.23 | 0.23 | 17.833 | 1568.85 |
| 199 | 38.60 | 5 | 54.45 | 0.66 | 17.833 | 1471.29 |
| 200 | 42.68 | 5 | 64.38 | 0.77 | 17.833 | 1491.12 |
| 200 | 42.36 | 10 | 63.58 | 0.76 | 17.833 | 1491.76 |
| 199 | 58.10 | 5 | 108.31 | 1.34 | 17.833 | 1446.85 |
| 200 | 102.07 | 5 | 268.27 | 3.06 | 17.833 | 1565.99 |
| 200 | 98.51 | 10 | 254.93 | 3.06 | 17.833 | 1488.12 |
| 200 | 145.30 | 5 | 430.05 | 4.47 | 17.833 | 1715.69 |
| 200 | 150.60 | 10 | 477.38 | 5.02 | 17.833 | 1695.85 |

$P_c$: confining pressure; $P_{f,u}$: argon pressure in the upstream reservoir; $K_f$: bulk modulus of argon; $A_v$: piston cross-sectional area; $V_u$: upstream reservoir volume estimated through Eq. (3.78).

### 4.1.2 Argon permeability

Argon permeability was obtained through pore-pressure re-equilibration between the upstream and downstream reservoirs, which is described in detail in *Section 3.5.2*. The rate constant parameter was determined from the process of pore-pressure equilibration, combined with the knowledge of sample geometries, pore-fluid properties and volumes of both reservoirs, yielding permeabilities for each type of synthetic sample (tabulated in *Appendix H*, plotted in Fig. 4.1) through Eq. (3.88).

With the confining pressure fixed between 90 and 100 MPa, pore-fluid pressure was varied to achieve different differential pressures. The requirements for pore-fluid pressure mentioned previously for a valid use of Eq. (3.88) were well satisfied in most cases but only marginally in the cases at the highest differential pressures, *i.e.*, lowest pore-fluid pressures with fixed confining pressure. Large uncertainties propagate into the calculated permeability at the lowest pore-fluid pressures when $\frac{\Delta p}{p_0}$ approaches 1.

There are two major sources of uncertainty in permeability calculation. The variation of pore-fluid properties during equilibration is the first source as described above. The average of the initial and final pore-fluid pressures in the upstream reservoir is shown in *Appendix H* with uncertainties of argon bulk modulus and viscosity related to the variation of pore-fluid pressure between its upper and lower limits. The second major source of uncertainty is associated with the rate constant obtained through logarithmic fit to the evolving pore-fluid

pressure in the upstream reservoir. The rate constant may vary slightly depending on the segment of data chosen. Various segments of data were fit to obtain the optimal rate constant and its variation.

The permeabilities of three synthetic samples: 1) glass-rod specimen; 2) low-porosity (~2%) glass-bead specimen; and 3) high-porosity (~5%) glass-bead specimen are presented as functions of differential pressure (Fig. 4.1). A general trend of decreasing permeability with increasing differential pressure is noticed for each sample. The rate of decrease in permeability with increasing differential pressure is larger at differential pressures less than 40 MPa and becomes milder beyond 40 – 50 MPa. The permeability of the high-porosity glass-bead sample is systematically higher than that of the low-porosity glass-bead sample, and the latter is in turn systematically higher than that of the glass-rod specimen. The permeabilities of the three samples are similar at differential pressures lower than 40 MPa but there are systematic differences in permeability at higher differential pressures. Pore fluid pressure could not reach equilibrium between the upstream and downstream reservoirs for the measurement on the glass-rod specimen with confining pressure of ~ 100 MPa, giving permeability below the detection limit of ~ $10^{-20}$ $m^2$.

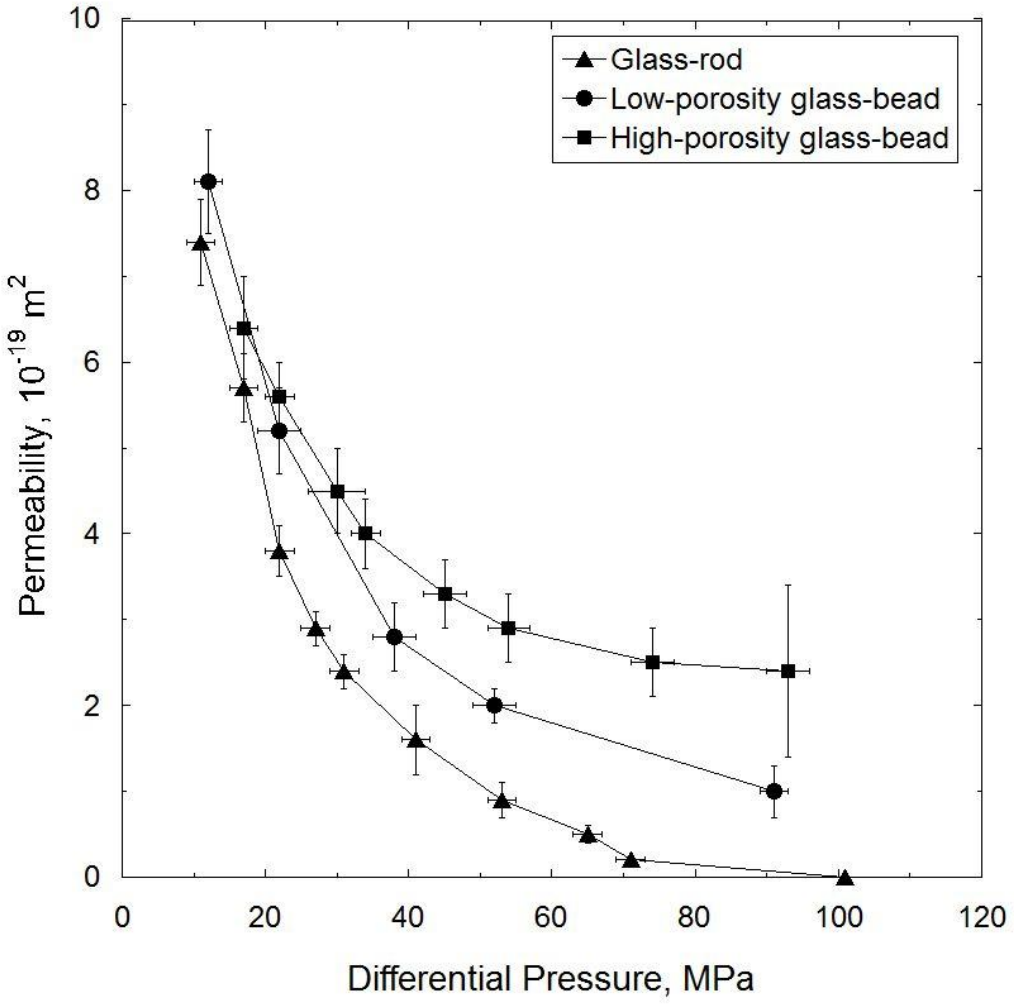


**Figure 4.1** Argon permeabilities measured at various differential pressures by a transient flow method on three thermally cracked specimens of synthetic glass media: 1) glass-rod specimen; 2) low-porosity (~2%) glass-bead specimen; and 3) high-porosity (~5%) glass-bead specimen. Numerical values are given in *Appendix H*.

## 4.2 Water Permeability

The permeability of a large-dimension glass-rod specimen (76.378 mm in length and 38.125 mm in diameter) was measured with water pore fluid on the resonance apparatus as described in *Section 3.4*. The confining pressure was kept at ~ 0.57 MPa (~ 83 psi) and water pressure was maintained by a servo-controlled pump at ~ 0.34 MPa (50 psi) on one end of the specimen with the other end of the specimen open to the atmosphere through a rubber tube. The differential pressure of ~ 0.23 MPa (~ 33 psi) was maintained for 2 hours to establish a laminar flow before the confining pressure was raised to a higher level for flow flux measurement.

The advance of water within the rubber tubing with an inner diameter of 1.397 mm over a period of time was monitored to estimate the flux through the cross-section of the specimen. The water permeability of the glass-rod specimen was then calculated from the measured flux and the stable water pressure gradient through Darcy's law (Eq. 3.77). The water pressure gradient was maintained throughout the measurements while the confining pressure was varied to achieve different differential pressures below 10 MPa.

The water permeability of the glass-rod specimen decreases by almost three orders of magnitude from $2.1 \times 10^{-17}$ $m^2$ at the lowest differential pressure of 1.3 MPa to $7.0 \times 10^{-20}$ $m^2$ at the highest differential pressure of 9.3 MPa (Fig. 4.2). Uncertainties were found in determining the position of water front within the rubber tubing. The slight variation in temperature ($\pm$ 2 °C) might also introduce uncertainty in viscosity of water by up to 5%. The overall uncertainty of permeability, therefore, is estimated to be ~ 10%.

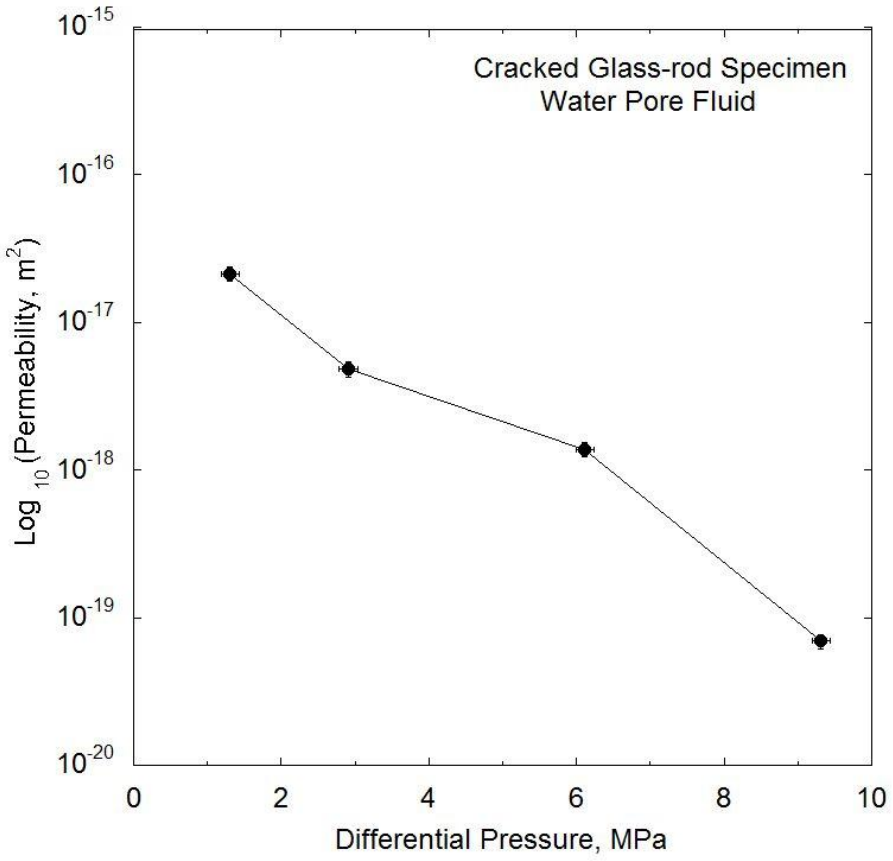


**Figure 4.2** Water permeability measured on a large-dimension glass-rod specimen as a function of differential pressure. Numerical values are provided in *Appendix I*.

# Chapter 5 Mechanical Properties at Low (mHz-Hz) Frequencies

The mechanical properties of synthetic samples have been measured, in the sequence of increasing frequency, by forced oscillation, resonance, and ultrasonic wave propagation. The results in the form of shear and Young's modulus will be presented in the following three chapters. This chapter will focus on the mechanical properties acquired by forced oscillation measurements at mHz-Hz frequencies, in both torsional and flexural modes, on the Jackson-Paterson Attenuation Apparatus at the Australian National University.

The measurements on each type of specimens were performed under dry, argon-, and water-saturated conditions in sequence. The confining and differential pressures of measurements were all below 150 MPa. For dry experiments, the confining pressure was first raised to the highest level to achieve good mechanical coupling between the components of the specimen assembly and the steel elastic standard. The measurements were then taken at different confining pressure levels during staged pressure reduction to the minimum pressure of about 10 MPa (Fig. 5.1). Argon pore fluid was introduced into the system, returned to the highest confining pressure following completion of the dry measurements, at the pore pressure required for the minimum differential pressure of 10 MPa. With the confining pressure fixed at the highest level, the argon pore-fluid pressure was then decreased in stages to ~ 10 MPa to create a trend of increasing differential pressure (Fig. 5.1). The argon pore-fluid pressure was then kept at ~ 10 MPa and the confining pressure was reduced by steps to create a trend of decreasing differential pressures (Fig. 5.1). At each differential pressure, a pore-pressure equilibration experiment was conducted before the mechanical tests to allow uniform argon pore-fluid pressure throughout the crack network of the specimen. At the end of argon saturated tests, argon pore fluid was dumped into the atmosphere, allowing the specimen to recover dry status. In some cases, dry measurement was repeated (*e.g.*, glass-rod specimen) to detect any evolution of the dry modulus due to absorption/desorption of trace amounts of moisture (Fig. 5.1). After that, water as new pore fluid was introduced into the system. The water pressure was kept at a fixed level between 11 MPa and 22 MPa while the confining pressure was raised incrementally to ~ 100 MPa and then decreased by steps to create the cycles of increasing and decreasing differential pressure, respectively (Fig. 5.1). The details of the steps of confining pressure, pore-fluid pressure, and differential pressure involved in the measurements are given in Fig. 5.1.

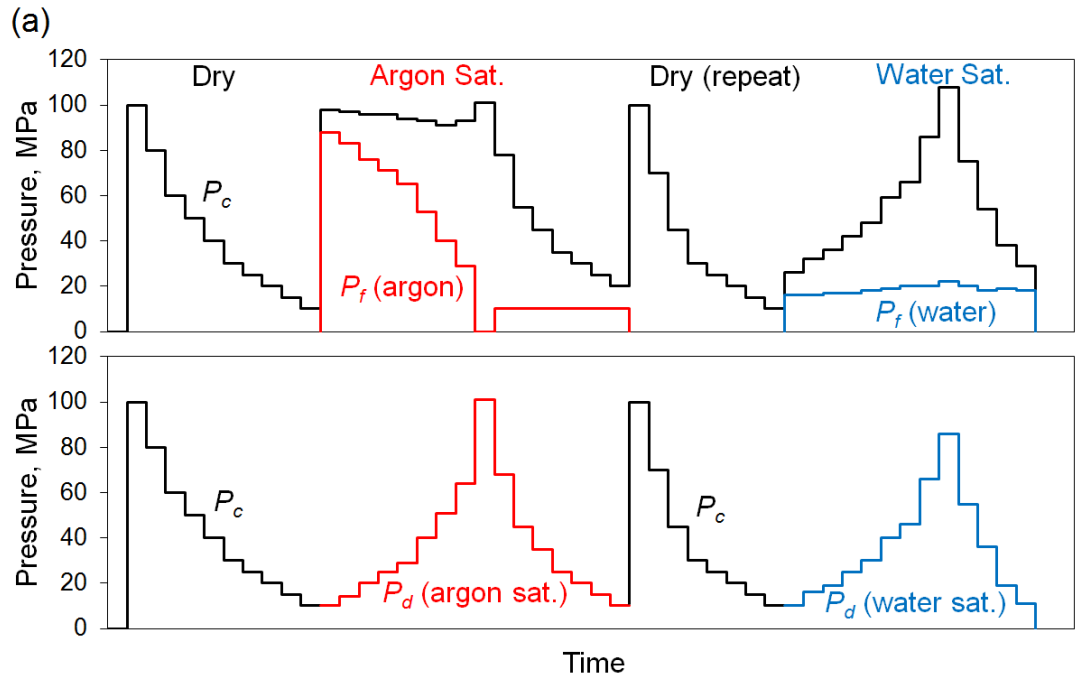
(a)
Dry
Argon Sat.
Dry (repeat)
Water Sat.
Pressure, MPa
120
100
80
60
40
20
0
$P_c$
$P_f$ (argon)
$P_f$ (water)
$P_d$ (argon sat.)
$P_d$ (water sat.)
Time

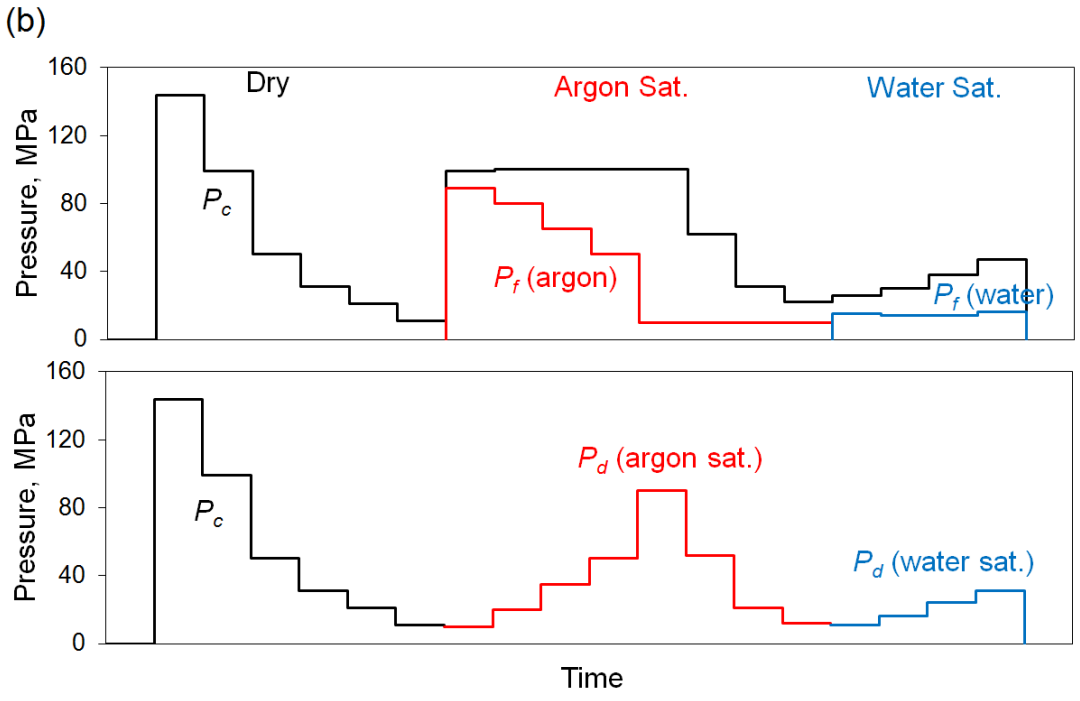
(b)
Dry
Argon Sat.
Water Sat.
Pressure, MPa
160
120
80
40
0
$P_c$
$P_f$ (argon)
$P_f$ (water)
$P_d$ (argon sat.)
$P_d$ (water sat.)
Time

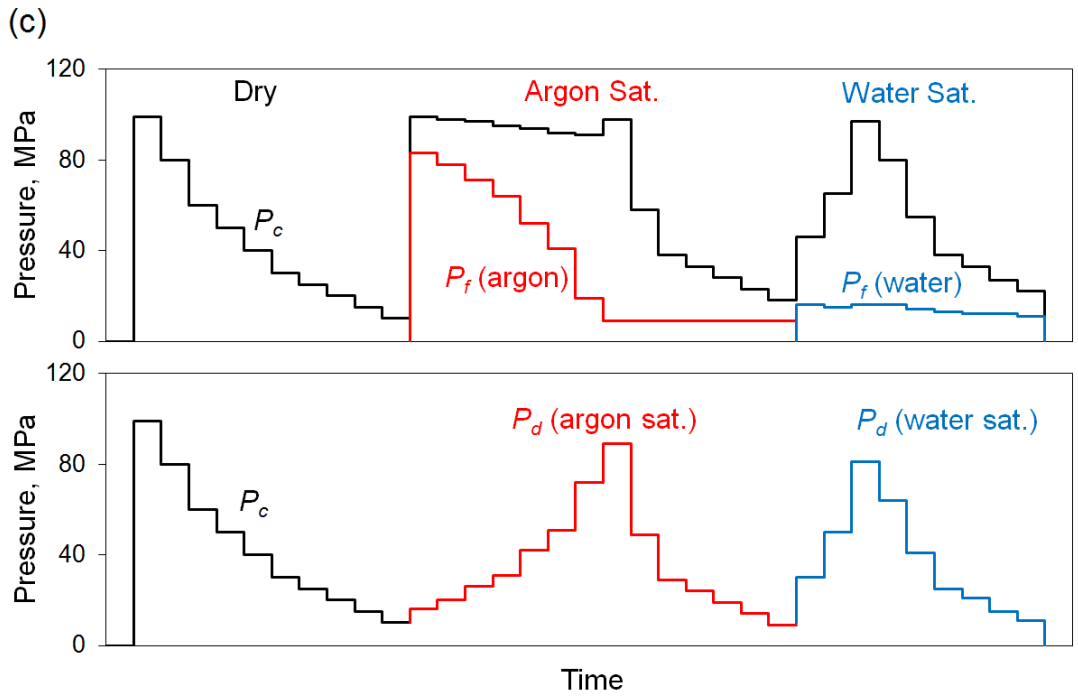


**Figure 5.1** The history of variation of confining pressure $P_c$, pore-fluid pressure $P_f$, and differential pressure $P_d$ involved in the measurements on (a) a glass-rod specimen; (b) a low-porosity glass-bead specimen; and (c) a high-porosity glass-bead specimen, under dry, argon saturated, and water saturated conditions. Numerical values are given in *Appendix J*.

Under each set of conditions of confining and pore pressure, the electromagnetic drivers on the Attenuation Apparatus were operated successively at 8 different frequencies: ~ 1.56 Hz, ~ 0.78 Hz, ~ 0.26 Hz, ~ 0.16 Hz, ~ 0.09 Hz, ~ 0.05 Hz, ~ 0.02 Hz, and ~ 0.01 Hz in either torsional or flexural mode to allow the shear or Young's modulus to be obtained at these frequencies.

## 5.1 Low-frequency Elastic Moduli of Glass-rod Specimen

A cracked soda-lime-silica glass-rod specimen (FDSL-1) of 150.220 ± 0.001 mm in length and 14.992 ± 0.001 mm in diameter was measured in torsional mode. The uncracked counterpart of the specimen, *i.e.*, the same glass-rod specimen before thermal cracking, was used in the reference assembly to take into account the pressure dependent interfacial effects between the components of the specimen assembly. Poor alignment of this assembly resulted in physical contact with the inner wall of the pressure vessel, precluding flexural mode forced oscillation. Therefore, no Young's modulus data were collected on this specimen at low frequencies. However, the torsional forced oscillation was not affected by this issue and the shear moduli of the specimen were collected as usual.

The measured shear modulus and internal friction at the various conditions of confining or differential pressure are plotted against frequency in Figure 5.2. The interaction between the condensed argon gas as the confining medium and the moving transducer plates becomes significant at higher frequencies, *i.e.*, 0.78 Hz and 1.56 Hz, and inadequate correction for this interaction makes data scattered. For this reason, the data measured at the highest frequency at 1.56 Hz is excluded from the plot. But minor scattering of shear modulus and more significant scattering of shear internal friction $1/Q_S$ can still be found at 0.78 Hz. The shear modulus almost shows no frequency dependence. The attenuation is also frequency independent for most cases except minor increase in attenuation with increasing frequency observed with argon saturation and in the repeated dry measurement (Fig. 5.2). Low attenuation values (below 0.003) are measured under all conditions. A systematic pressure dependence of attenuation for dry and argon-saturated conditions is noticed, with the highest attenuation obtained at the lowest confining or differential pressure.

The shear moduli obtained at frequencies from 0.01 Hz to 0.26 Hz are averaged to reveal more clearly the pressure dependence of the moduli (Fig. 5.3). The data at 0.78 Hz and 1.56 Hz are excluded from averaging as they are affected by the argon-transducer interaction. For the initial dry measurement, the shear modulus increases significantly with increasing confining pressure to ~ 50 MPa, thereafter decreases gently with increasing pressure until 100 MPa. With argon saturation, the shear moduli largely match the dry values and no stiffening is observed for both pressure strategies: *i.e.*, fixed confining pressure with decreasing pore-fluid pressure and fixed pore-fluid pressure with decreasing confining pressure, although there is evidence of some hysteresis between the cycles in which differential pressure is first increasing and then decreasing. In the repeated dry measurement after argon saturation, the trend of dry shear moduli with pressure is generally consistent with that observed in the initial dry measurement, although the shear moduli tend to be slightly higher in the repeat experiment. With water saturation, the pattern is one of higher shear moduli, *i.e.*, stiffening, below the differential pressure of ~ 50 MPa, with an increase of ~ 1 GPa (~ 4%) from the dry value at ~ 10 MPa. Beyond ~ 50 MPa, the shear moduli with water saturation approach the moduli measured under dry and argon saturated conditions. The shear moduli with water saturation in the increasing and decreasing differential pressure cycles are generally consistent, except for a noticeable hysteresis at the lowest pressure of ~10 MPa. A gentle decease in shear modulus with increasing pressure, similar to that observed in dry measurements beyond 50 MPa, is also noticed with water saturation.

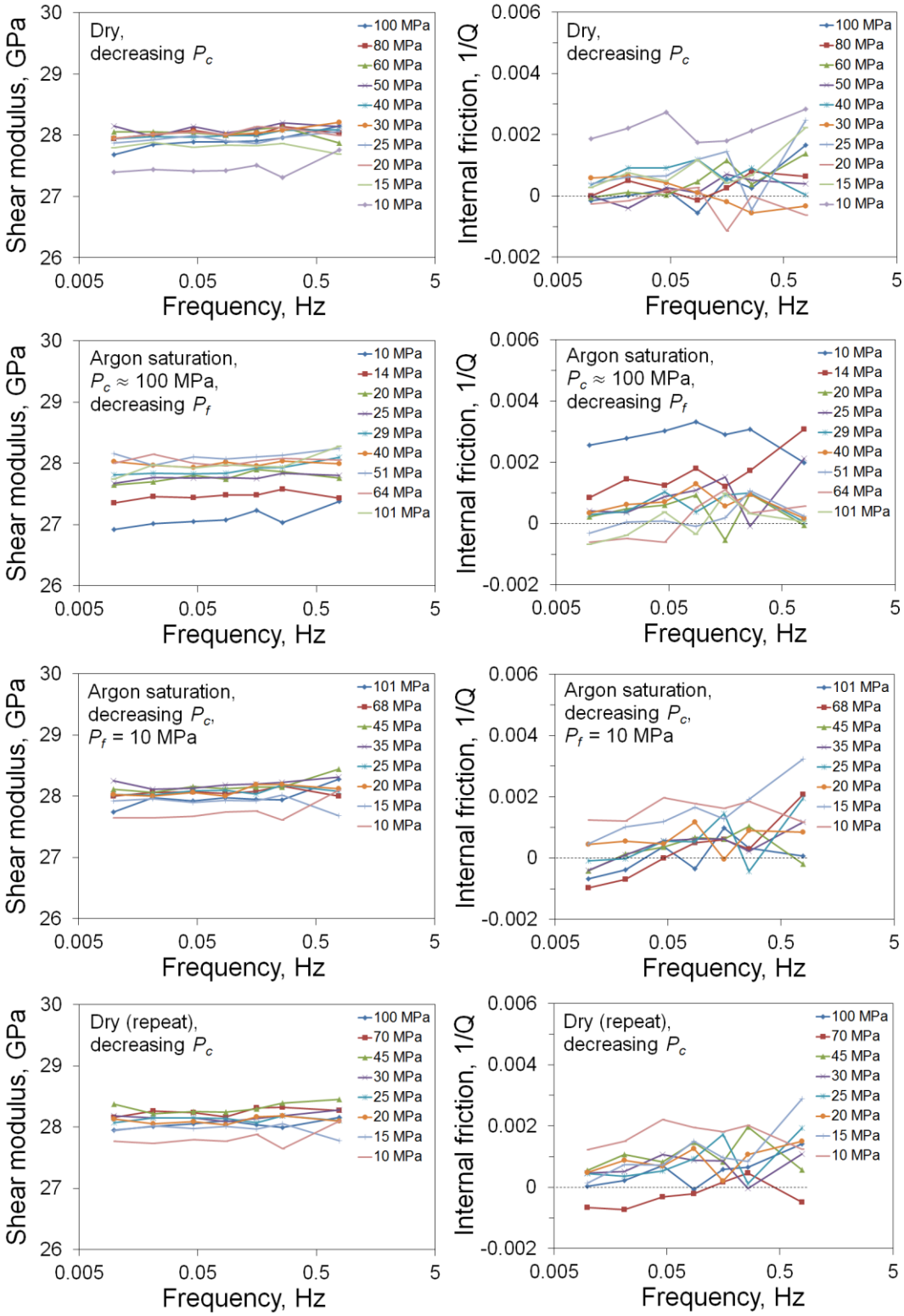
Dry,
decreasing $P_c$
100 MPa
80 MPa
60 MPa
50 MPa
40 MPa
30 MPa
25 MPa
20 MPa
15 MPa
10 MPa
Shear modulus, GPa
Internal friction, 1/Q
Frequency, Hz
Argon saturation,
$P_c \approx 100$ MPa,
decreasing $P_f$
10 MPa
14 MPa
20 MPa
25 MPa
29 MPa
40 MPa
51 MPa
64 MPa
101 MPa
Argon saturation,
decreasing $P_c$,
$P_f$ = 10 MPa
101 MPa
68 MPa
45 MPa
35 MPa
25 MPa
20 MPa
15 MPa
10 MPa
Dry (repeat),
decreasing $P_c$
100 MPa
70 MPa
45 MPa
30 MPa
25 MPa
20 MPa
15 MPa
10 MPa

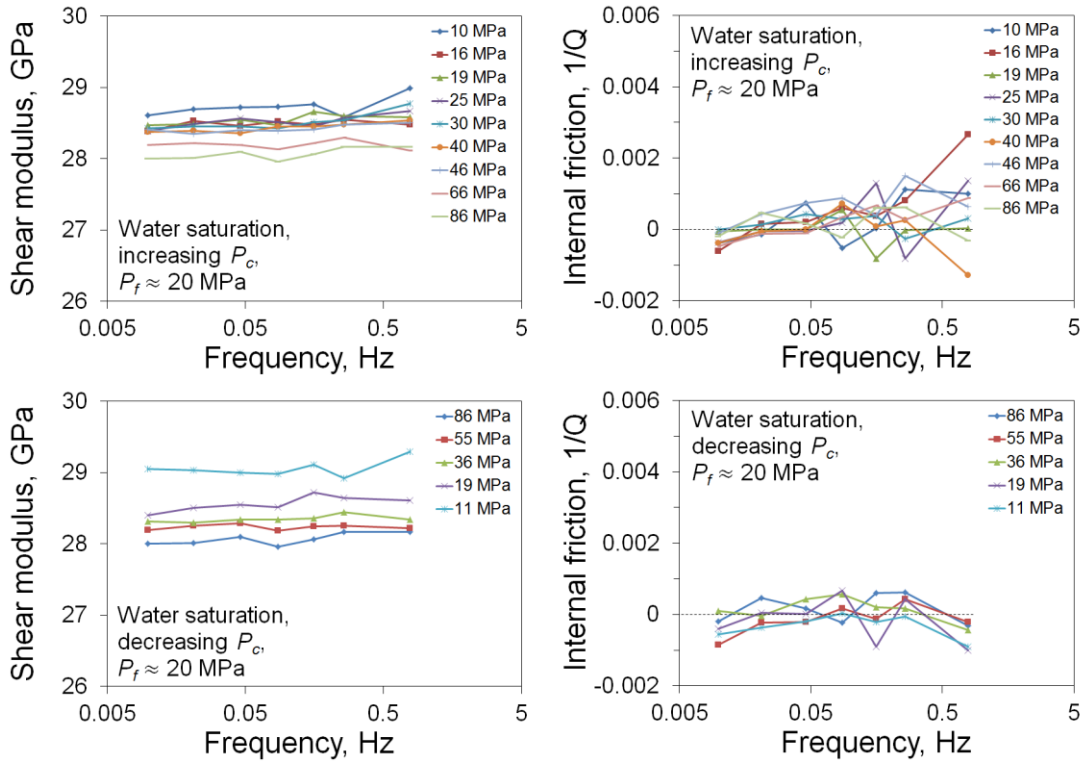


**Figure 5.2** The shear modulus of the soda-lime-silica glass-rod specimen (FDSL-1) measured at frequencies from ~ 0.01 Hz to ~ 0.78 Hz and different confining or differential pressures under dry, argon saturated, and water saturated conditions. The pressure shown is confining pressure in dry measurement, and differential pressure in argon and water saturated measurements. Numerical values are given in *Appendix J*.

In Fig. 5.3, the vertical error bars are associated with the uncertainties arising from the process of calibration, during which the conversion factor that relates the measured voltage to the displacement of transducer is estimated. The horizontal error bars are associated with the offset in the pore-pressure readings of the upstream and downstream reservoirs. In some cases with water saturation, apparently different fluid pressures were observed between the upstream and downstream reservoirs, which was partly caused by the drift of pore-pressure gauges and partly due to the extremely low water permeability of the cracked specimen under high differential pressures, hence less thorough pore-pressure equilibration between two reservoirs. The description of the origins of uncertainties in both modulus and pressure is applicable to all the other data presented in this chapter.

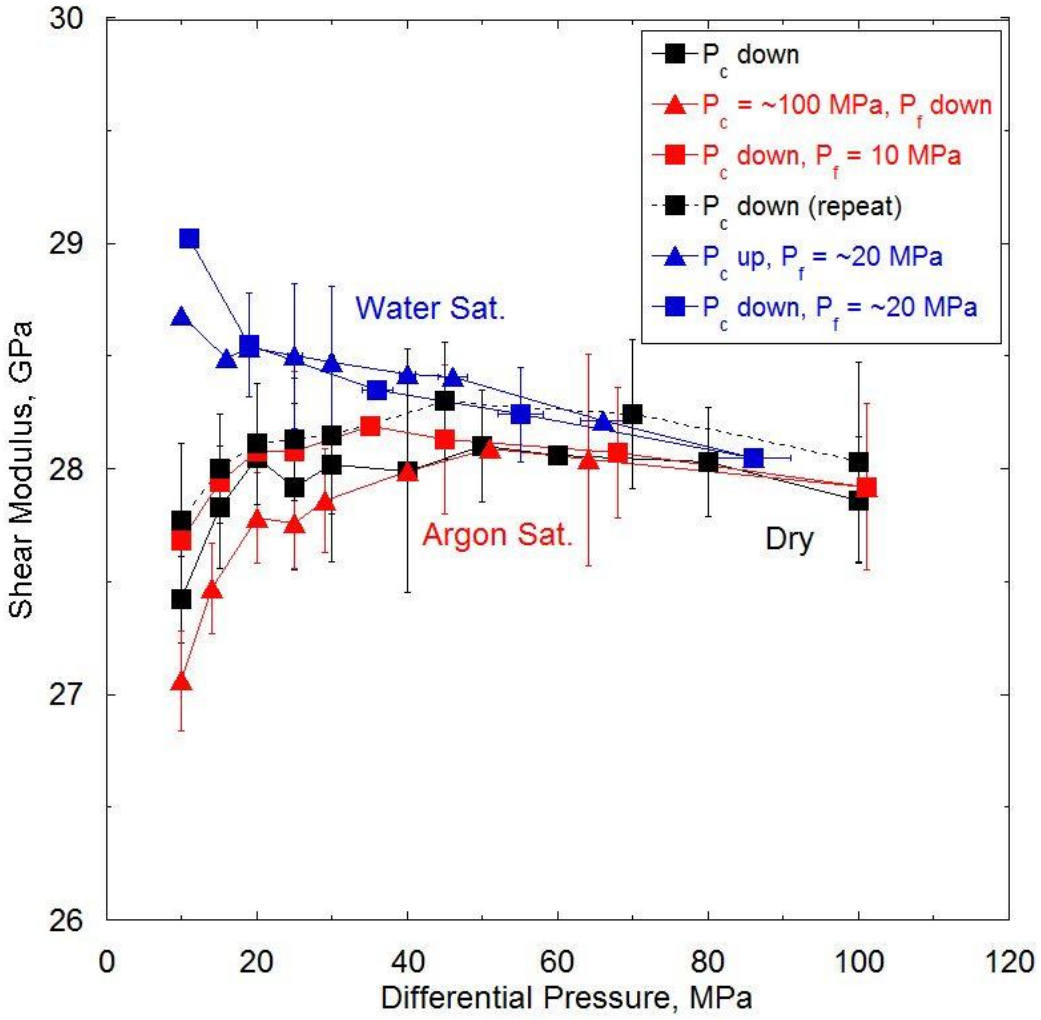


**Figure 5.3** The shear modulus of the cracked soda-lime-silica glass-rod specimen (FDSL-1) measured at different confining or differential pressures under dry, argon saturated, and water saturated conditions. The shear modulus shown here is the mean shear modulus averaged between 0.01 Hz – 0.26 Hz. Numerical values are given in *Appendix J*.

## 5.2 Low-frequency Elastic Moduli of Low-porosity Glass-bead Specimen

A compound low-porosity (~2%) glass-bead specimen (A-3-5) was tested in both torsional and flexural modes to yield shear and Young's moduli at different pressures successively under dry, argon-saturated, and water-saturated conditions. The composite glass-bead specimen has a total length of 150.125 $\pm$ 0.002 mm and an averaged diameter of 14.998 $\pm$ 0.001 mm. A composite control specimen comprising two fused silica cylinders was used, sandwiched between the same alumina connecting rods, as the elastic reference in a parallel experiment to take into account the interfacial effects at low differential pressures.

A weak frequency dependency of shear modulus is observed under all testing conditions, *i.e.*, dry, argon saturated, and water saturated conditions, with a higher shear modulus measured at a higher frequency (Fig. 5.4). At a given frequency, shear modulus is also noticed to be pressure dependent with a general increase in shear modulus with increasing confining or differential pressure. Low attenuation below 0.005 has been measured under all conditions, but noticeably higher than that of the glass-rod specimen, decreasing mildly with increasing frequency. The attenuation also shows pressure sensitivity at a given frequency, and a lower value of *1/Q*, in general, is observed at a higher pressure, *e.g.*, the lowest attenuation is observed at the highest differential pressure of 90 MPa with argon saturation.

As for the glass-rod specimen, the shear moduli collected at the first 6 frequencies from 0.01 Hz to 0.26 Hz, at a given pressure, are averaged and plotted against confining or differential pressures (Fig. 5.5). For dry condition, the shear modulus increases significantly with increasing pressure below 50 MPa and levels off beyond this pressure threshold. With argon saturation, the shear moduli are systematically higher than the dry moduli by as much as 1 GPa at $P_d$ = 10 MPa. Significant hysteresis is observed between the increasing and decreasing differential pressure cycles. Under water saturated condition, the shear modulus at the lowest differential pressure of ~ 10 MPa is comparable with that observed for argon saturation, whereas a marked increase in shear modulus is noticed beyond 10 MPa with water saturation.

The Young's modulus under dry condition increases with increasing pressure to 50 MPa, and thereafter decreases with increasing pressure until 100 MPa (Fig. 5.6). For argon saturation, significant stiffening is observed below 30 MPa before the Young's modulus approaches the dry values between 30 MPa and 50 MPa. The Young's modulus beyond 50 MPa becomes higher than the dry value again. For water saturation, the Young's modulus is systematically higher than those under dry and argon saturated conditions. For both argon and water saturated conditions, a decrease in Young's modulus with increasing differential pressure below 20 MPa is observed.

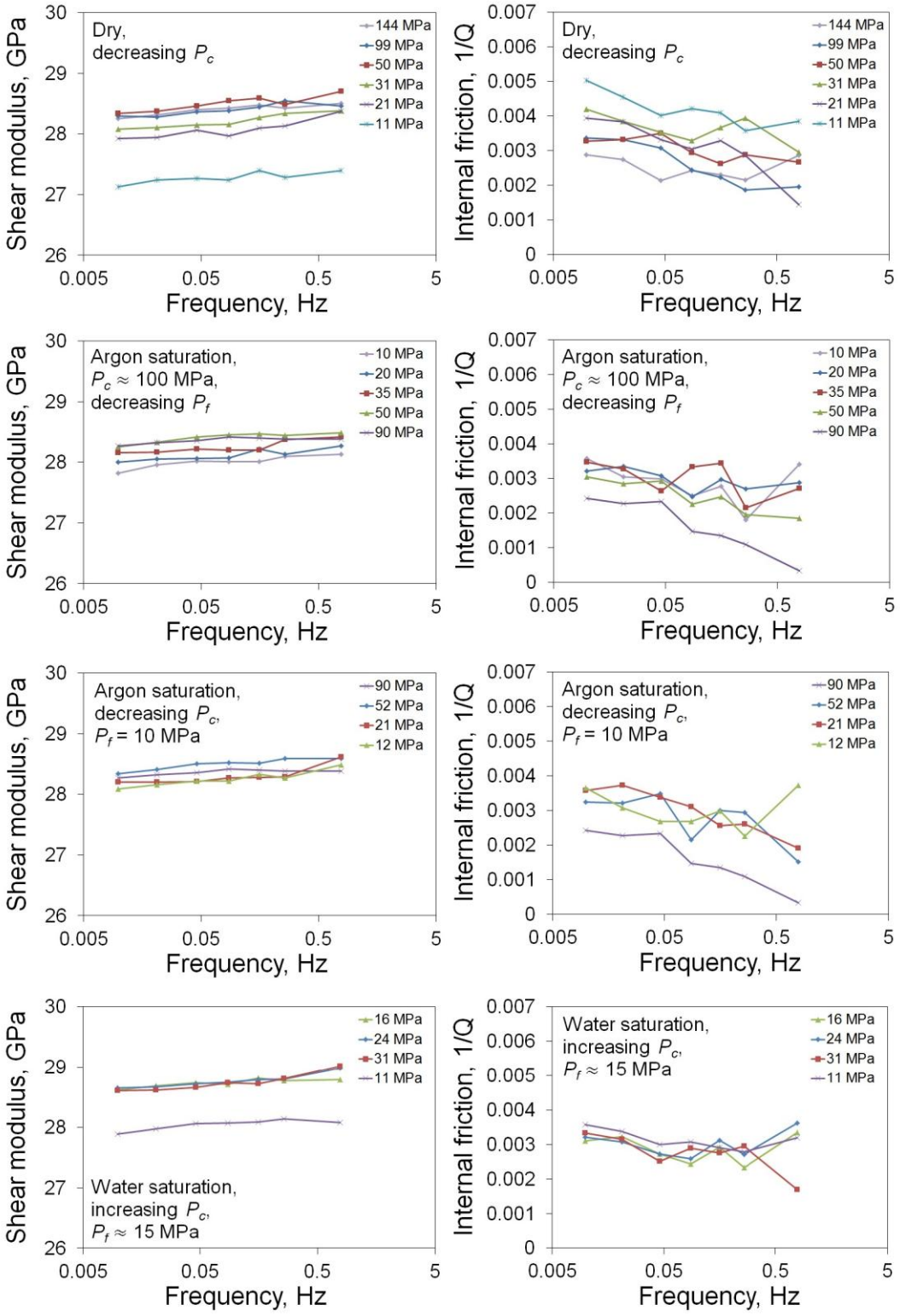


**Figure 5.4** The shear modulus of a compound low-porosity soda-lime-silica glass-bead specimen (A-3-5) measured at frequencies from ~ 0.01 Hz to ~ 0.78 Hz and different confining or differential pressures under dry, argon saturated, and water saturated conditions. The pressure shown is confining pressure in dry measurement, and differential pressure in argon and water saturated measurements. Numerical values are given in *Appendix J*.

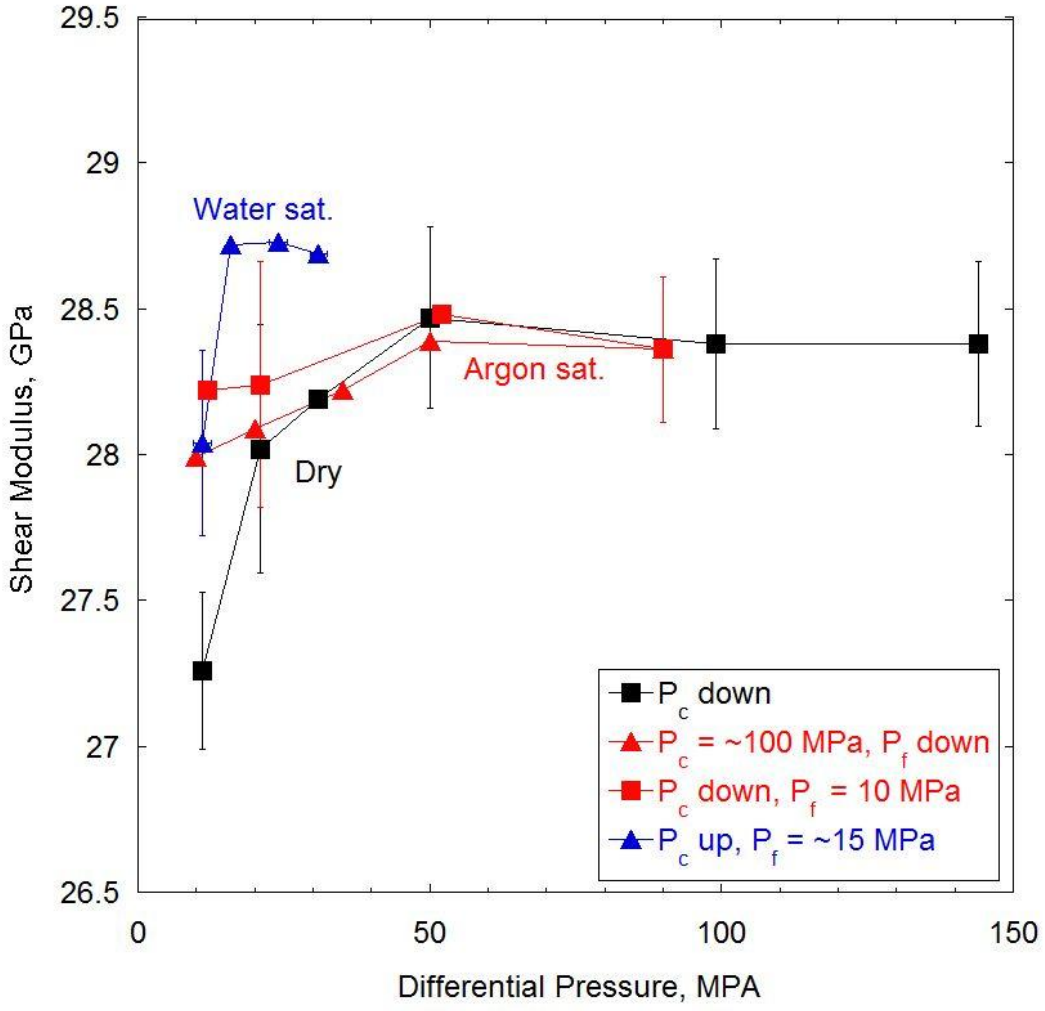


**Figure 5.5** The shear modulus of the cracked low-porosity soda-lime-silica glass-bead specimen (A-3-5) measured at different confining or differential pressures under dry, argon saturated, and water saturated conditions. The shear modulus shown here is the mean shear modulus averaged between 0.01 Hz – 0.26 Hz. Numerical values are given in *Appendix J*.

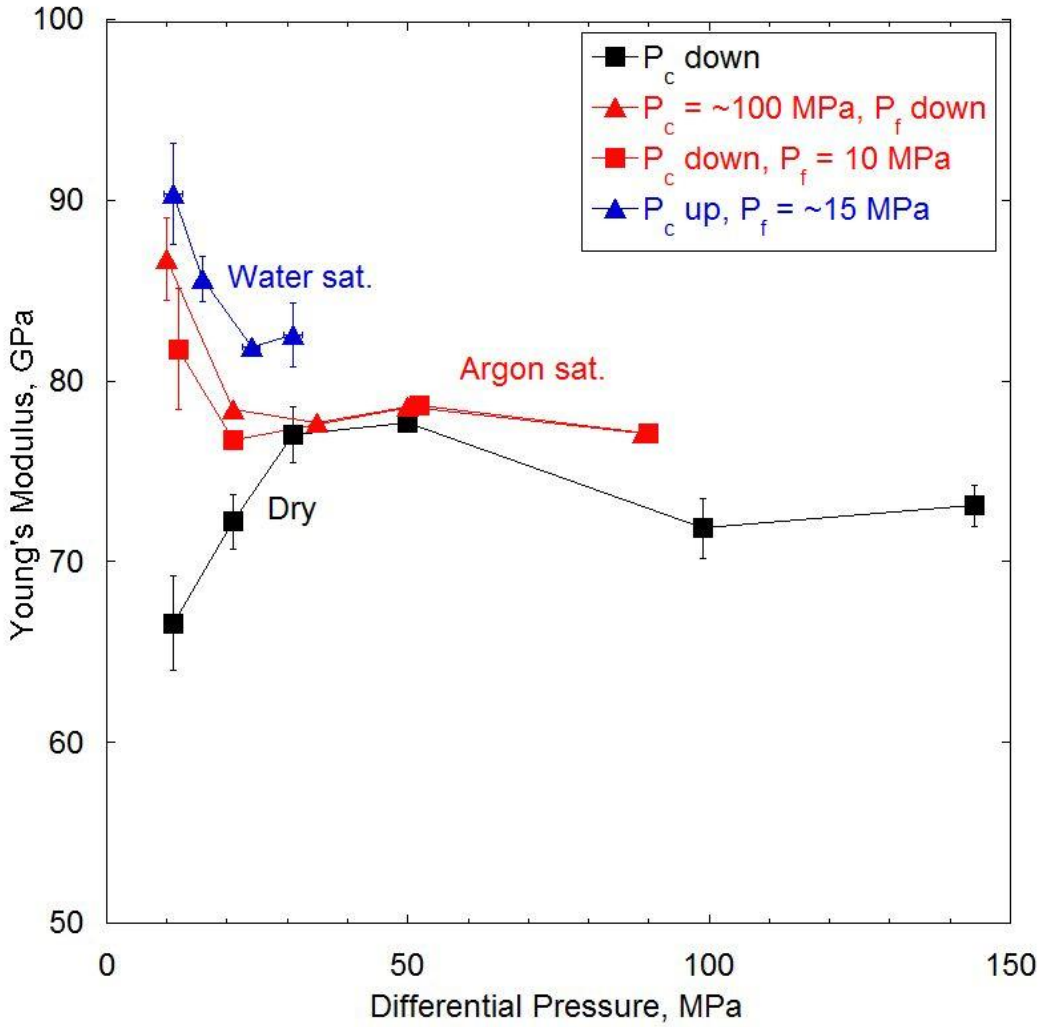


**Figure 5.6** The Young's modulus of the cracked low-porosity soda-lime-silica glass-bead specimen (A-3-5) measured at different confining or differential pressures under dry, argon saturated, and water saturated conditions. The Young's modulus shown here is the mean Young's modulus averaged between 0.01 Hz – 0.26 Hz. Numerical values are given in *Appendix J*.

## 5.3 Low-frequency Elastic Moduli of High-porosity Glass-bead Specimen

A compound cracked high-porosity (~5%) glass-bead specimen (YF – 1-3) was measured in both torsional and flexural modes to provide shear and Young's moduli at different pressures under dry, argon saturated, and water saturated conditions. The total length of the composite specimen is 150.052 $\pm$ 0.002 mm and the average diameter is 15.002 $\pm$ 0.001 mm. Forced oscillations in both torsional and flexural modes were performed before and after thermal cracking, and the results acquired on the uncracked specimen were used as control specimen to remove pressure dependent interfacial effects.

The shear moduli collected under all conditions are almost frequency independent between 0.01 Hz and 0.78 Hz (Fig. 5.7). Clear pressure sensitivity is observed at a given frequency under all conditions, with a higher shear modulus measured at a higher confining or differential pressure. Universally low attenuation of less than 0.005 is observed under all conditions, but the dissipation is consistently higher at the lowest differential pressures for dry and argon-saturated conditions. No obvious frequency dependence is noticed on the attenuation from 0.01 Hz to 0.26 Hz for all pressures under dry, argon saturated, and water saturated conditions. The data curves are still noticed to be somewhat scattered at 0.78 Hz.

The mean shear modulus is plotted as a function of pressure (Fig. 5.8). For dry measurement, the shear modulus increases with increasing pressure below ~ 50 MPa before levelling off until 100 MPa. With argon and water saturation, there is no systematic increase of the shear modulus relative to dry conditions, although there is a hint of hysteresis amongst the data for argon saturation.

The mean Young's modulus as a function of pressure is shown in Fig. 5.9. Under dry condition, the Young's modulus increases with pressure below 60 MPa. For argon saturation, the Young's modulus is systematically lower than the dry value for the entire pressure range except at the lowest pressure of 10 MPa. The Young's moduli measured with two pressure strategies with argon saturation, *i.e.*, fixed confining pressure with decreasing pore-fluid pressure and fixed pore-fluid pressure with decreasing confining pressure, show good reconciliation. With water saturation, the Young's modulus decreases with increasing pressure below ~ 20 MPa. The Young's modulus with water saturation intersects with the dry value at ~ 20 MPa, before levelling off until the highest pressure of ~ 80 MPa. Significant stiffening with water saturation has been noticed below the differential pressure of 20 MPa.

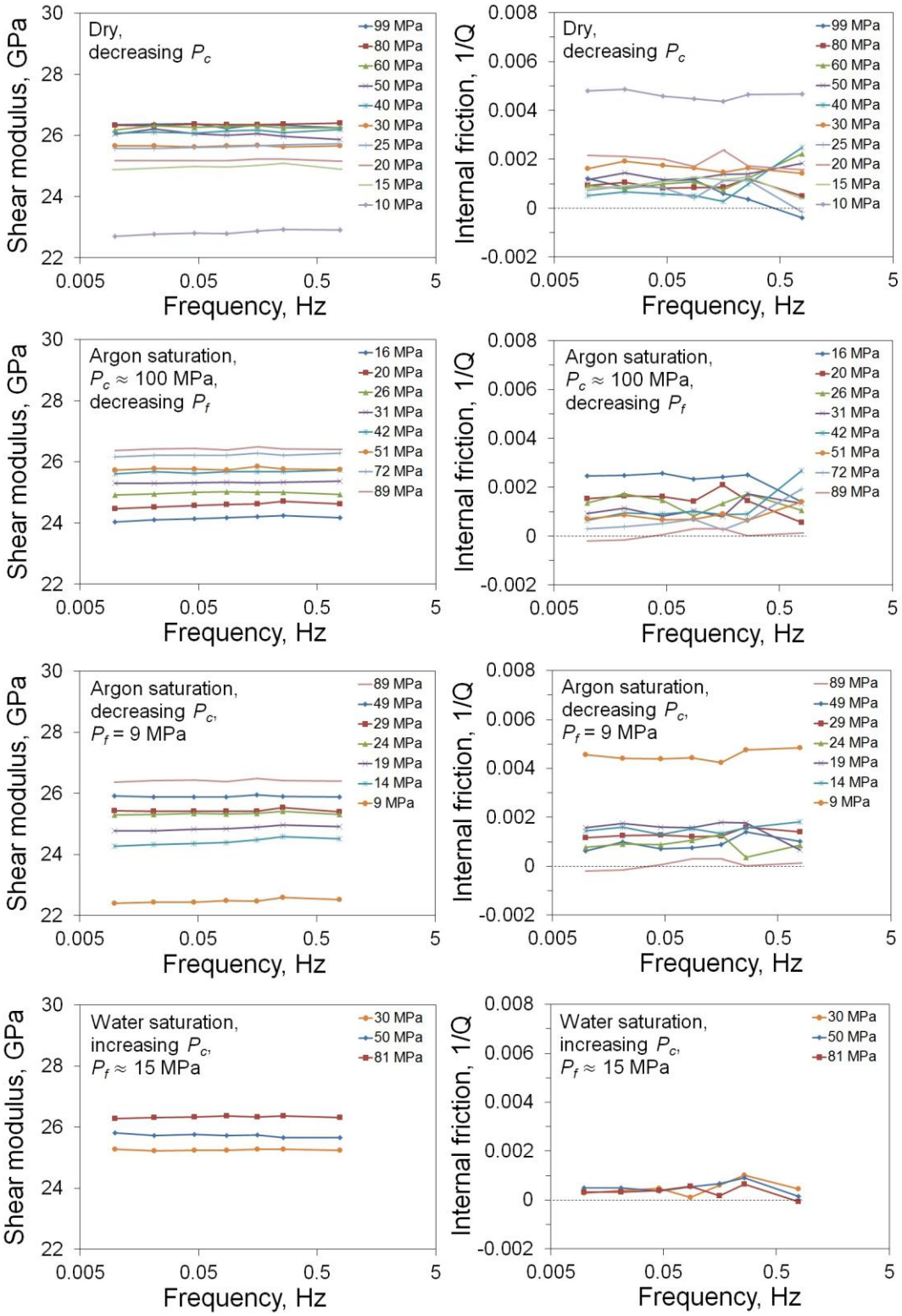
Dry,
decreasing $P_c$
99 MPa
80 MPa
60 MPa
50 MPa
40 MPa
30 MPa
25 MPa
20 MPa
15 MPa
10 MPa
Shear modulus, GPa
Internal friction, 1/Q
Frequency, Hz
Argon saturation,
$P_c \approx 100$ MPa,
decreasing $P_f$
16 MPa
20 MPa
26 MPa
31 MPa
42 MPa
51 MPa
72 MPa
89 MPa
Argon saturation,
decreasing $P_c$,
$P_f = 9$ MPa
89 MPa
49 MPa
29 MPa
24 MPa
19 MPa
14 MPa
9 MPa
Water saturation,
increasing $P_c$,
$P_f \approx 15$ MPa
30 MPa
50 MPa
81 MPa

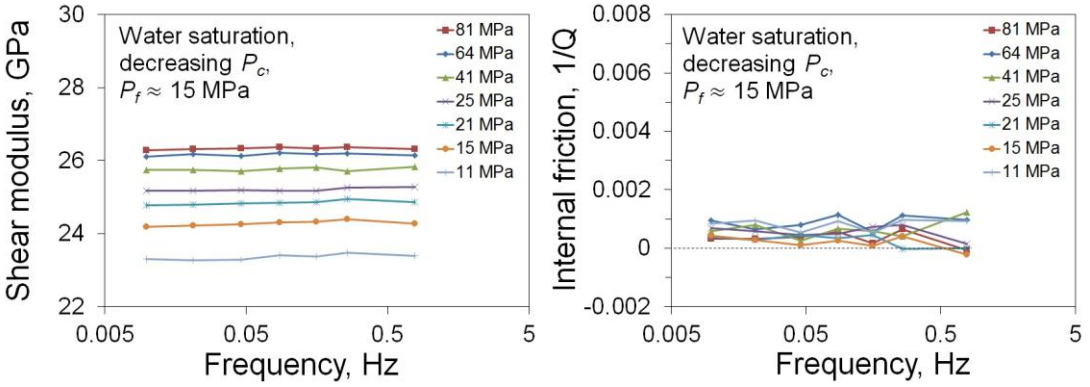


**Figure 5.7** The shear modulus of the composite high-porosity soda-lime-silica glass-bead specimen (YF-1-3) measured at frequencies from ~ 0.01 Hz to ~ 0.78 Hz and different confining or differential pressures under dry, argon saturated, and water saturated conditions. The pressure shown is confining pressure in dry measurement, and differential pressure in argon and water saturated measurements. Numerical values are given in *Appendix J*.

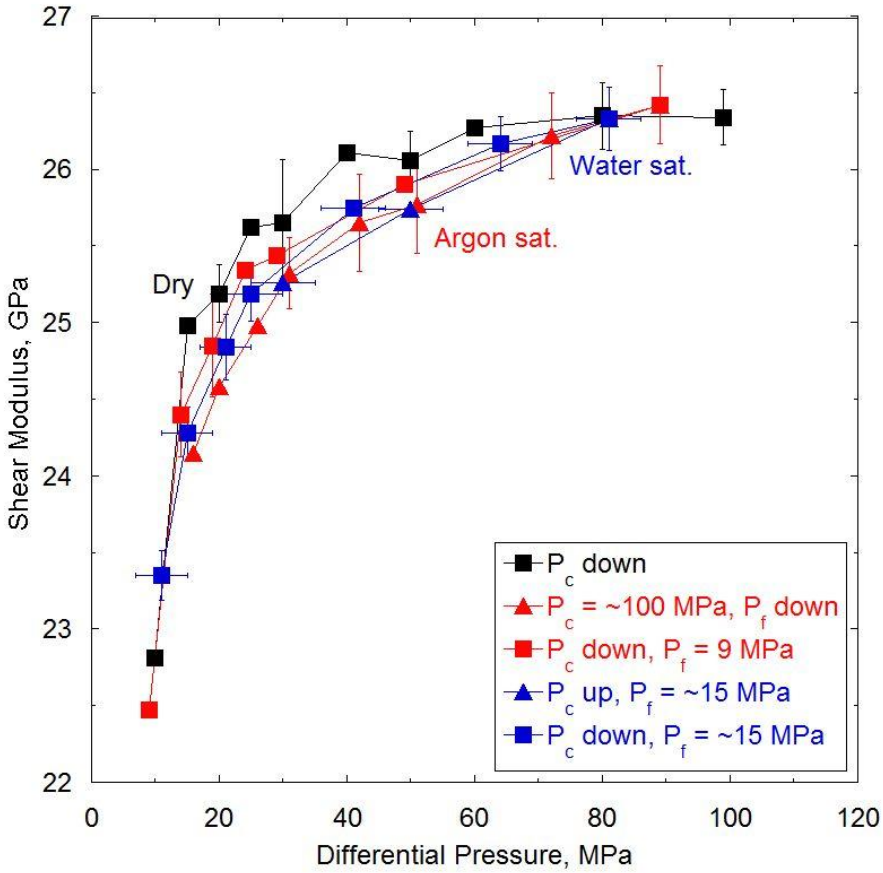


**Figure 5.8** The shear modulus of the cracked high-porosity soda-lime-silica glass-bead specimen (YF-1-3) measured at different confining or differential pressures under dry, argon saturated, and water saturated conditions. The shear modulus shown here is the mean shear modulus averaged between 0.01 Hz – 0.26 Hz. Numerical values are given in *Appendix J*.

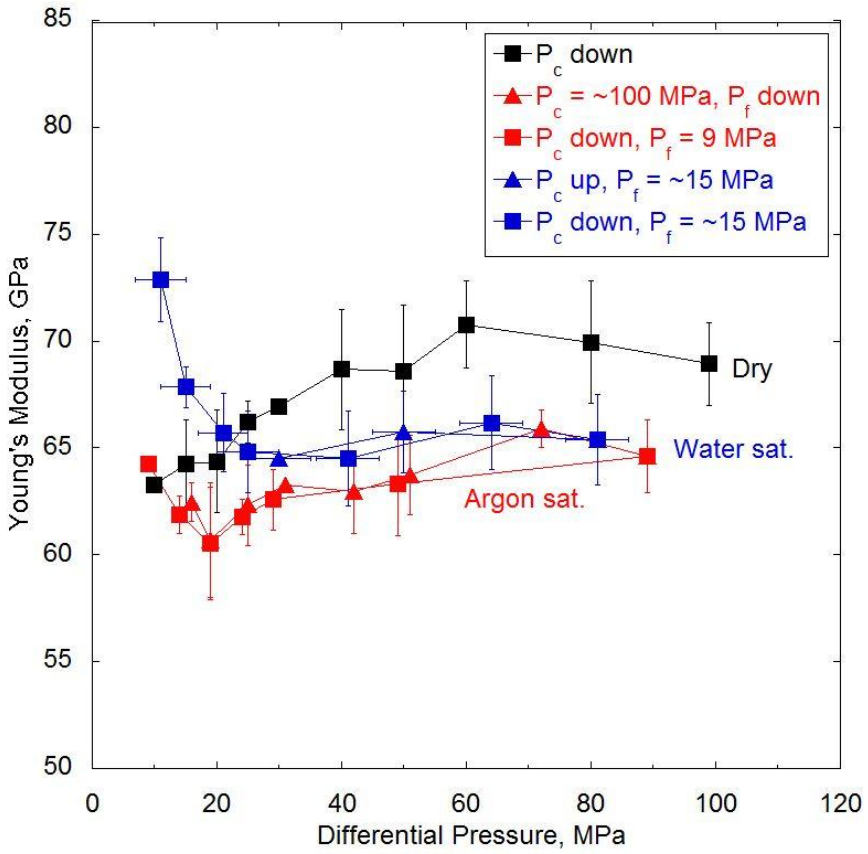


**Figure 5.9** The Young's modulus of the cracked high-porosity soda-lime-silica glass-bead specimen (YF-1-3) measured at different confining or differential pressures under dry, argon saturated, and water saturated conditions. The Young's modulus shown here is the mean Young's modulus averaged between 0.01 Hz – 0.26 Hz. Numerical values are given in *Appendix J*.

# Chapter 6 Mechanical Properties at Ultrasonic (MHz) Frequency

The mechanical properties of the three types of synthetic samples were also measured at ultrasonic (MHz) frequencies. The results reported in this chapter at ultrasonic frequency were collected at the University of Alberta, Canada. The details of this technique have been provided in *Section 3.3*.

For each type of synthetic sample, both P- and S-wave velocities were measured first on an uncracked specimen under dry condition, followed by measurements on a cracked specimen under dry, argon saturated, and water saturated conditions in sequence. The pore-fluid pressure of either argon or water was initially maintained at 10 MPa with varying confining pressure to achieve a series of differential pressures. In order to examine any sensitivity of the wave speeds and elastic moduli to the bulk modulus of the pore fluid, the pore-fluid pressure was then raised to 15 or 20 MPa (depending on the sealing condition) and a range of differential pressures was again achieved by varying the confining pressure. Each pressure adjustment was followed by adequate waiting time to allow a uniform distribution of pore fluid within the specimen before wavespeed measurement.

Eq. (3.71 – 3.73) are used then to convert the measured wavespeeds to (dynamic) shear and Young's moduli. In conversion, one also needs to know the bulk densities of dry and fluid-saturated samples. The bulk density of the dry sample at ambient conditions is directly calculated from its total mass and volume. The density of fluid-saturated sample $\rho$ is given by:

$$\rho = \rho_g(1-\phi) + \rho_f\phi = \rho_{dry} + \rho_f\phi\,, \tag{6.1}$$

where $\rho_g$ and $\rho_f$ are the grain density and fluid density, respectively; $\rho_{dry}$ is the dry bulk density of the sample; and $\phi$ is the total porosity of the sample. The argon density at the pore-pressure of 10 MPa and 20 MPa are 171.14 kg/m$^3$ and 353.27 kg/m$^3$, respectively (Gilgen *et al.*, 1994). The water density at ambient conditions is 998.21 kg/m$^3$.

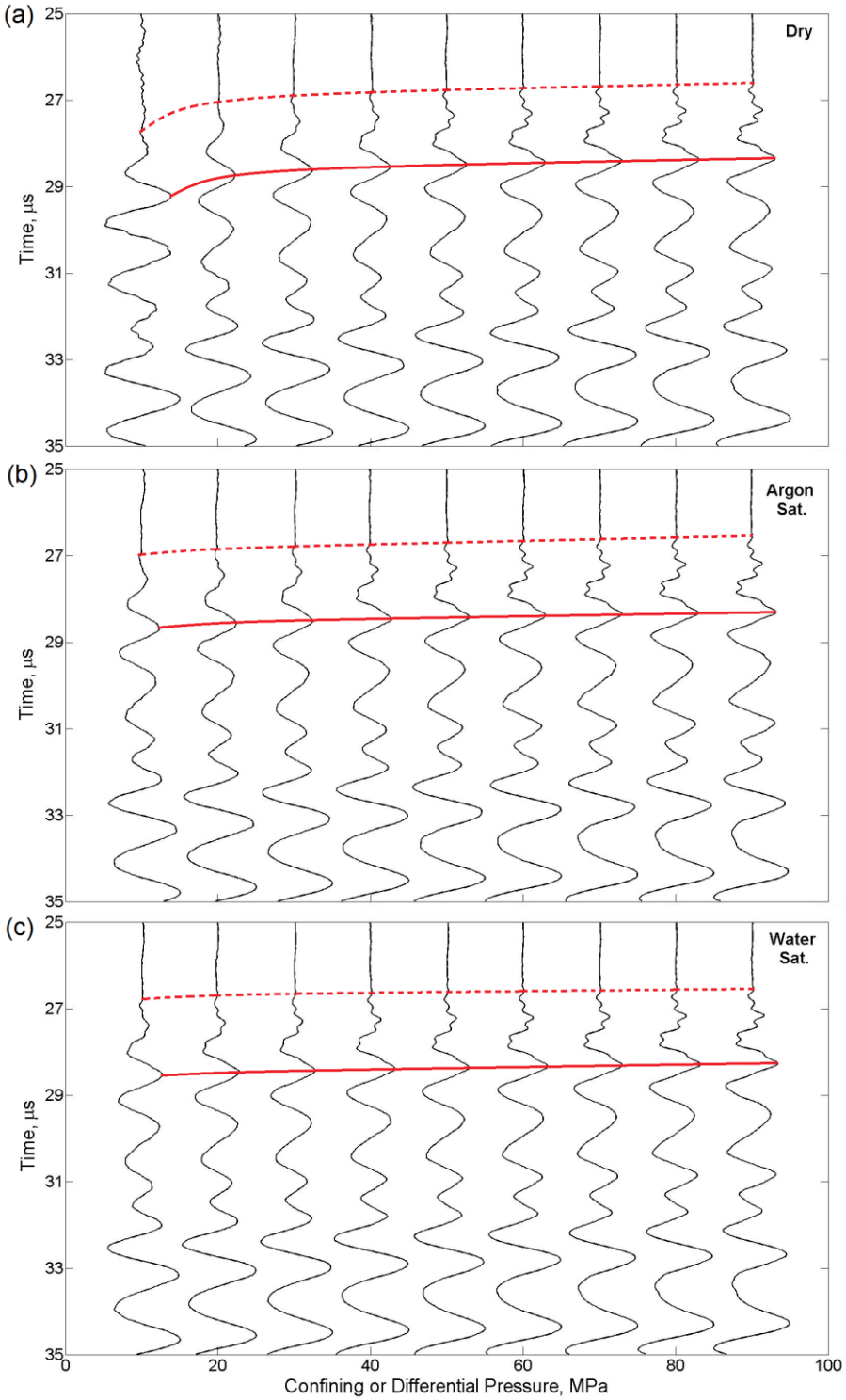


**Figure 6.1** An illustration of raw P-waveforms obtained on a cracked high-porosity glass-bead specimen (YF-1) at confining or differential pressures from 10 MPa to 90 MPa, under (a) dry, (b) argon saturated ($P_f$ = 10 MPa), and (c) water saturated ($P_f$ = 10 MPa) conditions in sequence. An obvious pressure dependence of the arrival time is noticed below 50 MPa under dry condition, which diminishes with fluid (either argon or water) saturation. The first arrival peak is sometimes broken, perhaps with superimposed higher frequency noise. Consequently, the second positive peak (red, solid) is consistently selected for the estimate of travel time rather than the first break (red, dashed).

The influence of fluid saturation is observed on the arrival times of P- and S-waves. An example of P-waveforms obtained on a high-porosity glass-bead specimen under dry, argon-, and water-saturated conditions (Fig. 6.1 a) demonstrates, under dry condition, an obvious pressure dependence of the arrival time, which however shows much less sensitivity to pressure when the specimen is saturated with argon or water (Fig. 6.1 b & c).

## 6.1 High-frequency Elastic Moduli of Glass-rod Specimen

An uncracked (FDS-3) and a cracked (FDS-2) glass-rod specimen were measured at ultrasonic frequency. The dimensions and weights of the samples are given in Table 2.3. The total porosity of FDS-2 is equal to the crack porosity on the cracked glass-rod specimen of $0.35 \pm 0.02\%$.

For the uncracked glass-rod specimen, the shear modulus and Young's modulus are ~ 31 GPa and ~ 75 GPa, respectively, and generally pressure independent for most of pressures below 100 MPa, except a minor pressure dependence observed below 20 MPa. The moduli measured in depressurisation match those obtained in pressurisation well (Fig. 6.2 a & c).

For the cracked glass-rod specimen, the shear and Young's moduli are significantly lower than their uncracked counterparts by ~ 3 GPa and ~ 6 GPa, respectively. A more significant pressure dependence of shear and Young's moduli is noticed below 20 MPa, increasing by ~ 3% from 10 MPa to 20 MPa. A much milder increase in moduli with pressure is observed beyond 20 MPa until 100 MPa. Hysteresis is noticed between the increasing and decreasing pressure cycles under dry condition and becomes more significant below 20 MPa.

For argon saturation, with argon pressure fixed at 10 MPa, the shear and Young's moduli are systematically higher than the dry moduli at pressures below 20 MPa and gradually approach the dry moduli with increasing differential pressure. With argon pore-fluid pressure kept at 20 MPa, the shear and Young's moduli are slightly higher than those measured with argon pressure fixed at 10 MPa, at the same differential pressure.

After being saturated with water, the shear and Young's moduli become even higher than those with argon saturation. Similarly, the moduli measured with 20 MPa in water pressure are slightly higher than those with 10 MPa in water pressure at the same differential pressure. With either argon or water saturation, moduli become less pressure dependent. The pressure sensitivity, which is observed below 20 MPa under dry condition, is absent under fluid-saturated conditions.

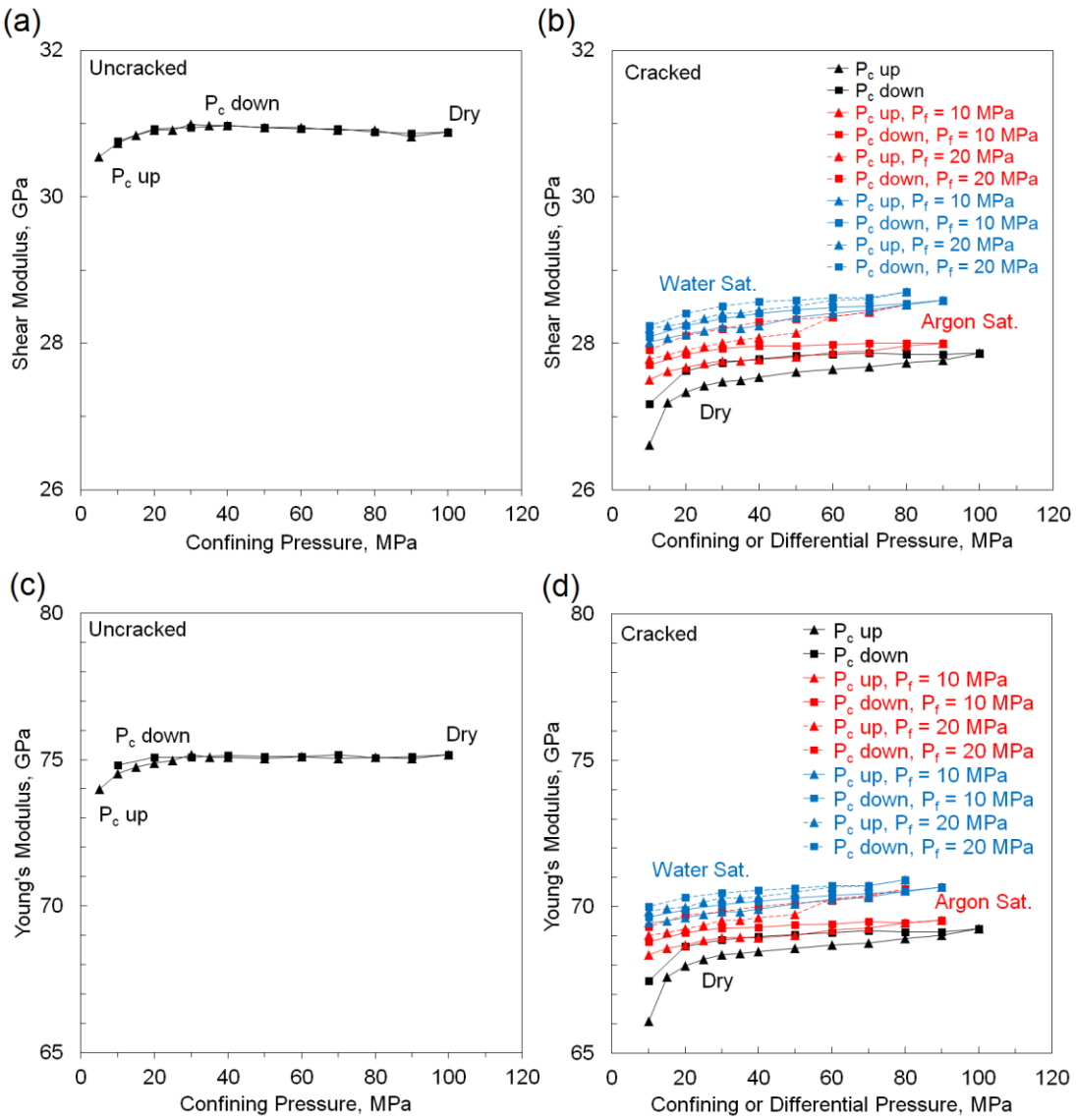


**Figure 6.2** The dry (a) shear and (c) Young's moduli of an uncracked glass-rod specimen. The (b) shear and (d) Young's moduli of a cracked glass-rod specimen obtained under dry (black), argon saturated (red) and water saturated (blue) conditions. The uncertainty associated with the determined moduli is about ± 0.5%. Numerical values are given in *Appendix K*.

## 6.2 High-frequency Elastic Moduli of Low-porosity Glass-bead Specimen

An uncracked (Y-2) and a cracked (A-5) low-porosity glass-bead specimen have been measured at ultrasonic frequency. The dimensions and weights of these samples are present in Table 2.3. The total porosity is equal to equant porosity of 3.2 ± 1.5% for the uncracked specimen. For the cracked specimen, the total porosity is 1.9 ± 0.7%, which consists of 1.8 ± 0.7% in equant porosity and 0.1% in crack porosity. The methods for estimating porosity are detailed in *Section 2.3*. The uncracked specimen was measured under dry condition. The

cracked specimen was measured under dry, argon saturated, and water saturated conditions in sequence.

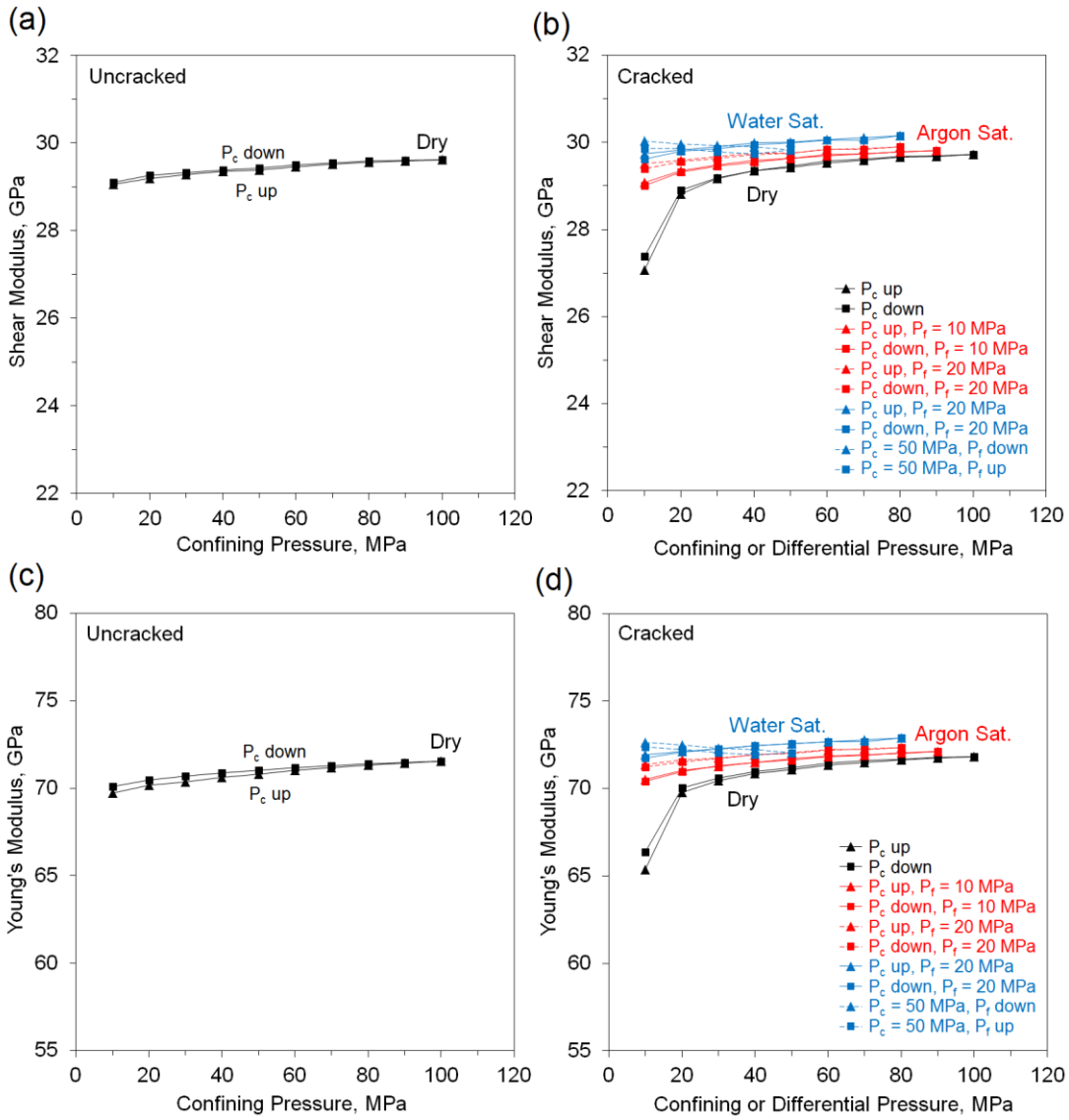


**Figure 6.3** The dry (a) shear and (c) Young's moduli of an uncracked low-porosity glass-bead specimen. The (b) shear and (d) Young's moduli of a cracked low-porosity glass-bead specimen under dry (black), argon saturated (red) and water saturated (blue) conditions. The uncertainty associated with the determined moduli is about ± 0.5%. Numerical values are given in *Appendix K*.

The moduli of the uncracked low-porosity glass-bead specimen are systematically lower than those of the uncracked glass-rod specimen, nicely illustrating the influence of porosity in weakening the matrix (Fig. 6.3 a & c). The shear and Young's moduli of the uncracked low-porosity glass-bead specimen show mildly increasing trends with increasing confining pressure. Minor hysteresis is noticed on the Young's modulus during the depressurisation, but no such hysteresis is observed on the shear modulus.

For the cracked specimen, the dry modulus increases significantly over the pressure range from 10 MPa to 50 MPa differential pressure but afterwards it increases slightly with pressure until 100 MPa differential pressure (Fig. 6.3 b & d).

With argon saturation, the pore-fluid pressure was initially kept at 10 MPa, and a series of differential pressures was achieved by varying the confining pressure. Under such a condition, the shear and Young's moduli are markedly higher than the dry moduli at pressures below 50 MPa and converge towards the dry moduli from 50 MPa to 100 MPa. At the second stage of argon saturation, the argon pore pressure was fixed at 20 MPa. The resultant shear and Young's moduli are systematically higher (by ~ 1%) than the values measured with 10 MPa in pore pressure at the same differential pressure.

With water saturation, the fluid pressure was maintained at 20 MPa during the first stage of measurements. The confining pressure was varied to cover the range of the desired differential pressures. During the second stage of water saturation, in contrast, the confining pressure was kept at 50 MPa throughout the entire measurements, with varying water pore pressure to achieve differential pressures from 10 MPa to 50 MPa. In general, the shear and Young's moduli with water saturation, for both strategies, are systematically higher than those measured with argon saturation by 1 – 2%. The modulus-differential pressure trends, obtained by two strategies, intersect at 50 MPa confining pressure and 20 MPa pore pressure. For differential pressures less than 30 MPa, the moduli measured with the second strategy, *i.e.*, fixed confining pressure of 50 MPa and pore pressures > 20 MPa, are higher than the values measured with the first strategy, *i.e.*, fixed pore-fluid pressure of 20 MPa. But the relationship is reversed beyond the differential pressure of 30 MPa with systematically higher moduli obtained with the strategy of fixed pore-fluid pressure of 20 MPa.

## 6.3 High-frequency Elastic Moduli of High-porosity Glass-bead Specimen

An uncracked (YF-4) and a cracked (YF-1) high-porosity glass-bead specimen were measured by ultrasonic wave propagation method. The dimensions and weights of the samples are listed in Table 2.3. The total porosity of uncracked specimen is equal to its equant porosity of 4.6 $\pm$ 1.2%. But for the cracked specimen, the total porosity, comprising both equant porosity of 5.4 $\pm$ 1.5% and crack porosity of 0.1%, is 5.5 $\pm$ 1.5%. As for the previous set of samples, the methods for determining porosity are detailed in *Section 2.3*.

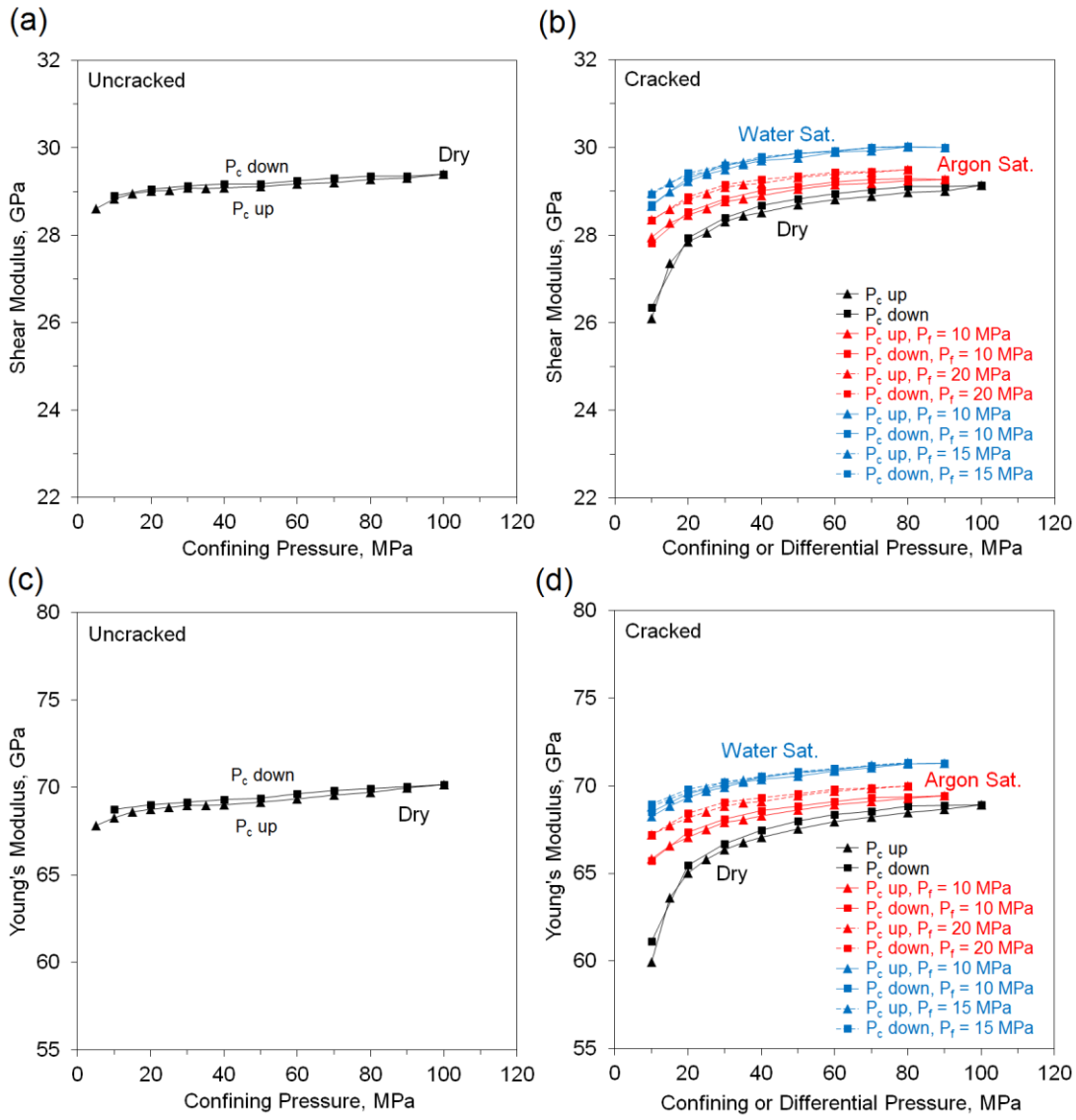


**Figure 6.4** The dry (a) shear and (c) Young's moduli of an uncracked high-porosity glass-bead specimen. The (b) shear and (d) Young's moduli of a cracked high-porosity glass-bead specimen under dry (black), argon saturated (red) and water saturated (blue) conditions. The uncertainty associated with the determined moduli is about ± 0.5%. Numerical values are given in *Appendix K*.

The shear modulus and Young's modulus of the uncracked specimen increase mildly with increasing pressure to 100 MPa (Fig. 6.4 a & c). For the cracked specimen, compared with the uncracked values, the shear moduli are reduced by about 2 GPa at 10 MPa and 0.3 GPa at 100 MPa, respectively. The Young's moduli are reduced by about 8 GPa at 10 MPa and 1 GPa at 100 MPa, respectively. Similar to the observations for the cracked low-porosity glass-bead specimen, a significant increase in modulus with increasing pressure is also noticed on the cracked high-porosity glass-bead specimen below 50 MPa. The increase in moduli with pressure becomes modest beyond 50 MPa until 100 MPa (Fig. 6.4 b & d).

The moduli become systematically higher when the specimen is saturated with argon. Marked stiffening is noticed at differential pressures lower than 50 MPa with argon saturation, and the shear and Young's moduli gradually approach the dry moduli beyond 50 MPa. The argon-saturation experiments also consist of two stages, with argon pore pressure fixed at 10 MPa and 20 MPa, respectively. At the same differential pressure, the moduli obtained at the pore-fluid pressure of 20 MPa are higher than those obtained at the pore-fluid pressure of 10 MPa.

With water saturation, the moduli become even higher than those measured with argon saturation. The water pressure was initially kept at 10 MPa. Due to the sealing condition of the water pump used in experiment, a water pore-fluid pressure of 15 MPa was used instead of 20 MPa in the second phase of the water-saturation experiments. The comparison still shows noticeably higher moduli obtained with water pressure of 15 MPa than those acquired with 10 MPa below 20 MPa in differential pressure. But beyond the differential pressure of 20 MPa, the moduli obtained by two strategies of water saturation are consistent.

## 6.4 Strain Measurement and Uncertainty Analysis

Strain gauges were glued on specimens to estimate the amount of pressure-induced shortening and to provide a measure of the zero frequency moduli for additional comparison to the low frequency tests. Valid signals were not consistently obtained from the strain gauges for two main reasons: 1) inadequate coupling between the strain gauge and the specimen; (2) disruption of the electrical connection between leads and the strain gauge during the re-sealing process. The strain measurements were conducted on all three types of synthetic samples, but with incomplete results. For a cracked glass-rod specimen (FDS-2), both the axial and tangential strains were successfully obtained (Fig. 6.5 a). On an uncracked low-porosity glass-bead specimen (Y-2), the axial strain was obtained during pressurisation (Fig. 6.5 b). Similarly, only the axial strain was measured on a cracked high-porosity glass-bead specimen (YF-2, Fig. 6.5 c).

The measurements indicate axial and circumferential strains of 0.07 - 0.09% over the pressure range of 10 to 100 MPa for both cracked and uncracked specimens in either axial or circumferential mode. For the cracked specimens, there is an additional axial strain of 0.03 – 0.06% below 10 MPa. But such anomalously large contribution to the total strain is absent circumferentially below 10 MPa on the cracked glass-rod specimen. The total axial strain at the highest confining pressure of 100 MPa is on the order of 0.1% for all these synthetic samples. The length of the specimen is assumed to be constant as that measured at ambient conditions during the calculation of wavespeeds with measured P- and S-wave travel times. The determined wavespeeds are therefore systematically overestimated by the amount as

much as about ± 6 m/s and ± 3 m/s for the P- and S-wave velocities, respectively, at 100 MPa, which are gradually reduced with decreasing confining pressure.

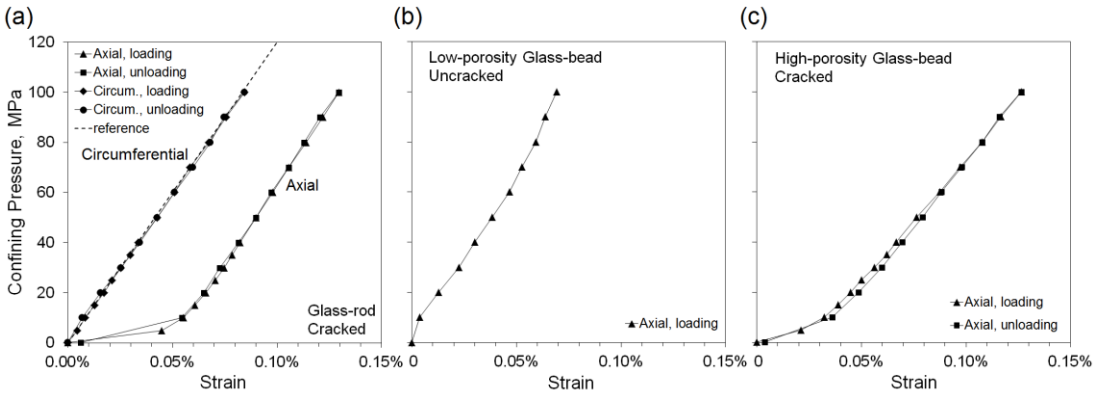


**Figure 6.5** (a) The axial and circumferential strains measured on a cracked glass-rod specimen at different confining pressures, compared with the reference of pure glass with 40 GPa bulk modulus; (b) the axial strain on an uncracked low-porosity glass-bead specimen; and (c) the axial strain on a cracked high-porosity glass-bead specimen. Numerical values are given in *Appendix L*.

Besides the sample shortening, another source of uncertainty arises from the estimate of the density of a fluid-saturated sample. The space occupied by pore fluid varies with pressure, therefore, it is difficult to determine the precise amount of fluid within the specimen at a given pressure and changes in fluid properties, hence the density of the fluid-saturated sample. The uncertainty in density may propagate into the shear and Young's moduli during the conversion from the measured P- and S-wave velocities.

# Chapter 7 Exploratory Measurements on Mechanical Properties at Intermediate (kHz) Frequency

Mechanical properties of synthetic samples at intermediate frequencies (kHz) have been determined by a resonance method. This set of measurements was conducted using the Split Hopkinson resonant bar in the Lawrence Berkeley National Laboratory, USA.

The diameter of samples, tested on either the Attenuation Apparatus at mHz-Hz or the instrument for ultrasonic wave propagation at MHz, is 15 mm. However, larger sample diameter of 38.1 mm is required for the Split Hopkinson resonant bar.

An exploratory set of measurements, the first ever made on synthetic samples, were performed on glass-rod specimens only. The raw soda-lime-silica glass rods were, like those tested on the Attenuation Apparatus at mHz-Hz frequencies, supplied by the Glass Workshop at the Australian National University, and precision ground into cylinders of 76.20 mm in length and 38.10 mm in diameter. A pair of the large-dimension glass rods was prepared and one of them was later thermally cracked. The uncracked glass-rod specimen was measured under dry condition and the cracked one was tested, in sequence, under dry, nitrogen saturated, and water saturated condition.

The bulk modulus and viscosity of pore fluid are expected to influence the fluid-flow behaviour, hence the mechanical response of the fluid saturated specimen to a sinusoidally varying stress. The pore pressure of nitrogen on a cracked glass-rod specimen was kept at 3.1 MPa. The bulk modulus and viscosity of nitrogen need to be compared with those of argon at the same pore pressure of 3.1 MPa before analysing the difference in the mechanical responses of fluid-saturated rocks. The pressure dependent bulk modulus of nitrogen is calculated from the density (Pieperbeck *et al.*, 1991) and speed of sound (Costa Gomes & Trusler, 1998) as functions of pressure. The pressure dependent viscosity is given by Kestin & Leidenfrost (1959). The bulk modulus and viscosity of nitrogen at 3.1 MPa are 4.6 MPa and 18.1 μPa·s, respectively, compared with 3.0 MPa (Stewart & Jacobsen, 1989) and 25.9 μPa·s (Vidal *et al.*, 1979) for argon at the same pressure. Therefore, nitrogen is slightly less compressible and less viscous than argon at 3.1 MPa at room temperature.

The resonance measurements were first performed on an uncracked glass-rod specimen (FDL-1). It was a dry test with the confining pressure increased from 0.3 MPa to 24.0 MPa and decreased back to 0.6 MPa.

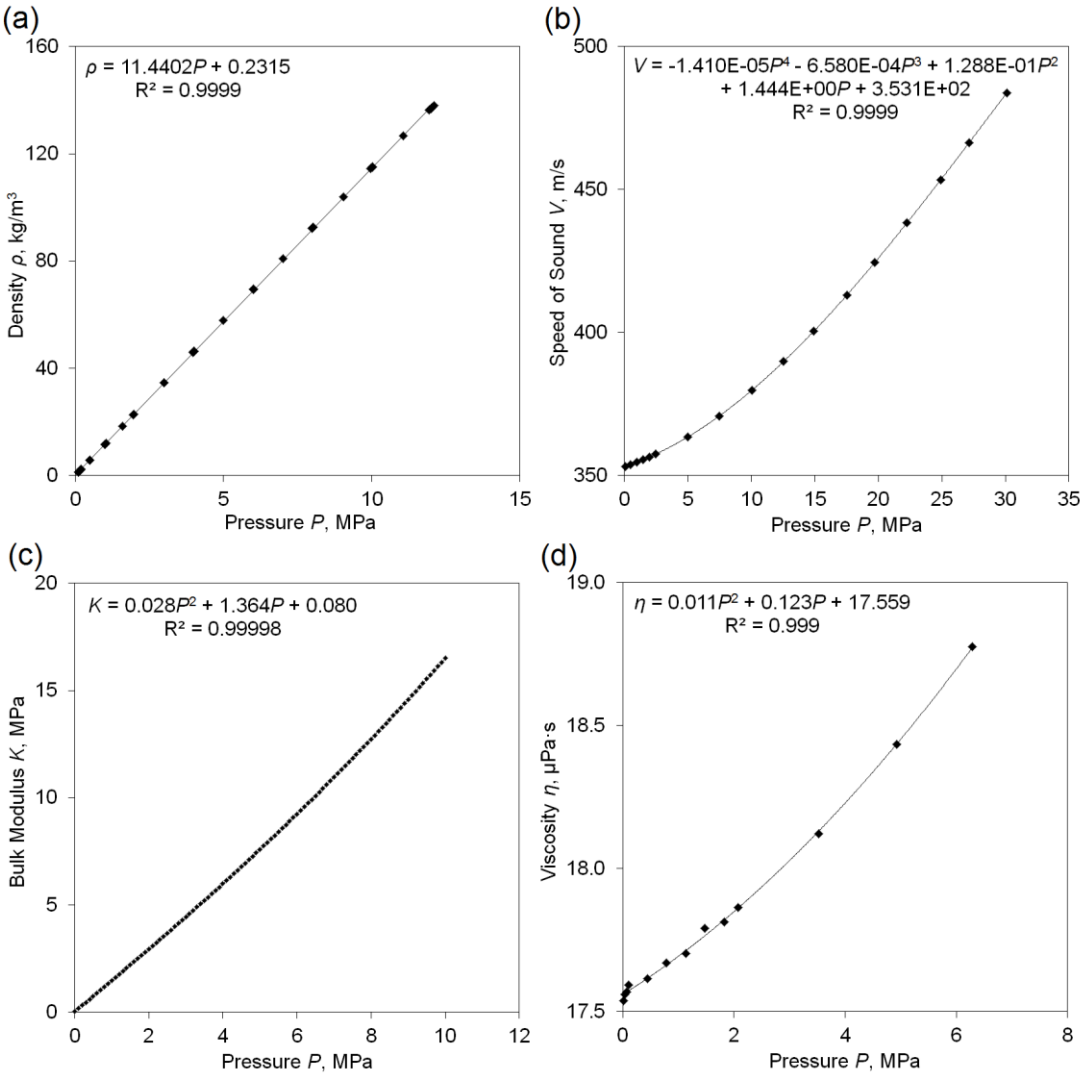


**Figure 7.1** Pressure dependent properties of nitrogen at room temperature (293-300 K): (a) density (Pieperbeck *et al.*, 1991); (b) Speed of sound (Costa Gomes & Trusler, 1998); (c) bulk modulus calculated from density and speed of sound; (d) viscosity (Kestin & Leidenfrost, 1959).

A significant increase in shear modulus with increasing pressure is observed below 10 MPa and a similar increase in Young's modulus is also noticed below 15 MPa. For the uncracked sample, this pressure dependence of moduli presumably reflects compliance in coupling between the stainless steel extension bars and the sample. The moduli become pressure independent beyond these pressure thresholds as expected for good coupling. Hysteresis is observed on both shear and Young's moduli during pressure cycling. The shear attenuation maintains a low level of ~ 0.002 except for minor pressure dependence noticed at the lowest pressures. However, for the extensional attenuation, considerable amount of attenuation is observed below 15 MPa, possibly caused by interfacial coupling between the

extension bars and specimen at low pressure, and the value becomes pressure independent and is reduced to below 0.002 beyond 15 MPa.

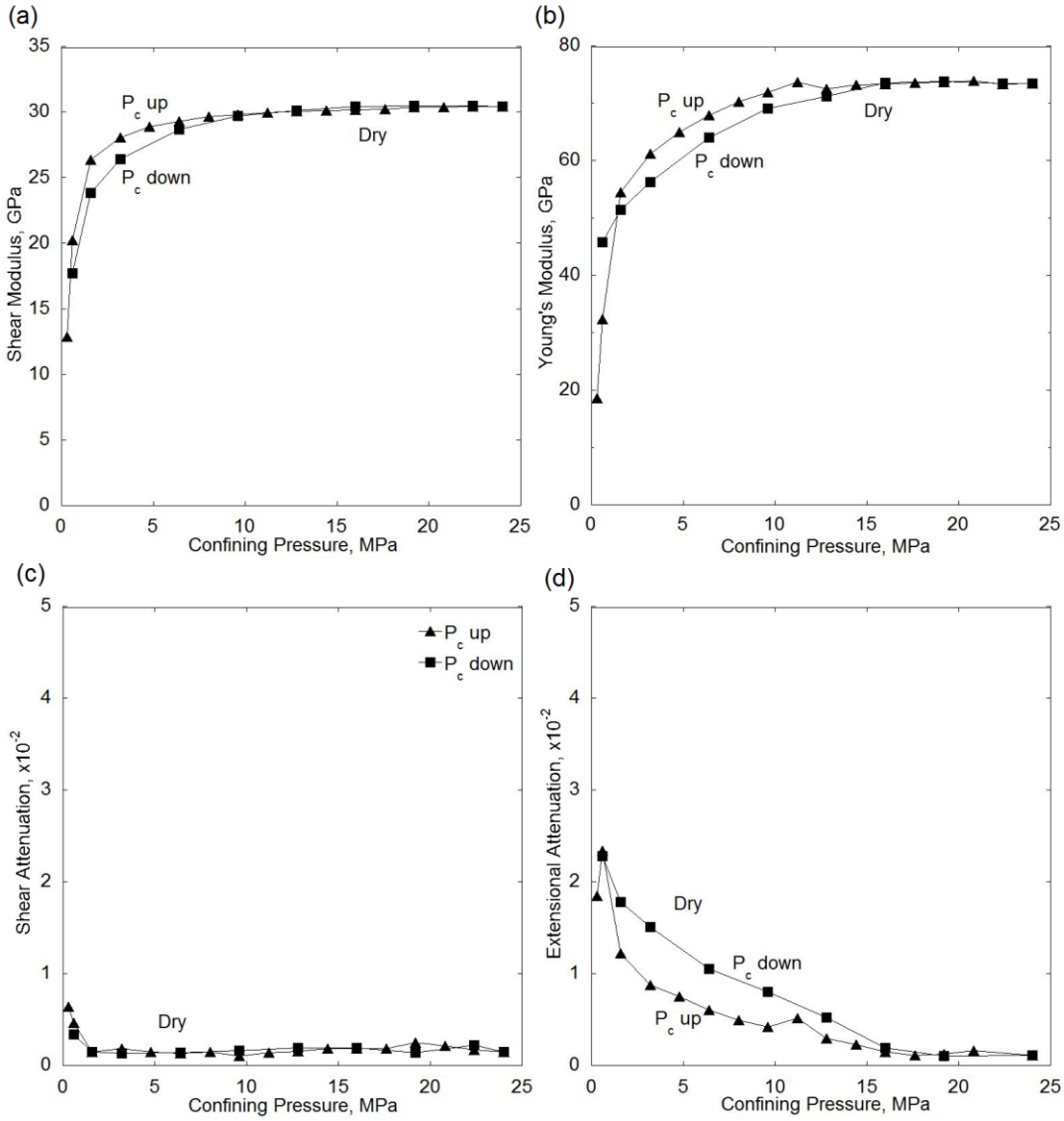


**Figure 7.2** Mechanical properties of an uncracked glass-rod specimen (FDL-1) measured at intermediate frequencies: (a) shear modulus ($\pm$ 1%) and (c) shear attenuation $1/2Q_G$; (b) Young's modulus ($\pm$ 1%) and (d) extensional attenuation $1/2Q_E$. Numerical values are given in *Appendix M*.

The measurements on the uncracked glass-rod sample provide important information concerning the amount and pressure range of the interfacial effect, which is used in the following measurements on the cracked glass-rod sample to exclude the interfacial effect from the measured moduli.

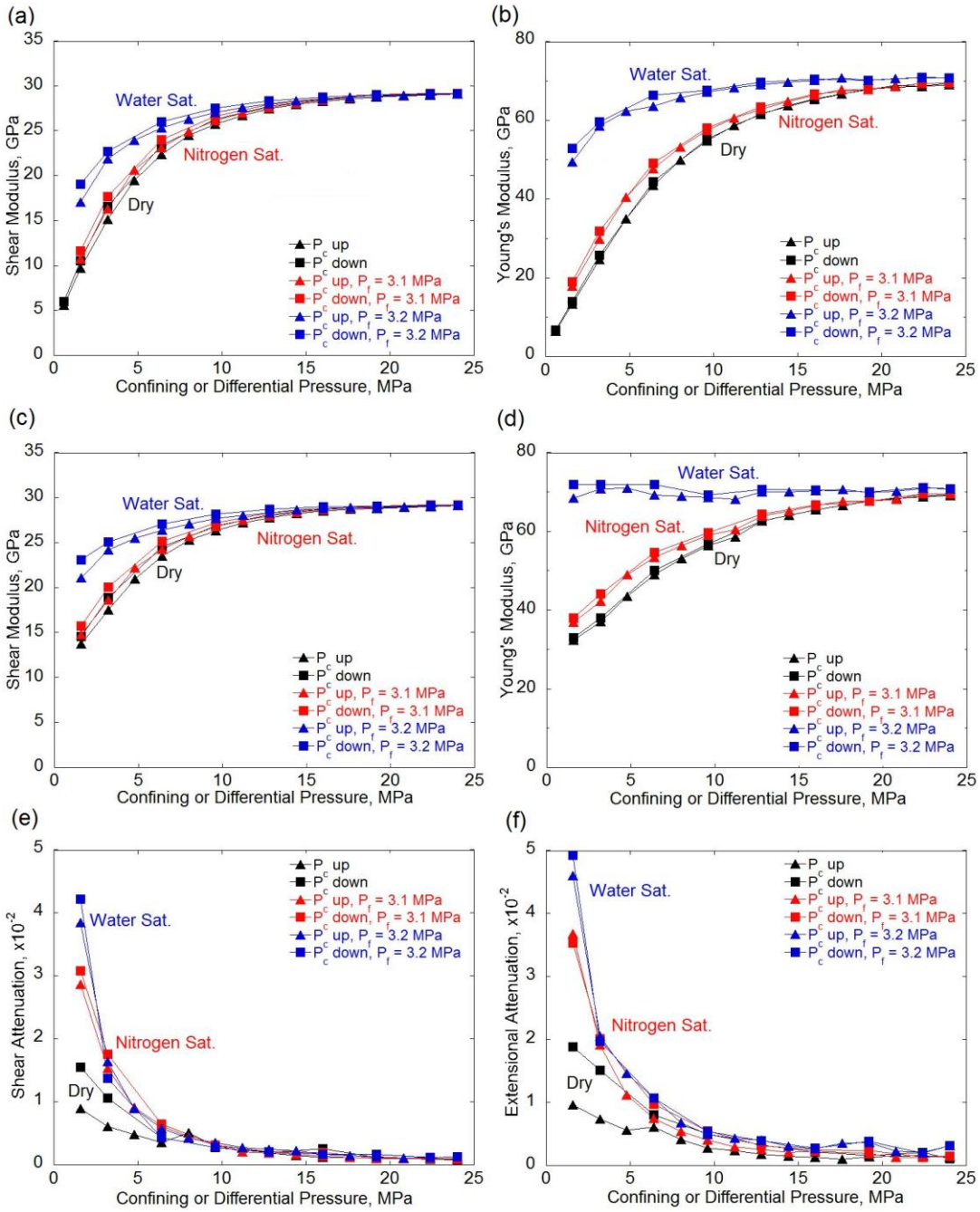


**Figure 7.3** (a) Shear modulus (± 1%), (b) Young's modulus (± 1%), (c) shear modulus corrected for interfacial compliance (± 1%), (d) Young's modulus corrected for interfacial compliance (± 1%), (e) shear attenuation, and (f) extensional attenuation of a cracked glass-rod specimen (FDL-2) measured at kHz by the Split Hopkinson resonant bar, under dry, nitrogen saturated, and water saturated condition in sequence. Numerical values are given in *Appendix M*.

Measurements have also been conducted on a cracked glass-rod specimen (FDL-2). The magnitude of the pressure-dependent interfacial effect is determined on the uncracked specimen as the modulus deficit with respect to the constant modulus observed beyond the pressure threshold in loading cycle (Fig. 7.2 a & b) and applicable to the cracked specimen.

Assuming reproducibility of the interfacial conditions, the interfacial effect is then subtracted from the measured shear and Young's moduli at a corresponding pressure on the cracked specimen (Fig. 7.3 a & b) to yield the "interface-adjusted" shear and Young's moduli (Fig. 7.3 c & d).

For the shear modulus of the cracked specimen, pressure dependence is noticed below 15 MPa with an increase in shear modulus with increasing pressure, and the trend levels off beyond 15 MPa. Modest stiffening is observed with nitrogen saturation. Due to minor hysteresis during pressure cycling, the nitrogen saturated shear modulus is compared with the dry modulus in the same pressure cycle, *i.e.*, either the up or the down cycle in differential pressure. The nitrogen saturated shear modulus reaches the dry modulus at higher pressures. With water saturation, the shear modulus shows a marked increase at pressures below 15 MPa and reaches the dry modulus at pressures beyond 15 MPa. For shear attenuation, relatively high values are observed below 10 MPa. The shear attenuation with water saturation is systematically higher than that with nitrogen saturation, and in turn higher than the dry attenuation.

For Young's modulus, a marked increase in modulus with increasing pressure is observed under both dry and nitrogen saturated conditions. In contrast, for water-saturated condition, the Young's modulus becomes almost independent of pressure for the entire pressure range. In terms of the amount of stiffening with fluid saturation, a modest increase in Young's modulus is observed with nitrogen saturation and a huge increase with water saturation. The extensional attenuation shows relatively high values below 10 MPa. The attenuation with water saturation systematically shows higher values than that with nitrogen saturation, and further higher than the values under dry condition. Beyond 10 MPa, the extensional attenuation shows consistently low values of 0.001 – 0.005 under all conditions.

# Chapter 8 Discussion

In this chapter, all the results present in preceding *Chapters 4* to *7* will be summarised and analysed. In *Section 8.1*, a micromechanical model to be used in this discussion is briefly reviewed. The pressure dependence of hydraulic and mechanical properties on the cracked synthetic samples is interpreted in terms of the crack/pore microstructure in *Section 8.2*. The micromechanical model will provide an insight into the crack aspect ratio distribution of each sample, inverted from the observed pressure-dependent ultrasonic wavespeeds. In *Section 8.3*, the discussion focuses on the influence of fluid saturation on mechanical properties of samples. The possible mechanisms to give stiffening or weakening of rocks with fluid saturation encountered in each set of measurements are discussed in *Section 8.3.1*. Accompanied by estimated characteristic frequencies in *Section 8.3.2*, a given fluid flow regime is attributed for each set of measurements in *Section 8.3.3*. The Gassmann equation and the micromechanical model are used to simulate the saturated isobaric and the saturated isolated behaviours, respectively. In *Section 8.3.4*, on each sample, the measurements at various frequencies are compared to provide dispersion. The amount of dispersion and the influences of fluid viscosity and microstructure on dispersion are also discussed. Finally, in *Section 8.3.5*, a brief discussion is given to the measured attenuation at seismic and intermediate frequencies.

## 8.1 Brief Review of Relevant Theory – A Micromechanical Model

The major theoretical methods of estimating the influence of fluid saturation on mechanical properties have been briefly surveyed in *Section 1.2*. The micromechanical model (David & Zimmerman, 2012) to be used in this chapter will be described first. This model belongs to the broad category of inclusion-based models, with specified geometries of inclusions but with no fluid communication. The nature of this model makes it appropriate for the saturated isolated regime.

The presence of pores and cracks softens the rock matrix, giving lower moduli relative to those of the fully dense solid. The modulus deficit and its pressure dependence, with proper assumptions, provide insight into the quantity and geometry of inclusions embedded in a solid. This micromechanical model allows inference of the microstructure of a specimen from its modulus deficit relative to that of the uncracked matrix. It is recalled that one of the major goals of this experimental study is to address the influence of microstructure on dispersion. To this end, it is desirable to use a model with specified inclusion geometries. The outcome of the inversion will be presented in *Section 8.2*. With the inferred microstructure, in a forward modelling exercise, the moduli of fluid-saturated medium are predictable from its dry modulus and the fluid properties. The modelled moduli will be compared with relevant observations in *Section 8.3*.

David & Zimmerman (2011) and David (2012) derive explicit expressions for the hydrostatic compliance (or compressibility) $P_u$ and shear compliance $Q_u$ of a fluid-saturated spheroidal inclusion via Eshelby's method. The complete forms of $P_u$ and $Q_u$ can be found in David (2012), as functions of the Poisson's ratio $v_0$ and bulk modulus $K_0$ of the solid, the fluid bulk modulus $K_f$, and the aspect ratio of the spheroid $\alpha$. For a dry spheroid, the expressions of the compressibility $P$ and shear compliance $Q$ can be obtained by letting the fluid bulk modulus $K_f$ approach zero.

The dry compressibility $P$ and shear compliance $Q$ of a spheroidal inclusion are used as inputs for an effective medium scheme to predict the overall elastic moduli of the dry medium. The differential effective medium (DEM) theory, applicable even at relatively high concentration of inclusions, is here used to relate the effective elastic moduli of a specimen to the compliances of individual inclusions (LeRavalec and Gu éguen, 1996) as:

$$(1-\phi)\frac{1}{K}\frac{dK}{d\phi} = -P(v)\ , \tag{8.1}$$

$$(1-\phi)\frac{1}{G}\frac{dG}{d\phi} = -Q(v)\ , \tag{8.2}$$

with the initial conditions: $K(\phi = 0) = K_0$ and $G(\phi = 0) = G_0$, where $\phi$ is porosity; $K$ and $G$ are the effective bulk and shear moduli, respectively; $v$ is the effective Poisson's ratio and

$\nu$ = (3$K$ - 2$G$) / (6$K$ + 2$G$); $P$ and $Q$ are the compressibility and shear compliance of a spheroidal inclusion, respectively; $K_0$ and $G_0$ are the bulk and shear moduli of the initial background medium, respectively. This set of coupled equations is applied progressively, *i.e.*, integrated from zero porosity to the desired level of porosity, to obtain the effective bulk and shear moduli.

The elastic modulus of a cracked medium with cracks of only relatively low aspect ratio increases with increasing pressure before reaching a plateau, indicating complete crack closure. However, equant or quasi-equant pores, with aspect ratios equal or close to 1, are hardly affected by pressure. The presence of such non-closable porosity accounts for the modulus deficit relative to the mineral modulus remaining at the highest pressure encountered in an experiment. The geometry, *i.e.*, effective aspect ratio, of the non-closable porosity can be inferred from the amount of the high-pressure modulus deficit.

The medium including the non-closable porosity is treated as the matrix within which the closable thin cracks are embedded. For thin cracks, the elastic moduli depend on both the volume fraction of cracks (crack porosity) and their aspect ratio combined in a quantity known as crack density $\Gamma$ proportional to crack porosity $\phi_c$ divided by crack aspect ratio $\alpha$. The relationship between crack porosity $\phi_c$ and crack density $\Gamma$ (Eq. 2.18):

$$\phi_c = \frac{4}{3}\pi\alpha\Gamma \,, \tag{8.3}$$

is combined with the expressions of $P$ and $Q$ given by David and Zimmerman (2011b) for an infinitely thin crack ($\alpha \to 0$):

$$P = \frac{4(1-\nu_0^2)}{3\pi\alpha(1-2\nu_0)} \,, \tag{8.4}$$

$$Q = \frac{8(1-\nu_0)(5-\nu_0)}{15\pi\alpha(2-\nu_0)} \,, \tag{8.5}$$

where $\nu_0$ is the Poisson's ratio of the initial background medium, *i.e.*, the solid containing (high-pressure) non-closable porosity in this case. By substituting Eq. (8.3 – 8.5) into the set of coupled equations (8.1 - 8.2), following a series of mathematical treatment, the differential effective medium scheme, linking the macroscopic effective moduli and microscopic compliance of thin cracks, can be written as functions of crack density $\Gamma$ that do not depend explicitly on crack aspect ratio:

$$\frac{K}{K^{hp}} = \frac{(1-2\nu^{hp})e^{-16\Gamma/9}}{1-2\nu^{hp}e^{-8\Gamma/5}} \,, \tag{8.6}$$

$$\frac{\nu}{\nu^{hp}} = e^{-8\Gamma/5} \,, \tag{8.7}$$

where $K$ and $v$ are the effective bulk modulus and the Poisson's ratio of the medium; $K^{hp}$ and $v^{hp}$ are the bulk modulus and the Poisson's ratio of the matrix, which is composed of both minerals and (high-pressure) non-closable porosity; and $\Gamma$ is the crack density. The crack density at a given pressure $\Gamma(P)$ can be found by inversion of the observed elastic moduli.

Crack closure with pressure relates crack aspect ratio $\alpha$ to pressure $P$. We are able to change $\Gamma(P)$ into $\Gamma(\alpha)$ using this change of variables. If a distribution of crack aspect ratios is assumed, the zero-pressure distribution of crack aspect ratios can be obtained from the pressure-dependent crack density as (David and Zimmerman, 2012):

$$\alpha^i = \frac{3}{4\pi}\int_{\Gamma^i}^{\Gamma(\alpha)} \frac{[C_{bc}^{(\Gamma)} - C_{bc}^{hp}]}{\Gamma}\frac{dP}{d\Gamma}d\Gamma \ , \tag{8.8}$$

$$\gamma(\alpha) = -\frac{d\Gamma}{d\alpha}, \tag{8.9}$$

where $\alpha^i$ is the crack aspect ratio at zero pressure that will be closed at pressure $P$; $\Gamma^i$ is the crack density at zero pressure; $C_{bc}^{(\Gamma)}$ is the bulk compressibility of the cracked medium, related to the observed P- and S-wavespeeds as $C_{bc} = \frac{1}{K} = [\rho\left(V_p^2 - \frac{4}{3}V_s^2\right)]^{-1}$; $C_{bc}^{hp}$ is the bulk compressibility of the matrix containing minerals and high-pressure non-closable pores; $P$ is pressure; and $\gamma(\alpha)$ is defined as the aspect ratio distribution of the crack density (Zimmerman, 1991a).

Considering the relationship between crack porosity and crack density (Eq. 8.3), a crack porosity distribution function *c(α)* is defined as:

$$c(\alpha) = \frac{4\pi\alpha}{3}\gamma(\alpha), \tag{8.10}$$

where $\gamma(\alpha)$ is the aspect ratio distribution function of crack density. Similar to *Γ(α)* as the cumulative crack density, the cumulative crack porosity *C(α)* is defined as:

$$C(\alpha) = \int_0^\alpha c(\alpha)d\alpha. \tag{8.11}$$

So far, the microstructure of a cracked medium in terms of the geometry of inclusions and its distribution is quantified. With the inferred microstructure, the elastic moduli of the medium when all its inclusions (*i.e.*, both cracks and equant pores) are fully saturated with a fluid can be predicted in a forward modelling exercise.

For this purpose, Eq. (8.1) – (8.2) are modified to incorporate fluid properties as:

$$(1-\phi)\frac{1}{K}\frac{dK}{d\phi} = -P_u(1-\xi) \ , \tag{8.12}$$

$$(1-\phi)\frac{1}{G}\frac{dG}{d\phi} = -Q_u, \tag{8.13}$$

where $P_u$ and $Q_u$ are the compressibility and shear compliance of the undrained spheroidal inclusion, the full expressions of which are given in David (2012); and $\xi = K_f/K$ is the ratio between the fluid bulk modulus $K_f$ and the effective bulk modulus at the current level of porosity. The coupled DEM equations (8.12) and (8.13) need to be solved *iteratively* through a thought experiment, in which cracks in a fluid-saturated medium are re-opened by steps with a decreasing pressure from the highest pressure. The newly re-opened cracks are progressively incorporated into the matrix which accordingly evolves with decreasing pressure. Details of calculation procedure are given in David and Zimmerman (2012).

## 8.2 Pressure Dependent Crack Closure – Permeability and Elasticity

In order to gain a broad view of the experimental results, summary figures with all the measured shear and Young's moduli from mHz to MHz on three types of synthetic samples are provided first (Fig. 8.1 & 8.2). For shear modulus, a broadband measurement has been performed, from mHz, through kHz, to MHz frequencies, on the glass-rod specimen, and at mHz and MHz frequencies on the glass-bead specimens (Fig. 8.1). The Young's modulus has been measured at kHz and MHz frequencies on the glass-rod specimen, and at mHz and MHz frequencies on the glass-bead specimens (Fig. 8.2).

### 8.2.1 General features

A marked decrease in permeability and a significant increase in elastic modulus have been observed on cracked samples of this study with increasing pressure. This pressure dependence of hydraulic and mechanical properties is attributed to crack closure by increasing pressure, resulting in a less permeable and stiffer rock.

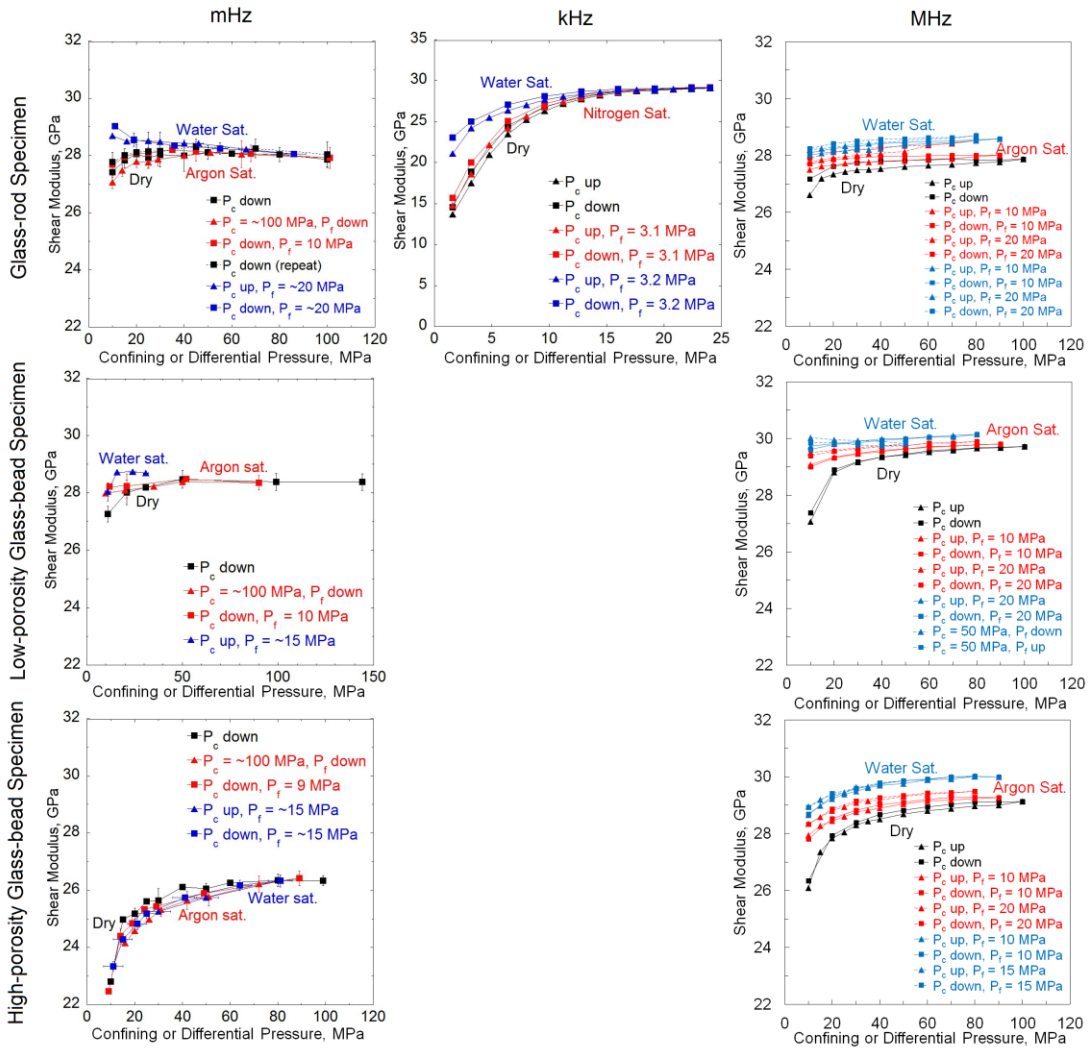


**Figure 8.1** A summary of the broadband (mHz-MHz) measurements of shear moduli for the suite of synthetic glass media. The data derive from forced oscillation, resonance bar, and ultrasonic wave propagation tests on glass-rod, low-porosity glass-bead, and high-porosity glass-bead specimens. The shear moduli are plotted on a common scale except the result for the glass-rod specimen at kHz frequency, for which the interfacial compliance at low pressure introduces larger variation in modulus.

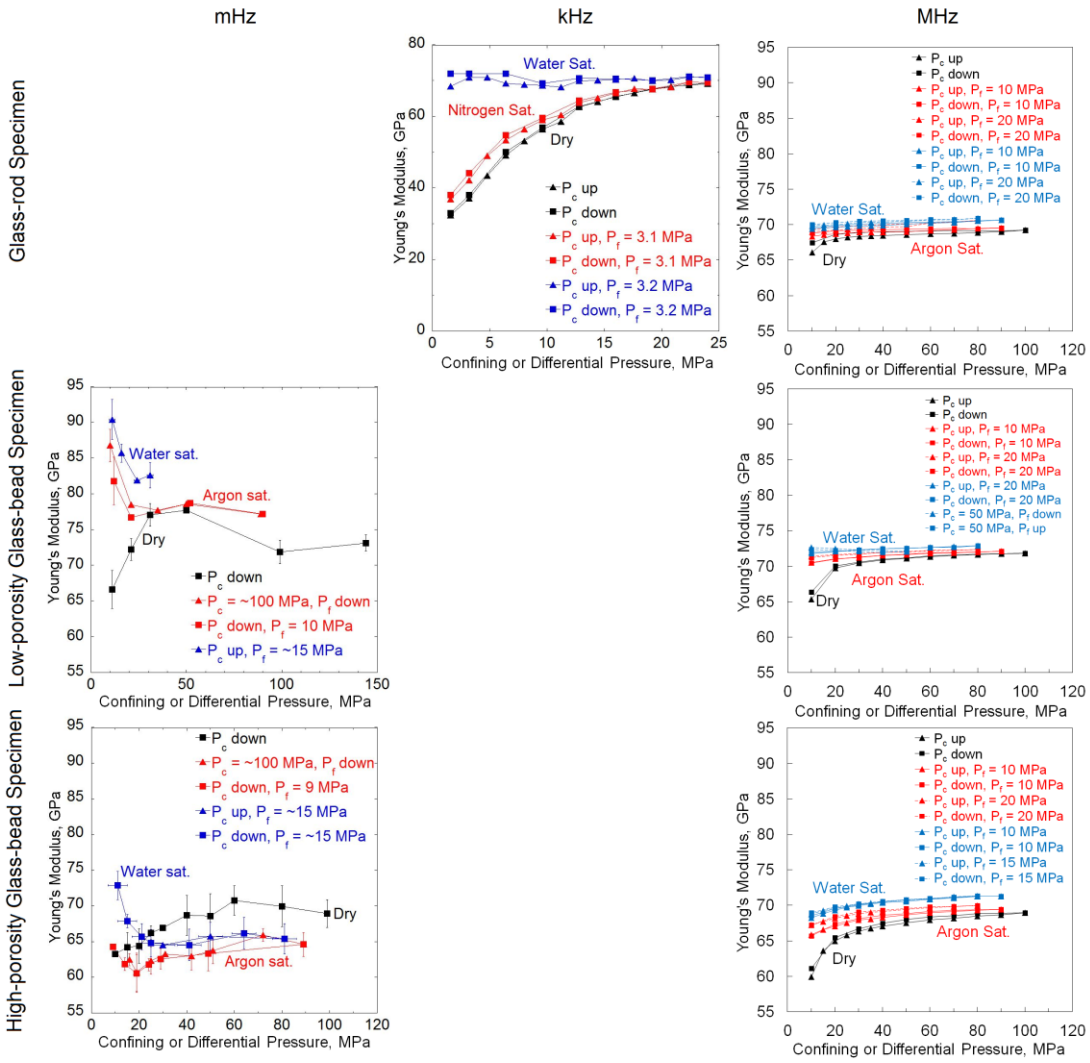


**Figure 8.2** A summary of the broadband (mHz-MHz) measurements of Young's moduli for the suite of synthetic glass media. The data derive from forced oscillation, resonance bar, and ultrasonic wave propagation tests on glass-rod, low-porosity glass-bead, and high-porosity glass-bead specimens. The Young's moduli are plotted on a common scale except the result for the glass-rod specimen at kHz frequency, for which the interfacial compliance at low pressure introduces larger variation in modulus.

Closure of a crack by pressure will contribute to the increased overall stiffness of a rock. The effective modulus of the rock is expected to reach a stable value as soon as all cracks within the rock are closed by pressure. The observation on most of the synthetic samples is consistent with the argument except in some cases a minor decrease in modulus with pressure, instead of a constant modulus, is noticed after crack closure, *e.g.*, shear modulus of the glass-rod specimen at mHz frequency (Fig. 8.1) and Young's modulus of the low-porosity glass-bead specimen at mHz frequency (Fig. 8.2). This is explained by the unusual negative pressure derivative of shear and Young's moduli for silica-rich material. The pressure derivatives of shear modulus, bulk modulus, and Young's modulus of fused silica are -3.5, -6.3, and -9.2, respectively (Gerlich & Kennedy, 1978). When cracks are firmly closed by pressure, a cracked silica-rich rock then behaves like an intact one, and the pressure dependence is dominated by the negative pressure derivative of modulus. The ongoing crack closure and the negative pressure derivative of modulus compete with each other, masking the gently decreasing trend of modulus with increasing pressure in some cases.

A minimum constant permeability is reached once all cracks are closed by pressure, eliminating channels for fluid flow. It is also noticed on the permeability results (Fig. 4.1) that the constant permeability of the high-porosity glass-bead specimen after crack closure is higher than that of the low-porosity glass-bead specimen, which is in turn higher than that of the glass-rod specimen. This is explained by the role of equant porosity in contributing to permeability, and a specimen with higher equant porosity, assuming the residual connectivity between these pores, may have a higher residual constant permeability when cracks are closed. Comparison shows that the water permeability (Fig. 4.2) is lower than the argon permeability (Fig. 4.1) by an order of magnitude at a common differential pressure near 10 MPa. This is presumably attributed to 1) less cracking in the interior of the large-diameter specimen for the resonance tests; and 2) a chemical rather than strictly hydraulic interaction between (polar) water and the glass crack surfaces at low permeabilities. For the latter case, the chemical interaction between the polar fluid and silica-rich surfaces in narrow crack "throats" could result in additional drag on the fluid beyond that associated with the usual viscosity.

### 8.2.2 Crack closure pressure

The crack closure pressure for a thin spheroidal crack is approximated by the product of mineral's Young's modulus $E$ and the crack aspect ratio $\alpha$ (Walsh, 1965, Eq. 1.10). The Young's modulus of a typical soda-lime-silica glass is 72 GPa, and the pressure for crack closure, considering the mean initial aspect ratio observed on each type of the synthetic

samples (Table 2.4), would be ~140 MPa, ~70 MPa, and ~70 MPa for the glass-rod specimen, the low-porosity glass-bead specimen, and the high-porosity glass-bead specimen, respectively. Taking into account the uncertainty in estimating the mean initial aspect ratio on the polished cross-section of a specimen, hence the uncertainty in the estimates of crack closure pressures, the theoretical predictions are broadly consistent with the in-situ observations of the crack closure pressures required to establish nearly pressure-independent moduli and permeabilities on the glass-bead specimens (Table 8.1).

However, for the glass-rod specimen, the observed pressures for crack closure are 40 MPa and 70 MPa for mechanical and hydraulic measurements, respectively, on the Attenuation Apparatus, and 30 MPa for the ultrasonic wavespeed measurements, beyond which the pressure sensitivity of either moduli or permeability becomes much less significant. It is recalled that a substantial deficit of modulus remains at the highest pressure of 100 MPa in ultrasonic measurements (Fig. 6.2). In the absence of pores in this material, these observations suggest that crack closure may be inhibited by fragmentation of material to a greater degree than in the glass-bead specimens. The observed pressures for crack closure between 30 and 70 MPa may thus reflect the closure of those cracks which are free of fragmentation at crack interface. This possibly explains the discrepancy between the observed and predicted crack-closure pressures on the glass-rod specimen.

Table 8.1 Crack Closure Pressure

Unit: MPa

| | | Glass-rod | Low-porosity Glass-bead | High-porosity Glass-bead |
|---|---|---|---|---|
| Prediction | | ~140 | ~70 | ~70 |
| Observation * | Low-f shear modulus | ~40 | ~50 | ~60 |
| | High-f moduli | ~30 | ~50 | ~60 |
| | Permeability | ~70 | ~90 | ~70 |

*Crack closure pressure in observation is defined as the pressure for closure of most closable cracks, beyond which an almost constant modulus or permeability is expected.

### 8.2.3 Aspect ratio distribution

As explained in *Section 8.1*, the observed ultrasonic P- and S-wave velocities as functions of pressure under dry condition are used to invert for the microstructure of each synthetic sample. The bulk and shear moduli derived from the measured P- and S-wave velocities at the highest pressure, *i.e.*, 100 MPa, and their deficits relative to the bulk and shear moduli of the fully dense soda-lime-silica glass provide the aspect ratios of stiff pores. Such an analysis has been performed only for the porous samples, *i.e.*, glass-bead specimens. The inferred aspect ratios of stiff pores are 0.345 and 0.453 for the low-porosity and high-porosity glass-bead specimens, respectively. The aspect ratios of these non-closable pores are less than 1 as for a perfect spherical pore, but much higher than that of a thin crack on the order of $10^{-3}$. The solid glass medium with embedded non-closable pores forms the matrix within which closable cracks are embedded.

Through Eq. (8.6) – (8.7), the crack density $\Gamma(P)$ is inferred from the moduli derived from the measured ultrasonic wavespeeds at each pressure. The aspect ratio distribution of crack density (Eq. 8.9) and cumulative porosity (Eq. 8.11) are finally inferred from the pressure dependent crack density $\Gamma(P)$ on each cracked sample. The inversion yields crack aspect ratios on all samples generally less than $5\times10^{-4}$ (Fig. 8.3 a, c, e). The aspect ratio distribution $\gamma(\alpha)$ for crack density for each specimen (Fig. 8.3 a, c, e) decreases monotonically with increasing aspect ratio. Compared with the observed aspect ratios of $1.9\times10^{-3}$, $9.5\times10^{-4}$, and $9.5\times10^{-4}$ on the glass-rod, low-porosity glass-bead, and high-porosity glass-bead specimens, respectively, the inferred aspect ratios are consistently smaller by one order of magnitude. It needs to be noticed that the surface of sample cross-section has been well polished before being examined by optical microscopy. The apparent apertures of cracks could possibly be artificially increased during the process of polishing, giving a larger aspect ratio. The total crack porosity of each sample is indicated by the cumulative porosity at the highest aspect ratio (Fig. 8.3 b, d, f). The inferred total crack porosities of the glass-rod, low-porosity glass-bead, and high-porosity glass-bead specimens are 0.007%, 0.011%, and 0.025%, respectively. These values are systematically lower than the observed ones determined by the volumetric increase associated with thermal cracking, which are 0.35%, 0.08%, and 0.14% for the glass-rod, low-porosity glass-bead, and high-porosity glass-bead specimens, respectively. The discrepancy between the observed and inferred crack porosities can be explained by: 1) not all the measured crack porosity is closable crack porosity; 2) crack shapes are idealised in modelling.

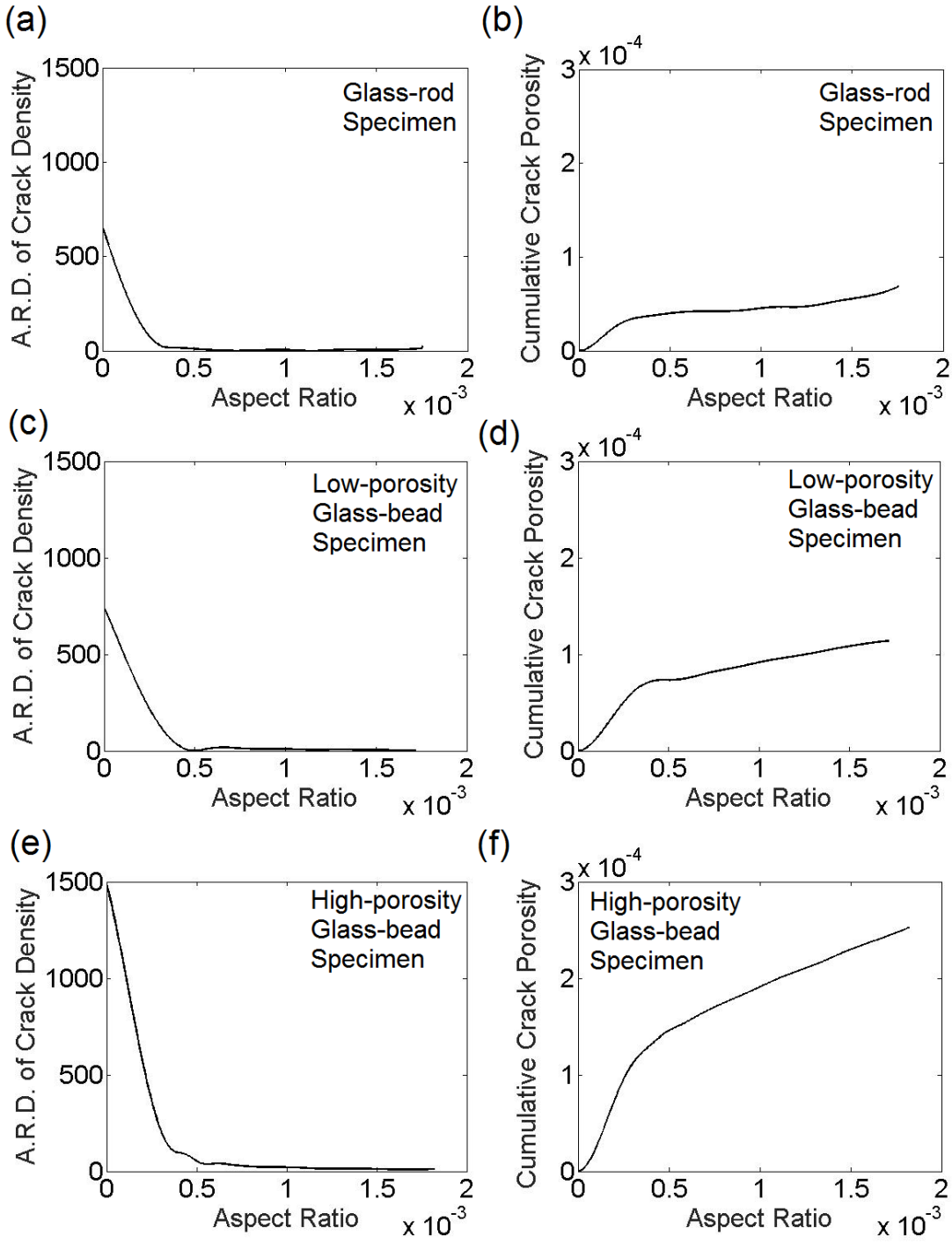


**Figure 8.3** (a, c, e) Aspect ratio distribution of crack density $\gamma(\alpha)$ (Eq. 8.9) and (b, d, f) associated cumulative crack porosity $C(\alpha)$ (Eq. 8.11) on the glass-rod, low-porosity glass-bead, and high-porosity glass-bead specimens, inferred from the measured pressure-dependent ultrasonic P- and S-wave velocities.

## 8.3 Fluid Saturation

### 8.3.1 Mechanical stiffening and weakening with fluid saturation

*Fluid incompressibility & stiffening*

The bulk modulus of a medium is expected to increase when it is saturated with a fluid. This argument is true regardless of the frequency at which the bulk modulus is measured as long as the specimen is not completely drained. When a cracked medium is saturated with a fluid more incompressible than air, the incompressibility of the fluid tends to resist a net volumetric reduction of the rock matrix, which in turn increases the overall bulk modulus of the medium. This notion is embodied in the Biot-Gassmann low-frequency model (Gassmann, 1951; Biot, 1956 a & b).

In contrast, whether or not shear modulus is increased depends on the status of saturating fluid within the crack network of the medium, and may thus be time or frequency dependent. The Biot-Gassmann theory predicts a shear modulus independent of fluid saturation at low frequency. The rationale behind this is no net volumetric change for the connected inclusions under shear stress. This will not hold once the pore pressure is not completely equilibrated and/or the cracks within the medium have a preferential orientation. The locally unrelaxed pore pressure is expected to increase the shear modulus as well.

The Young's modulus of a medium draws effects from both the bulk modulus and shear modulus (Eq. 3.73). To this end, regardless of the response of shear modulus, an increase in bulk modulus with fluid saturation results in an increase in Young's modulus.

Increased shear and Young's moduli after being saturated with either argon (or nitrogen) or water have been observed on all types of samples at intermediate to ultrasonic frequencies in this study. The observation agrees with the notion that the incompressibility of unrelaxed fluid increases the overall stiffness of a rock.

However, a shear modulus equal to that of the dry medium is expected for saturated isobaric conditions, and drainage of the specimen to an external reservoir is required if the bulk modulus is not to be stiffened by the fluid saturation. These conditions could be encountered at low frequencies.

At seismic frequencies in this study, for the glass-rod specimen in shear mode, stiffening with water saturation has been noticed but no change with argon saturation. The low-porosity glass-bead specimen shows higher shear and Young's moduli with both argon and water saturation at low differential pressures. The shear modulus of the high-porosity glass-bead specimen is observed to be independent of fluid saturation (with both argon and

water saturation), whereas a marked stiffening with water and a resolvable stiffening with argon are noticed in Young's modulus at low differential pressures.

*Fluid incompressibility vs. density effect in ultrasonic S-wave velocity*

The increase in P-wave velocity with water saturation on sandstones has been commonly reported by researchers at intermediate to ultrasonic frequencies (King, 1966; Gregory, 1976; Winkler and Nur, 1982; Winkler, 1985). It becomes more complicated for S-wave velocity with fluid saturation, and either an increase (Baechle *et al.*, 2005) or a decrease (Winkler and Nur, 1982; Winkler, 1985) in S-wave velocity has been reported. The increase in S-wave velocity is normally attributed to the unrelaxed pore-fluid pressure at relatively high frequency, and the fluid contained in cracks with particular orientations is expected to respond to the compressed matrix and increase the overall rigidity of the fluid-saturated medium. The fluid-related stiffening becomes less significant when cracks are progressively closed by pressure before the fluid is completely expelled from cracks. It needs to be remembered that S-wave velocity varies inversely as the square root of the overall density of a fluid-saturated rock. The saturation with fluid increases the overall density, and may therefore reduce the S-wave velocity.

The fluid effects on modulus and density compete with each other. The former effect is most significant at the lowest differential pressure as the cracks are widely open to contain fluid, allowing the density effect to be masked. The S-wave velocity of the fluid-saturated medium is normally found to be higher than the dry value in this case. The cracks are gradually closed by pressure, giving less fluid involved. The density effect then dominates, showing a decrease in S-wave velocity of the fluid-saturated medium. In consequence, a cross-over is noticed for the dry and fluid-saturated S-wave velocity with elevated pressure in some cases (King, 1966; David *et al.*, 2013). In this study, however, the "wet" S-wave velocity with either gas or water saturation is noticed to be systematically higher than the dry S-wave velocity, probably explained as the shear stiffening due to fluid saturation always dominates over the density effect over the entire pressure range. Another possible explanation will be given in the following subsection.

*Surface free energy reduction & weakening*

The absorption of a tiny amount of moisture is capable of significantly reducing the surface free energy at grain contacts, inducing a weakening of a rock matrix (Tittmann & Housley, 1973; Tittmann, 1977, 1978; Pandit & King, 1979; Spencer, 1981; Tutuncu & Sharma, 1992; Adam *et al.*, 2006; Adelinet *et al.*, 2010; Pimienta *et al.*, 2014). In this study, a minor weakening in shear modulus and a moderate weakening in Young's modulus with both

argon and water saturation at mHz have been observed on the high-porosity glass-bead specimen, most probably related to the surface free energy reduction due to absorption of moisture.

The reduction of surface free energy would be an effect associated with the contact surface area of inclusions. Keeping other factors fixed, the sample with larger inner surface area would incur a more significant reduction of free energy. This is consistent with our observation as the most significant surface free energy reduction is noticed on the high-porosity glass-bead specimen, which has the highest equant porosity and is expected to have the largest inner surface area (giving a similar pore size distribution between the low-porosity and high-porosity glass bead samples) among the three types of samples.

The mechanical stiffening/weakening associated with fluid saturation is summarised on all the synthetic samples over the entire frequency range in this study. The variation in modulus due to fluid saturation is expressed as a percentage change with respect to the dry modulus measured with the same technique on the same sample (*Appendix N*). An obvious advantage of using percentage change in modulus is that any systematic differences between dry moduli measured by different techniques are excluded. The direct comparison between the "wet" modulus measured at different frequencies is only valid when the dry modulus of the specimen is exactly the same. The hysteresis of the elastic behaviour of a cracked sample is commonly observed in laboratory, especially when the sample needs to be loaded and tested on different machines. To this end, it is more appropriate to compare the relative changes in modulus due to fluid saturation rather than its absolute values among different techniques.

### 8.3.2 Characteristic frequencies

Various fluid flow regimes are theoretically predicted with increasing frequency, and these regimes are demarcated by characteristic frequencies. In order to decide which fluid-flow regime is relevant, not only the elastic response, *i.e.*, the percentage change in moduli, of the fluid-saturated sample, but also the estimated characteristic frequency will provide useful evidence.

The frequency separating undrained from drained behaviour of a sample (Cleary, 1978) is:

$$f_{dr} = \frac{kK_f}{\phi\eta l^2}, \tag{8.14}$$

where $k$ is the permeability of the sample, $K_f$ is the bulk modulus of the pore-fluid used, $\phi$ is the porosity of the sample, $\eta$ is the viscosity of the fluid, and $l$ is the typical dimension of the sample. For $k = 10^{-19}$ - $10^{-18}$ m$^2$, $K_f = 9.8$ MPa, $\eta = 29.2$ μPa s, $\phi = 2\%$, and $l = 75$ mm (half-length of the specimen) for a cracked glass sample with argon pressure fixed at 10 MPa, and $K_f = 2.2$ GPa, $\eta = 1.0$ mPa s for water pressure kept at 10 MPa, the characteristic frequencies related to the transition from the drained to the undrained regime are 0.3 - 3 mHz and 2 - 20 mHz for argon and water saturation, respectively.

The characteristic frequencies estimated are slightly less than or comparable with the frequency band that used in the forced oscillation experiments from 10 mHz to 260 mHz. It needs to be noticed that the uncertainties in the petrophysical parameters would propagate into the estimated characteristic frequency. But it still tells that the fluid flow behaves in the way that quite close to the transition of regimes, and further evidences from the mechanical response of the sample to the fluid saturation needs to be included to confidently identify the fluid flow regime. As Young's modulus combines the bulk and shear moduli (Eq. 3.73), the sensitivity of bulk modulus to fluid drainage will pass on to Young's modulus to make it a good indicator for the transition from the drained regime to the undrained regime.

It is noticed that $f_{dr}$ for water saturation is higher than that for argon saturation, which contradicts the intuitive expectation that water, as a more viscous fluid, would require a longer timescale for draining than argon. This is because both the bulk modulus and the viscosity of a fluid play roles in the expression of characteristic frequency (Eq. 8.14), and the reduction in bulk modulus, by replacing water with argon, dominates over the reduction in viscosity at 10 MPa, giving an even lower $f_{dr}$ for argon saturation. The draining frequencies for argon and water, broadly speaking, are on the same order of magnitude, and the similar values of $f_{dr}$ can be understood physically as follows. The much lower viscosity of argon than water means that there will be a larger flux of argon for a given pressure gradient. However, because the bulk modulus for argon is so much lower, much more fluid

needs to flow to contribute the same change in pressure. Accordingly, the characteristic timescales need not be so different (Lu, 1996). The situation is reversed at a higher argon pressure, *e.g.*, 100 MPa. This unusual relationship between the draining frequencies for argon and water provides an extra indicator for fluid-flow regime at low pore pressures, *i.e.*, stiffening with water saturation indicating undrained conditions would also provide the evidence for the undrained condition for argon saturation.

Table 8.2 Characteristic Frequencies

| | Drained | $f_{dr}$ | Saturated Isobaric | $f_{sq}$ | Saturated Isolated |
|---|---|---|---|---|---|
| Argon saturation | | 0.3 - 3 mHz | | ~ 1 MHz | |
| Water saturation | | 2 - 20 mHz | | ~ 40 kHz | |

The characteristic frequency that separates the saturated isolated regime from the saturated isobaric regime (O'Connell & Budiansky, 1977; Palmer & Traviolia, 1980) is:

$$f_{sq} = \frac{K_0 \alpha^3}{\eta}, \tag{8.15}$$

where $K_0$ is the bulk modulus of the mineral material making up rock, $\alpha$ is the aspect ratio of a crack, and $\eta$ is the viscosity of pore fluid. Giving $K_0$ = 40 GPa for soda-lime-silica glass, $\alpha = 10^{-3}$ for the cracks in the synthetic samples, $\eta$ = 29.2 μPa s and 1.0 mPa s for argon and water saturation at 10 MPa, respectively, the estimated characteristic frequencies separating the saturated isobaric and saturated isolated regimes are ~ 1 MHz and ~ 40 kHz for argon and water saturation, respectively. As $f_{sq} \sim \alpha^3$, the characteristic frequency is extremely sensitive to the crack aspect ratio, the estimate would be lowered by a factor of $10^3$ if the crack aspect ratio is reduced by an order of magnitude by pressure. The results presented in this study were all collected beyond 10 MPa, the actual aspect ratio would be less than the nominal mean aspect ratio of $10^{-3}$ determined at ambient conditions. To this end, the characteristic frequency $f_{sq}$ presented in Table 8.2 are the upper bound of $f_{sq}$, the actual transition from the saturated isobaric regime to the saturated isolated regime would be expected at lower frequencies. Accordingly, for both argon and water saturation, conditions corresponding to the saturated isolated regime are expected for all the measurements conducted at 1 MHz with the ultrasonic wave propagation.

### 8.3.3 Fluid-flow regimes

*Section 8.3.1* and *8.3.2* provide evidences for fluid-flow regimes based on the change in elastic modulus with fluid saturation and the characteristic frequencies, respectively. It is not difficult to attribute the fluid-flow regime for a sample at a particular frequency based on the findings from these two aspects.

As we have discussed in the last section, saturated isolated conditions are expected at ~1 MHz from the estimated characteristic frequency, and this expectation is reinforced by the observed stiffening of the shear modulus in each case. However, the fluid-flow regime at seismic frequency needs further analysis based on the change in elastic modulus before making a judgement.

Table 8.3 Fluid-flow Regimes

| **Specimen Type** | **Saturant** | **Fluid-flow Regime** | | |
|---|---|---|---|---|
| | | **10 – 260 mHz** | **1-3 kHz** | **1 MHz** |
| Glass-rod specimen | Argon or nitrogen sat. | Saturated isobaric | Transition | Saturated isolated |
| | Water sat. | Saturated isolated | Saturated isolated | Saturated isolated |
| Low-porosity glass-bead specimen | Argon sat. | Transition | - | Saturated isolated |
| | Water sat. | Transition | - | Saturated isolated |
| High-porosity glass-bead specimen | Argon sat. | Saturated isobaric | - | Saturated isolated |
| | Water sat. | Saturated isobaric | - | Saturated isolated |

For the glass-rod specimen, the increase in shear modulus with water saturation indicates conditions in which pore pressure perturbations are unrelaxed by fluid flow (Fig. 8.1). Based on the analysis of the percentage change in shear modulus at different frequencies at a fixed differential pressure of 10 MPa, the sample should be in the saturated isolated regime as a constant change in shear modulus of ~ 4% is observed over the entire band of frequency from 10 mHz to 1 MHz (*Appendix N-1*). It is recalled that, with all the other conditions held, an undrained condition for argon saturation is inferred if the same sample is undrained with water saturation (Table 8.2). Considering the unchanged shear

modulus, the glass-rod sample should be in the saturated isobaric regime with argon saturation. An ongoing increase in the percentage change of shear modulus, from 1.5% at kHz to 2.7% at MHz, indicates that the resonance technique actually detects the transition between the saturated isobaric regime and the saturated isolated regime.

The low-porosity glass-bead specimen, saturated with either argon or water, has already reached the transition from the saturated isobaric regime to the saturated isolated regime, as evidenced by, for both argon and water saturation, 1) increases in shear modulus below 30 MPa (Fig. 8.1); and 2) smaller percentage changes in shear modulus on saturation at mHz than at MHz frequencies. The absence of resonance data makes it impossible to make the judgment at kHz frequency, whereas the sample should maintain within the saturated isolated regime at 1 MHz from the theoretical estimation of the characteristic frequency.

On the high-porosity glass-bead specimen, a shear modulus insensitive to fluid saturation has been observed at mHz frequency, indicating either a drained or saturated isobaric condition (Fig. 8.1). Further evidence is provided by the measured Young's modulus, with a marked increase with water saturation and a resolvable increase with argon saturation at the differential pressure of 10 MPa (Fig. 8.2). This clearly confirms the undrained condition for water saturation. In terms of argon saturation, recalling the characteristic frequency for an undrained condition is even lower than that for water at the pore-fluid pressure of 10 MPa, and an undrained condition for water should also confirm an undrained status for argon saturation under such a circumstance. Therefore, the sample with both argon and water saturation should be in the saturated isobaric regime at mHz frequencies. Similarly, the fluid-saturated sample is expected to be in the saturated isolated regime at 1 MHz based on the theoretical characteristic frequency and stiffened moduli.

The fluid-flow regime for each sample at a particular frequency has thus been decided and listed in Table 8.3. A further emphasis will be given for each fluid-flow regime in the following sections.

#### 8.3.3.1 Saturated isobaric regime

In the saturated isobaric regime, stress-induced pore pressure perturbations are relaxed by fluid flow over the entire sample within a half period of oscillation, providing a shear modulus unchanged from that of the dry material and an increase in bulk modulus. This regime is described by the Biot-Gassmann theory (Eq. 1.1 - 1.2). The argon saturated glass-rod specimen and the high-porosity glass-bead specimen with both argon and water saturation at mHz frequency clearly belong to saturated isobaric regime. However, the Gassmann prediction on the glass-rod specimen at mHz frequency is hindered by the

absence of the Young's modulus of the sample. The Biot-Gassmann theory, therefore, is only applied to the high-porosity glass-bead specimen at mHz frequencies.

In the Gassmann prediction, the Young's modulus is essentially unchanged with argon saturation due to the high compressibility of argon at relatively low fluid pressure, whereas a modest increase in Young's modulus is predicted at differential pressures below 40 MPa with water saturation. The water saturation accounts for ~ 1% stiffening at 20 MPa, which gradually diminishes as the differential pressure is increased (Fig. 8.4).

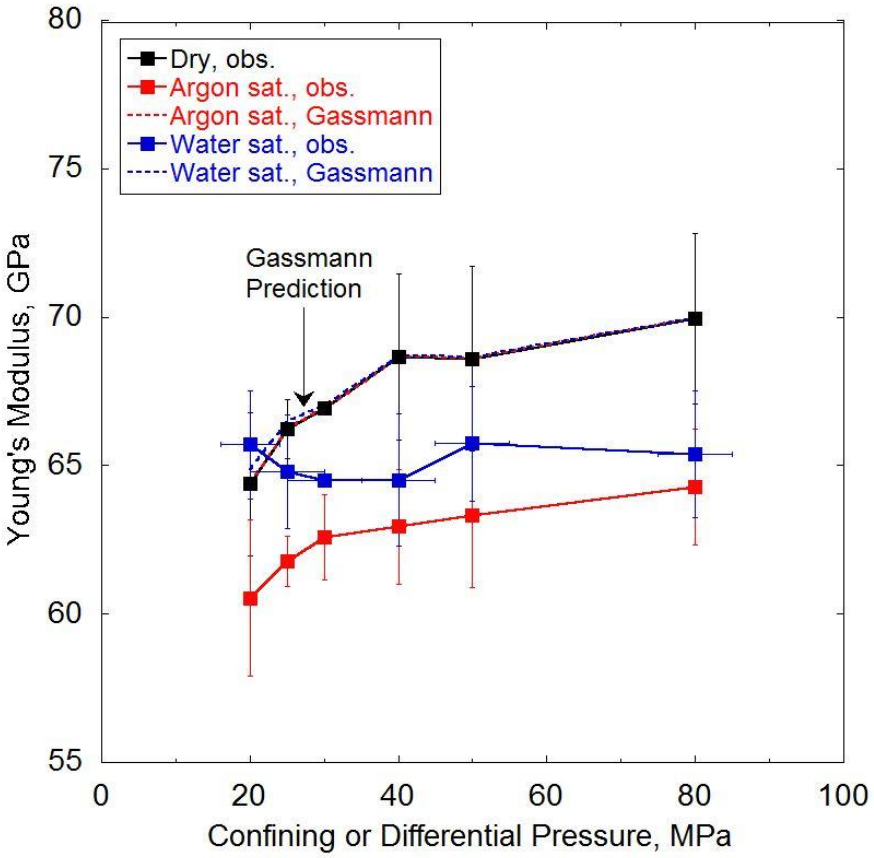


**Figure 8.4** Young's modulus of the high-porosity glass-bead specimen saturated with either argon or water is predicted by the Biot-Gassmann equation from the dry modulus measured at mHz frequency.

The observations reproduced in Fig. 8.4 show that, the measured Young's modulus with either argon or water saturation is well below the dry modulus as probably subject to the surface free energy reduction at grain contacts and crack surfaces due to the absorption of moisture. In this case, therefore, comparison of the water- and argon-saturated moduli may provide the best indication of the stiffening associated with water saturation – which is substantially greater than Gassmann's prediction for the water-saturated specimen.

8.3.3.2 Saturated isolated regime

The distance that a pore fluid can travel is gradually limited by an increasing frequency, until the fluid behaves as if isolated among adjacent inclusions. Under such an unrelaxed condition for pore fluid, the suppression of fluid equilibration makes extra contribution to the overall rigidity of the fluid-saturated rock through the incompressibility of fluid. Although the relative motion between the fluid-phase and the solid-phase within an individual inclusion has not been completely prohibited in the saturated isolated regime, an exercise to introduce a fluid as the second phase into the solid matrix still becomes a reasonable approximation when the fluid communication, *i.e.*, squirt flow, among neighbouring inclusions are suppressed. This is the reason that the saturated isolated regime can be appropriately modelled by the effective medium theory.

The microstructure, in terms of the aspect ratios of stiff pores and cracks, has been inferred by the previous inversion of the pressure-dependent dry moduli determined from the ultrasonic wavespeeds. The wavespeeds on the three types of synthetic samples saturated with either argon or water are then predicted from such inferred microstructure and fluid properties through differential effective medium theory (Fig. 8.5).

On the glass-rod specimen, a good match of P-wave velocity between the model and observation is achieved (Fig. 8.5a). But the predicted S-wave velocity is systematically lower than the observation, especially for water saturation (Fig. 8.5b). The "wet" wavespeeds are expected to roughly converge to the "dry" wavespeeds at high pressure when fluid is expelled from closed cracks. However, the bulk of the 0.35% measured crack porosity, although of relatively low aspect ratio, remains unclosed at the highest pressure of the experiment, and its water saturation has not been accounted for in the effective medium calculation. The model is even noticed to underestimate the P-wave velocity at low differential pressures (Fig. 8.5c). The reconciliation between the model and observation becomes even worse on the high-porosity glass-bead specimen (Fig. 8.5 e & f). The "wet" wavespeeds with both argon and water saturation are systematically underestimated.

This model captures well for bulk modulus (Fig. 8.6), leading to a better prediction of P-wave velocity than S-wave velocity for a fluid-saturated rock. However, in a qualitative sense, the model still captures some of the nature for the S-wave velocity of fluid-saturated rocks. For instance, the competition between the fluid incompressibility and density effect is reflected as a cross-over between the dry velocity and predicted velocity with water saturation (Fig. 8.5 e & f). It is also recalled (Fig. 8.3) that the model underestimates the crack porosity for these synthetic specimens.

The failure in reconciling the prediction with observation in some cases is explained as follows: 1) this model was initially developed for Fontainebleau sandstones (David &

Zimmerman, 2012) which are characterised by an unusually narrow distribution of crack aspect ratios. It is the first time to apply the model to thermally cracked synthetic glass materials; 2) the idealised thin spheroidal shape in the model may be not suitable for the real thermal cracks observed on these samples; 3) the model assumes a random distribution of cracks, whereas the preferred orientations noticed on the glass-bead specimens may violate this assumption. This notion is confirmed by the observed difference between the axial and circumferential strains on the glass-rod specimen (Fig. 6.5). A similar anisotropic distribution of crack network on a thermally cracked glass cylinder has also been reported by Mallet *et al.* (2013). 4) strain gauge measurements indicate a significant amount of crack closure occurring below 10 MPa, however, the lack of ultrasonic velocity data below 10 MPa means that the crack density function $\Gamma(P)$ is unconstrained at lower pressure, and interpolated data are used instead; 5) the failure of the measured fluid-saturated velocity to converge to the dry velocity at the highest pressure is probably caused by residual unclosed cracks saturated with fluid at the highest pressure.

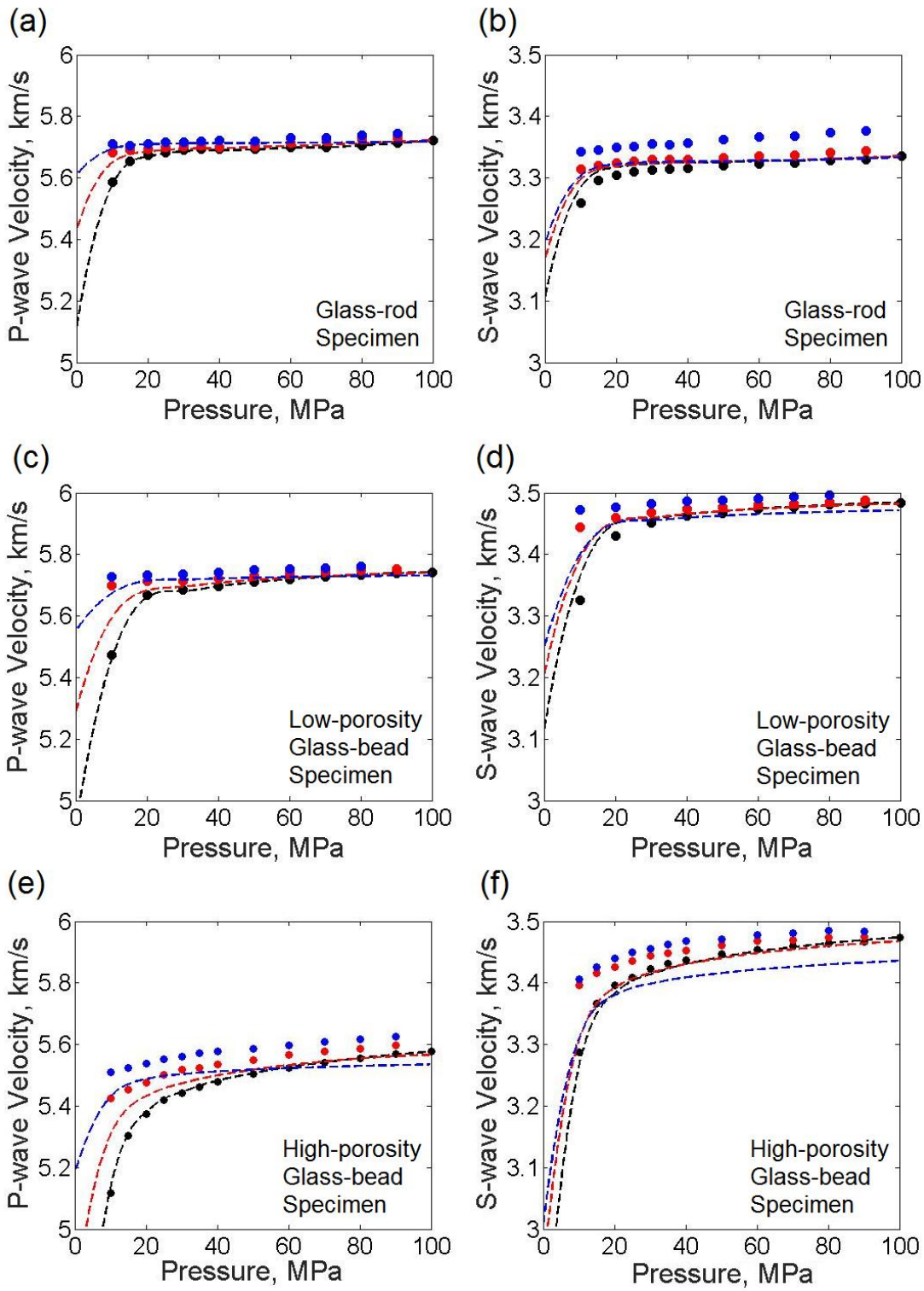


**Figure 8.5** Predictions (dashed lines) for the P- and S-wave velocities with either argon (red) or water (blue) saturation from the differential effective medium model (David & Zimmerman, 2012) on the glass-rod (a & b), low-porosity glass-bead (c & d), and high-porosity glass-bead (e & f) specimens. The prediction is based on the previously inferred microstructure of samples and fluid properties. The predictions are compared with the measurements (solid symbols).

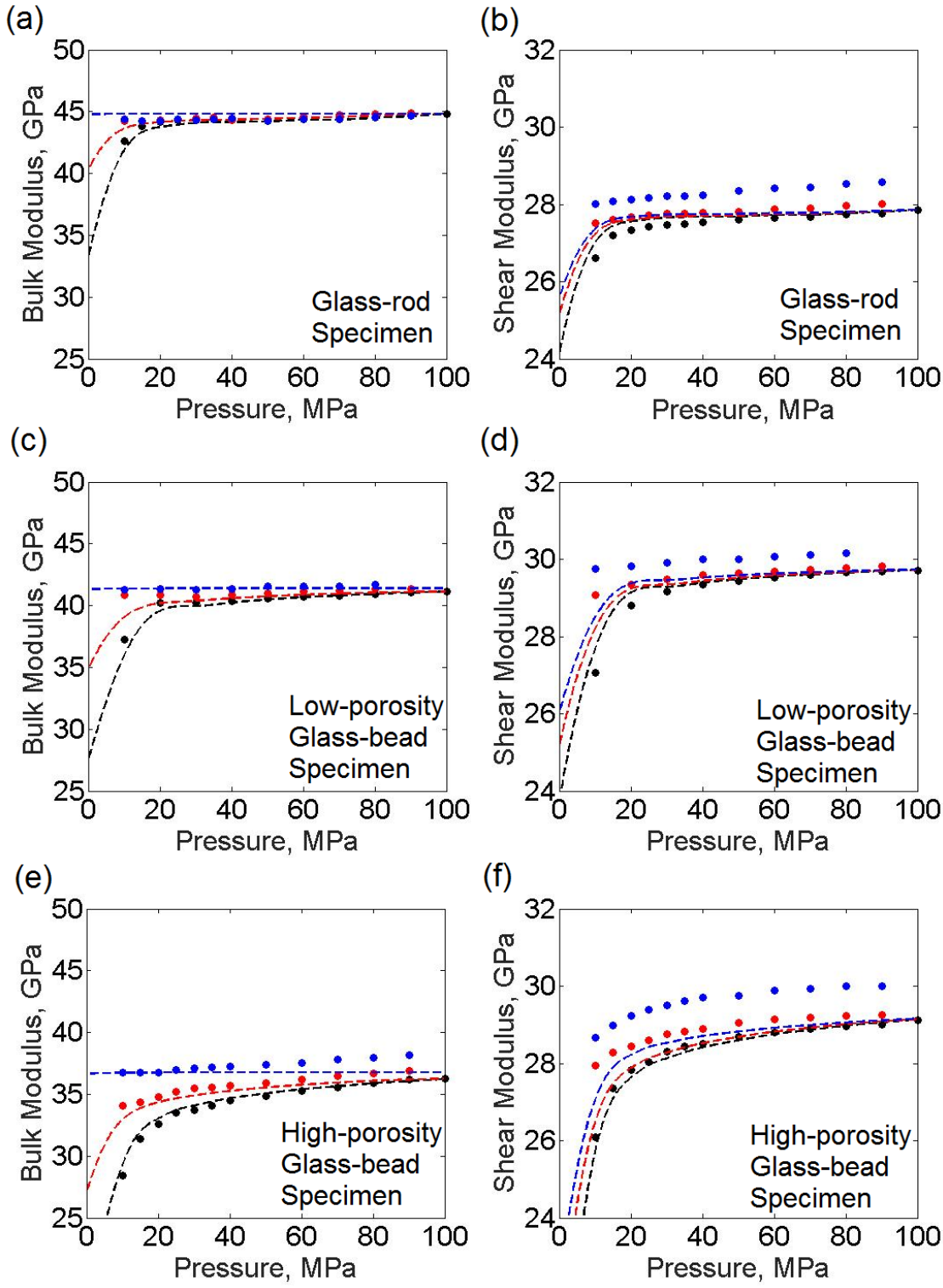


**Figure 8.6** Predictions (dashed lines) for the bulk and shear moduli with either argon (red) or water (blue) saturation from the differential effective medium model (David & Zimmerman, 2012) on the glass-rod (a & b), low-porosity glass-bead (c & d), and high-porosity glass-bead (e & f) specimens. The prediction is based on the previously inferred microstructure of samples and fluid properties. The predictions are compared with the measurements (solid symbols).

### 8.3.4 Dispersion

8.3.4.1 The amount of dispersion

In *Chapter 1*, alternative ways defining the amount of dispersion have been reviewed. In this study, considering the way of expressing the influence of fluid saturation at each frequency, *i.e.*, percentage change in modulus, the amount of dispersion in shear modulus $D_G$ and Young's modulus $D_E$ are defined as:

$$D_G = \Delta G_{HF} - \Delta G_{LF}, \tag{8.16}$$

$$D_E = \Delta E_{HF} - \Delta E_{LF}\ , \tag{8.17}$$

where $\Delta G_{HF}$ and $\Delta E_{HF}$ are the percentage change in shear and Young's modulus at MHz, respectively; and $\Delta G_{LF}$ and $\Delta E_{LF}$ are the percentage change in shear and Young's modulus at mHz, respectively.

The change in modulus due to fluid saturation is presented in Fig. 8.7 at each frequency. For shear modulus, generally speaking, the largest dispersion appears at the lowest differential pressure of 10 MPa. For the glass-rod specimen at a differential pressure of 10 MPa, considering the uncertainty of the change in modulus of about 1% at each frequency, water saturation gives zero dispersion between mHz and MHz frequencies, whereas argon saturation provides a dispersion of shear modulus of ~ 3% between these frequencies. The observation at 1.5 kHz reveals half the total dispersion, *i.e.*, 1.5%, for argon saturation (Fig. 8.7a). For this glass-rod specimen, the analysis in *Section 8.3.3* is recalled that saturated isolated conditions prevail at all frequencies for water saturation, whereas argon saturation probes saturated isobaric, transitional, and saturated isolated conditions at sub-Hz, kHz, and MHz frequencies, respectively.

For the argon saturated low-porosity glass-bead specimen, a dispersion of ~ 3% is observed for shear modulus at a differential pressure of 10 MPa between mHz and MHz frequencies. Water saturation doubles the dispersion, giving ~ 6%, between mHz and MHz frequencies (Fig. 8.7c). These reflect the transition, for both argon and water saturations, to saturated isolated condition. The dispersions in shear modulus are ~ 8% and ~ 9% for argon and water saturation, respectively, between mHz and MHz frequencies on a high-porosity glass-bead specimen at the differential pressure of 10 MPa (Fig. 8.7e), reflecting the transition from saturated isobaric to saturated isolated conditions.

The second distinct feature of shear dispersion is that the amount of dispersion is suppressed by pressure. The highest dispersion, observed at the lowest differential pressure of 10 MPa, is gradually reduced by increasing pressure on all types of samples with either argon or water saturation. The role of saturating fluid explains the dispersion and the amount

of fluid, therefore, is directly linked to the extent of such influence on the elastic behaviour of the cracked sample. The space of cracks is expected to be gradually reduced by increasing pressure, resulting in less fluid to be contained in the sample to play the role in dispersion. As a result, the shear dispersion $D_G$ is a function of pressure. Winkler (1985, 1986) noticed a similar trend of reduced dispersion of P- and S-wave velocities by elevated pressure on Berea sandstones with brine and oil saturation. Adelinet *et al.* (2010) and Fortin *et al.* (2014) have also found a similar pressure dependence of bulk modulus dispersion between seismic and ultrasonic frequencies on Icelandic basalt. This relation is also noticed by Pimienta *et al.* (2015) on Fontainebleau sandstones.

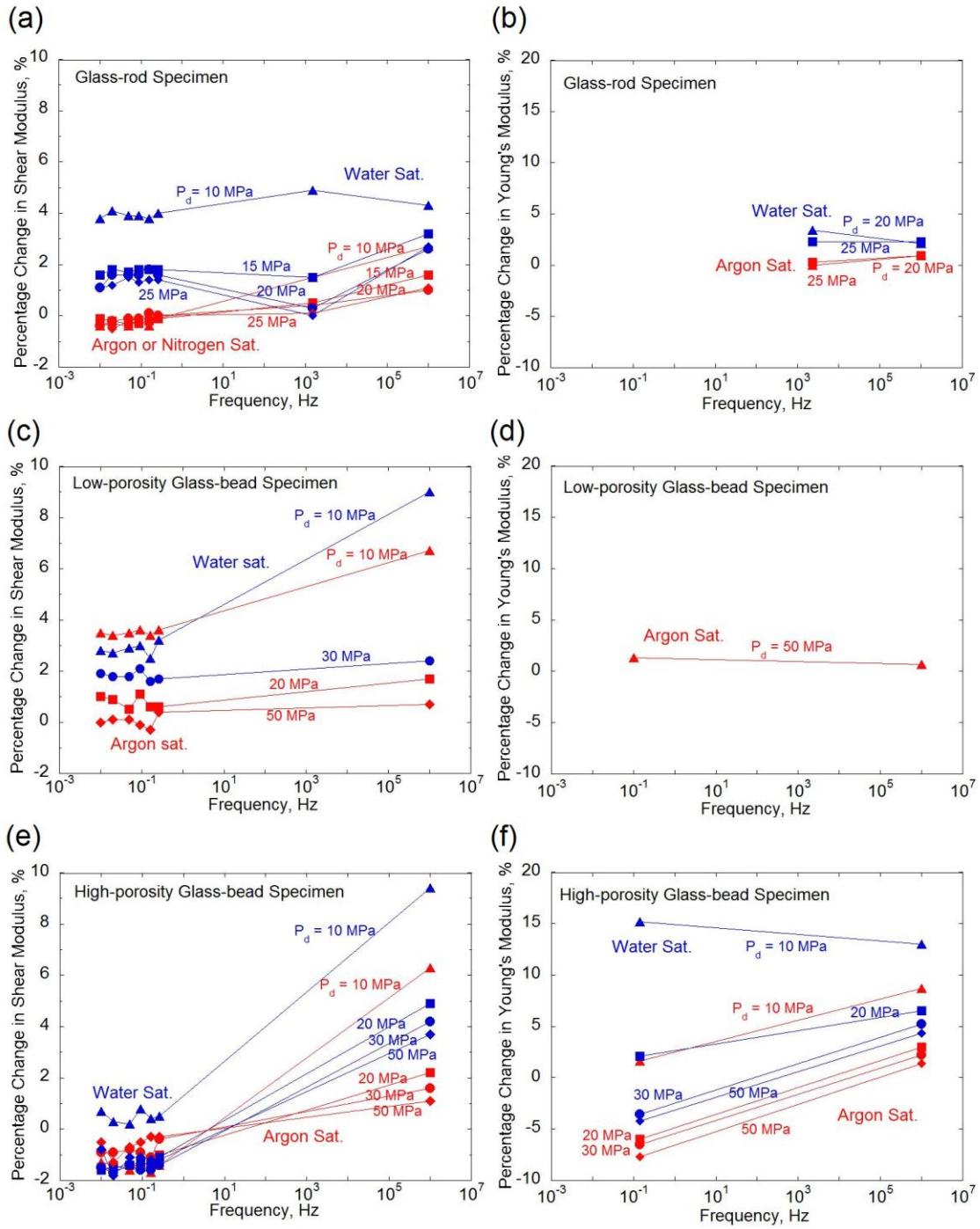


**Figure 8.7** Percentage change in either shear or Young's modulus of (a & b) the glass-rod specimen; (c & d) the low-porosity glass-bead specimen; and (e & f) the high-porosity glass-bead specimen with either argon (red) or water (blue) saturation at differential pressures below 50 MPa, at frequencies from mHz to MHz.

No change in bulk modulus is expected during the transition from the saturated isobaric regime to the saturated isolated regime for a medium containing only pores or only cracks, but may arise from squirt flow between cracks and pores (Fig. 1.3). The dispersion of bulk modulus is expected to be passed on to the dispersion of Young's modulus. A systematically higher percentage change in Young's modulus is noticed at higher frequency on the high-

porosity glass-bead specimen, compared with the almost non-dispersive nature on the other two types of samples (Fig. 8.7 b, d, f). This might be explained as that the high-porosity glass-bead specimen has the largest volume of contrasting inclusions (pores and cracks) to provide the highest dispersion of Young's modulus by squirt flow.

Taking the derivative of Eq. (3.73), the fractional change of bulk modulus $\delta K/K$ can be expressed in terms of the fractional changes of Young's modulus $\delta E/E$ and shear modulus $\delta G/G$.

$$\frac{\delta K}{K} = \left(\frac{\delta E}{E} - f_G \frac{\delta G}{G}\right) / (1 - f_G)\,, \tag{8.18}$$

where $f_G = \frac{E}{3G} = \frac{3K}{3K+G}$. In this way, the fractional change of bulk modulus for the high-porosity (~ 5%) glass-bead specimen (Fig. 8.8) is estimated from the measured percentage changes in shear and Young's moduli (Fig. 8.7 e & f). For soda-lime-silica glass, the value of the coefficient $f_G$, taking $E$ = 70 GPa and $G$ = 30 GPa, is about 0.8.

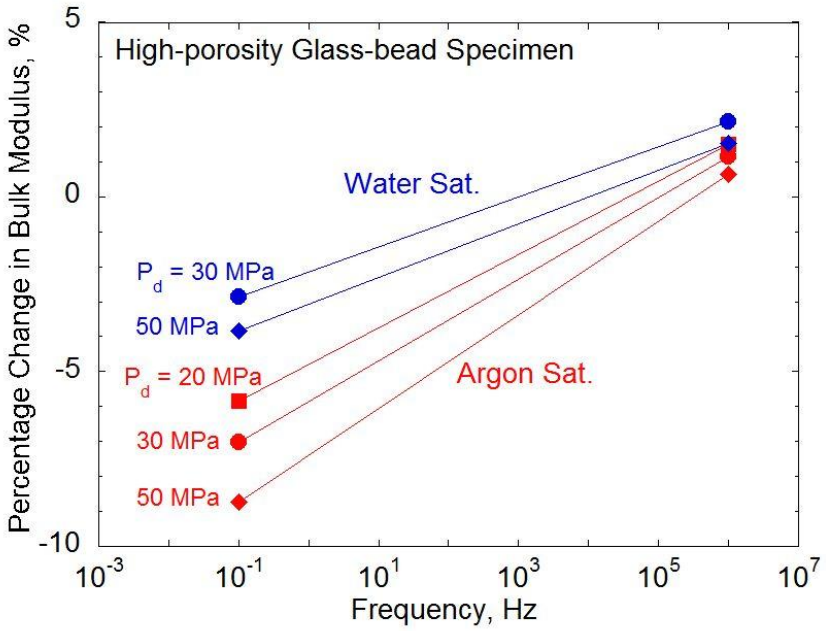


**Figure 8.8** Percentage change in bulk modulus of the high-porosity (~ 5%) glass-bead specimen, which is calculated from the measured percentage changes in shear and Young's moduli, with either argon (red) or water (blue) saturation at differential pressures below 50 MPa, at frequencies from mHz to MHz.

A dispersion of 5 -10% in bulk modulus is observed for both argon and water saturation between 0.1 Hz and 1 MHz (Fig. 8.8). This further strengthens the case for squirt flow between the connected cracks and pores during the transition from saturated isobaric to saturated isolated regime.

The maximum dispersion of shear, Young's, and bulk moduli related to squirt flow is on the order of 10% in this study. The maximum dispersion reported in the past research (Table 8.4) shows it is quite common to observe the dispersion of P- and S-wave velocity of ~ 20%, and up to 40% for the dispersion of bulk modulus. In relating the percentage change of wave speeds and moduli, one needs to remember that:

$$v^2 \sim \frac{M}{\rho}, \tag{8.19}$$

$$2\frac{\delta v}{v} = \frac{\delta M}{M}, \tag{8.20}$$

where $v$ is the velocity, $M$ is the modulus, and $\rho$ is the density. This indicates the fractional change in modulus should be twice that in wave speed for the same medium.

The dispersion of shear modulus of ~2% is reported by Adam *et al.* (2006) on brine saturated carbonate. But the shear modulus reported is calculated from the measured Young's modulus and Poisson's ratio. This again highlights the importance of this study to provide a direct measurement on the dispersion of shear modulus.

Table 8.4 Dispersion in Literature

| Authors | Sample Material | Saturant | Low-frequency Limit | High-frequency Limit | Max. Local-flow Dispersion |
|---|---|---|---|---|---|
| King (1966); Winkler (1986) | Berea sandstone | kerosene | Gassmann | Ultrasonic | Dispersion of $V_P$ = 10%<br>Dispersion of $V_S$ = 10%<br>($P_d$ = 5 MPa, $\phi$ = 20.5%) |
| Murphy (1984); Winkler (1986) | Spirit river sandstone | water | Gassmann | Ultrasonic | Dispersion of $V_P$ = 16%<br>Dispersion of $V_S$ = 16%<br>($P_d$ = 5 MPa, $\phi$ = 4.6%) |
| Murphy (1984) | Microcracked granite | water | 2 kHz, Resonant bar | 7 kHz, Resonant bar | Dispersion of $V_E$ = 5%<br>($\phi$ = 0.8%) |

$V_p$: P-wave velocity; $V_s$: S-wave velocity; $V_E$: extensional velocity; $P_d$: differential pressure; $\phi$: porosity.

Table 8.4 (Continued) Dispersion in Literature

| Authors | Sample Material | Saturant | Low-frequency Limit | High-frequency Limit | Max. Local-flow Dispersion |
|---|---|---|---|---|---|
| Winkler (1985) | Berea sandstone | Brine | Low-frequency Biot | 0.4 MHz, ultrasonic | Dispersion of $V_P$ = 4.4%, Dispersion of $V_S$ = 4.6% ($P_d$ = 5 MPa, $\phi$ = 20.3%) |
| | | Oil | | | Dispersion of $V_P$ = 17.1%, Dispersion of $V_S$= 19.0% ($P_d$ = 5 MPa, $\phi$ = 20.3%) |
| | Fused glass beads (uncracked) | Brine | | | Dispersion of $V_P$ = 1.5%, Dispersion of $V_S$ = 4.6% ($\phi$ = 31.5%) |
| | | Oil | | | Dispersion of $V_P$ = -0.2%, Dispersion of $V_S$ = 0.6% ($\phi$ = 31.5%) |

$V_p$: P-wave velocity; $V_s$: S-wave velocity; $\phi$: porosity; $P_d$: differential pressure.

Table 8.4 (Continued) Dispersion in Literature

| Authors | Sample Material | Saturant | Low-frequency Limit | High-frequency Limit | Max. Local-flow Dispersion |
|---|---|---|---|---|---|
| Batzle *et al.* (2006) | Foxhills Sandstone | Glycerine | 10 Hz, extensional forced oscillation | 1 MHz, ultrasonic | Dispersion of $V_P \approx 40\%$ ($t$ = 63 ℃, $\phi$ = 26%) |
| Adam *et al.* (2006) | Carbonate | Brine | Gassmann for shear modulus, extensional forced oscillation at 100 Hz for bulk modulus | 0.8 MHz, ultrasonic | $D_G \approx 2\%$ ($P_d$ = 31 MPa, $\phi$ = 1.6%)<br>$D_K \approx 40\%$ ($P_d$ = 31 MPa, $\phi$ = 34%) |
| David *et al.* (2014) | Fontainebleau sandstone | Water | Gassmann | 1 MHz, ultrasonic | $D_K \approx 30\%$ ($P_d$ = 5 MPa, $\phi$ = 13%)<br>$D_K \approx 17\%$ ($P_d$ = 5 MPa, $\phi$ =4%) |
| | | Glycerine | | | $D_K \approx 20\%$ ($P_d$ = 5 MPa, $\phi$ =13%)<br>$D_K \approx 10\%$ ($P_d$ = 5 MPa, $\phi$ = 4%) |

$V_p$: P-wave velocity; $\phi$: porosity; $t$: temperature; $D_G$: shear modulus dispersion; $D_K$: bulk modulus dispersion; $P_d$: differential pressure.

Table 8.4 (Continued) Dispersion in Literature

| Authors | Sample Material | Saturant | Low-frequency Limit | High-frequency Limit | Max. Local-flow Dispersion |
|---|---|---|---|---|---|
| Fortin *et al.* (2014) | Icelandic basalt | Water | Gassmann | 1 MHz, ultrasonic | $D_K \approx 40\%$ ($P_d$ = 10 MPa, $\phi_{cr}$ = 1%, and $\phi_{eq}$ = 7%) |
| Mikhaltsevitch *et al.* (2014) | Sandstone | Water | 0.1 Hz, extensional forced oscillation & Gassmann | 120 Hz, extensional forced oscillation | $D_E \approx 5\%$<br>$D_K \approx 13\%$<br>$D_G \approx 0\%$<br>($P_d$ = 2.5 MPa) |
| Pimienta e*t al.* (2015) | Fontainebleau sandstone | Glycerine | 0.4 Hz, hydrostatic forced oscillation & Gassmann | 0.5 MHz, ultrasonic | $D_K \approx 36\%$ ($P_d \approx$ 1 MPa, $\phi$ = 7%) |

$\phi_{cr}$: crack porosity; $\phi_{eq}$: equant porosity; $\phi$: porosity; $D_E$: Young's modulus dispersion; $D_G$: shear modulus dispersion; $D_K$: bulk modulus dispersion; $P_d$: differential pressure.

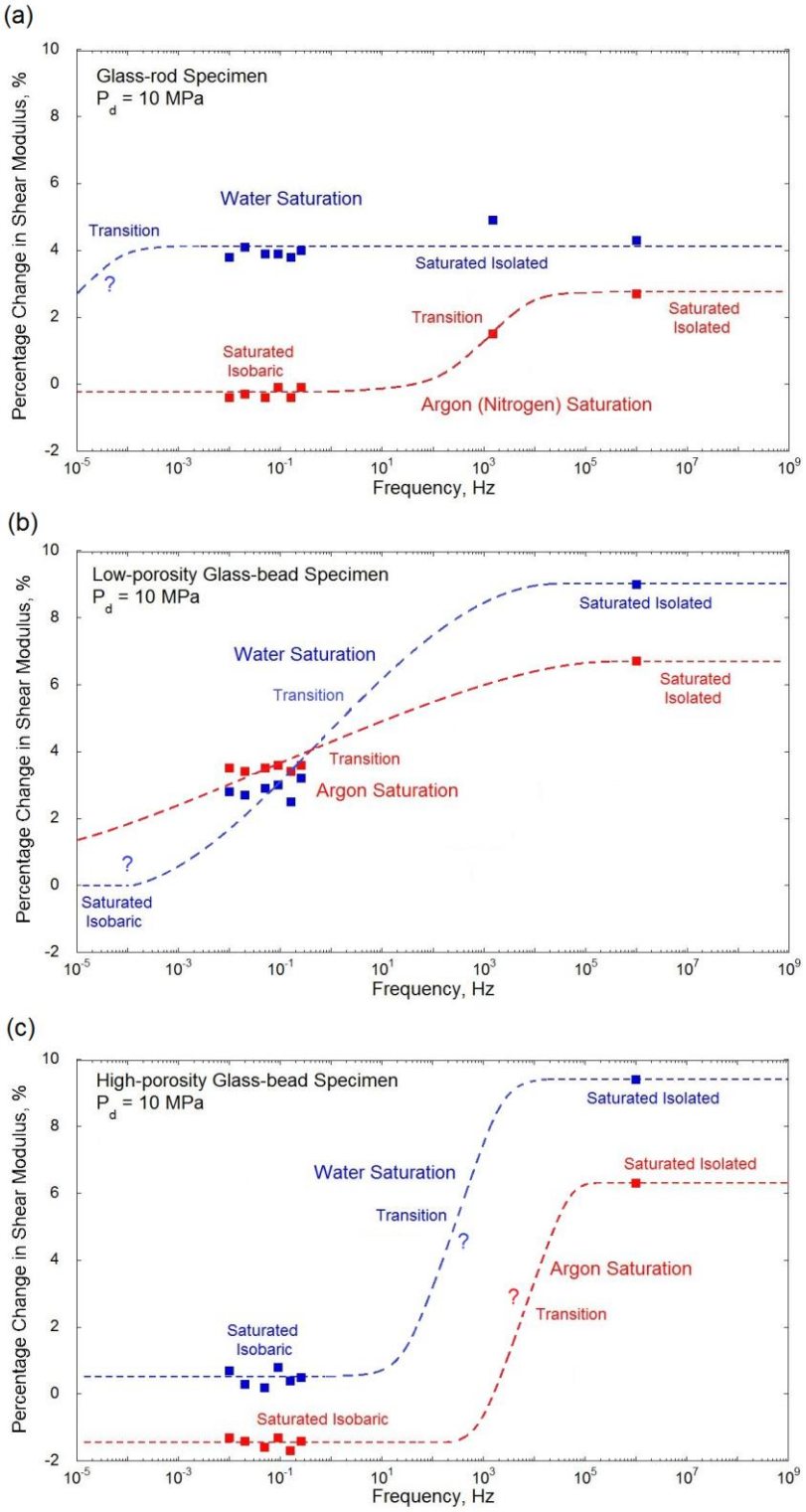


**Figure 8.9** Percentage change in shear modulus, as a function of frequency, is plotted at differential pressure of 10 MPa for the (a) glass-rod, (b) low-porosity glass-bead, and (c) high-porosity glass-bead specimens. The fluid-flow regimes and related transitions are labelled based on the discussion in *Section 8.3.3*. The conceptual dashed lines are constrained by the observation in a semi-quantitative way. The segment with a question mark indicates the absence of constraint.

#### 8.3.4.2 The frequency bandwidth of transition

In order to reconcile the observed dispersion of shear modulus with the conceptual framework of fluid-flow regimes summarised in *Section 1.2.4*, the fluid flow regimes are assigned to each dataset based on discussions in *Section 8.3.3*, and the conceptual lines (dashed) are added to the observations at differential pressure of 10 MPa (Fig. 8.9). In this way, it is easier to identify the frequency bandwidth of fluid-flow regime transition and the shift of characteristic frequency due to the change in fluid viscosity.

A broad transition is inferred from the measurements on the samples, spanning a few orders of magnitude in frequency (Fig. 8.9). The characteristic frequency between the saturated isobaric and the saturated isolated regimes depends strongly on the aspect ratio of cracks, as the frequency is proportional to the cube of crack aspect ratio. In reality, crack aspect ratios commonly vary within 1 – 2 orders of magnitude. The breadth of the distribution of crack aspect ratios reflects not only the initial aspect ratio distribution at ambient conditions but also the influence of pressure on crack aspect ratios. To this end, a much wider transition zone spanning a few orders of magnitude in frequency would be reasonable.

#### 8.3.4.3 Dispersion and fluid viscosity

In hydro-mechanical models, the fluid-flow related dispersion, without exception, depends on fluid viscosity. The relation is obvious as the timescale of fluid flow depends on the viscosity of that fluid (Eq. 8.14 - 8.15). A number of previous studies have proven that the fluid-flow related dispersion observed between mHz and MHz in laboratory, regardless of the global flow (Spencer, 1981; Dunn, 1986 & 1987; Pimienta *et al.*, 2015) or the local flow (Jones & Nur, 1983; Batzle *et al.*, 2006), the characteristic frequencies are inversely proportional to the fluid viscosity.

In this study, two fluids (argon and water) with contrasting viscosity are used to vary the timescale of fluid flow. At the fluid pressure of 10 MPa and room temperature, the viscosities of argon and water are 29.2 μPa s and 1.0 mPa s, respectively, differing ~ 30-fold. The characteristic frequency with argon saturation is then expected to be 1 – 2 orders of magnitude higher than that of water saturation. The results for the glass-rod specimen provide qualitative support for this argument, *i.e.*, a less viscous fluid (argon) shifting the characteristic frequency of squirt flow to a higher frequency.

Quantitatively however, the interpretation presented in Fig. 8.9a suggests that the squirt flow transitions for argon and water saturation are separated by at least 6 orders of magnitude, significantly more than can be explained by the difference in viscosity. One possible explanation is that the crack aspect ratio at the same differential pressure may vary

between two consecutive pressure cycles. The glass-rod specimen fabricated from fully dense soda-lime-silica glass may slightly differ from the glass-bead specimens in interaction with polar fluid. The surface of some cracks of the glass-rod specimen may interact with the unwanted moisture in the pressure vessel and pore-fluid lines during argon saturation. Some of the cracks may refuse to fully open during unloading and give lower aspect ratios by 1 – 2 orders of magnitude at the same differential pressure in the following pressure cycle with water saturation. The influence of lower aspect ratio is amplified by the cubic relationship between the characteristic frequency and the aspect ratio. The phenomenon is absent on both glass-bead specimens, probably due to the different way of sample fabrication, *i.e.*, fusing loose glass beads. For the low-porosity glass bead specimen, however, similar squirt-flow frequencies are observed with both fluids, inconsistent with the predicted shift of transition frequency due to the change in fluid viscosity (Fig. 8.9b).

#### 8.3.4.4 Dispersion and sample microstructure

Dispersion and attenuation used to be commonly related to grain boundary friction as a microscopic mechanism on polycrystalline rocks. Winkler *et al.* (1979) explicitly demonstrated that this mechanism is only related to strain amplitude greater than $10^{-6}$ at low confining pressure on natural sandstones. The mechanism would be applicable to both dry and fluid-saturated rocks as long as sliding occurs at grain boundaries. If this mechanism is applicable, at a higher frequency, more relative displacement is expected to occur between contacting grains within a given period of time, converting more energy into heat. At the early stage of this study, a series tests beyond differential pressure of 10 MPa has been conducted on the synthetic samples with various strain amplitudes (on the order of $10^{-6}$) by varying driver voltages. No strain-amplitude dependence of modulus has been noticed at seismic frequencies. This excludes the grain boundary friction as the source of attenuation, leaving focus on the fluid-flow related mechanism only.

This study not only focuses on the fluid-flow related dispersion on a single sample with particular microstructure, but also attempts to explore the influence of sample microstructure on dispersion by measuring on a series of samples with various equant porosities.

If squirt flow is an intergranular phenomenon between the more compressible cracks and much less compressible equant pores, the magnitude of dispersion, therefore, can be manipulated by varying the concentration ratio of these two contrasting inclusions. The measurements on the series of synthetic samples reveal that the amount of shear dispersion, regardless of saturant, increases with increasing equant porosity (Table 8.5). To understand the underlying physical mechanism, the relevant theories are carefully examined.

As previously argued, inclusion-based models, which give emphasis on the inclusion geometries, are best suited to analysing the influence of microstructure on dispersion. The derivation in O'Connell and Budiansky (1977) is based on a group of randomly distributed ellipsoidal cracks with no spherical pores present. In contrast, Endres and Knight (1997), which assumes the presence of both compliant cracks and rigid spherical pores, seems to be more applicable to this study. Endres and Knight (1997) and its followers, *e.g.*, Adelinet *et al.* (2011), Chapman *et al.* (2002), assume a fixed quantity of total porosity but varying crack fractions, defined as the volumetric ratio between the cracks and spherical pores. These models predict zero bulk dispersion when the crack volume fraction equals either 0 or 1, corresponding to the presence of pure spherical pores or pure cracks, respectively. A peak of bulk dispersion appears somewhere between the two extreme crack fractions. However, the shear dispersion increases with the crack fraction monotonically. In this study, the crack volume fractions of glass-bead specimens are close to 0.1 and the aspect ratios are ~$10^{-3}$. The observed shear dispersion is below 10%, lower than the predicted value of between 10% and 20% (Endres & Knight, 1997; Adelinet *et al.*, 2011). The amount of shear dispersion is also found to increase with decreasing crack fraction by progressively introducing equant pores in the total amount of inclusions. The finding of this research is inconsistent with Endres and Knight (1997) and its followers. The discrepancy probably results from the basic assumption of random distribution of cracks in these models, whereas cracks with preferred orientations are noticed on the synthetic specimens.

Table 8.5 Dispersion in Shear Modulus

| Specimen Type | Equant Porosity | Dispersion in Shear Modulus between mHz and MHz * | |
|---|---|---|---|
| | | Argon Saturation | Water Saturation |
| Glass-rod specimen | 0% | ~ 3% | 0% |
| Low-porosity glass-bead specimen | ~ 2% | ~ 3% | ~ 6% |
| High-porosity glass-bead specimen | ~ 5% | ~ 8% | ~ 9% |

*All the values of dispersion in shear modulus are determined at the differential pressure of 10 MPa.

In sample preparation, the process of introducing thermal cracks by quenching results in particular orientations of cracks and the quantity of cracks cannot be precisely managed. Considering the uncertainty in orientations and interconnections of cracks, the ambient crack porosities, which are 0.35%, 0.08%, and 0.14%, respectively, for the glass-rod, low-porosity glass-bead, and high-porosity glass-bead samples, would probably be close enough to have a similar level of influence on the elasticity. The increase in equant porosity is expected to do nothing but simply increase the volume of stiffer region to contrast the compliant cracks, allowing more crack-pore relaxation, hence a higher level of dispersion under shear stress.

### 8.3.5 Attenuation

In linear viscoelastic materials, the Kramers-Kronig relation links dispersion of modulus or velocity to attenuation. This theoretical constraint is commonly used to check the causality between dispersion and attenuation. In practice, if dispersion of modulus and part of attenuation peak are detected by experiments, the Kramers-Kronig relation is applied to attenuation peak to check the validity of dispersion or vice versa (Adam *et al.*, 2009; Mikhaltsevitch *et al.*, 2014).

In this study, the attenuation measured by forced oscillation is consistently low ($1/Q < 0.005$). The highest and most systematically frequency and pressure dependent dissipation in forced torsional oscillation was observed for the low-porosity glass-bead specimen (Fig. 5.4).

There, dissipation increases consistently towards lower frequencies towards a possible dissipation peak located beyond the experimental range at $f < 0.01$ Hz. At any given frequency, the measured dissipation decreases with increasing pressure as expected with crack closure. These observations of higher dissipation than for the other specimens are not inconsistent with the interpretation of the fluid-saturated moduli as indicative of the squirt flow transition. The limited detecting frequency bandwidth (less than two orders of magnitude in frequency) just samples a small part of the attenuation peak, which is expected to span eight orders of magnitude in frequency. A broader detecting frequency is needed in order to recover the entire attenuation peak.

The attenuations for the argon saturated glass-rod and high-porosity glass-bead specimens are also noticed to increase with reduced pressure at mHz frequencies (Fig. 5.2 & 5.7), explained as gradually re-opened cracks with reduced differential pressure to contain more fluid, hence higher fluid-flow related dissipation.

Strong dissipation at low differential pressures (< 5 MPa) for the glass rod specimen at kHz frequency is an order of magnitude higher than for forced oscillation tests (Fig. 7.3). For nitrogen saturation, the high dissipation is consistent with the suggestion from the modulus data of transition between saturated isobaric and saturated isolated conditions. However, dissipation is even higher for water saturation – where no such transition is being invoked. The attenuation is suppressed by higher pressure when fluid is expelled from the closed cracks.

# Chapter 9 Conclusions and Future Work

## 9.1 Summary of Results and Discussion

In order to explore the long-standing issue of the fluid-flow related dispersion in elastic properties of a fluid-saturated rock, a broadband measurement (mHz – MHz) has been conducted on a suite of synthetic cracked glass samples with various equant porosities, saturated with either argon or water. In such a manner, the influence of fluid viscosity and sample microstructure on dispersion has been studied over the entire frequency band. The experimental results have been compared with relevant fluid-substitution theories, such as the poroelastic theory, the effective medium theory, and their derivatives, in order to gain further insight into the behaviour of the fluid-saturated sample. A number of conclusions are drawn from this study.

Upgrade of arrangements for computer control and data acquisition on the Jackson-Paterson Attenuation Apparatus

The computer control and data acquisition system on the Jackson-Paterson Attenuation Apparatus has been successfully upgraded, in order to 1) achieve improved resolution in the measurement of signals in the forced oscillation by using an 18-bit A/D converter; 2) to develop the capacity for remote switching of operation between torsional and flexural modes of oscillation; 3) to implement improved low-pass filtering of the displacement-time series, adaptively varied with imposed oscillation frequency. With a series of tests, a stable performance has been achieved for the new system with the establishment of improved procedure for data acquisition and formatting.

Fabrication and characterisation of cracked glass media

The recipe of fabricating cracked soda-lime-silica glass-rod specimen and cracked glass-bead specimens with specified equant porosity have been successfully developed. Mensuration and mechanical testing of the resulting materials before and after thermal cracking directly constrain both the total crack density and the effect on the elastic moduli of the newly introduced cracks. There is some evidence of preferred orientation of the cracks reflecting the cylindrical symmetry of the thermal stress field. The synthetic samples with well characterised microstructure provide useful analogues on which the fluid saturation theories can be systematically tested. The co-existence of cracks and spherical pores with contrasting stiffness maximises the chance to capture the grain-scale squirt flow, and the specimen with cracks only provides useful contrast.

Evidence for pressure-induced crack closure

The measured elastic moduli increase systematically with increasing pressure towards a pressure-independent plateau at the highest experimentally accessed pressures ~ 100 MPa. Permeabilities measured with the transient decay method and argon pore fluid are found to decrease systematically with increasing pressure towards a plateau at the highest pressures. The pressure-dependent modulus and permeability provide clear evidence of pressure-induced crack closure on all cracked samples. Although the pressures for crack closure on the glass-bead specimens generally agree with the theoretical estimates, the absence of observation at lower pressures (< 10 MPa) complicates the robust estimation of the distribution of crack aspect ratios. Compared with the glass-bead specimens, a much larger modulus deficit remains in the glass-rod material at ~ 100 MPa pressure – suggesting more fragmentation associated with more energetic fracturing in the medium with zero initial porosity.

Access to undrained conditions

The specimens are of consistently very low permeability ranging with (argon) differential pressure between $10^{-19}$ and $10^{-18}$ $m^2$, and are an order of magnitude lower for water as pore fluid. Such low permeabilities provide access to conditions ranging with increasing frequency between saturated isobaric and saturated isolated – free from the complication of draining by stress-induced global fluid flow. For the forced-oscillation tests, the prior measurement of permeability by the transient decay method, guarantees uniform pore pressure throughout the low-permeability specimen.

Influence of fluid saturation on elastic properties

Increases in shear and Young's moduli associated with fluid saturation (either argon or water) have been observed on all three types of synthetic cracked samples at MHz frequency. This again confirms the limitation of a narrow poroelastic theory, *i.e.*, the Gassmann equation, which proposes a shear modulus that is unchanged on fluid saturation. The effect of the inhibition of local squirt flow at sufficiently high frequencies must be taken into account as dealing with the fluid-saturated seismic properties for both P- and S-waves.

Identification of fluid-flow regimes

Various fluid-flow regimes have been accessed on the three types of cracked samples, the identification of which is based on the mechanical response to fluid saturation and the estimated characteristic frequencies separating different fluid-flow regimes. The saturated isolated condition has been probed on all the samples with either argon or water saturation at MHz frequency. For the water-saturated glass-rod specimen, the saturated isolated condition has been observed to be maintained across the mHz-MHz frequency range, whereas, for

argon saturation, the saturated isobaric regime and the squirt-flow transition have been probed at mHz and kHz frequencies, respectively. A transition between the saturated isobaric and saturated isolated regimes has also been noticed in mHz-Hz forced oscillation tests on the low-porosity glass-bead specimen with either argon or water saturation. For such low permeability samples, the Gassmann equation may thus be invalid even at seismic frequencies with water saturation. This emphasises that caution must be taken in the application of the Gassmann equation even at the commonly believed "appropriate" frequency, *i.e.*, seismic frequencies. The high-porosity glass-bead specimen with both argon and water saturation is maintained in the saturated isobaric regime at mHz frequency, and the Gassmann equation also seems to underestimate the influence of water saturation on the Young's modulus.

Modulus dispersion

The amount of shear dispersion is greatest at the lowest differential pressure of 10 MPa for all kinds of samples, and is progressively suppressed by increasing pressure. This is consistent with pressure-induced crack closure diminishing the role of fluid-filled cracks. The amount of shear dispersion reaches as much as ~10% for either argon or water saturation between mHz and MHz frequency. The Young's modulus is most complete on the high-porosity glass-bead specimen on which a similar dispersion is observed between mHz and MHz frequency. The transition between fluid-flow regimes may possibly span a few orders of magnitude in frequency, explained by the extreme sensitivity of the characteristic frequency to crack geometry. Fluid with higher viscosity (water *vs.* argon) shifts the characteristic frequency for squirt flow to a lower value as expected from theoretical expressions for the characteristic frequencies for fluid flow. The shear dispersion with either argon or water saturation increases with increasing equant porosity (or decreased crack fraction) on these synthetic cracked samples.

Attenuation

Dissipation measured in forced oscillation at mHz frequencies is consistently lower than 0.005. However, for the low-porosity glass-bead specimen, $Q^{-1}$ increases with decreasing frequency towards a possible peak at frequency < 0.01 Hz, and decreases with increasing pressure. More intense dissipation, by an order of magnitude, is observed at low differential pressures in the kHz resonance measurements on the fluid-saturated glass-rod specimen. These observations of increased attenuation may correlate with transitions between the fluid flow regimes.

## 9.2 Implication for the Interpretation of Seismological Data in the Field

This experimental study has explored and quantified the difference between the Gassmann regime and the conventional laboratory measurements at ultrasonic frequencies. The dispersion in shear modulus and Young's modulus could be as high as ~ 10% at differential pressure of ~ 10 MPa, and is gradually reduced by increasing differential pressure. This magnitude of dispersion may slightly vary from case to case depending on the microstructure of the sample, but this experimental outcome at least provides a quantitative estimate of the extent by which inhibition of stress-induced local squirt flow influences the elastic properties of fluid-saturated media.

On the other hand, the widespread acceptance of the validity of the Biot-Gassmann theory also needs to be carefully treated, as the broadband measurement reveals shear stiffening even at mHz frequencies on the glass-rod and low-porosity glass-bead samples with very low crack aspect ratios. The active seismic method is performed at tens of Hz in the field. This level of frequency is normally taken for granted as the safe frequency for the Gassmann equation. The finding of this study reminds the users of the Gassmann equation that shear stiffening can even occur at mHz frequencies in rocks of sufficiently low permeability.

The interpretation of the seismic data in the regions saturated with pore fluids, such as the reservoirs for oil and gas, geothermal, or carbon dioxide sequestration, must take into account the influence of time-dependent fluid flow on seismic wave velocities and attenuation.

## 9.3 Future Work

Among a range of factors that could influence the elastic behaviour of fluid-saturated rocks, only the geometry of inclusions, fluid viscosity and frequency have been emphasised in this study. The other factors, such as the chemical interaction between the solid and fluid phases, the temperature related matrix or fluid phase transformation, mineral melting, preferred orientation of cracks, among many others, have not been explored. The experiment has been designed to minimise but not necessarily completely exclude other potential factors, for instance, the observed preferred orientation of cracks in the samples, and chemical interaction between water as polar pore fluid and the silica-rich glass matrix, especially at low permeabilities. This sheds light on the possible improvement in future. The elastic anisotropy arising from the preferred orientation of thermal cracks could be explored, along with the use of non-polar pore fluids of relatively high viscosity.

There is a much larger residual modulus deficit evident in the dry data at the highest pressure for the glass-rod specimen than for the glass-bead materials. This is consistent with the results from the DEM modelling that the glass-rod specimen with the highest measured crack porosity (0.35%) shows the smallest amount of closable porosity (0.007%). This comparison suggests that pressure-induced crack closure is much more difficult in the glass-rod materials – presumably because there has been more irreversible damage (fragmentation) during thermal cracking of the glass-rod material. This raises the possibility that thermal fracturing is a somewhat different process in the absence of pre-existing pores. Accordingly, it could be very interesting in future work to quench glass-rod material from lower temperatures than 500 ℃ in the expectation that the resulting cracks might be more readily closed by applied pressure.

Another direction of future work is to minimise and/or better correct for any interfacial compliance, and to improve the modelling of flexural oscillation data in part by introducing the more appropriate cantilevered rather than propped boundary conditions at the lower end of the beam on the Jackson-Paterson Attenuation Apparatus.

In addition, more inter-laboratory comparison of data obtained with complementary techniques, such as the Spencer- and ENS-type low-frequency instruments for uniaxially extensional/compressional and hydrostatic mode forced oscillations, respectively, on shared materials is an important part of the way forward. In such a way, a complete depiction of the transition between the saturated isobaric and the saturated isolated regime is promised.

# REFERENCES


Adam, L., M. Batzle, and I. Brevik, 2006, Gassmann's fluid substitution and shear modulus variability in carbonates at laboratory seismic and ultrasonic frequencies: *Geophysics*, **71**, F173-F183.

Adam, L., and M. Batzle, 2008, Elastic properties from laboratory measurements at seismic and ultrasonic frequencies: *The Leading Edge, Special Section: Carbonates*, 1026-1032.

Adam, L., M. Batzle, K. T. Lewallen, and K. van Wijk, 2009, Seismic wave attenuation in carbonates: *Journal of Geophysical Research*, **114**, B06208.

Adelinet, M., J. Fortin, Y. Guéguen, A. Schubnel, and L. Geoffroy, 2010, Frequency and fluid effects on elastic properties of basalt: experimental investigations: *Geophysical Research Letters*, **37**, L02303.

Adelinet, M., J. Fortin, and Y. Guéguen, 2011, Dispersion of elastic moduli in a porous-cracked rock: Theoretical predictions for squirt-flow: *Tectonophysics*, **503**, 173-181.

Amalokwu, K., A. I. Best, J. Sothcott, M. Chapman, T. Minshull, and X. Li, 2014, Water saturation effects on elastic wave attenuation in porous rocks with aligned fractures: *Geophysical Journal International*, **197**, 943-947.

Batzle, M., D. Han, and J. Castagna, 1999, Fluids and frequency dependent seismic velocity of rocks: Annual International Meeting, SEG, Expanded Abstracts.

Batzle, M. L., D. Han, and R. Hofmann, 2006, Fluid mobility and frequency-dependent seismic velocity – Direct measurements: *Geophysics*, **71**, N1-N9.

Benson, P., P. Meredith, and A. Schubnel, 2006, Role of void space geometry in permeability evolution in crustal rocks at elevated pressure: *Journal of Geophysical Research*, **111**, B12203.

Berge, P. A., B. P. Bonner, and J. G. Berryman, 1995, Ultrasonic velocity-porosity relationships for sandstone analogs made from fused glass beads: *Geophysics*, **60**, 108-119.

Berryman, J. G., 1995, Mixture theories for rock properties. *In* T. J. Ahrens, eds., Rock Physics and Phase Relations: a Handbook of Physical Constants: American Geophysical Union, Washington, DC, 205-228.

Biot, M. A., 1956a, Theory of propagation of elastic waves in a fluid-saturated porous solid, I. Lower frequency range: *Journal of the Acoustical Society of America*, **28**, 168-178.

Biot, M. A., 1956b, Theory of propagation of elastic waves in a fluid-saturated porous solid – II: Higher frequency range: *Journal of the Acoustical Society of America*, **28**, 179-191.

Bourbié, T., O. Coussy, and B. Zinszner, 1987, Acoustics of porous media: Gulf Publishing Co., Houston, TX.

Bouzidi, Y., and D. R. Schmitt, 2009, Measurement of the speed and attenuation of the Biot slow wave using a large ultrasonic transmitter: *Journal of Geophysical Research*, **114**, B08201.

Brace, W. F., J. B. Walsh, and W. T. Frangos, 1968, Permeability of granite under high pressure: *Journal of Geophysical Research*, **73**, 2225-2236.

Brennan, B. J., and F. D. Stacey, 1977, Frequency dependence of elasticity of rock – test of seismic velocity dispersion: *Nature*, **268**, 220-222.

Brennan, B. J., 1981, Linear viscoelastic behaviour in rocks, *in* F. D. Stacey, M. S. Paterson, and A. Nicolas, eds., Anelasticity in the Earth: American Geophysical Union Geodynamics Series, 4, 13-22.

Budiansky, B., 1965, On the elastic moduli of some heterogeneous materials: *Journal of the Mechanics and Physics of Solids*, **13**, 223-227.

Budiansky, B., and R. J. O'Connell, 1980, Bulk dissipation in heterogeneous media, *In* S. Nemat Nasser, eds., Solid Earth Geophysics and Geotechnology: American Society of Mechanical Engineers, New York, 1-10.

Cadoret, T., D. Marion, and B. Zinszner, 1995, Influence of frequency and fluid-distribution on elastic wave velocities in partially saturated limestones: *Journal of Geophysical Research*, **100**, 9789-9803.

Chapman, M., S. V. Zatsepin, and S. Crampin, 2002, Derivation of a microstructural poroelastic model: *Geophysical Journal International*, **151**, 427-451.

Chen R., F. Lu, Y. Lin, P. Zhao, J. Li and K. Xia, 2009, A critical review of Split Hopkinson Pressure Bar Technique: *Advances in Mechanics*, **39(5)**, 576-587.

Clark, V. A., B. R. Tittmann, and T. W. Spencer, 1980, Effect of volatiles on attenuation (Q-1) and velocity in sedimentary rocks: *Journal of Geophysical Research*, **85**, 5190-5198.

Cleary, M. P., 1978, Elastic and dynamic response regimes of fluid-impregnated solids with diverse microstructures: *International Journal of Solids and Structures*, **14**, 795-819.

Cleary, M. P., I. W. Chen, and S. M. Lee, 1980, Self-consistent techniques for heterogeneous media: *Journal of the Engineering Mechanics Division – ASCE*, **106**, 861-887.

Cnudde V., and M. N. Boone, 2013, High-resolution X-ray computed tomography in geosciences: A review of the current technology and applications: *Earth-Science Reviews*, **123**, 1-17.

Costa Gomes, M. F., and J. P. M. Trusler, 1998, The speed of sound in nitrogen at temperatures between T = 250 K and T = 350 K and at pressures up to 30 MPa: *Journal of Chemical Thermodynamics*, **30**, 527-534.

Darcy, H., 1856, Les Fontaines Publiques de la Ville de Dijon. Paris: Dalmont.

David, E. C., and R. W. Zimmerman, 2011, Compressibility and shear compliance of spheroidal pores: Exact derivation via the Eshelby tensor, and asymptotic expressions in limiting cases: *International Journal of Solids and Structures*, **48**, 680-686.

David, E. C., 2012, The effect of stress, pore fluid and pore structure on elastic wave velocities in sandstones: Ph.D. thesis, Imperial College London.

David, E. C., and R. W. Zimmerman, 2012, Pore structure model for elastic wave velocities in fluid-saturated sandstones: *Journal of Geophysical Research*, **117**, B07210.

David, E. C., J. Fortin, A. Schubnel, Y. Guéguen, and R. W. Zimmerman, 2013, Laboratory measurements of low- and high- frequency elastic moduli in Fontainebleau sandstone: *Geophysics*, **78**, D369-D379.

Delle Piane, C., A. Arena, J. Sarout, L. Esteban, and E. Cazes, 2015, Micro-crack enhanced permeability in tight rocks: An experimental and microstructural study: *Tectonophysics*, **665**, 149-156.

Digby, P. J., 1981, The effective elastic moduli of porous granular rocks: *Journal of Applied Mechanics*, **48**, 803-808.

Ding, P., B. Di, D. Wang, J. Wei, and X. Li, 2014, P and S wave anisotropy in fractured media: Experimental research using synthetic samples: *Journal of Applied Geophysics*, **109**, 1-6.

Domenico, S. N., 1977, Elastic properties of unconsolidated porous sand reservoirs: *Geophysics*, **42**, 1339-1368.

Dullien, F. A. L., 1992, Porous media: fluid transport and pore structure: Academic Press, San Diego, California.

Dunn, K. J., 1986, Acoustic attenuation in fluid-saturated porous cylinders at low frequencies: *Journal of Acoustical Society of America*, **79**, 1709-1721.

Dunn, K. J., 1987, Sample boundary effect in acoustic attenuation of fluid-saturated porous cylinders: *Journal of Acoustical Society of America*, **81**, 1259-1266.

Dvorkin, J., and A. Nur, 1993, Dynamic poroelasticity: a unified model with the squirt and the Biot mechanism: *Geophysics*, **58**, 524-533.

Dvorkin, J., R. Nolen-Hoeksema, and A. Nur, 1994, The squirt-flow mechanism: macroscopic description: *Geophysics*, **59**, 428-438.

Dvorkin, J., G. Mavko, and A. Nur, 1995, Squirt flow in fully saturated rocks: *Geophysics*, **60**, 97-107.

Endres, A. L., and R. J. Knight, 1997, Incorporating pore geometry and fluid pressure communication into modelling the elastic behaviour of porous rocks: *Geophysics*, **62**, 106-117.

Eshelby, J. D., 1957, The determination of the elastic field of an ellipsoidal inclusion, and related problems: *Proceedings of the Royal Society of London A*, **241**, 376-396.

Fortin, J., A. Schubnel, and Y. Guéguen, 2005, Elastic wave velocities and permeability evolution during compaction of Bleurswiller sandstone: *International Journal of Rock Mechanics and Mining Sciences*, **42**, 873-889.

Fortin, J., L. Pimienta, Y. Guéguen, A. Schubnel, E. C. David, and M. Adelinet, 2014, Experimental results on the combined effects of frequency and pressure on the dispersion of elastic waves in porous rocks: *The Leading Edge*, **33**, 648-654.

Gassmann, F., 1951, Uber die Elasticität Poröser Medien [On the elasticity of porous media], Vierteljahrsschrift der Naturforschenden Gesellschaft in Zürich, **96**, 1-23.

Gerlich, D., and G. C. Kennedy, 1978, 2nd pressure derivatives of the elastic moduli of fused quartz: *Journal of Physics and Chemistry of Solids*, **39**, 1189-1191.

Giesche, H., 2006, Mercury porosimetry: a general (practical) overview: *Particle and Particle Systems Characterisation*, **23**, 1-11.

Gilgen, R., R. Kleinrahm, and W. Wagner, 1994, Measurement and correlation of the (pressure, density, temperature) relation of argon: I. The homogeneous gas and liquid regions in the temperature range from 90 K to 340 K at pressures up to 12 MPa: *Journal of Chemical Thermodynamics*, **26**, 383-398.

Gregory, A. R., 1976, Fluid saturation effects on dynamic elastic properties of sedimentary rocks: *Geophysics*, **41**, 895-921.

Griggs, D. T., 1936, Deformation of rocks under high confining pressures: *Journal of Geology*, **44**, 541-577.

Guéguen, Y., and V. Palciauskas, 1994, Introduction to the physics of rocks: Princeton University Press, Princeton, New Jersey.

Guéguen, Y., and J. Sarout, 2011, Characteristics of anisotropy and dispersion in cracked medium: *Tectonophysics*, **503**, 165-172.

Gurevich, B., D. Makarynska, O. B. de Paula, and M. Pervukhina, 2010, A simple model for squirt-flow dispersion and attenuation in fluid-saturated granular rocks: *Geophysics*, **75**, N109 - N120.

Hashin, Z., and S. Shtrikman, 1963, A variational approach to the elastic behaviour of multiphase materials: *Journal of the Mechanics and Physics of Solids*, **11**, 127-140.

Henyey, F. S., and N. Pomphrey, 1982, Self-consistent elastic moduli of a cracked solid: *Geophysical Research Letters*, **9**, 903-906.

Hill, R., 1965, A self-consistent mechanics of composite materials: *Journal of the Mechanics and Physics of Solids*, **13**, 213-222.

Hsieh, P. A., J. V. Tracy, C. E. Neuzil, J. D. Bredehoeft, and S. E. Silliman, 1981, A transient laboratory method for determining the hydraulic properties of 'tight' rocks – I. Theory: *International Journal of Rock Mechanics, Mining Sciences, and Geomechanics Abstracts*, **18**, 245-252.

Jackson, I., H. Niesler, and D. J. Weidner, 1981, Explicit correction of ultrasonically determined elastic wave velocities for transducer-bond phase shifts: *Journal of Geophysical Research,* **86**, *3736-3748*.

Jackson, I., M. S. Paterson, H. Niesler, and R. M. Waterford, 1984, Rock anelasticity measurements at high pressure, low strain amplitude and seismic frequency: *Geophysical Research Letters*, **11**, 1235-1238.

Jackson, I., and M. S. Paterson, 1987, Shear modulus and internal friction of calcite rocks at seismic frequencies: pressure, frequency and grain size dependence: *Physics of the Earth and Planetary Interiors*, **45**, 349-367.

Jackson, I., 1991, The petrophysical basis for the interpretation of seismological models for the continental lithosphere: *Geological Society of Australia Special Publication*, **17**, 81-114.

Jackson, I., and M. S. Paterson, 1993, A high-pressure, high-temperature apparatus for studies of seismic wave dispersion and attenuation: *Pure and Applied Geophysics*, **141**, 445-466.

Jackson, I., H. Schijns, D. R. Schmitt, J. Mu, and A. Delmenico, 2011, A versatile facility for laboratory studies of viscoelastic and poroelastic behaviour of rocks: *Review of Scientific Instruments*, **82**, 064501.

Jaeger, J. C., N. G. W. Cook, and R. W. Zimmerman, 2007, Fundamentals of rock mechanics, Blackwell, Oxford.

Johnson, D. L., and T. J. Plona, 1982, Acoustic slow waves and the consolidation transition: *Journal of Acoustical Society of America*, **72**, 556-565.

Johnston, D. H., M. N. Toksöz, and A. Timur, 1979, Attenuation of seismic waves in dry and saturated rocks: II. Mechanisms: *Geophysics*, **44**, 691-711.

Jones, T. D., and A. Nur, 1983, Velocity and attenuation in sandstone at elevated temperatures and pressures: *Geophysical Research Letters*, **10**, 140-143.

Jones, T. D., 1986, Pore fluids and frequency-dependent wave propagation in rocks: *Geophysics*, **51**, 1939-1953.

Kestin, J., and W. Leidenfrost, 1959, An absolute determination of the viscosity of eleven gases over a range of pressures: *Physica,* **25**, 1033-1062.

King, M. S., 1966, Wave velocities in rocks as a function of changes in overburden pressure and pore fluid saturants: *Geophysics*, **31**, 50-73.

King, M. S., J. R. Marsden, and J. W. Dennis, 2000, Biot dispersion for P- and S-wave velocities in partially and fully saturated sandstones: *Geophysical Prospecting*, **48**, 1075-1089.

King, M. S., and J. R. Marsden, 2002, Velocity dispersion between ultrasonic and seismic frequencies in brine-saturated reservoir sandstones: *Geophysics*, **67**, 254-258.

Kuster, G. T., and M. N. Toksöz, 1974, Velocity and attenuation of seismic waves in two-phase media: Part I. Theoretical formulations: *Geophysics*, **39**, 587-606.

LeRavalec, M. and Y. Guéguen, 1996, High- and low-frequency elastic moduli for a saturated porous/cracked rock – Differential self-consistent and poroelastic theories: *Geophysics*, **61**, 1080-1094.

Lu, C., 1996, Shear mode anelasticity of thermally cracked and fluid-saturated rocks: Ph.D. thesis, Australian National University.

Lu, C., and I. Jackson, 2006, Low-frequency seismic properties of thermally cracked and argon-saturated granite: *Geophysics*, **71**, F147-F159.

McCann, C., and J. Sothcott, 2009, Sonic to ultrasonic Q of sandstones and limestones: Laboratory measurements at in situ pressures: *Geophysics*, **74**, WA93-101.

Madonna, C., and N. Tisato, 2013, A new seismic wave attenuation module to experimentally measure low-frequency attenuation in extensional mode: *Geophysical Prospecting*, **61**, 302-314.

Mallet, C., J. Fortin, Y. Guéguen, and F. Bouyer, 2013, Effective elastic properties of cracked solids: an experimental investigation: *International Journal of Fracture*, **182**, 275-282.

Mavko, G., and A. Nur, 1975, Melt squirt in the asthenosphere: *Journal of Geophysical Research*, **80**, 1444-1448.

Mavko, G. M., and D. Jizba, 1991, Estimating grain-scale fluid effects on velocity dispersion in rocks: *Geophysics*, **56**, 1940-1949.

McLaughlin, R., 1977, A study of the differential scheme for composite materials: *International Journal of Engineering Science*, **15**, 237-244.

Mikhaltsevitch, V., M. Lebedev, and B. Gurevich, 2011, A low-frequency apparatus for characterising the mechanical properties of rocks: 73rd Annual International Conference and Exhibition, EAGE, Extended Abstracts.

Mikhaltsevitch, V., M. Lebedev, and B. Gurevich, 2014, A laboratory study of low-frequency wave dispersion and attenuation in water-saturated sandstones: *The Leading Edge*, **33**, 616-622.

Molyneux, J., and D. R. Schmitt, 2000, Compressional-wave velocities in attenuating media: A laboratory physical model study: *Geophysics*, **65**, 1162-1167.

Moos, D., and M. D. Zoback, 1983, In situ studies of velocities in fractured crystalline rocks: *Journal of Geophysical Research*, **88**, 2345-2358.

Murphy, W. F., 1982, Effects of partial water saturation on attenuation in Massilon sandstones and Vycor porous glass: *Journal of Acoustical Society of America*, **71**, 1458-1468.

Murphy, W. F., 1984, Seismic to ultrasonic velocity drift: intrinsic absorption and dispersion in crystalline rock: *Geophysical Research Letters*, **11**, 1239-1242.

Murphy, W. F., III, K. W. Winkler, and R. L. Kleinberg, 1984, Contact microphysics and viscous relaxation in sandstones, *In* D.L. Johnson, and P. N. Sen, eds., Physics and Chemistry of Porous Media: American Institute of Physics, New York, 176-190.

Nakagawa, S., 2011, Split Hopkinson resonant bar test for sonic-frequency acoustic velocity and attenuation measurements of small, isotropic geological samples: *Review of Scientific Instruments*, **82**, 044901.

Nakagawa, S., T. J. Kneafsey, T. M. Daley, B. M. Freifeld, and E. V. Rees, 2013, Laboratory seismic monitoring of supercritical CO2 flooding in sandstone cores using the Split Hopkinson Resonant Bar technique with concurrent x-ray Computed Tomography imaging: *Geophysical Prospecting*, **61**, 254-269.

Norris, A. N., 1985, A differential scheme for the effective moduli of composites: *Mechanics of Materials*, **4**, 1-16.

O'Connell, R. J., and B. Budiansky, 1974, Seismic velocities in dry and saturated cracked solids: *Journal of Geophysical Research*, **79**, 5412-5426.

O'Connell, R. J., and B. Budiansky, 1977, Viscoelastic properties of fluid-saturated cracked solids: *Journal of Geophysical Research*, **82**, 5719-5735.

O'Hara, S. G., 1985, Influence of pressure, temperature, and pore fluid on the frequency-dependent attenuation of elastic waves in Berea sandstone: *Physical Review A*, **32**, 472-488.

O'Hara, S. G., 1989, Elastic-wave attenuation in fluid-saturated Berea sandstone: *Geophysics*, **54**, 785-788.

Olin, M., 2011, Low-frequency seismic properties of synthetic sandstone: B.Eng. thesis, Australian National University.

Paffenholz, J., and H. Burkhardt, 1989, Absorption and modulus measurements in the seismic frequency and strain range on partially saturated sedimentary rocks: *Journal of Geophysical Research*, **94**, 9493-9507.

Pandit, B. I., and M. S. King, 1979, The variation of elastic wave velocities and quality factor q of a sandstone with moisture content: *Canadian Journal of Earth Sciences*, **16**, 2187-2195.

Paterson, M. S., 1970, A high-pressure, high-temperature apparatus for rock deformation: *International Journal of Rock Mechanics and Mining Sciences*, **7**, 517-526.

Palciauskas, V. V., 1992, Compressional to shear wave velocity ratio of granular rocks: Role of rough grain contacts: *Geophysical Research Letters*, **19**, 1683-1686.

Palmer, I. D., and M. L. Traviola, 1980, Attenuation by squirt flow in undersaturated gas sands: *Geophysics*, **45**, 1780-1792.

Peselnick, L., and W. F. Outerbridge, 1961, Internal friction in shear and shear modulus of Solenhofen limestone over a frequency range of 10 cycles per second: *Journal of Geophysical Research*, **66**, 581-588.

Pieperbeck, N., R. Kleinrahm, and W. Wagner, 1991, Results of (pressure, density, temperature) measurements on methane and on nitrogen in the temperature range from 273.15 K to 323.15 K at pressures up to 12 MPa using a new apparatus for accurate gas-density measurements: *Journal of Chemical Thermodynamics*, **23**, 175-194.

Pimienta, L., J. Fortin, and Y. Guéguen, 2014, Investigation of elastic weakening in limestone and sandstone samples from moisture adsorption: *Geophysical Research International*, **199**, 335-347.

Pimienta, L., J. Fortin, and Y. Guéguen, 2015, Bulk modulus dispersion and attenuation in sandstones: *Geophysics*, **80**, D111-D127.

Plona, T. J., 1980, Observation of a second bulk compressional wave in a porous medium at ultrasonic frequencies: *Applied Physics Letters*, **36**, 259-261.

Rathore, J. S., E. Fjaer, R. M. Holt, and L. Renlie, 1994, P- and S-wave anisotropy of a synthetic sandstone with controlled crack geometry: *Geophysical Prospecting*, **43**, 711-728.

Reuss, A., 1929, Berechnung der Fliessgrenzen von Mischkristallen auf Grund der Plastizitätsbedingung für Einkristalle: *Z. Ang. Math. Mech.*, **9**, 49-58.

Richardson, M. D., K. L. Williams, K. B. Briggs, and E. I. Thorsos, 2002, Dynamic measurement of sediment grain compressibility at atmospheric pressure: Acoustic applications: *Journal of Oceanic Engineering*, **27**, 593-601.

Sams, M. S., J. P. Neep, M. H. Worthington, and M. S. King, 1997, The measurement of velocity dispersion and frequency-dependent intrinsic attenuation in sedimentary rocks: *Geophysics*, **62**, 1456-1464.

Sarout, J., 2012, Impact of pore space topology on permeability, cut-off frequencies and validity of wave propagation theories: *Geophysical Journal International*, **189**, 481-492.

Sen, P. N., C. Scala, and M. H. Cohen, 1981, A self-similar model for sedimentary rocks with application to the dielectric constant of fused glass beads: *Geophysics*, **46**, 781-795.

Spencer, J. W., 1981, Stress relaxations at low frequencies in fluid saturated rocks: attenuation and modulus dispersion: *Journal of Geophysical Research*, **86**, 1803-1812.

Stacey, F. D., J. M. W. Rynn, E. C. Little, and C. Croskell, 1969, Displacement and tilt transducers of 140 dB range: *Journal of Scientific Instruments (Journal of Physics E)*, 2, 945-949.

Stewart, R. B., and R. T. Jacobsen, 1989, Thermodynamic properties of argon from the triple point to 1200 K with pressure to 1000 MPa: *Journal of Physical and Chemical Reference Data*, **18**, 639-798.

Tanikawa, W., and T. Shimamoto, 2009, Comparison of Klinkenberg-corrected gas permeability and water permeability in sedimentary rocks: *International Journal of Rock Mechanics and Mining Sciences*, **46**, 229-238.

Thomsen, L., 1985, Biot-consistent elastic moduli of porous rocks: low frequency limit: *Geophysics*, **50**, 2797-2807.

Tillotson, P., J. Sothcott, A. I. Best, M. Chapman, and X.-Y. Li, 2012, Experimental verification of the fracture density and shear-wave splitting relationship using synthetic silica cemented sandstones with a controlled fracture geometry: *Geophysical Prospecting*, **60**, 516-525.

Tisato, N., and C. Madonna, 2012, Attenuation at low seismic frequencies in partially saturated rocks: Measurements and description of a new apparatus: *Journal of Applied Geophysics*, **86**, 44-53.

Tittmann, B. R., and R. M. Housley, 1973, High q (low internal friction) observed in a strongly outgassed terrestrial analog of lunar basalt: *Physica Status Solidi (b)*, **56**, K109-K111.

Tittmann, B. R., 1977, Lunar rock q in 3000-5000 range achieved in laboratory: *Philosophical Transactions of the Royal Society A, Mathematical, Physical, and Engineering Sciences*, **285**, 475-479.

Tittmann, B. R., 1978, Internal friction measurements and their implications in seismic q structure models of the crust: *Geophysical Monograph Series*, **20**, 197-213.

Tittmann, B. R., V. A. Clark, J. M. Richardson, and T. W. Spencer, 1980, Possible mechanism for seismic attenuation in rocks containing small amounts of volatiles: *Journal of Geophysical Research*, **85**, 5199-5208.

Toksöz, M. N., D. H. Johnston, and A. Timur, 1979, Attenuation of seismic waves in dry and saturated rocks: I. Laboratory measurements: *Geophysics*, **44**, 681-690.

Tutuncu, A. N., and M. M. Sharma, 1992, The influence of fluids on grain contact stiffness and frame moduli in sedimentary rocks: *Geophysics*, **57**, 1571-1582.

Vidal, D., R. Tufeu, Y. Garrabos, and B. Le Neindre, 1979, Thermophysical properties of noble gases at room temperature up to 1 GPa, *in* B. Vodar and P. Marteau, eds., High pressure science and technologies: Pergamon Press.

Voigt, W., 1928, *Lehrbuch der Krystallphysik [Textbook of Crystal Physics]*, Teubner, Leipzig.

Von Karman, T., 1911, Festigkeitsversuche unter allseitigem Druck [Strength measurements under uniform pressure]: *Z Verein deutsch Ing*, **55**, 1749-1757.

Vo-Thanh, D, 1990, Effects of fluid viscosity on shear-wave attenuation in saturated sandstones: *Geophysics*, **55**, 712-722.

Walsh, J. B., 1965, The effect of cracks on the compressibility of rocks: *Journal of Geophysical Research*, **70**, 381-389.

Washburn, E. W., 1921, The dynamics of capillary flow: *Physical Review*, **17**, 273-283.

White, J. E., 1986, Biot-Gardner theory of extensional waves in porous rods: *Geophysics*, **51**, 742-745.

Winkler, K. W., A. Nur, and M. Gladwin, 1979, Friction and seismic attenuation in rocks: *Nature*, **277**, 528-531.

Winkler, K., W., and A. Nur, 1982, Seismic attenuation: Effects of pore fluids and frictional sliding: *Geophysics*, **47**, 1-15.

Winkler, K. W., 1983, Contact stiffness in granular porous materials: comparison between theory and experiment: *Geophysical Research Letters*, **10**, 1073-1076.

Winkler, K. W., 1985, Dispersion analysis of velocities and attenuation in Berea sandstone: *Journal of Geophysical Research*, **90**, 6793-6800.

Winkler, K.W., 1986, Estimates of velocity dispersion between seismic and ultrasonic frequencies: *Geophysics*: **51**, 183-189.

Wu, T. T., 1966, The effect of inclusion shape on the elastic moduli of a two-phase material: *International Journal of Solids and Structures*, **2**, 1-8.

Wyllie, M. R. J., A. R. Gregory, and L. W. Gardner, 1956, Elastic wave velocities in heterogeneous and porous media: *Geophysics*, **1**, 41-70.

Xia, K., 2009, Split Hopkinson pressure bar (SHPB) tests on rocks: *News Journal-International Society for Rock Mechanics*, **12**, 72-75.

Yam, H., 2011, $CO_2$ rock physics: A laboratory study: M.Sc. thesis, Department of Physics, University of Alberta.

Zhang, S., M. S. Paterson, and S. F. Cox (1994), Porosity and permeability evolution during hot isostatic pressing of calcite aggregates: *Journal of Geophysical Research*, **99**, 15741-15760.

Zimmerman, R. W., 1991a, Compressibility of Sandstones: Elsevier, Amsterdam.

Zimmerman, R. W., 1991b, Elastic moduli of a solid containing spherical inclusions: *Mechanics of Materials*, **12**, 17-24.

# APPENDIX A

## Derivation of Torsional and Flexural Sensitivities in Torsional Forced Oscillation

In Fig. 3.6, $r_1$ is the individual transducer ratio of the three-plate transducer A-AB-B when the other transducer C-CD-D is grounded, which corresponds to the capacitive reactance ratio between plates B-AB and plates A-B. Similarly, $r_2$ is the capacitive reactance ratio between plates C-CD and plates C-D. The inductance ratio is denoted as $r_{/\!/}$ when both individual three-plate capacitance transducers are connected in the circuitry. In order to derive the torsional and flexural sensitivities, the relation among $r_1$, $r_2$, and $r_{/\!/}$ needs to be determined first.

It is recalled that capacitance $C = \frac{\varepsilon A}{d}$ and capacitive reactance $X_C = \frac{1}{\omega C}$, and assumed that a two-plate capacitor with the spacing between the parallel plates is equal to the fixed spacing $D$ (= 1.95 mm) between plates A-B or plates C-D, then

$$C_0 = \frac{\varepsilon A}{D}, \tag{A-1}$$

$$X_0 = \frac{1}{\omega C_0}. \tag{A-2}$$

From expression (Eq. 3.18) we know that the ratio read from the balanced ratio transformer can be viewed as either the reactance ratio or the spacing ratio between left-hand side two plates and the total. Then we have (Fig. 3.6 a):

$$X_{A-AB} = X_0 \cdot (1 - r_1), \tag{A-3}$$

$$X_{AB-B} = X_0 \cdot r_1, \tag{A-4}$$

$$X_{C-CD} = X_0 \cdot r_2, \tag{A-5}$$

$$X_{CD-D} = X_0 \cdot (1 - r_2). \tag{A-6}$$

It is recalled the way to calculate the equivalent reactance from individual reactance, the equivalent reactance for plates A-AB and plates CD-D connected in parallel is:

$$\mathrm{X}_{A-D} = \frac{X_{A-AB} X_{CD-D}}{X_{A-AB} + X_{CD-D}} = \frac{X_0 \cdot (1-r_1) \cdot X_0 \cdot (1-r_2)}{X_0 \cdot (1-r_1) + X_0 \cdot (1-r_2)} = \frac{X_0 \cdot (1-r_1) \cdot (1-r_2)}{2 - r_1 - r_2}. \tag{A-7}$$

Similarly, we have

$$\mathrm{X}_{B-C} = \frac{X_{AB-B} X_{C-CD}}{X_{AB-B} + X_{C-CD}} = \frac{X_0 \cdot r_1 \cdot X_0 \cdot r_2}{X_0 \cdot r_1 + X_0 r_2} = \frac{X_0 \cdot r_1 \cdot r_2}{r_1 + r_2}. \tag{A-8}$$

Since the bridge shown in Fig. 3.6 (a) is balanced with null reading from the potentiometer, the inductance ratio $r_{/\!/}$ read from the ratio transformer reflects the reactance ratio for the capacitive arm. It also needs to be noticed that the set of plates A-AB-D-CD is connected in series with the set of plates C-CD-B-AB. The parallel inductance ratio $r_{/\!/}$ then can be expressed as a function of $r_1$ and $r_2$ as:

$$r_{/\!/} = \frac{X_{B-C}}{X_{A-D}+X_{B-C}} = \frac{\frac{X_0 \cdot r_1 \cdot r_2}{r_1+r_2}}{\frac{X_0 \cdot (1-r_1)\cdot(1-r_2)}{2-r_1-r_2}+\frac{X_0 \cdot r_1 \cdot r_2}{r_1+r_2}} = \frac{r_1 \cdot r_2 \cdot (2-r_1-r_2)}{r_1(1-r_1)+r_2(1-r_2)} . \quad \text{(A-9)}$$

The relationship between the parallel combination ratio $r_{/\!/}$ and individual transducer ratios $r_1$ and $r_2$ has been found as above. The equation can be further rearranged as:

$$r_{/\!/} = r_1 \frac{r_2(1-r_2)}{r_1(1-r_1)+r_2(1-r_2)} + r_2 \frac{r_1(1-r_1)}{r_1(1-r_1)+r_2(1-r_2)} , \quad \text{(A-10)}$$

and notice that

$$\frac{r_2(1-r_2)}{r_1(1-r_1)+r_2(1-r_2)} + \frac{r_1(1-r_1)}{r_1(1-r_1)+r_2(1-r_2)} = 1 , \quad \text{(A-11)}$$

which means the parallel combination ratio $r_{/\!/}$ is the weighted average of individual ratios $r_1$ and $r_2$. This relationship is routinely checked during data acquisition by comparing the measured $r_1$, $r_2$, and $r_{/\!/}$ and to ensure $r_{/\!/}$ falling into the reasonable range bounded by $r_1$ and $r_2$.

What we have discussed so far is for the situation of balanced bridge only. In the case of forced oscillation, the bridge balance is disturbed and an out-of-balance ratio $\delta r_{/\!/}$ is monitored. From the relationship derived above, it can be inferred that the bridge imbalance in parallel mode $\delta r_{/\!/}$ can be contributed by the imbalances of individual ratios $\delta r_1$ and $\delta r_2$:

$$\delta r_{/\!/} = \frac{\partial r_{/\!/}}{\partial r_1}\delta r_1 + \frac{\partial r_{/\!/}}{\partial r_2}\delta r_2 , \quad \text{(A-12)}$$

and then rewrite the expression as:

$$\delta r_{/\!/} = \frac{\partial r_{/\!/}}{\partial r_1}\delta r_1 + \frac{\partial r_{/\!/}}{\partial r_2}\delta r_2 = \left(\frac{\partial r_{/\!/}}{\partial r_1}+\frac{\partial r_{/\!/}}{\partial r_2}\right)\left(\frac{\delta r_1+\delta r_2}{2}\right) + \left(\frac{\partial r_{/\!/}}{\partial r_1}-\frac{\partial r_{/\!/}}{\partial r_2}\right)\left(\frac{\delta r_1-\delta r_2}{2}\right) , \quad \text{(A-13)}$$

where $\delta r_T = \frac{\delta r_1+\delta r_2}{2}$, the arithmetic mean of individual imbalances, is the torsional mode component of the bridge imbalance; $A_T = \frac{\partial r_{/\!/}}{\partial r_1}+\frac{\partial r_{/\!/}}{\partial r_2}$, as the coefficient of the torsion-mode imbalance, is the torsional mode sensitivity of the parallel combination of transducers; $\delta r_F = \frac{\delta r_1-\delta r_2}{2}$, the halved difference between individual imbalances, is the flexural mode

component of the bridge imbalance; and $A_F = \frac{\partial r_{/\!/}}{\partial r_1} - \frac{\partial r_{/\!/}}{\partial r_2}$, the coefficient of the flexure-mode imbalance, is the flexural mode sensitivity of the parallel combination of transducers. In the ideal situation with pure torsion mode, $\delta r_1$ and $\delta r_2$ should be exactly the same. But in reality, any flexural behaviour of the specimen assembly beam makes $\delta r_1$ and $\delta r_2$ unequal, and the difference between them is the flexural contamination.

If we are interested in the explicit expressions of torsion- and flexure-mode sensitivities $A_T$ and $A_F$, it gives:

$$\frac{\partial r_{/\!/}}{\partial r_1} = \frac{\partial}{\partial r_1}\left[\frac{r_1 r_2(2-r_1-r_2)}{r_1(1-r_1)+r_2(1-r_2)}\right] = \frac{r_2(2-2r_1-r_2)[r_1(1-r_1)+r_2(1-r_2)]-r_1 r_2(2-r_1-r_2)(1-2r_1)}{[r_1(1-r_1)+r_2(1-r_2)]^2}, \quad \text{(A-14)}$$

$$\frac{\partial r_{/\!/}}{\partial r_2} = \frac{\partial}{\partial r_2}\left[\frac{r_1 r_2(2-r_1-r_2)}{r_1(1-r_1)+r_2(1-r_2)}\right] = \frac{r_1(2-2r_2-r_1)[r_1(1-r_1)+r_2(1-r_2)]-r_1 r_2(2-r_1-r_2)(1-2r_2)}{[r_1(1-r_1)+r_2(1-r_2)]^2}, \quad \text{(A-15)}$$

$$A_T = \frac{\partial r_{/\!/}}{\partial r_1} + \frac{\partial r_{/\!/}}{\partial r_2} = 1 + \frac{(r_1-r_2)^2[(1-r_1)(1-r_2)+r_1 r_2]}{[r_1(1-r_1)+r_2(1-r_2)]^2}, \quad \text{(A-16)}$$

$$A_F = \frac{\partial r_{/\!/}}{\partial r_1} - \frac{\partial r_{/\!/}}{\partial r_2} = \frac{(r_2^2-r_1^2)(1-r_1-r_2)(2-r_1-r_2)}{[r_1(1-r_1)+r_2(1-r_2)]^2}. \quad \text{(A-17)}$$

# APPENDIX B

## Derivation of the Moment Curvature Equation of Bernoulli-Euler Theory

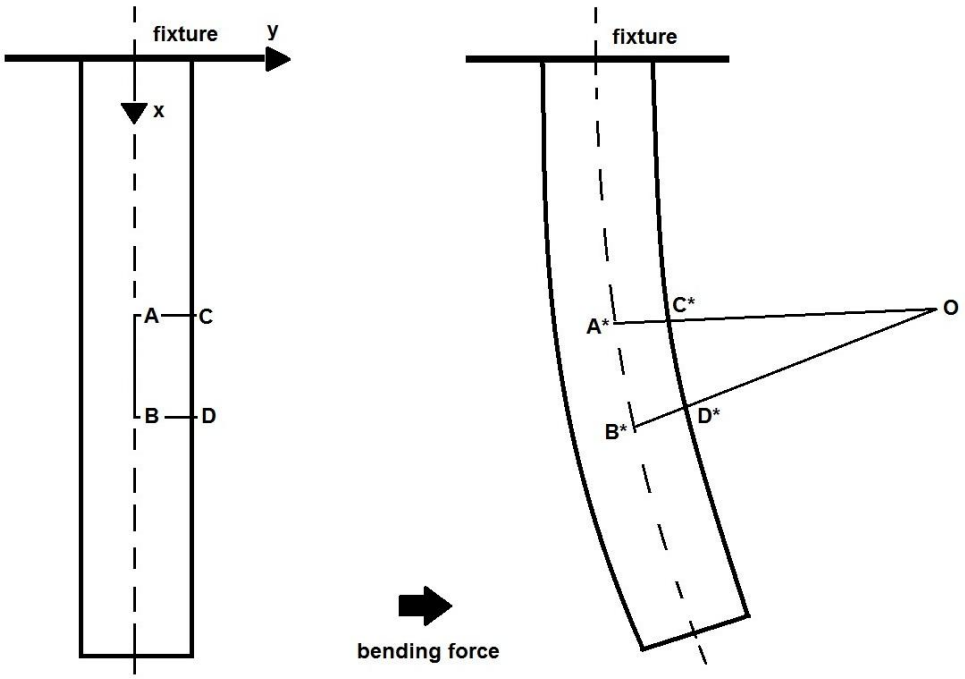


**Figure B-1** An illustration of the specimen-elastic standard beam before and after the application of a bending force. Line segments AB and CD are deformed into A*B* and C*D*.

The specimen assembly, elastic standard, and other steel members form an integral beam under pressure. The beam is fixed at the top, located at the coupling point between the upper steel piston and the furnace plug on the attenuation apparatus. The dashed line indicates the neutral surface perpendicular to the *x*-*y* plane, on which the strain is zero. With a bending force applied at the bottom of the beam by a pair of electromagnetic drivers, the right-hand side of the neutral surface experiences axial compression and the left-hand side of the neutral surface is subject to axial tension. Line segment AB is on the neutral surface and another line segment CD is located somewhere away from the neutral surface by distance *y*. After bending, line segments AB and CD become A*B* and C*D*. Remember the strain-free assumption for the neutral surface, giving the unchanged length of line segment AB:

$$\overline{AB} = \overline{A^*B^*} \, . \qquad \text{(B-1)}$$

However, the line segment CD is changed to C*D* with its axial strain expressed as:

$$\varepsilon_x = \frac{\overline{C^*D^*} - \overline{CD}}{\overline{CD}}. \tag{B-2}$$

Assume the radius of curvature $\overline{OA^*} = \overline{OB^*} = \rho$, $\angle A^*OB^* = \theta$, and recall the strain-free assumption of the neutral surface, then we have:

$$\overline{AB} = \overline{A^*B^*} = \rho \cdot \theta \tag{B-3}$$

The second important assumption in derivation is the strains in *y* and *z* directions are negligible compared with that in *x* direction:

$$\overline{AC} = \overline{BD} = \overline{A^*C^*} = \overline{B^*D^*} = y \tag{B-4}$$

Then $\overline{CD}$ and $\overline{C^*D^*}$ can be expressed with $\overline{AB}$ as:

$$\overline{CD} = \overline{AB} \tag{B-5}$$

$$\overline{C^*D^*} = (\rho - y) \cdot \theta = \rho \cdot \theta - y \cdot \theta = \overline{AB} - y \cdot \theta \tag{B-6}$$

Combine Eq. (B-2), (B-3), (B-5) and (B-6), it gives:

$$\varepsilon_x = \frac{\overline{AB} - y \cdot \theta - \overline{AB}}{\rho \cdot \theta} = -\frac{y}{\rho} \tag{B-7}$$

and notice that:

$$\sigma_x = E \cdot \varepsilon_x \tag{B-8}$$

Then the axial stress (in x direction) is expressed as:

$$\sigma_x(x, y) = -\frac{E \cdot y}{\rho(x)} \tag{B-9}$$

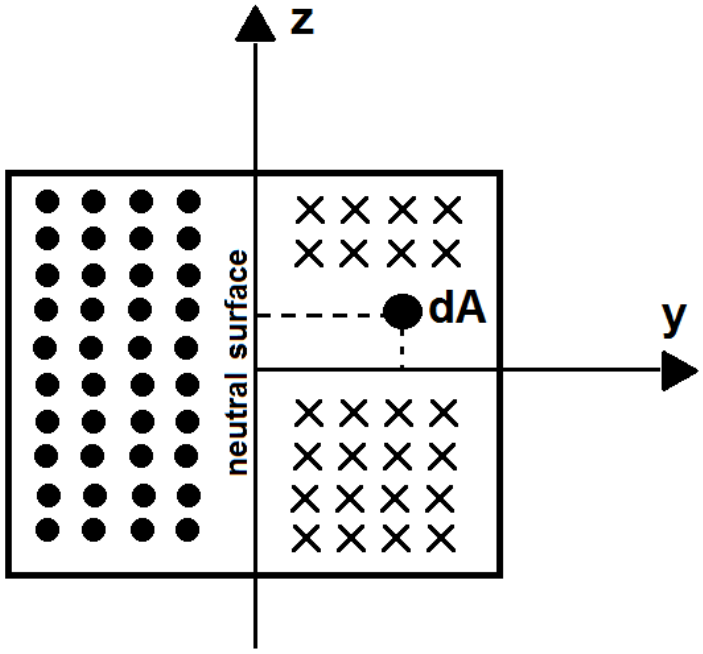


**Figure B-2** A cross section on the y-z plane with the neutral surface along the z axis. The stress on the right-hand side of the neutral surface points towards the paper, but the stress on the left-hand side of the neutral surface points towards readers. dA (x, y, z) is an infinitesimal area.

The bending moment at *dA (x, y, z)* is:

$$dM = -y \cdot \sigma_x(x, y) \cdot dA \, . \tag{B-10}$$

The negative sign is to keep the convention that compression in the $+y$ fibres of the beam is produced by a positive bending moment. Integral on the total cross section and combine Eq.(B-9):

$$M = \int_A \, -y \cdot \sigma_x(x, y) \cdot dA = \int_A \, \frac{E \cdot y^2}{\rho(x)} dA \tag{B-11}$$

Assume that the radius of curvature at a given $x$ is constant and area moment of inertia is defined as $I = \int_A \, y^2 dA$, giving:

$$M = \frac{EI}{\rho} \tag{B-12}$$

where the reciprocal of the radius of curvature $\kappa = \frac{1}{\rho}$ is defined as the curvature and this equation is also known as the moment-curvature equation of Bernoulli-Euler beam theory. If the deflection of the beam at $x$ is denoted as $v(x)$, the curvature $\kappa$ can be approximated by $\frac{\partial^2 v}{\partial x^2}$, giving:

$$E(x)I(x)\frac{\partial^2 v}{\partial x^2} = M(x) \tag{B-13}$$

where *E*, *I*, and *M* are the Young's modulus, the area moment of inertia of the beam cross-section, and the local bending moment, respectively. The product *EI* is called the flexural rigidity of the beam.

# APPENDIX C

## Finite Difference Method for Filament Elongation Model

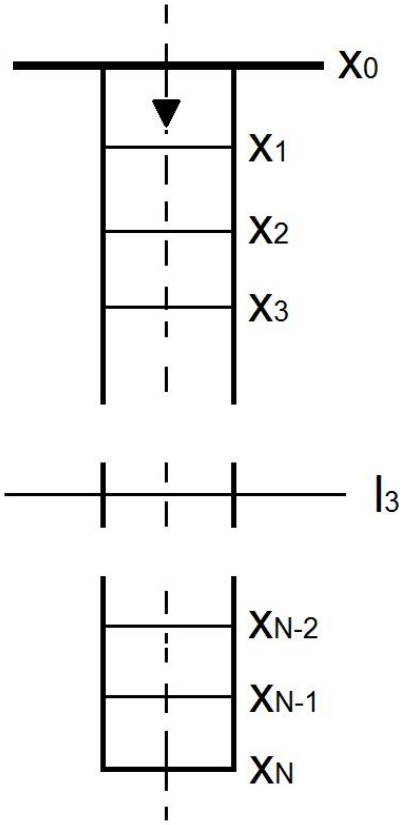


**Figure C-1** An schematic illustration of dividing the entire beam into N small intervals with equal lengths.

In order to solve the moment-curvature equation numerically, the entire beam is split into *N* small intervals of equal length *h*. The first and the second derivatives of the deflection of the beam $\frac{\partial v}{\partial x}$ and $\frac{\partial^2 v}{\partial x^2}$ are approximated by the central differences as:

$$\frac{\partial v}{\partial x} = \frac{v_{i+1} - v_{i-1}}{2h} \tag{C-1}$$

$$\frac{\partial^2 v}{\partial x^2} = \frac{\frac{v_{i+1} - v_i}{h} - \frac{v_i - v_{i-1}}{h}}{h} = \frac{v_{i-1} - 2v_i + v_{i+1}}{h^2} \tag{C-2}$$

The moment-curvature equation then can be written as:

$$v_{i-1} - 2v_i + v_{i+1} = \frac{h^2 M_i}{(EI)_i} \qquad \text{i=1, 2, 3 … N} \tag{C-3}$$

For *i = 0*, the boundary condition is $v_0 = 0$ and $v'_0 = 0$, the latter of which giving:

$$\nu'_0 = \frac{\nu_1 - \nu_{-1}}{2h} = 0 \tag{C-4}$$

Then it gives:

$$\nu_1 = \nu_{-1} \tag{C-5}$$

The finite difference equation for $i = 0$ is written as:

$$\nu_{-1} - 2\nu_0 + \nu_1 = 2\nu_1 = \frac{h^2 M_0}{(EI)_0} \tag{C-6}$$

Combined with Eq. (3.57):

$$2\nu_1 - \frac{h^2(L - x_0)}{(EI)_0} R_L = \frac{h^2 F(l_3 - x_0)}{(EI)_0} \tag{C-7}$$

For $i = 1$, the finite difference equation is:

$$-2\nu_1 + \nu_2 - \frac{h^2(L - x_1)}{(EI)_1} R_L = \frac{h^2 F(l_3 - x_1)}{(EI)_1} \tag{C-8}$$

For arbitrary $i \geq 2$ such that $x_i < l_3$, the finite difference equation is:

$$\nu_{i-1} - 2\nu_i + \nu_{i+1} - \frac{h^2(L - x_i)}{(EI)_i} R_L = \frac{h^2 F(l_3 - x_i)}{(EI)_i} \tag{C-9}$$

For $l_3 \leq x_i \leq L$, combined with Eq. (3.58), the finite difference equation is:

$$\nu_{i-1} - 2\nu_i + \nu_{i+1} - \frac{h^2(L - x_i)}{(EI)_i} R_L = 0 \tag{C-10}$$

In particular, for $i = N\text{-}1$, considering the boundary condition that $\nu_N = 0$ as the lower end of the elastic standard is weekly propped by a spiral vent tube, the finite difference equation is:

$$\nu_{N-2} - 2\nu_{N-1} - \frac{h^2(L - x_{N-1})}{(EI)_{N-1}} R_L = 0 \tag{C-11}$$

Equations (C-7) to (C-11) then constitute a set of N linear equations for *i = 0, N-1*:

$$
\begin{array}{l}
\text{i = 0} \\
\text{i = 1} \\
\text{i = 2} \\
\text{i = 3} \\
\text{x < } l_3 \\
\text{x} \geq l_3 \\
\text{i = N-3} \\
\text{i = N-2} \\
\text{i = N-1}
\end{array}
\begin{bmatrix}
2 & 0 & 0 & 0 & \ldots & -\frac{h^2(L-x_0)}{(EI)_0} \\
-2 & 1 & 0 & 0 & \ldots & -\frac{h^2(L-x_1)}{(EI)_1} \\
1 & -2 & 1 & 0 & \ldots & -\frac{h^2(L-x_2)}{(EI)_2} \\
0 & 1 & -2 & 1 & \ldots & -\frac{h^2(L-x_3)}{(EI)_3} \\
\ldots & & & & & \\
\ldots & & & & & \\
\ldots & 1 & -2 & 1 & 0 & -\frac{h^2(L-x_{N-3})}{(EI)_{N-3}} \\
\ldots & 0 & 1 & -2 & 1 & -\frac{h^2(L-x_{N-2})}{(EI)_{N-2}} \\
\ldots & 0 & 0 & 1 & -2 & -\frac{h^2(L-x_{N-1})}{(EI)_{N-1}}
\end{bmatrix}
\begin{bmatrix} v_1 \\ v_2 \\ v_3 \\ v_4 \\ \\ \\ v_{N-2} \\ v_{N-1} \\ R_L \end{bmatrix}
=
\begin{bmatrix} \frac{h^2F(l_3-x_0)}{(EI)_0} \\ \frac{h^2F(l_3-x_1)}{(EI)_1} \\ \frac{h^2F(l_3-x_2)}{(EI)_2} \\ \frac{h^2F(l_3-x_3)}{(EI)_3} \\ \\ \\ 0 \\ 0 \\ 0 \end{bmatrix}
$$

The *N* linear equations with *N* unknowns $v_1 \ldots v_{N-1}$, and $R_L$ are solved to yield the deflection of the entire beam, including the deflections of particular interest at the upper transducer station $v(l_1)$ and the lower transducer station $v(l_2)$, in which $l_1$ and $l_2$ are the distances from the top end of the beam to the upper and lower transducer stations, respectively (Fig. 3.20).

# APPENDIX D

## Differential Attenuation - Spectral Ratio Method

Comparing the amplitude spectra in the frequency domain of an observed waveform to a reference is commonly referred to as the spectral ratio method. It is the conventional method in determining attenuation in ultrasonic wave transmission measurements (Boubié *et al.*, 1987). In this method, two spectral amplitudes are compared and the ratio between them reflects attenuation in specimen. The spectral amplitude of a wave $A(f,x)$ is expressed as (Molyneux & Schmitt, 2000):

$$A(f,x) = A_0(f)e^{-\alpha(f)x}G(f,x)\,, \tag{D-1}$$

where $A_0(f)$ is the amplitude spectrum of the pulse input to the sample, $\alpha(f)$ is the attenuation coefficient, $G$ is the geometric coefficient associated with geometric divergence and losses due to transmission, and reflection at the boundaries of the sample, $f$ is frequency and $x$ is the distance travelled through the sample by the ultrasonic wave.

In an ideal measurement of the attenuation, one would have two samples identical in physical properties but differing only in length and hence propagation distance. One could easily then take the ratios of the two observed waveforms in order to determine the attenuation. This strategy is employed in pulse-echo measurements where the amplitude spectra of two successive echoes are compared. This is not possible in the pulse-transmission geometry used here. For pulse transmission, the change in propagation distance can be achieved by either placing the pulser and receiver at different locations on the specimen or physically changing the length of the specimen. In both cases, a significant change in geometric coefficient $G(f,x)$ is unavoidable. Assuming two ultrasonic pulses travelling different distances $x_1$ and $x_2$, the ratio of spectral amplitudes is:

$$\frac{A_1(f,x_1)}{A_2(f,x_2)} = e^{\alpha(f)(x_2-x_1)}\frac{G(f,x_1)}{G(f,x_2)}, \tag{D-2}$$

Notice that the amplitude spectrum of the input pulse $A_0(f)$ and the attenuation coefficient $\alpha(f)$ are independent of distance. Take the natural logarithm for the expression above:

$$ln\frac{A_1(f,x_1)}{A_2(f,x_2)} = \alpha(f)(x_2 - x_1) + ln\frac{G(f,x_1)}{G(f,x_2)}. \quad \text{(D-3)}$$

This tells that the attenuation coefficient of specimen (unit: 1/m) can be determined using the ratio of the spectral amplitudes with knowledge of the differential travel distance, and an understanding of any geometric effects. This expression provides the absolute attenuation coefficient of a specimen associated with energy loss due to fluid saturation and different pressure conditions.

The expression (Eq. D-3) is used in determining the absolute value of the attenuation coefficient. Here we adapt it instead to calculate a differential attenuation coefficient following the approach developed by Yam (2010). In this case we simply use for the reference one of the waveforms obtained during a given suite of measurements. This has the disadvantage that we cannot obtain a value for the absolute attenuation. It has the advantage of many differential techniques that we are able to sense small variations in the attenuation that may not be observed in the direct measurements. The geometric effects are neglected as no change in geometric setup during the measurements except fluid saturation and pressure conditions. The pressure-dependent sample shortening is assumed to be negligible. This gives:

$$\Delta\alpha(f) = \alpha_2(f) - \alpha_1(f) = \frac{1}{l} ln\frac{A_1(f)}{A_2(f)}, \quad \text{(D-4)}$$

where $A_1(f)$ and $\alpha_1(f)$ are the reference spectral amplitude and attenuation coefficient, respectively; $A_2(f)$ and $\alpha_2(f)$ are the spectral amplitude and attenuation coefficient, respectively, determined at a pressure other than the reference pressure; $l$ is the length of the specimen; and $\Delta\alpha(f)$ is the differential attenuation coefficient.

The differential attenuation coefficient reflects the relative attenuation caused by the change in differential pressure and thus the status of fluid saturation with respect to a reference pressure. To make it simple, the lowest differential pressure encountered in a set of measurements with pore fluid is normally used as the reference. The spectral amplitudes obtained at differential pressures other than the reference are compared with that at the lowest differential pressure (reference) to yield differential attenuation coefficients.

In practice, each P- or S-wave time series is windowed for successive 2048 data points from the first arrival. A Fast Fourier Transform (FFT) is performed to convert the time series into amplitude spectrum (Fig. D-1, a & c). Finally, the spectral amplitude obtained at a particular differential pressure is compared with that at the reference differential pressure of 10 MPa to provide the differential attenuation coefficient (Fig. D-1, b & d).

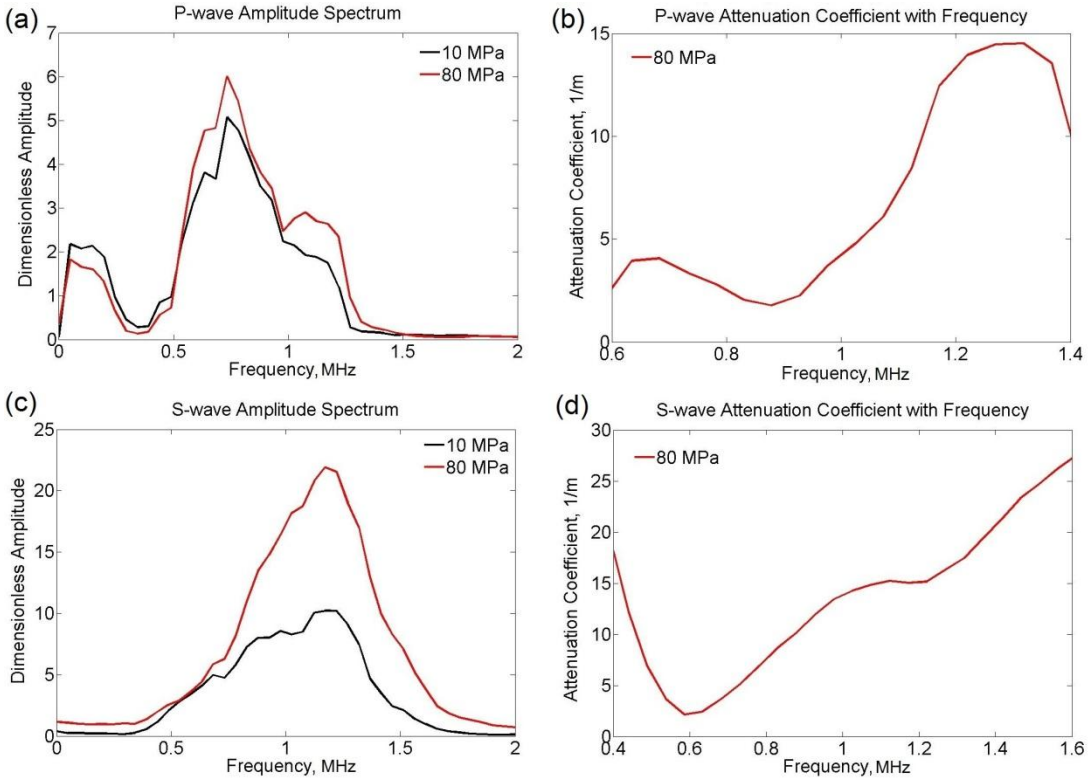


**Figure D-1** Left) Spectrum of dimensionless amplitudes after Fast Fourier Transform from either the (a) P- or (c) S-wave time series at differential pressures of 10 MPa (reference) and 80 MPa, respectively; Right) Spectral (differential) attenuation coefficient $\Delta\alpha(f)$ at 80 MPa for either(b) P- or (d) S-wave. The uncertainty associated with the determined attenuation coefficient is on the order of 10 $m^{-1}$.

The amplitude spectrum shows that the energy at the nominal 1 MHz frequency emitted by the piezoelectric ceramic transducers shifts to 0.7 MHz for P-wave and 1.2 MHz for S-wave, probably caused by adding the aluminium end caps to the transducers. The energy is also dispersed by the presence of attenuation, indicated by a broader peak from 0.4 to 1.5 MHz for P-wave (Fig. D-1, a) and from 0.4 to 2 MHz for S-wave (Fig. D-1, c). The spectrum beyond the high-energy band of frequencies is contaminated by noise and thus only are the spectral amplitudes within 0.4 – 1.5 MHz for P-wave and 0.4 – 2 MHz for S-wave chosen to yield differential attenuation coefficients (Fig. D-1, b & d).

# APPENDIX E

## Electrical Circuitry for Strain Gauge Measurement

A Wheatstone bridge is required to measure the unknown electrical resistance of a strain gauge. If the electrical resistance of the strain gauge is of interest, a bridge can be constructed in a way illustrated in Fig. E-1. Two resistors of known resistance ($R$ for each) are connected in series to form one arm of the bridge. The other arm consists of another resistor of known resistance ($R$) and the resistor of unknown resistance. Two arms of the bridge are connected in parallel with a potentiometer connected in between. The bridge is excited by a 2.5 V DC voltage. The two arms of the bridge are balanced if the potentiometer reads zero between Point A and B. In this case, the resistance of the unknown is exactly $R$. Any departure of the unknown resistance from $R$ will create an out-of-balance voltage between two arms, detected by the potentiometer.

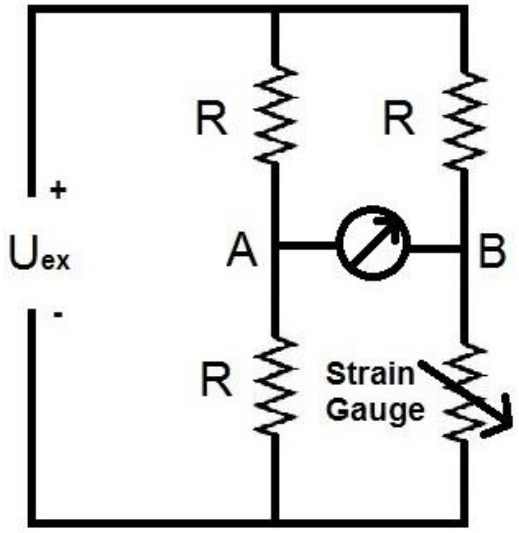


**Figure E-1** The configuration of an electrical bridge to determine the resistance and thus strain of an unknown resistor. If more than one strain gauge is used in experiments, *e.g.*, an axial strain gauge and a tangential strain gauge used at the same time, the circuitry for the other strain gauges can be constructed in the same way as that for the first one.

Firstly, the voltage between the two arms of the bridge is measured at ambient conditions as $U_0$ with an excitation voltage $U_{ex,0}$. The resistances of the strain gauge and the known resistor are denoted as $R_0$ and $R$. The out-of-balance voltage $U_0$ at ambient conditions can be expressed as:

$$U_0 = (\frac{R}{2R} - \frac{R}{R+R_0})U_{ex,0} \ . \qquad \text{(E-1)}$$

The system is then pressurised to a desired pressure level, and the voltage between the arms under pressure $U_1$ is measured with an excitation voltage $U_{ex,1}$. The resistance of the strain gauge under pressure changes to $R_1$. This gives:

$$U_1 = (\frac{R}{2R} - \frac{R}{R+R_1})U_{ex,1} \, . \tag{E-2}$$

The change in voltage ratio, defined as the ratio between the arm voltage and the excitation voltage, due to pressurisation is:

$$\Delta U_r = \frac{U_0}{U_{ex,0}} - \frac{U_1}{U_{ex,1}} = \frac{R}{R+R_1} - \frac{R}{R+R_0} \, . \tag{E-3}$$

Also notice the linear relationship between the strain $\varepsilon$ and the percentage change in the resistance of a strain gauge:

$$\frac{\Delta R}{R_0} = \frac{R_1 - R_0}{R_0} = GF \cdot \varepsilon \, , \tag{E-4}$$

where *GF* is the gauge factor. By combing Eq. (E-3) and (E-4), the strain $\varepsilon$ is expressed as:

$$\Delta U_r = -\frac{GF \cdot \varepsilon}{(\frac{R}{R_0} + GF \cdot \varepsilon + 1)(1 + \frac{R_0}{R})} \, . \tag{E-5}$$

Since $R \approx R_0$ at ambient, the equation above is rewritten as:

$$\Delta U_r = -\frac{GF \cdot \varepsilon}{2(GF \cdot \varepsilon + 2)} \, . \tag{E-6}$$

Rearrange the equation above, the strain $\varepsilon$ is expressed as:

$$\varepsilon = \frac{-4\Delta U_r}{(2\Delta U_r + 1)GF} \, . \tag{E-7}$$

# Appendix F Piston Traversing Experiment

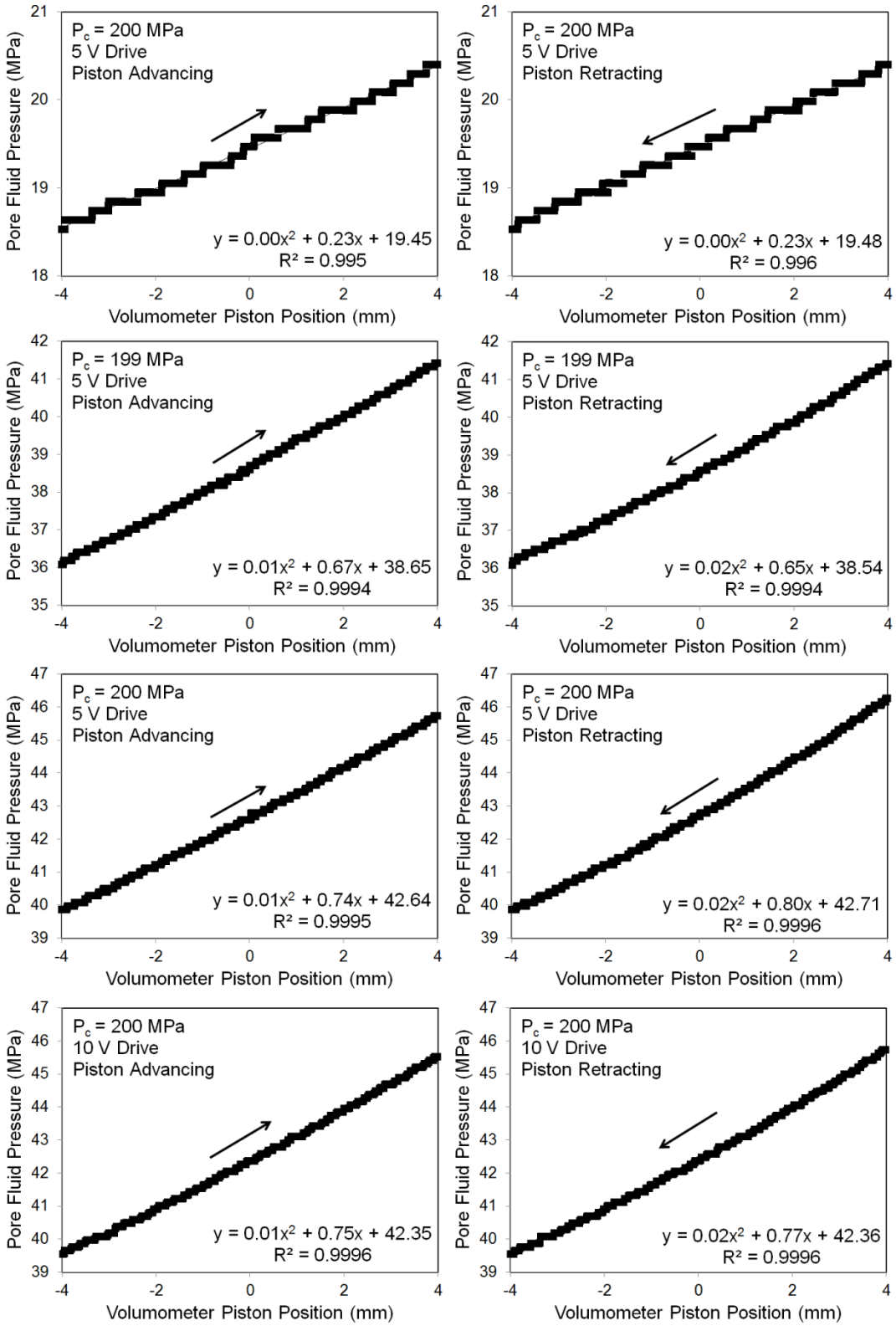

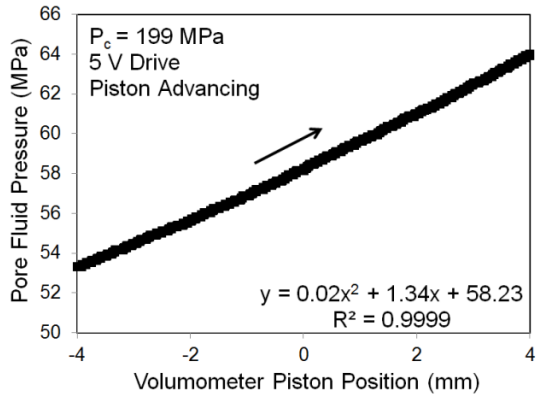
$P_c$ = 199 MPa
5 V Drive
Piston Advancing
y = 0.02x² + 1.34x + 58.23
R² = 0.9999
Pore Fluid Pressure (MPa)
Volumometer Piston Position (mm)

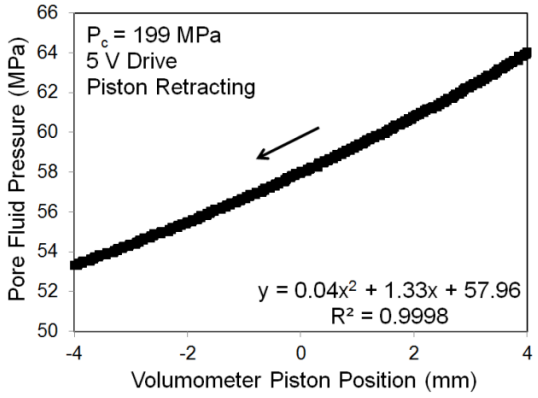
$P_c$ = 199 MPa
5 V Drive
Piston Retracting
y = 0.04x² + 1.33x + 57.96
R² = 0.9998
Pore Fluid Pressure (MPa)
Volumometer Piston Position (mm)

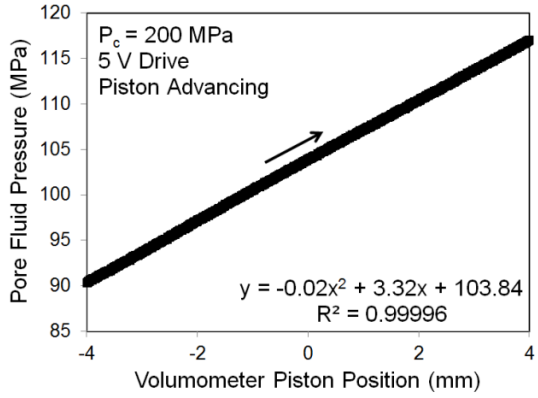
$P_c$ = 200 MPa
5 V Drive
Piston Advancing
y = -0.02x² + 3.32x + 103.84
R² = 0.99996
Pore Fluid Pressure (MPa)
Volumometer Piston Position (mm)

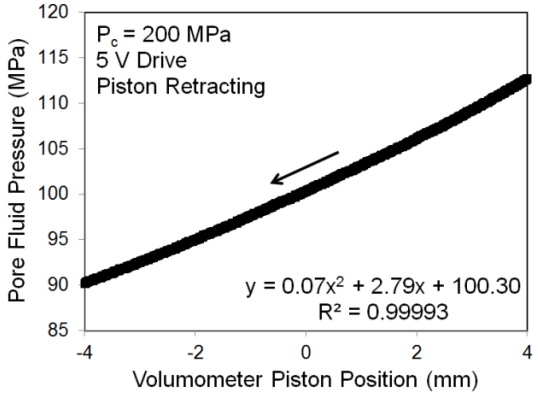
$P_c$ = 200 MPa
5 V Drive
Piston Retracting
y = 0.07x² + 2.79x + 100.30
R² = 0.99993
Pore Fluid Pressure (MPa)
Volumometer Piston Position (mm)

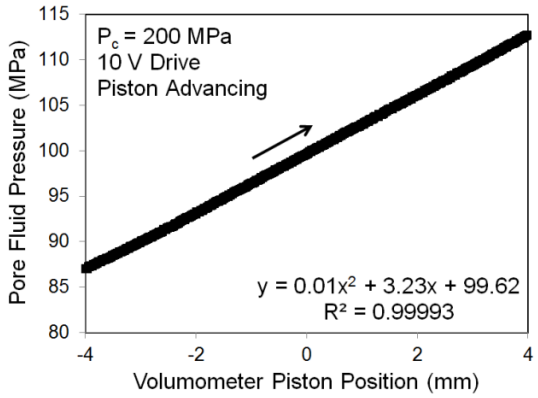
$P_c$ = 200 MPa
10 V Drive
Piston Advancing
y = 0.01x² + 3.23x + 99.62
R² = 0.99993
Pore Fluid Pressure (MPa)
Volumometer Piston Position (mm)

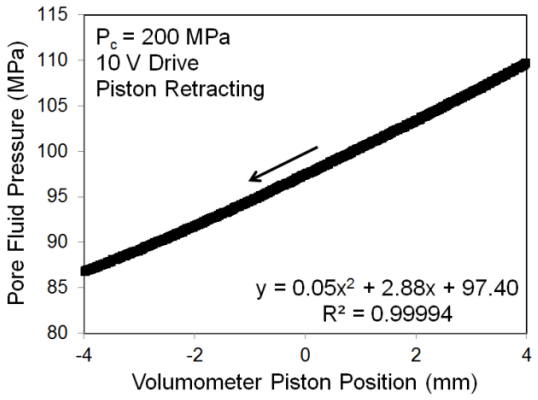
$P_c$ = 200 MPa
10 V Drive
Piston Retracting
y = 0.05x² + 2.88x + 97.40
R² = 0.99994
Pore Fluid Pressure (MPa)
Volumometer Piston Position (mm)

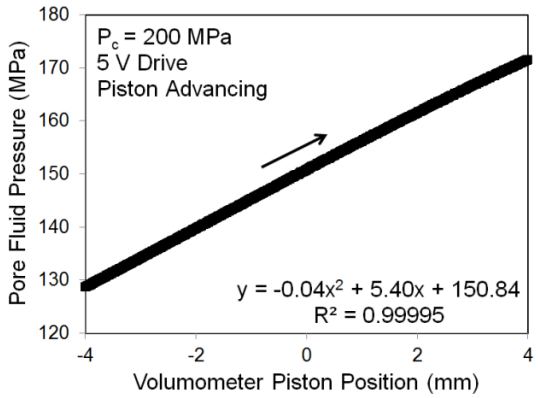
$P_c$ = 200 MPa
5 V Drive
Piston Advancing
y = -0.04x² + 5.40x + 150.84
R² = 0.99995
Pore Fluid Pressure (MPa)
Volumometer Piston Position (mm)

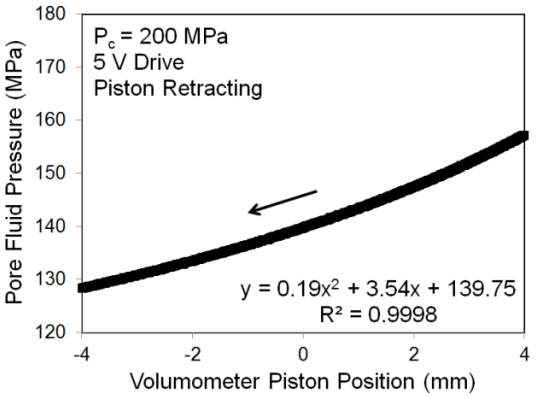
$P_c$ = 200 MPa
5 V Drive
Piston Retracting
y = 0.19x² + 3.54x + 139.75
R² = 0.9998
Pore Fluid Pressure (MPa)
Volumometer Piston Position (mm)

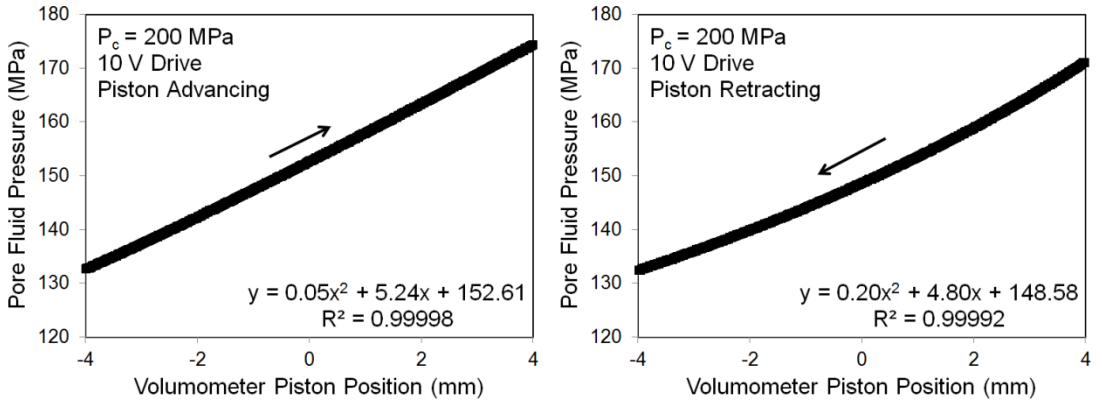


*The measurement at low pore-fluid pressure, involving smaller change in pore-fluid pressure during piston traversing, is limited by the resolution of pore-fluid pressure gauge of 0.1 MPa, resulting in a zig-zag shape curve.

# Appendix G Pore-pressure Equilibration Experiment

## G-1 Glass-rod Specimen

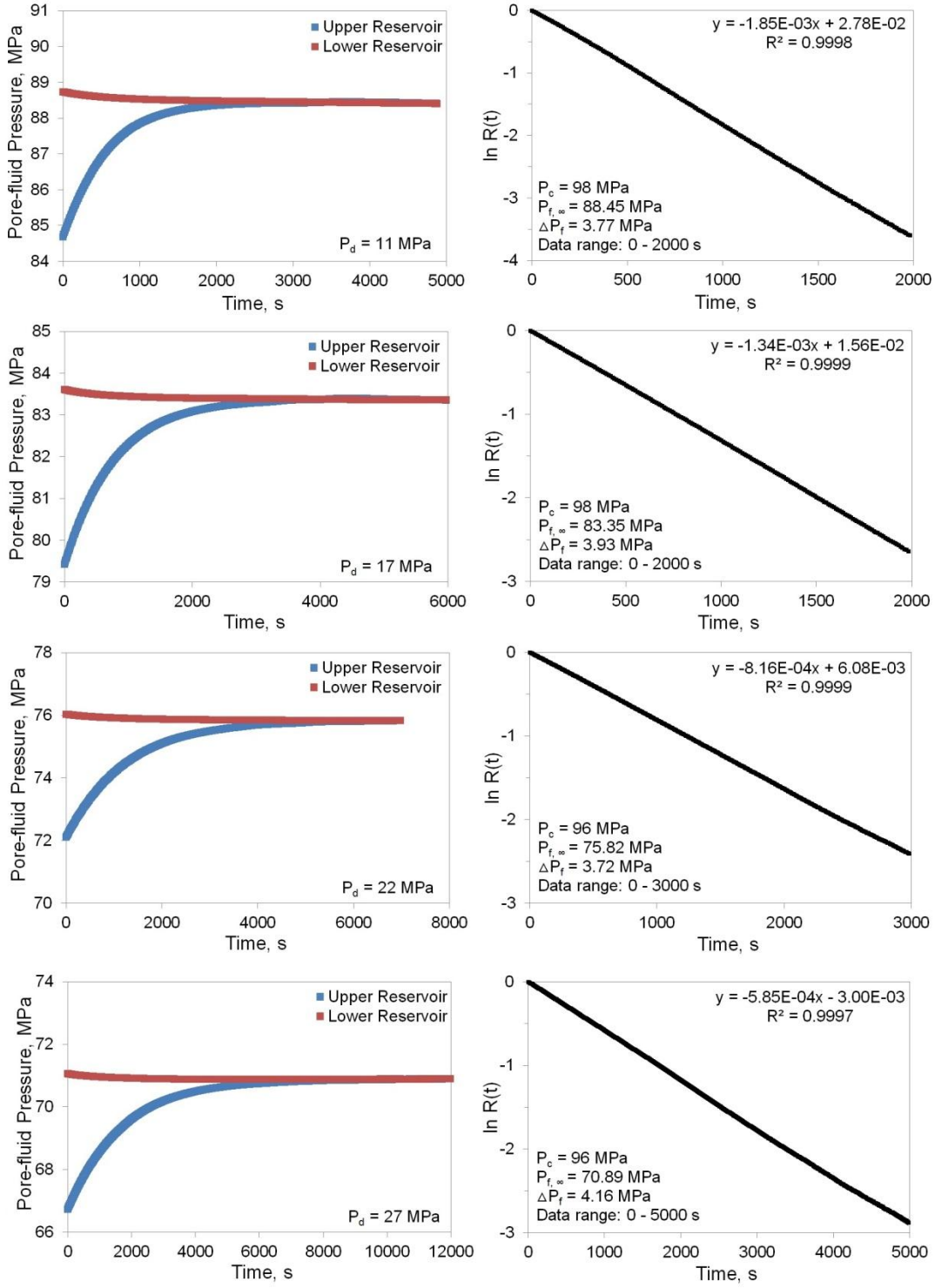

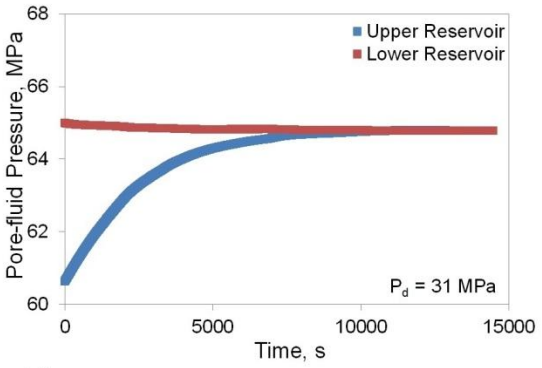
Upper Reservoir
Lower Reservoir
Pore-fluid Pressure, MPa
Time, s
$P_d$ = 31 MPa

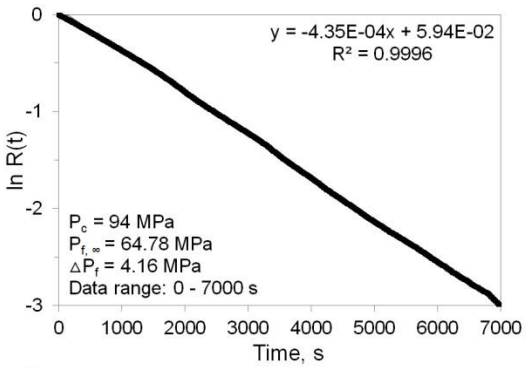
y = -4.35E-04x + 5.94E-02
R² = 0.9996
ln R(t)
Time, s
$P_c$ = 94 MPa
$P_{f,\infty}$ = 64.78 MPa
$\Delta P_f$ = 4.16 MPa
Data range: 0 - 7000 s

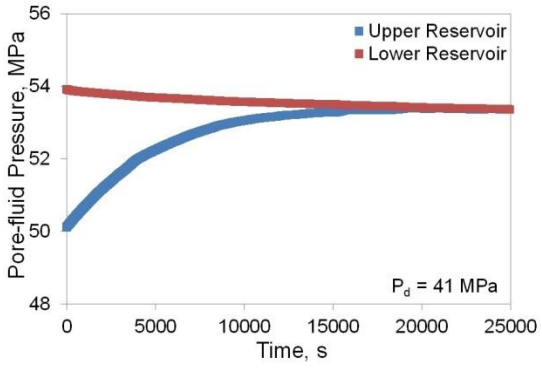
Upper Reservoir
Lower Reservoir
Pore-fluid Pressure, MPa
Time, s
$P_d$ = 41 MPa

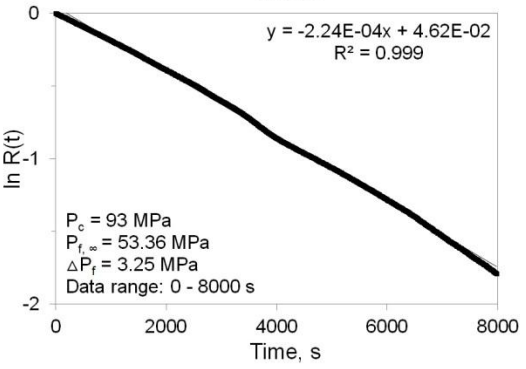
y = -2.24E-04x + 4.62E-02
R² = 0.999
ln R(t)
Time, s
$P_c$ = 93 MPa
$P_{f,\infty}$ = 53.36 MPa
$\Delta P_f$ = 3.25 MPa
Data range: 0 - 8000 s

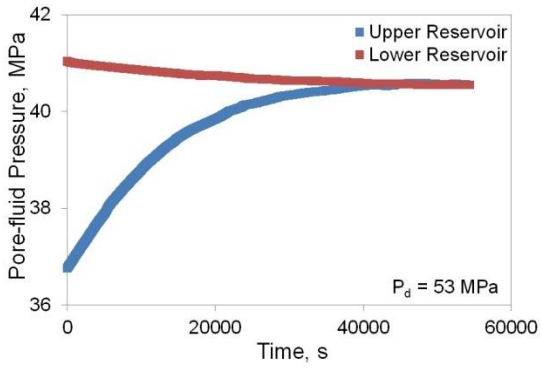
Upper Reservoir
Lower Reservoir
Pore-fluid Pressure, MPa
Time, s
$P_d$ = 53 MPa

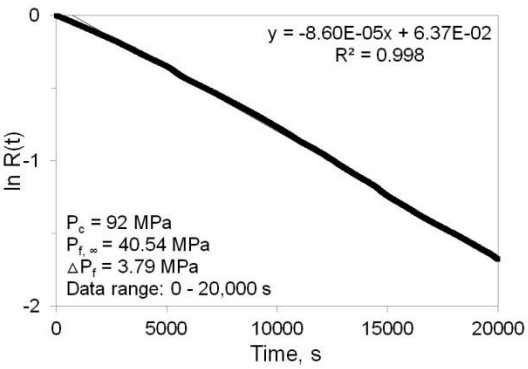
y = -8.60E-05x + 6.37E-02
R² = 0.998
ln R(t)
Time, s
$P_c$ = 92 MPa
$P_{f,\infty}$ = 40.54 MPa
$\Delta P_f$ = 3.79 MPa
Data range: 0 - 20,000 s

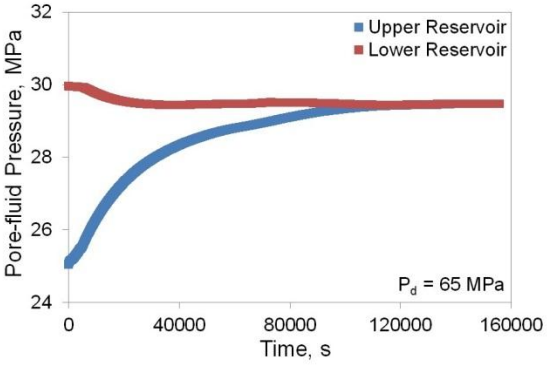
Upper Reservoir
Lower Reservoir
Pore-fluid Pressure, MPa
Time, s
$P_d$ = 65 MPa

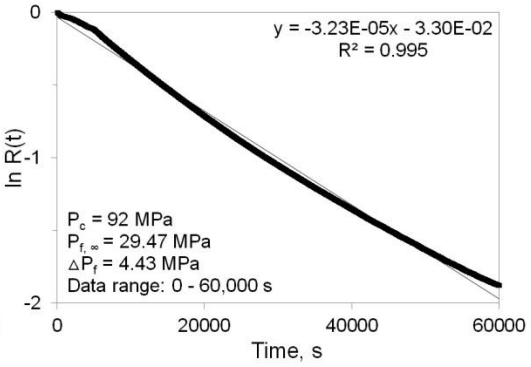
y = -3.23E-05x - 3.30E-02
R² = 0.995
ln R(t)
Time, s
$P_c$ = 92 MPa
$P_{f,\infty}$ = 29.47 MPa
$\Delta P_f$ = 4.43 MPa
Data range: 0 - 60,000 s

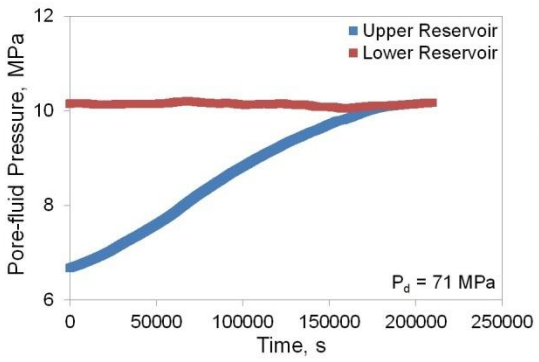


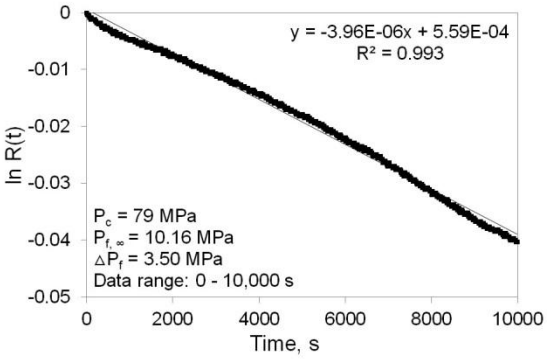


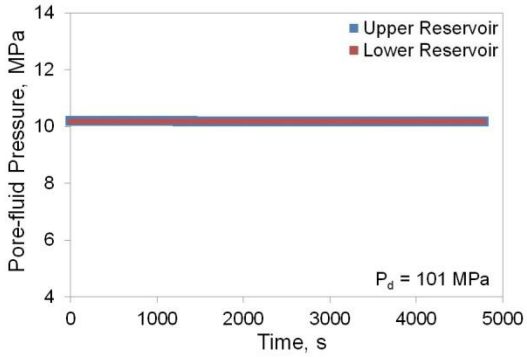


*Minor difference in reading on the upstream and downstream pore-fluid pressure meters was noticed at the end of pore-pressure equilibration experiment. This was explained as the non-linear behaviour of the pore-fluid pressure gauge of the upstream reservoir. The behaviour of the pore-fluid pressure gauge of the downstream reservoir was noticed to be more reliable and used as the reference to offset the recorded pore-fluid pressure of the upstream reservoir to provide a common value of pore-fluid pressure at the end of pore-pressure equilibration.

** Pore-fluid pressures in the upstream and downstream reservoirs, at the highest differential pressure of 101 MPa, could not reach equilibrium, giving permeability below the detection limit of ~ $10^{-20}$ $m^2$.

## G-2 Low-porosity Glass-bead Specimen

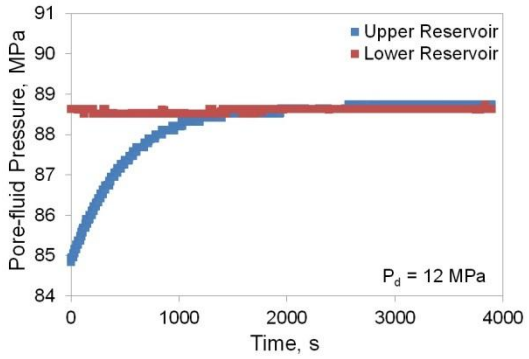


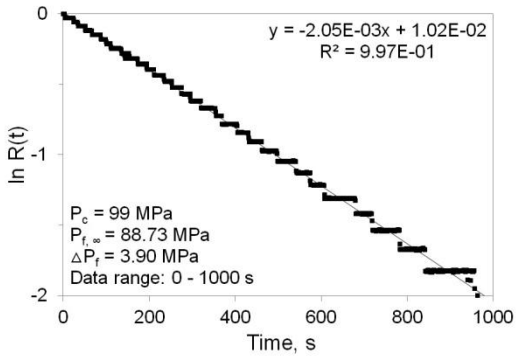


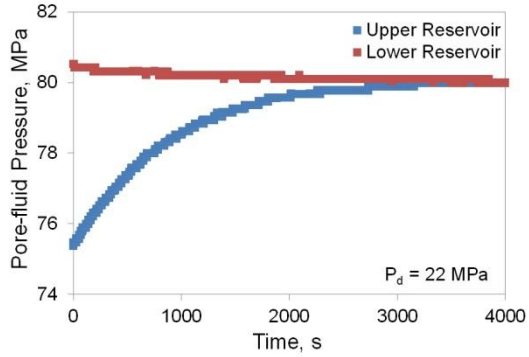


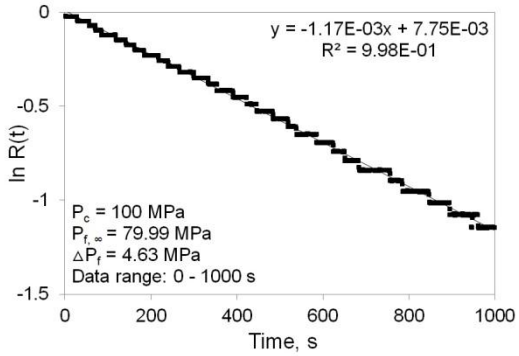


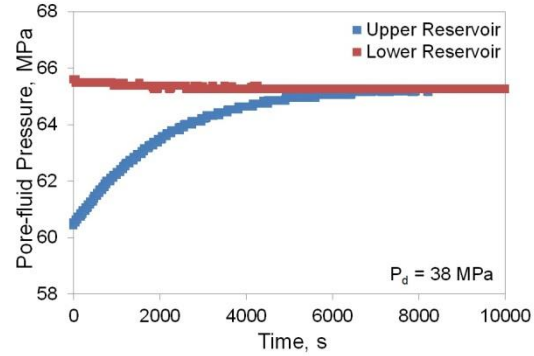


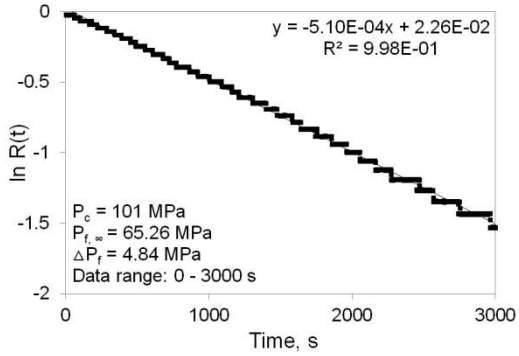


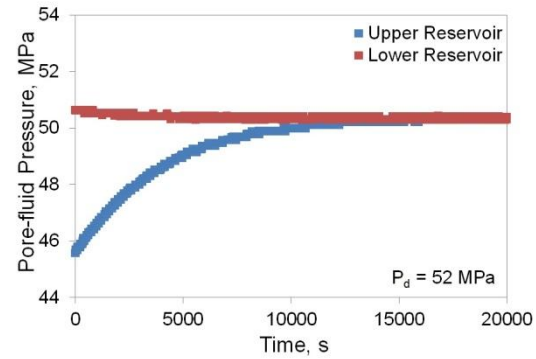


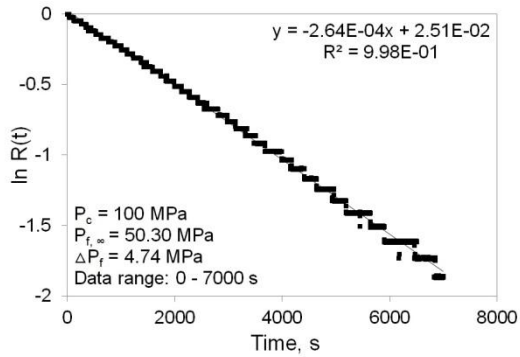

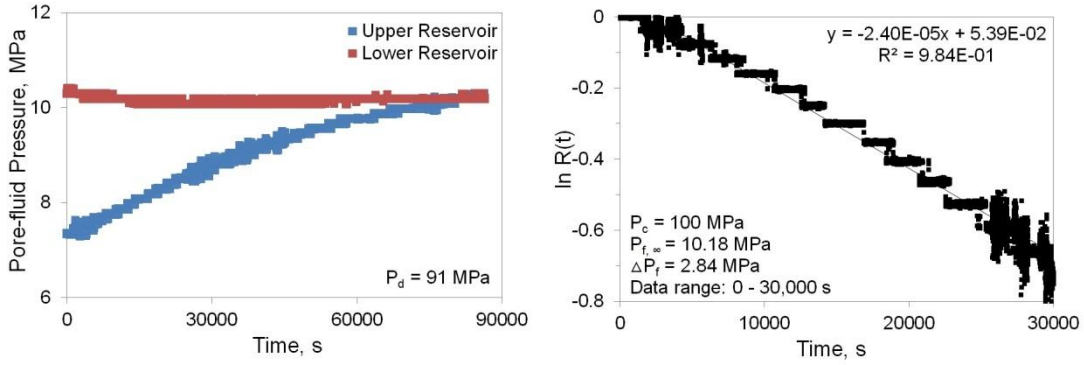


*These measurements are affected by the low resolution of pore-fluid pressure meters of 0.1 MPa, showing zig-zag shape for the pressure – time curve.

**Minor difference in reading on the upstream and downstream pore-fluid pressure meters was noticed at the end of pore-pressure equilibration experiment. This was explained as the non-linear behaviour of the pore-fluid pressure gauge of the upstream reservoir. The behaviour of the pore-fluid pressure gauge of the downstream reservoir was noticed to be more reliable and used as the reference to offset the recorded pore-fluid pressure of the upstream reservoir to provide a common value of pore-fluid pressure at the end of pore-pressure equilibration.

## G-3 High-porosity Glass-bead Specimen

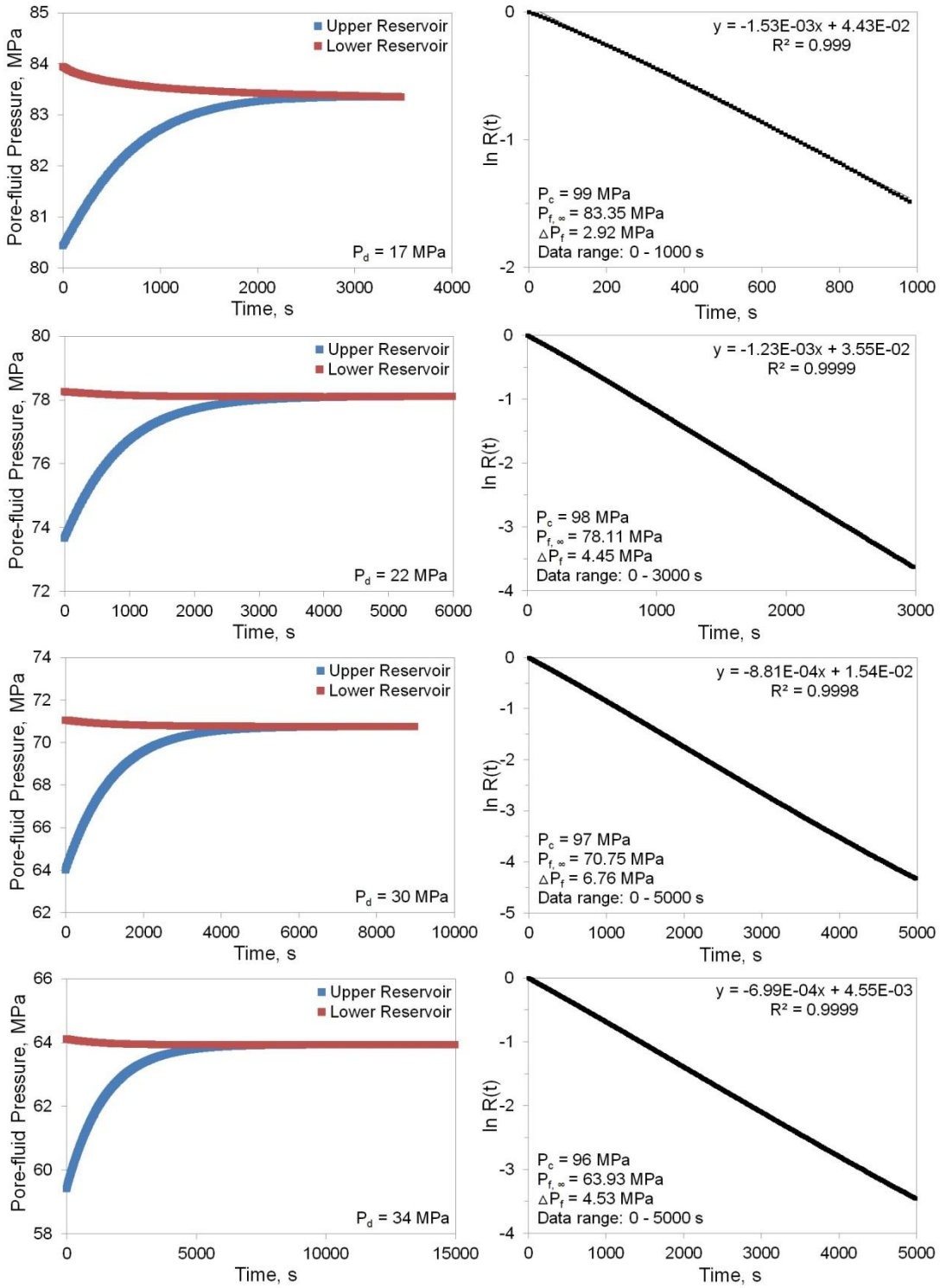

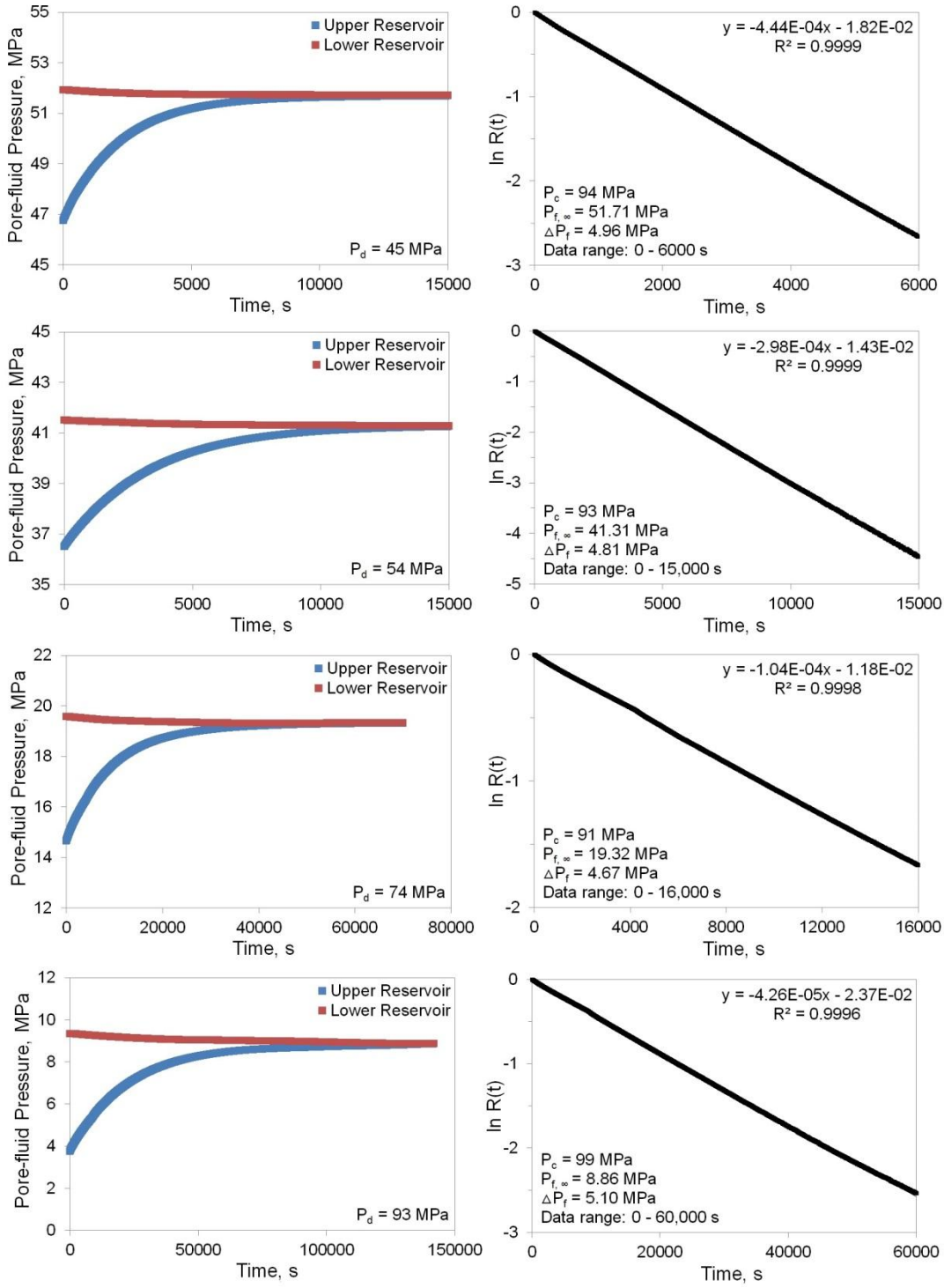


*Minor difference in reading on the upstream and downstream pore-fluid pressure meters was noticed at the end of pore-pressure equilibration experiment. This was explained as the non-linear behaviour of the pore-fluid pressure gauge of the upstream reservoir. The behaviour of the pore-fluid pressure gauge of the downstream reservoir was noticed to be more reliable and used as the reference to offset the recorded pore-fluid pressure of the upstream reservoir to provide a common value of pore-fluid pressure at the end of pore-pressure equilibration.

## APPENDIX H

# Argon Permeability

Table H-1 Argon Permeability of Cracked Glass-rod Specimen

| $P_d$, MPa | $P_c$, MPa | $P_f$, MPa | $K_f$, MPa | $\eta$, μPa·s | $L_s$, mm | $A_s$, mm$^2$ | $A$, 1/s | $k$, $10^{-19}$ m$^2$ |
|---|---|---|---|---|---|---|---|---|
| 11±2 | 98 | 87±2 | 208.79±7.29 | 65.46±0.89 | | | $1.85\times10^{-3}$ | 7.4±0.5 |
| 17±2 | 98 | 81±2 | 189.00±7.45 | 63.00±0.93 | | | $1.34\times10^{-3}$ | 5.7±0.4 |
| 22±2 | 96 | 74±2 | 161.65±6.71 | 59.49±0.88 | 150.220 ±0.001 | 176.53 ±0.02 | $8.16\times10^{-4}$ | 3.8±0.3 |
| 27±2 | 96 | 69±2 | 143.51±7.23 | 57.05±0.99 | | | $5.85\times10^{-4}$ | 2.9±0.2 |
| 31±2 | 94 | 63±2 | 123.02±6.85 | 54.15±0.99 | | | $4.35\times10^{-4}$ | 2.4±0.2 |

$P_d$: differential pressure; $P_c$: confining pressure; $P_f$: pore-fluid pressure; $K_f$: bulk modulus of argon; $\eta$: argon viscosity; $L_s$: sample length; $A_s$: sample cross-sectional area; $A$: rate constant; $k$: permeability.

Table H-1 (Continued) Argon Permeability of Cracked Glass-rod Specimen

| $P_d$, MPa | $P_c$, MPa | $P_f$, MPa | $K_f$, MPa | $\eta$, μPa·s | $L_s$, mm | $A_s$, $mm^2$ | $A$, 1/s | $k$, $10^{-19}$ $m^2$ |
|---|---|---|---|---|---|---|---|---|
| 41±2 | 93 | 52±2 | 89.12±4.77 | 48.96±0.77 | | | $2.24±0.5 \times 10^{-4}$ | 1.6±0.4 |
| 53±2 | 92 | 39±2 | 54.57±4.51 | 42.76±0.90 | | | $8.60±2 \times 10^{-5}$ | 0.9±0.2 |
| 65±2 | 92 | 27±2 | 31.65±3.87 | 37.36±1.05 | 150.220 ±0.001 | 176.53 ±0.02 | $3.23±0.5 \times 10^{-5}$ | 0.5±0.1 |
| 71±2 | 79 | 8±2 | 8.20±1.73 | 28.44±0.83 | | | $3.96±0.5 \times 10^{-6}$ | 0.2±0.0 |
| 101 | 101 | ~ 0 | - | - | | | - | ~ 0 |

$P_d$: differential pressure; $P_c$: confining pressure; $P_f$: pore-fluid pressure; $K_f$: bulk modulus of argon; $\eta$: argon viscosity; $L_s$: sample length; $A_s$: sample cross-sectional area; $A$: rate constant; $k$: permeability.

Table H-2 Argon Permeability of Cracked Low-porosity Glass-bead Specimen

| $P_d$, MPa | $P_c$, MPa | $P_f$, MPa | $K_f$, MPa | $\eta$, μPa·s | $L_s$, mm | $A_s$, $mm^2$ | $A$, 1/s | $k$, $10^{-19}$ $m^2$ |
|---|---|---|---|---|---|---|---|---|
| 12±2 | 99 | 87±2 | 209.62±7.55 | 65.56±0.92 | | | 2.05±0.05 ×$10^{-3}$ | 8.1±0.6 |
| 22±3 | 100 | 78±3 | 175.16±8.60 | 61.25±1.10 | | | 1.17±0.05 ×$10^{-3}$ | 5.2±0.5 |
| 38±3 | 101 | 63±3 | 123.48±8.00 | 54.22±1.15 | 150.125 ±0.001 | 176.67 ±0.02 | 5.10±0.5 ×$10^{-4}$ | 2.8±0.4 |
| 52±3 | 100 | 48±3 | 78.32±6.66 | 47.16±1.12 | | | 2.64±0.1 ×$10^{-4}$ | 2.0±0.2 |
| 91±2 | 100 | 9±2 | 8.54±1.41 | 28.60±0.67 | | | 2.40±0.5 ×$10^{-5}$ | 1.0±0.3 |

$P_d$: differential pressure; $P_c$: confining pressure; $P_f$: pore-fluid pressure; $K_f$: bulk modulus of argon; $\eta$: argon viscosity; $L_s$: sample length; $A_s$: sample cross-sectional area; $A$: rate constant; $k$: permeability.

Table H-3 Argon Permeability of Cracked High-porosity Glass-bead Specimen

| $P_d$, MPa | $P_c$, MPa | $P_f$, MPa | $K_f$, MPa | $\eta$, μPa·s | $L_s$, mm | $A_s$, mm$^2$ | $A$, 1/s | $k$, $10^{-19}$ m$^2$ |
|---|---|---|---|---|---|---|---|---|
| 17±2 | 99 | 82±2 | 190.91±5.55 | 63.24±0.69 | 150.052 ±0.001 | 176.76 ±0.02 | $1.53\pm0.1\times10^{-3}$ | 6.4±0.6 |
| 22±2 | 98 | 76±2 | 168.59±8.17 | 60.40±1.05 | | | $1.23\times10^{-3}$ | 5.6±0.4 |
| 30±4 | 97 | 67±4 | 138.58±11.67 | 56.37±1.60 | | | $8.81\times10^{-4}$ | 4.5±0.5 |
| 34±2 | 96 | 62±2 | 119.67±7.38 | 53.66±1.07 | | | $6.99\times10^{-4}$ | 4.0±0.4 |

$P_d$: differential pressure; $P_c$: confining pressure; $P_f$: pore-fluid pressure; $K_f$: bulk modulus of argon; $\eta$: argon viscosity; $L_s$: sample length; $A_s$: sample cross-sectional area; $A$: rate constant; $k$: permeability.

Table H-3 (Continued) Argon Permeability of Cracked High-porosity Glass-bead Specimen

| $P_d$, MPa | $P_c$, MPa | $P_f$, MPa | $K_f$, MPa | $\eta$, μPa·s | $L_s$, mm | $A_s$, mm$^2$ | $A$, 1/s | $k$, $10^{-19}$ m$^2$ |
|---|---|---|---|---|---|---|---|---|
| 45±3 | 94 | 49±3 | 81.93±7.11 | 47.77±1.18 | 150.052 ±0.001 | 176.76 ±0.02 | $4.44\times10^{-4}$ | 3.3±0.4 |
| 54±3 | 93 | 39±3 | 55.17±5.80 | 42.88±1.14 | | | $2.98\times10^{-4}$ | 2.9±0.4 |
| 74±3 | 91 | 17±3 | 17.22±2.83 | 32.50±1.11 | | | $1.04\times10^{-4}$ | 2.5±0.4 |
| 93±3 | 99 | 6±3 | 6.15±2.49 | 27.44±1.21 | | | $4.26\times10^{-5}$ | 2.4±1.0 |

$P_d$: differential pressure; $P_c$: confining pressure; $P_f$: pore-fluid pressure; $K_f$: bulk modulus of argon; $\eta$: argon viscosity; $L_s$: sample length; $A_s$: sample cross-sectional area; $A$: rate constant; $k$: permeability.

# Appendix I Water Permeability of Glass-rod Specimen

| $P_c$, MPa | $P_d$, MPa | $\Delta L$, mm | $\Delta t$, s | Water flux $q$, m/s | Water viscosity $\eta$, mPa·s | Pressure gradient $\Delta P_f/\Delta x$, MPa/m | Permeability $k$, $m^2$ |
|---|---|---|---|---|---|---|---|
| 1.5 | 1.3±0.1 | 10±1 | 197±1 | $6.8\pm0.7\times10^{-8}$ | $1.00\pm0.05$ | 3.2±0.1 | $2.1\pm0.2\times10^{-17}$ |
| 3.1 | 2.9±0.1 | 11±1 | 960±1 | $1.5\pm0.2\times10^{-8}$ | | | $4.8\pm0.5\times10^{-18}$ |
| 6.3 | 6.1±0.1 | 17±1 | 5160±1 | $4.4\pm0.4\times10^{-9}$ | | | $1.4\pm0.2\times10^{-18}$ |
| 9.5 | 9.3±0.1 | 1±1 | 6060±1 | $2.2\pm0.2\times10^{-10}$ | | | $7.0\pm0.8\times10^{-20}$ |

$P_c$: confining pressure; $P_d$: differential pressure; $\Delta L$: advance of water front in rubber tubing between two successive readings; $\Delta t$: time interval between two successive readings corresponding to the measured $\Delta L$. Permeability $k$ is calculated through Darcy's law given by Eq. (3.77).

# Appendix J Low-frequency (mHz) Mechanical Data

Table J-1 Cracked Glass-rod Specimen – Shear Modulus

| Saturation Condition | $P_c$, MPa | $P_f$, MPa | $P_d$, MPa | $G$, GPa | | | | | | | $\bar{G}$, GPa |
|---|---|---|---|---|---|---|---|---|---|---|---|
| | | | | 0.01 Hz | 0.02 Hz | 0.05 Hz | 0.09 Hz | 0.16 Hz | 0.26 Hz | 0.78 Hz | |
| Dry, decreasing $P_c$ | 100 | 0 | 100 | 27.68 | 27.85 | 27.89 | 27.89 | 27.91 | 27.96 | 28.15 | 27.86±0.28 |
| | 80 | 0 | 80 | 27.94 | 28.02 | 28.08 | 28.00 | 28.01 | 28.14 | 28.04 | 28.03±0.24 |
| | 60 | 0 | 60 | 28.05 | 28.05 | 28.04 | 28.00 | 28.10 | 28.13 | 27.87 | 28.06±0.00 |
| | 50 | 0 | 50 | 28.15 | 27.98 | 28.14 | 28.04 | 28.11 | 28.20 | 28.14 | 28.10±0.25 |
| | 40 | 0 | 40 | 27.94 | 27.98 | 27.97 | 27.99 | 27.99 | 28.08 | 28.09 | 27.99±0.54 |
| | 30 | 0 | 30 | 27.95 | 28.01 | 28.05 | 28.00 | 28.04 | 28.08 | 28.21 | 28.02±0.43 |
| | 25 | 0 | 25 | 27.87 | 27.92 | 27.99 | 27.91 | 27.86 | 27.96 | 28.06 | 27.92±0.37 |
| | 20 | 0 | 20 | 27.94 | 28.02 | 28.05 | 28.01 | 28.14 | 28.12 | 27.99 | 28.05±0.00 |
| | 15 | 0 | 15 | 27.79 | 27.88 | 27.80 | 27.84 | 27.83 | 27.86 | 27.69 | 27.83±0.27 |
| | 10 | 0 | 10 | 27.40 | 27.44 | 27.41 | 27.42 | 27.51 | 27.31 | 27.76 | 27.42±0.19 |

$P_c$: confining pressure; $P_f$: pore-fluid pressure; $P_d$: differential pressure; $G$: shear modulus; $\bar{G}$: average shear modulus from 0.01 Hz to 0.26 Hz.

Table J-1 (Continued) Cracked Glass-rod Specimen – Shear Modulus

| Saturation Condition | $P_c$, MPa | $P_f$, MPa | $P_d$, MPa | $G$, GPa | | | | | | | $\bar{G}$, GPa |
|---|---|---|---|---|---|---|---|---|---|---|---|
| | | | | 0.01 Hz | 0.02 Hz | 0.05 Hz | 0.09 Hz | 0.16 Hz | 0.26 Hz | 0.78 Hz | |
| Argon saturation, $P_c \approx 100$ MPa, decreasing $P_f$ | 98 | 88 | 10 | 26.92 | 27.02 | 27.05 | 27.08 | 27.23 | 27.03 | 27.38 | $27.06 \pm 0.22$ |
| | 97 | 83 | 14 | 27.35 | 27.46 | 27.44 | 27.48 | 27.48 | 27.58 | 27.43 | $27.47 \pm 0.20$ |
| | 96 | 76 | 20 | 27.65 | 27.70 | 27.80 | 27.74 | 27.90 | 27.86 | 27.76 | $27.78 \pm 0.20$ |
| | 96 | 71 | 25 | 27.67 | 27.77 | 27.76 | 27.77 | 27.75 | 27.84 | 27.80 | $27.76 \pm 0.20$ |
| | 94 | 65 | 29 | 27.81 | 27.84 | 27.83 | 27.84 | 27.92 | 27.93 | 28.10 | $27.86 \pm 0.23$ |
| | 93 | 53 | 40 | 28.03 | 27.97 | 27.93 | 28.02 | 27.96 | 28.04 | 27.99 | $27.99 \pm 0.00$ |
| | 91 | 40 | 51 | 28.16 | 27.97 | 28.11 | 28.07 | 28.11 | 28.13 | 28.24 | $28.09 \pm 0.00$ |
| | 93 | 29 | 64 | 28.00 | 28.15 | 28.00 | 27.96 | 28.04 | 28.08 | 28.05 | $28.04 \pm 0.47$ |
| | 101 | 0* | 101 | 27.74 | 27.98 | 27.92 | 27.98 | 27.95 | 27.94 | 28.28 | $27.92 \pm 0.37$ |

*Pore-pressure equilibrium cannot be achieved between the upstream and downstream reservoirs, indicating the cracks of the specimen are fully closed and pore-fluid pressure is zero.

Table J-1 (Continued) Cracked Glass-rod Specimen – Shear Modulus

| Saturation Condition | $P_c$, MPa | $P_f$, MPa | $P_d$, MPa | $G$, GPa | | | | | | | $\bar{G}$, GPa |
|---|---|---|---|---|---|---|---|---|---|---|---|
| | | | | 0.01 Hz | 0.02 Hz | 0.05 Hz | 0.09 Hz | 0.16 Hz | 0.26 Hz | 0.78 Hz | |
| Argon saturation, decreasing $P_c$, $P_f$ = 10 MPa | 101 | 0* | 101 | 27.74 | 27.98 | 27.92 | 27.98 | 27.95 | 27.94 | 28.28 | 27.92 ±0.37 |
| | 78 | 10 | 68 | 28.00 | 28.06 | 28.07 | 28.04 | 28.08 | 28.17 | 28.00 | 28.07 ±0.29 |
| | 55 | 10 | 45 | 28.12 | 28.07 | 28.16 | 28.13 | 28.15 | 28.15 | 28.44 | 28.13 ±0.33 |
| | 45 | 10 | 35 | 28.26 | 28.12 | 28.14 | 28.19 | 28.21 | 28.23 | 28.32 | 28.19 ±0.00 |
| | 35 | 10 | 25 | 28.03 | 28.02 | 28.09 | 28.10 | 28.04 | 28.18 | 28.08 | 28.08 ±0.35 |
| | 30 | 10 | 20 | 28.03 | 28.00 | 28.06 | 28.00 | 28.19 | 28.19 | 28.12 | 28.08 ±0.00 |
| | 25 | 10 | 15 | 27.92 | 27.96 | 27.90 | 27.93 | 27.92 | 28.02 | 27.68 | 27.94 ±0.00 |
| | 20 | 10 | 10 | 27.65 | 27.65 | 27.67 | 27.74 | 27.76 | 27.61 | 28.10 | 27.68 ±0.00 |

*Pore-pressure equilibrium cannot be achieved between the upstream and downstream reservoirs, indicating the cracks of the specimen are fully closed and pore-fluid pressure is zero.

Table J-1 (Continued) Cracked Glass-rod Specimen – Shear Modulus

| Saturation Condition | $P_c$, MPa | $P_f$, MPa | $P_d$, MPa | $G$, GPa | | | | | | | $\bar{G}$, GPa |
|---|---|---|---|---|---|---|---|---|---|---|---|
| | | | | 0.01 Hz | 0.02 Hz | 0.05 Hz | 0.09 Hz | 0.16 Hz | 0.26 Hz | 0.78 Hz | |
| Dry (repeat), decreasing $P_c$ | 100 | 0 | 100 | 27.95 | 28.01 | 28.05 | 28.11 | 28.04 | 27.99 | 28.16 | 28.03±0.44 |
| | 70 | 0 | 70 | 28.16 | 28.26 | 28.24 | 28.17 | 28.31 | 28.32 | 28.27 | 28.24±0.33 |
| | 45 | 0 | 45 | 28.37 | 28.22 | 28.26 | 28.25 | 28.30 | 28.40 | 28.45 | 28.30±0.26 |
| | 30 | 0 | 30 | 28.18 | 28.15 | 28.15 | 28.09 | 28.14 | 28.18 | 28.28 | 28.15±0.35 |
| | 25 | 0 | 25 | 28.07 | 28.15 | 28.15 | 28.14 | 28.07 | 28.18 | 28.11 | 28.13±0.27 |
| | 20 | 0 | 20 | 28.13 | 28.05 | 28.09 | 28.04 | 28.17 | 28.18 | 28.10 | 28.11±0.27 |
| | 15 | 0 | 15 | 27.94 | 28.02 | 27.98 | 28.01 | 27.97 | 28.05 | 27.78 | 28.00±0.24 |
| | 10 | 0 | 10 | 27.77 | 27.73 | 27.79 | 27.77 | 27.88 | 27.65 | 28.10 | 27.77±0.34 |

Table J-1 (Continued) Cracked Glass-rod Specimen – Shear Modulus

| Saturation Condition | $P_c$, MPa | $P_f$, MPa | $P_d$, MPa | $G$, GPa | | | | | | | $\bar{G}$, GPa |
|---|---|---|---|---|---|---|---|---|---|---|---|
| | | | | 0.01 Hz | 0.02 Hz | 0.05 Hz | 0.09 Hz | 0.16 Hz | 0.26 Hz | 0.78 Hz | |
| Water saturation, increasing $P_c$, $P_f \approx 20$ MPa | 26 | 16 | 10 | 28.61 | 28.69 | 28.72 | 28.73 | 28.76 | 28.58 | 28.99 | 28.68 ±0.00 |
| | 32 | 16 | 16 | 28.38 | 28.53 | 28.46 | 28.52 | 28.48 | 28.55 | 28.48 | 28.49 ±0.00 |
| | 36 | 17±1 | 19±1 | 28.47 | 28.49 | 28.55 | 28.47 | 28.66 | 28.6 | 28.58 | 28.54 ±0.00 |
| | 42 | 17±1 | 25±1 | 28.39 | 28.49 | 28.56 | 28.51 | 28.45 | 28.57 | 28.67 | 28.50 ±0.32 |
| | 48 | 18 | 30 | 28.43 | 28.45 | 28.45 | 28.43 | 28.51 | 28.54 | 28.77 | 28.47 ±0.34 |
| | 59 | 19±1 | 40±1 | 28.37 | 28.39 | 28.36 | 28.45 | 28.45 | 28.48 | 28.54 | 28.42 ±0.00 |
| | 66 | 20±2 | 46±2 | 28.41 | 28.35 | 28.40 | 28.39 | 28.41 | 28.48 | 28.50 | 28.41 ±0.00 |
| | 86 | 20±3 | 66±3 | 28.19 | 28.22 | 28.19 | 28.13 | 28.22 | 28.30 | 28.12 | 28.21 ±0.00 |
| | 108 | 22±5 | 86±5 | 28.00 | 28.01 | 28.10 | 27.96 | 28.06 | 28.17 | 28.16 | 28.05 ±0.00 |

Table J-1 (Continued) Cracked Glass-rod Specimen – Shear Modulus

| Saturation Condition | $P_c$, MPa | $P_f$, MPa | $P_d$, MPa | $G$, GPa | | | | | | | $\bar{G}$, GPa |
|---|---|---|---|---|---|---|---|---|---|---|---|
| | | | | 0.01 Hz | 0.02 Hz | 0.05 Hz | 0.09 Hz | 0.16 Hz | 0.26 Hz | 0.78 Hz | |
| Water saturation, decreasing $P_c$, $P_f \approx 20$ MPa | 108 | 22±5 | 86±5 | 28.00 | 28.01 | 28.10 | 27.96 | 28.06 | 28.17 | 28.16 | 28.05±0.00 |
| | 75 | 20±3 | 55±3 | 28.19 | 28.26 | 28.29 | 28.19 | 28.24 | 28.26 | 28.22 | 28.24±0.21 |
| | 54 | 18±2 | 36±2 | 28.32 | 28.30 | 28.34 | 28.34 | 28.36 | 28.45 | 28.34 | 28.35±0.00 |
| | 38 | 19±1 | 19±1 | 28.40 | 28.50 | 28.55 | 28.51 | 28.72 | 28.64 | 28.61 | 28.55±0.23 |
| | 29 | 18 | 11 | 29.05 | 29.03 | 29.00 | 28.98 | 29.11 | 28.92 | 29.29 | 29.02±0.00 |

Table J-2 Cracked Glass-rod Specimen – Shear Attenuation

| Saturation Condition | $P_c$, MPa | $P_f$, MPa | $P_d$, MPa | $1/Q_G$ | | | | | | |
|---|---|---|---|---|---|---|---|---|---|---|
| | | | | 0.01 Hz | 0.02 Hz | 0.05 Hz | 0.09 Hz | 0.16 Hz | 0.26 Hz | 0.78 Hz |
| Dry, decreasing $P_c$ | 100 | 0 | 100 | -0.00016 | 0.00001 | 0.00020 | -0.00056 | 0.00057 | 0.00026 | 0.00167 |
| | 80 | 0 | 80 | -0.00001 | 0.00050 | 0.00017 | -0.00014 | 0.00026 | 0.00080 | 0.00063 |
| | 60 | 0 | 60 | -0.00005 | 0.00012 | 0.00003 | 0.00047 | 0.00116 | 0.00038 | 0.00138 |
| | 50 | 0 | 50 | 0.00000 | -0.00040 | 0.00027 | 0.00010 | 0.00070 | 0.00051 | 0.00040 |
| | 40 | 0 | 40 | 0.00037 | 0.00092 | 0.00091 | 0.00119 | 0.00050 | 0.00092 | 0.00003 |
| | 30 | 0 | 30 | 0.00059 | 0.00065 | 0.00044 | 0.00010 | -0.00020 | -0.00055 | -0.00033 |
| | 25 | 0 | 25 | 0.00039 | 0.00062 | 0.00065 | 0.00119 | 0.00146 | -0.00044 | 0.00247 |
| | 20 | 0 | 20 | -0.00026 | -0.00016 | 0.00018 | 0.00027 | -0.00114 | -0.00001 | -0.00063 |
| | 15 | 0 | 15 | 0.00028 | 0.00076 | 0.00048 | 0.00118 | 0.00042 | 0.00067 | 0.00223 |
| | 10 | 0 | 10 | 0.00187 | 0.00221 | 0.00273 | 0.00174 | 0.00180 | 0.00213 | 0.00283 |

$P_c$: confining pressure; $P_f$: pore-fluid pressure; $P_d$: differential pressure; $1/Q_G$: shear attenuation.

Table J-2 (Continued) Cracked Glass-rod Specimen – Shear Attenuation

| Saturation Condition | $P_c$, MPa | $P_f$, MPa | $P_d$, MPa | $1/Q_G$ | | | | | | |
|---|---|---|---|---|---|---|---|---|---|---|
| | | | | 0.01 Hz | 0.02 Hz | 0.05 Hz | 0.09 Hz | 0.16 Hz | 0.26 Hz | 0.78 Hz |
| Argon saturation, $P_c \approx 100$ MPa, decreasing $P_f$ | 98 | 88 | 10 | 0.00256 | 0.00278 | 0.00303 | 0.00333 | 0.00290 | 0.00307 | 0.00199 |
| | 97 | 83 | 14 | 0.00085 | 0.00145 | 0.00124 | 0.00180 | 0.00122 | 0.00173 | 0.00308 |
| | 96 | 76 | 20 | 0.00023 | 0.00048 | 0.00060 | 0.00093 | -0.00054 | 0.00096 | -0.00005 |
| | 96 | 71 | 25 | 0.00040 | 0.00035 | 0.00088 | 0.00109 | 0.00152 | -0.00009 | 0.00213 |
| | 94 | 65 | 29 | 0.00030 | 0.00040 | 0.00103 | 0.00037 | 0.00093 | 0.00101 | 0.00004 |
| | 93 | 53 | 40 | 0.00034 | 0.00061 | 0.00070 | 0.00130 | 0.00057 | 0.00094 | 0.00016 |
| | 91 | 40 | 51 | -0.00032 | 0.00005 | 0.00008 | -0.00010 | 0.00019 | 0.00108 | 0.00024 |
| | 93 | 29 | 64 | -0.00061 | -0.00049 | -0.00061 | 0.00051 | 0.00110 | 0.00034 | 0.00056 |
| | 101 | 0* | 101 | -0.00068 | -0.00038 | 0.00037 | -0.00035 | 0.00099 | 0.00032 | 0.00007 |

*Pore-pressure equilibrium cannot be achieved between the upstream and downstream reservoirs, indicating the cracks of the specimen are fully closed and pore-fluid pressure is zero.

Table J-2 (Continued) Cracked Glass-rod Specimen – Shear Attenuation

| Saturation Condition | $P_c$, MPa | $P_f$, MPa | $P_d$, MPa | $1/Q_G$ | | | | | | |
|---|---|---|---|---|---|---|---|---|---|---|
| | | | | 0.01 Hz | 0.02 Hz | 0.05 Hz | 0.09 Hz | 0.16 Hz | 0.26 Hz | 0.78 Hz |
| Argon saturation, decreasing $P_c$, $P_f$ = 10 MPa | 101 | 0* | 101 | -0.00068 | -0.00038 | 0.00037 | -0.00035 | 0.00099 | 0.00032 | 0.00007 |
| | 78 | 10 | 68 | -0.00097 | -0.00070 | -0.00001 | 0.00049 | 0.00059 | 0.00030 | 0.00208 |
| | 55 | 10 | 45 | -0.00042 | 0.00013 | 0.00036 | 0.00067 | 0.00062 | 0.00103 | -0.00019 |
| | 45 | 10 | 35 | -0.00040 | 0.00010 | 0.00056 | 0.00061 | 0.00062 | 0.00023 | 0.00118 |
| | 35 | 10 | 25 | -0.00009 | -0.00003 | 0.00056 | 0.00054 | 0.00145 | -0.00044 | 0.00196 |
| | 30 | 10 | 20 | 0.00045 | 0.00055 | 0.00046 | 0.00118 | -0.00004 | 0.00090 | 0.00084 |
| | 25 | 10 | 15 | 0.00047 | 0.00101 | 0.00119 | 0.00165 | 0.00128 | 0.00192 | 0.00323 |
| | 20 | 10 | 10 | 0.00124 | 0.00121 | 0.00197 | 0.00179 | 0.00163 | 0.00185 | 0.00117 |

*Pore-pressure equilibrium cannot be achieved between the upstream and downstream reservoirs, indicating the cracks of the specimen are fully closed and pore-fluid pressure is zero.

Table J-2 (Continued) Cracked Glass-rod Specimen – Shear Attenuation

| Saturation Condition | $P_c$, MPa | $P_f$, MPa | $P_d$, MPa | $1/Q_G$ | | | | | | |
|---|---|---|---|---|---|---|---|---|---|---|
| | | | | 0.01 Hz | 0.02 Hz | 0.05 Hz | 0.09 Hz | 0.16 Hz | 0.26 Hz | 0.78 Hz |
| Dry (repeat), decreasing $P_c$ | 100 | 0 | 100 | 0.00003 | 0.00022 | 0.00071 | -0.00008 | 0.00058 | 0.00066 | 0.00141 |
| | 70 | 0 | 70 | -0.00066 | -0.00073 | -0.00031 | -0.00022 | 0.00016 | 0.00047 | -0.00050 |
| | 45 | 0 | 45 | 0.00056 | 0.00107 | 0.00083 | 0.00146 | 0.00083 | 0.00197 | 0.00056 |
| | 30 | 0 | 30 | 0.00047 | 0.00051 | 0.00108 | 0.00087 | 0.00085 | -0.00004 | 0.00109 |
| | 25 | 0 | 25 | 0.00044 | 0.00035 | 0.00053 | 0.00093 | 0.00173 | 0.00012 | 0.00193 |
| | 20 | 0 | 20 | 0.00048 | 0.00087 | 0.00069 | 0.00126 | 0.00020 | 0.00107 | 0.00151 |
| | 15 | 0 | 15 | 0.00014 | 0.00075 | 0.00073 | 0.00150 | 0.00097 | 0.00084 | 0.00288 |
| | 10 | 0 | 10 | 0.00123 | 0.00151 | 0.00220 | 0.00196 | 0.00182 | 0.00202 | 0.00124 |

Table J-2 (Continued) Cracked Glass-rod Specimen – Shear Attenuation

| Saturation Condition | $P_c$, MPa | $P_f$, MPa | $P_d$, MPa | $1/Q_G$ | | | | | | |
|---|---|---|---|---|---|---|---|---|---|---|
| | | | | 0.01 Hz | 0.02 Hz | 0.05 Hz | 0.09 Hz | 0.16 Hz | 0.26 Hz | 0.78 Hz |
| Water saturation, increasing $P_c$, $P_f \approx 20$ MPa | 26 | 16 | 10 | -0.00039 | -0.00014 | 0.00075 | -0.00053 | 0.00004 | 0.00113 | 0.00099 |
| | 32 | 16 | 16 | -0.00061 | 0.00015 | 0.00020 | 0.00061 | 0.00038 | 0.00082 | 0.00266 |
| | 36 | 17±1 | 19±1 | -0.00006 | 0.00000 | 0.00000 | 0.00055 | -0.00081 | -0.00003 | 0.00004 |
| | 42 | 17±1 | 25±1 | -0.00037 | -0.00006 | -0.00003 | 0.00019 | 0.00129 | -0.00081 | 0.00136 |
| | 48 | 18 | 30 | 0.00000 | 0.00013 | 0.00044 | 0.00029 | 0.00038 | -0.00026 | 0.00032 |
| | 59 | 19±1 | 40±1 | -0.00039 | -0.00005 | -0.00001 | 0.00072 | 0.00009 | 0.00026 | -0.00129 |
| | 66 | 20±2 | 46±2 | -0.00011 | 0.00042 | 0.00073 | 0.00088 | 0.00040 | 0.00150 | 0.00064 |
| | 86 | 20±3 | 66±3 | -0.00048 | -0.00013 | -0.00011 | 0.00035 | 0.00068 | 0.00027 | 0.00088 |
| | 108 | 22±5 | 86±5 | -0.00020 | 0.00046 | 0.00017 | -0.00023 | 0.00059 | 0.00063 | -0.00032 |

Table J-2 (Continued) Cracked Glass-rod Specimen – Shear Attenuation

| Saturation Condition | $P_c$, MPa | $P_f$, MPa | $P_d$, MPa | $1/Q_G$ | | | | | | |
|---|---|---|---|---|---|---|---|---|---|---|
| | | | | 0.01 Hz | 0.02 Hz | 0.05 Hz | 0.09 Hz | 0.16 Hz | 0.26 Hz | 0.78 Hz |
| Water saturation, decreasing $P_c$, $P_f \approx 20$ MPa | 108 | 22±5 | 86±5 | -0.00020 | 0.00046 | 0.00017 | -0.00023 | 0.00059 | 0.00063 | -0.00032 |
| | 75 | 20±3 | 55±3 | -0.00086 | -0.00023 | -0.00021 | 0.00017 | -0.00013 | 0.00042 | -0.00021 |
| | 54 | 18±2 | 36±2 | 0.00009 | -0.00004 | 0.00042 | 0.00056 | 0.00020 | 0.00017 | -0.00044 |
| | 38 | 19±1 | 19±1 | -0.00040 | 0.00005 | 0.00002 | 0.00068 | -0.00090 | 0.00042 | -0.00100 |
| | 29 | 18 | 11 | -0.00056 | -0.00036 | -0.00019 | 0.00003 | -0.00020 | -0.00005 | -0.00090 |

Table J-3 Cracked Low-porosity Glass-bead Specimen – Elastic Moduli

| Saturation Condition | $P_c$, MPa | $P_f$, MPa | $P_d$, MPa | $G$, GPa | | | | | | | $\bar{G}$, GPa | $\bar{E}$, GPa |
|---|---|---|---|---|---|---|---|---|---|---|---|---|
| | | | | 0.01 Hz | 0.02 Hz | 0.05 Hz | 0.09 Hz | 0.16 Hz | 0.26 Hz | 0.78 Hz | | |
| Dry, Decreasing $P_c$ | 144 | 0 | 144 | 28.25 | 28.31 | 28.40 | 28.43 | 28.48 | 28.42 | 28.51 | 28.38 ±0.28 | 73.11 ±1.15 |
| | 99 | 0 | 99 | 28.29 | 28.28 | 28.36 | 28.38 | 28.44 | 28.55 | 28.46 | 28.38 ±0.29 | 71.84 ±1.64 |
| | 50 | 0 | 50 | 28.34 | 28.37 | 28.46 | 28.55 | 28.59 | 28.49 | 28.70 | 28.47 ±0.31 | 77.68 ±0.00 |
| | 31 | 0 | 31 | 28.08 | 28.11 | 28.15 | 28.16 | 28.27 | 28.34 | 28.38 | 28.19 ±0.00 | 77.03 ±1.57 |
| | 21 | 0 | 21 | 27.92 | 27.94 | 28.06 | 27.97 | 28.10 | 28.13 | 28.37 | 28.02 ±0.43 | 72.21 ±1.51 |
| | 11 | 0 | 11 | 27.13 | 27.24 | 27.27 | 27.24 | 27.40 | 27.28 | 27.40 | 27.26 ±0.27 | 66.61 ±2.63 |

$P_c$: confining pressure; $P_f$: pore-fluid pressure; $P_d$: differential pressure; $G$: shear modulus; $\bar{G}$: average shear modulus from 0.01 Hz to 0.26 Hz; $\bar{E}$: average Young's modulus from 0.01 Hz to 0.26 Hz.

Table J-3 (Continued) Cracked Low-porosity Glass-bead Specimen – Elastic Moduli

| Saturation Condition | $P_c$, MPa | $P_f$, MPa | $P_d$, MPa | $G$, GPa | | | | | | | $\bar{G}$, GPa | $\bar{E}$, GPa |
|---|---|---|---|---|---|---|---|---|---|---|---|---|
| | | | | 0.01 Hz | 0.02 Hz | 0.05 Hz | 0.09 Hz | 0.16 Hz | 0.26 Hz | 0.78 Hz | | |
| Argon saturation, $P_c \approx 100$ MPa, decreasing $P_f$ | 99 | 89 | 10 | 27.82 | 27.96 | 28.02 | 28.01 | 28.01 | 28.10 | 28.13 | 27.99 ±0.00 | 86.74 ±2.26 |
| | 100 (99) | 80 (78) | 20 (21) | 28.00 | 28.05 | 28.06 | 28.07 | 28.22 | 28.13 | 28.27 | 28.09 ±0.00 | 78.45 ±0.00 |
| | 100 | 65 | 35 | 28.16 | 28.17 | 28.22 | 28.20 | 28.20 | 28.37 | 28.42 | 28.22 ±0.00 | 77.68 ±0.00 |
| | 100 | 50 | 50 | 28.25 | 28.33 | 28.42 | 28.45 | 28.47 | 28.44 | 28.49 | 28.39 ±0.00 | 78.59 ±0.00 |
| | 100 (99) | 10 | 90 (89) | 28.27 | 28.32 | 28.36 | 28.42 | 28.40 | 28.38 | 28.38 | 28.36 ±0.25 | 77.13 ±0.00 |

Table J-3 (Continued) Cracked Low-porosity Glass-bead Specimen – Elastic Moduli

| Saturation Condition | $P_c$, MPa | $P_f$, MPa | $P_d$, MPa | $G$, GPa | | | | | | | $\bar{G}$, GPa | $\bar{E}$, GPa |
|---|---|---|---|---|---|---|---|---|---|---|---|---|
| | | | | 0.01 Hz | 0.02 Hz | 0.05 Hz | 0.09 Hz | 0.16 Hz | 0.26 Hz | 0.78 Hz | | |
| Argon saturation, decreasing $P_c$, $P_f$ = 10 MPa | 100 (99) | 10 | 90 (89) | 28.27 | 28.32 | 28.36 | 28.42 | 28.40 | 28.38 | 28.38 | 28.36 ±0.25 | 77.13 ±0.00 |
| | 62 | 10 | 52 | 28.34 | 28.41 | 28.50 | 28.52 | 28.51 | 28.59 | 28.59 | 28.48 ±0.00 | 78.66 ±0.00 |
| | 31 | 10 | 21 | 28.20 | 28.20 | 28.21 | 28.27 | 28.28 | 28.29 | 28.62 | 28.24 ±0.42 | 76.71 ±0.00 |
| | 22 | 10 | 12 | 28.09 | 28.16 | 28.22 | 28.22 | 28.33 | 28.27 | 28.49 | 28.22 ±0.00 | 81.77 ±3.33 |

Table J-3 (Continued) Cracked Low-porosity Glass-bead Specimen – Elastic Moduli

| Saturation Condition | $P_c$, MPa | $P_f$, MPa | $P_d$, MPa | $G$, GPa | | | | | | | $\bar{G}$, GPa | $\bar{E}$, GPa |
|---|---|---|---|---|---|---|---|---|---|---|---|---|
| | | | | 0.01 Hz | 0.02 Hz | 0.05 Hz | 0.09 Hz | 0.16 Hz | 0.26 Hz | 0.78 Hz | | |
| water saturation, increasing $P_c$, $P_f \approx 15$ MPa | 26 | 15 ±1.5 | 11 ±1.5 | 27.89 | 27.98 | 28.06 | 28.07 | 28.09 | 28.14 | 28.08 | 28.04 ±0.32 | 90.36 ±2.79 |
| | 30 | 14 ±0.5 | 16 ±0.5 | 28.62 | 28.69 | 28.74 | 28.72 | 28.82 | 28.78 | 28.79 | 28.72 ±0.00 | 85.67 ±1.25 |
| | 38 | 14 ±1.5 | 24 ±1.5 | 28.65 | 28.67 | 28.72 | 28.75 | 28.79 | 28.80 | 28.98 | 28.73 ±0.00 | 81.89 ±0.00 |
| | 47 | 16 ±1.5 | 31 ±1.5 | 28.61 | 28.62 | 28.66 | 28.74 | 28.72 | 28.81 | 29.01 | 28.69 ±0.00 | 82.57 ±1.76 |

Table J-4 Cracked Low-porosity Glass-bead Specimen – Shear Attenuation

| Saturation Condition | $P_c$, MPa | $P_f$, MPa | $P_d$, MPa | $1/Q_G$ | | | | | | |
|---|---|---|---|---|---|---|---|---|---|---|
| | | | | 0.01 Hz | 0.02 Hz | 0.05 Hz | 0.09 Hz | 0.16 Hz | 0.26 Hz | 0.78 Hz |
| Dry, Decreasing $P_c$ | 144 | 0 | 144 | 0.00288 | 0.00274 | 0.00215 | 0.00242 | 0.00230 | 0.00216 | 0.00286 |
| | 99 | 0 | 99 | 0.00336 | 0.00333 | 0.00308 | 0.00244 | 0.00223 | 0.00186 | 0.00196 |
| | 50 | 0 | 50 | 0.00328 | 0.00332 | 0.00351 | 0.00295 | 0.00263 | 0.00288 | 0.00267 |
| | 31 | 0 | 31 | 0.00420 | 0.00385 | 0.00354 | 0.00330 | 0.00367 | 0.00394 | 0.00296 |
| | 21 | 0 | 21 | 0.00394 | 0.00383 | 0.00332 | 0.00305 | 0.00329 | 0.00286 | 0.00144 |
| | 11 | 0 | 11 | 0.00504 | 0.00455 | 0.00402 | 0.00422 | 0.00410 | 0.00358 | 0.00386 |

$P_c$: confining pressure; $P_f$: pore-fluid pressure; $P_d$: differential pressure; $1/Q_G$: shear attenuation.

Table J-4 (Continued) Cracked Low-porosity Glass-bead Specimen – Shear Attenuation

| Saturation Condition | $P_c$, MPa | $P_f$, MPa | $P_d$, MPa | $1/Q_G$ | | | | | | |
|---|---|---|---|---|---|---|---|---|---|---|
| | | | | 0.01 Hz | 0.02 Hz | 0.05 Hz | 0.09 Hz | 0.16 Hz | 0.26 Hz | 0.78 Hz |
| Argon saturation, $P_c \approx 100$ MPa, decreasing $P_f$ | 99 | 89 | 10 | 0.00358 | 0.00305 | 0.00299 | 0.00250 | 0.00278 | 0.00180 | 0.00342 |
| | 100 (99) | 80 (78) | 20 (21) | 0.00321 | 0.00336 | 0.00308 | 0.00248 | 0.00297 | 0.00271 | 0.00288 |
| | 100 | 65 | 35 | 0.00348 | 0.00328 | 0.00264 | 0.00333 | 0.00345 | 0.00216 | 0.00272 |
| | 100 | 50 | 50 | 0.00304 | 0.00285 | 0.00292 | 0.00226 | 0.00247 | 0.00196 | 0.00185 |
| | 100 (99) | 10 | 90 (89) | 0.00244 | 0.00228 | 0.00233 | 0.00148 | 0.00136 | 0.00110 | 0.00034 |

Table J-4 (Continued) Cracked Low-porosity Glass-bead Specimen – Shear Attenuation

| Saturation Condition | $P_c$, MPa | $P_f$, MPa | $P_d$, MPa | $1/Q_G$ | | | | | | |
|---|---|---|---|---|---|---|---|---|---|---|
| | | | | 0.01 Hz | 0.02 Hz | 0.05 Hz | 0.09 Hz | 0.16 Hz | 0.26 Hz | 0.78 Hz |
| Argon saturation, decreasing $P_c$, $P_f$ = 10 MPa | 100 (99) | 10 | 90 (89) | 0.00244 | 0.00228 | 0.00233 | 0.00148 | 0.00136 | 0.00110 | 0.00034 |
| | 62 | 10 | 52 | 0.00324 | 0.00322 | 0.00349 | 0.00216 | 0.00300 | 0.00294 | 0.00152 |
| | 31 | 10 | 21 | 0.00358 | 0.00373 | 0.00338 | 0.00311 | 0.00256 | 0.00261 | 0.00191 |
| | 22 | 10 | 12 | 0.00365 | 0.00308 | 0.00269 | 0.00269 | 0.00299 | 0.00226 | 0.00373 |

Table J-4 (Continued) Cracked Low-porosity Glass-bead Specimen – Shear Attenuation

| Saturation Condition | $P_c$, MPa | $P_f$, MPa | $P_d$, MPa | $1/Q_G$ | | | | | | |
|---|---|---|---|---|---|---|---|---|---|---|
| | | | | 0.01 Hz | 0.02 Hz | 0.05 Hz | 0.09 Hz | 0.16 Hz | 0.26 Hz | 0.78 Hz |
| water saturation, increasing $P_c$, $P_f \approx 15$ MPa | 26 | 15 ±1.5 | 11 ±1.5 | 0.00358 | 0.00339 | 0.00301 | 0.00307 | 0.00292 | 0.00280 | 0.00320 |
| | 30 | 14 ±0.5 | 16 ±0.5 | 0.00310 | 0.00323 | 0.00273 | 0.00245 | 0.00294 | 0.00233 | 0.00336 |
| | 38 | 14 ±1.5 | 24 ±1.5 | 0.00322 | 0.00308 | 0.00273 | 0.00259 | 0.00313 | 0.00272 | 0.00362 |
| | 47 | 16 ±1.5 | 31 ±1.5 | 0.00334 | 0.00316 | 0.00252 | 0.00291 | 0.00277 | 0.00296 | 0.00170 |

Table J-5 Cracked High-porosity Glass-bead Specimen – Elastic Moduli

| Saturation Condition | $P_c$, MPa | $P_f$, MPa | $P_d$, MPa | $G$, GPa | | | | | | | $\bar{G}$, GPa | $\bar{E}$, GPa |
|---|---|---|---|---|---|---|---|---|---|---|---|---|
| | | | | 0.01 Hz | 0.02 Hz | 0.05 Hz | 0.09 Hz | 0.16 Hz | 0.26 Hz | 0.78 Hz | | |
| Dry, decreasing $P_c$ | 99 | 0 | 99 | 26.35 | 26.37 | 26.39 | 26.23 | 26.35 | 26.33 | 26.24 | 26.34 ±0.18 | 68.93 ±1.94 |
| | 80 | 0 | 80 | 26.33 | 26.32 | 26.36 | 26.35 | 26.35 | 26.36 | 26.41 | 26.35 ±0.22 | 69.94 ±2.87 |
| | 60 | 0 | 60 | 26.18 | 26.31 | 26.26 | 26.29 | 26.32 | 26.24 | 26.25 | 26.27 ±0.00 | 70.77 ±2.05 |
| | 50 | 0 | 50 | 26.04 | 26.21 | 26.05 | 26.01 | 26.05 | 25.97 | 25.87 | 26.06 ±0.19 | 68.60 ±3.10 |
| | 40 | 0 | 40 | 26.08 | 26.10 | 26.08 | 26.15 | 26.17 | 26.09 | 26.20 | 26.11 ±0.00 | 68.67 ±2.80 |
| | 30 | 0 | 30 | 25.66 | 25.66 | 25.62 | 25.66 | 25.68 | 25.63 | 25.65 | 25.65 ±0.41 | 66.93 ±0.00 |
| | 25 | 0 | 25 | 25.57 | 25.58 | 25.61 | 25.62 | 25.66 | 25.70 | 25.73 | 25.62 ±0.00 | 66.23 ±0.98 |
| | 20 | 0 | 20 | 25.17 | 25.17 | 25.18 | 25.18 | 25.23 | 25.22 | 25.16 | 25.19 ±0.19 | 64.38 ±2.42 |
| | 15 | 0 | 15 | 24.88 | 24.94 | 24.99 | 24.96 | 25.01 | 25.09 | 24.89 | 24.98 ±0.00 | 64.23 ±2.07 |
| | 10 | 0 | 10 | 22.70 | 22.76 | 22.81 | 22.78 | 22.87 | 22.92 | 22.91 | 22.81 ±0.00 | 63.25 ±0.00 |

$P_c$: confining pressure; $P_f$: pore-fluid pressure; $P_d$: differential pressure; $G$: shear modulus; $\bar{G}$: average shear modulus from 0.01 Hz to 0.26 Hz; $\bar{E}$: average Young's modulus from 0.01 Hz to 0.26 Hz.

Table J-5 (Continued) Cracked High-porosity Glass-bead Specimen – Elastic Moduli

| Saturation Condition | $P_c$, MPa | $P_f$, MPa | $P_d$, MPa | $G$, GPa | | | | | | | $\bar{G}$, GPa | $\bar{E}$, GPa |
|---|---|---|---|---|---|---|---|---|---|---|---|---|
| | | | | 0.01 Hz | 0.02 Hz | 0.05 Hz | 0.09 Hz | 0.16 Hz | 0.26 Hz | 0.78 Hz | | |
| Argon saturation, $P_c \approx 100$ MPa, decreasing $P_f$ | 99 | 83 | 16 | 24.02 | 24.10 | 24.14 | 24.17 | 24.20 | 24.24 | 24.17 | 24.15 ±0.00 | 62.47 ±0.88 |
| | 98 | 78 | 20 | 24.47 | 24.51 | 24.57 | 24.61 | 24.62 | 24.71 | 24.62 | 24.58 ±0.00 | 60.70 ±2.68 |
| | 97 | 71 | 26 | 24.91 | 24.95 | 25.00 | 25.01 | 25.00 | 25.00 | 24.94 | 24.98 ±0.00 | 62.33 ±1.89 |
| | 95 | 64 | 31 | 25.30 | 25.30 | 25.32 | 25.33 | 25.31 | 25.33 | 25.36 | 25.32 ±0.23 | 63.25 ±0.00 |
| | 94 | 52 | 42 | 25.60 | 25.67 | 25.63 | 25.68 | 25.67 | 25.67 | 25.72 | 25.65 ±0.32 | 62.94 ±1.94 |
| | 92 | 41 | 51 | 25.73 | 25.78 | 25.76 | 25.72 | 25.84 | 25.77 | 25.74 | 25.77 ±0.32 | 63.74 ±1.86 |
| | 91 | 19 | 72 | 26.16 | 26.22 | 26.22 | 26.21 | 26.28 | 26.22 | 26.28 | 26.22 ±0.28 | 65.92 ±0.88 |
| | 98 | 9 | 89 | 26.37 | 26.42 | 26.44 | 26.38 | 26.48 | 26.41 | 26.40 | 26.42 ±0.25 | 64.61 ±1.69 |

Table J-5 (Continued) Cracked High-porosity Glass-bead Specimen – Elastic Moduli

| Saturation Condition | $P_c$, MPa | $P_f$, MPa | $P_d$, MPa | $G$, GPa | | | | | | | $\bar{G}$, GPa | $\bar{E}$, GPa |
|---|---|---|---|---|---|---|---|---|---|---|---|---|
| | | | | 0.01 Hz | 0.02 Hz | 0.05 Hz | 0.09 Hz | 0.16 Hz | 0.26 Hz | 0.78 Hz | | |
| Argon saturation, decreasing $P_c$, $P_f$ = 9 MPa | 98 | 9 | 89 | 26.37 | 26.42 | 26.44 | 26.38 | 26.48 | 26.41 | 26.40 | 26.42 ±0.25 | 64.61 ±1.69 |
| | 58 | 9 | 49 | 25.91 | 25.88 | 25.88 | 25.89 | 25.96 | 25.90 | 25.88 | 25.90 ±0.00 | 63.32 ±2.43 |
| | 38 | 9 | 29 | 25.43 | 25.42 | 25.41 | 25.42 | 25.41 | 25.54 | 25.40 | 25.44 ±0.00 | 62.58 ±1.43 |
| | 33 | 9 | 24 | 25.29 | 25.31 | 25.35 | 25.34 | 25.34 | 25.42 | 25.31 | 25.34 ±0.00 | 61.77 ±0.84 |
| | 28 | 9 | 19 | 24.78 | 24.78 | 24.83 | 24.84 | 24.90 | 24.96 | 24.91 | 24.85 ±0.33 | 60.54 ±2.62 |
| | 23 | 9 | 14 | 24.28 | 24.33 | 24.36 | 24.39 | 24.48 | 24.58 | 24.52 | 24.40 ±0.28 | 61.86 ±0.88 |
| | 18 | 9 | 9 | 22.40 | 22.44 | 22.44 | 22.49 | 22.48 | 22.59 | 22.52 | 22.47 ±0.00 | 64.24 ±0.00 |

Table J-5 (Continued) Cracked High-porosity Glass-bead Specimen – Elastic Moduli

| Saturation Condition | $P_c$, MPa | $P_f$, MPa | $P_d$, MPa | $G$, GPa | | | | | | | $\bar{G}$, GPa | $\bar{E}$, GPa |
|---|---|---|---|---|---|---|---|---|---|---|---|---|
| | | | | 0.01 Hz | 0.02 Hz | 0.05 Hz | 0.09 Hz | 0.16 Hz | 0.26 Hz | 0.78 Hz | | |
| Water saturation, increasing $P_c$, $P_f \approx 15$ MPa | 46 | 16±5 | 30±5 | 25.28 | 25.22 | 25.25 | 25.24 | 25.27 | 25.27 | 25.24 | 25.26±0.00 | 64.49±0.00 |
| | 65 | 15±5 | 50±5 | 25.82 | 25.73 | 25.76 | 25.72 | 25.75 | 25.66 | 25.66 | 25.74±0.00 | 65.74±1.92 |
| | 97 | 16±5 | 81±5 | 26.28 | 26.32 | 26.33 | 26.37 | 26.33 | 26.37 | 26.32 | 26.33±0.21 | 65.39±2.13 |

Table J-5 (Continued) Cracked High-porosity Glass-bead Specimen – Elastic Moduli

| Saturation Condition | $P_c$, MPa | $P_f$, MPa | $P_d$, MPa | $G$, GPa | | | | | | | $\bar{G}$, GPa | $\bar{E}$, GPa |
|---|---|---|---|---|---|---|---|---|---|---|---|---|
| | | | | 0.01 Hz | 0.02 Hz | 0.05 Hz | 0.09 Hz | 0.16 Hz | 0.26 Hz | 0.78 Hz | | |
| Water saturation, decreasing $P_c$, $P_f \approx 15$ MPa | 97 | 16 ±5 | 81 ±5 | 26.28 | 26.32 | 26.33 | 26.37 | 26.33 | 26.37 | 26.32 | 26.33 ±0.21 | 65.39 ±2.13 |
| | 80 | 16 ±5 | 64 ±5 | 26.11 | 26.18 | 26.13 | 26.21 | 26.17 | 26.19 | 26.14 | 26.17 ±0.18 | 66.18 ±2.21 |
| | 55 | 14 ±5 | 41 ±5 | 25.75 | 25.75 | 25.71 | 25.78 | 25.81 | 25.71 | 25.83 | 25.75 ±0.00 | 64.52 ±2.21 |
| | 38 | 13 ±5 | 25 ±5 | 25.17 | 25.17 | 25.19 | 25.18 | 25.18 | 25.27 | 25.27 | 25.19 ±0.18 | 64.80 ±1.91 |
| | 33 | 12 ±4 | 21 ±4 | 24.77 | 24.79 | 24.83 | 24.85 | 24.87 | 24.95 | 24.87 | 24.84 ±0.21 | 65.70 ±1.83 |
| | 27 | 12 ±4 | 15 ±4 | 24.20 | 24.22 | 24.27 | 24.30 | 24.32 | 24.40 | 24.28 | 24.28 ±0.17 | 67.85 ±0.95 |
| | 22 | 11 ±4 | 11 ±4 | 23.30 | 23.27 | 23.28 | 23.41 | 23.38 | 23.48 | 23.39 | 23.35 ±0.16 | 72.86 ±1.97 |

Table J-6 Cracked High-porosity Glass-bead Specimen – Shear Attenuation

| Saturation Condition | $P_c$, MPa | $P_f$, MPa | $P_d$, MPa | $1/Q_G$ | | | | | | |
|---|---|---|---|---|---|---|---|---|---|---|
| | | | | 0.01 Hz | 0.02 Hz | 0.05 Hz | 0.09 Hz | 0.16 Hz | 0.26 Hz | 0.78 Hz |
| Dry, decreasing $P_c$ | 99 | 0 | 99 | 0.00120 | 0.00086 | 0.00110 | 0.00117 | 0.00060 | 0.00036 | -0.00040 |
| | 80 | 0 | 80 | 0.00092 | 0.00106 | 0.00083 | 0.00085 | 0.00087 | 0.00120 | 0.00049 |
| | 60 | 0 | 60 | 0.00094 | 0.00080 | 0.00099 | 0.00107 | 0.00076 | 0.00122 | 0.00223 |
| | 50 | 0 | 50 | 0.00116 | 0.00144 | 0.00116 | 0.00121 | 0.00138 | 0.00139 | 0.00184 |
| | 40 | 0 | 40 | 0.00052 | 0.00068 | 0.00059 | 0.00053 | 0.00027 | 0.00100 | 0.00249 |
| | 30 | 0 | 30 | 0.00162 | 0.00192 | 0.00175 | 0.00164 | 0.00147 | 0.00165 | 0.00143 |
| | 25 | 0 | 25 | 0.00074 | 0.00090 | 0.00085 | 0.00042 | 0.00112 | 0.00115 | -0.00016 |
| | 20 | 0 | 20 | 0.00215 | 0.00212 | 0.00201 | 0.00171 | 0.00237 | 0.00173 | 0.00158 |
| | 15 | 0 | 15 | 0.00083 | 0.00091 | 0.00108 | 0.00128 | 0.00117 | 0.00128 | 0.00038 |
| | 10 | 0 | 10 | 0.00481 | 0.00487 | 0.00458 | 0.00448 | 0.00436 | 0.00466 | 0.00467 |

$P_c$: confining pressure; $P_f$: pore-fluid pressure; $P_d$: differential pressure; $1/Q_G$: shear attenuation.

Table J-6 (Continued) Cracked High-porosity Glass-bead Specimen – Shear Attenuation

| Saturation Condition | $P_c$, MPa | $P_f$, MPa | $P_d$, MPa | $1/Q_G$ | | | | | | |
|---|---|---|---|---|---|---|---|---|---|---|
| | | | | 0.01 Hz | 0.02 Hz | 0.05 Hz | 0.09 Hz | 0.16 Hz | 0.26 Hz | 0.78 Hz |
| Argon saturation, $P_c \approx 100$ MPa, decreasing $P_f$ | 99 | 83 | 16 | 0.00245 | 0.00249 | 0.00257 | 0.00233 | 0.00241 | 0.00252 | 0.00141 |
| | 98 | 78 | 20 | 0.00153 | 0.00164 | 0.00162 | 0.00142 | 0.00209 | 0.00145 | 0.00055 |
| | 97 | 71 | 26 | 0.00137 | 0.00172 | 0.00148 | 0.00083 | 0.00134 | 0.00174 | 0.00105 |
| | 95 | 64 | 31 | 0.00092 | 0.00115 | 0.00082 | 0.00103 | 0.00079 | 0.00173 | 0.00133 |
| | 94 | 52 | 42 | 0.00064 | 0.00096 | 0.00090 | 0.00102 | 0.00089 | 0.00091 | 0.00267 |
| | 92 | 41 | 51 | 0.00072 | 0.00087 | 0.00067 | 0.00070 | 0.00090 | 0.00064 | 0.00141 |
| | 91 | 19 | 72 | 0.00030 | 0.00039 | 0.00053 | 0.00069 | 0.00025 | 0.00064 | 0.00192 |
| | 98 | 9 | 89 | -0.00020 | -0.00014 | 0.00006 | 0.00031 | 0.00031 | 0.00001 | 0.00012 |

Table J-6 (Continued) Cracked High-porosity Glass-bead Specimen – Shear Attenuation

| Saturation Condition | $P_c$, MPa | $P_f$, MPa | $P_d$, MPa | $1/Q_G$ | | | | | | |
|---|---|---|---|---|---|---|---|---|---|---|
| | | | | 0.01 Hz | 0.02 Hz | 0.05 Hz | 0.09 Hz | 0.16 Hz | 0.26 Hz | 0.78 Hz |
| Argon saturation, decreasing $P_c$, $P_f$ = 9 MPa | 98 | 9 | 89 | -0.00020 | -0.00014 | 0.00006 | 0.00031 | 0.00031 | 0.00001 | 0.00012 |
| | 58 | 9 | 49 | 0.00064 | 0.00100 | 0.00071 | 0.00075 | 0.00090 | 0.00140 | 0.00101 |
| | 38 | 9 | 29 | 0.00117 | 0.00126 | 0.00128 | 0.00121 | 0.00123 | 0.00160 | 0.00140 |
| | 33 | 9 | 24 | 0.00079 | 0.00090 | 0.00089 | 0.00105 | 0.00129 | 0.00037 | 0.00086 |
| | 28 | 9 | 19 | 0.00158 | 0.00176 | 0.00160 | 0.00157 | 0.00179 | 0.00178 | 0.00067 |
| | 23 | 9 | 14 | 0.00146 | 0.00160 | 0.00130 | 0.00154 | 0.00134 | 0.00157 | 0.00182 |
| | 18 | 9 | 9 | 0.00456 | 0.00441 | 0.00438 | 0.00444 | 0.00423 | 0.00476 | 0.00484 |

Table J-6 (Continued) Cracked High-porosity Glass-bead Specimen – Shear Attenuation

| Saturation Condition | $P_c$, MPa | $P_f$, MPa | $P_d$, MPa | $1/Q_G$ | | | | | | |
|---|---|---|---|---|---|---|---|---|---|---|
| | | | | 0.01 Hz | 0.02 Hz | 0.05 Hz | 0.09 Hz | 0.16 Hz | 0.26 Hz | 0.78 Hz |
| Water saturation, increasing $P_c$, $P_f \approx 15$ MPa | 46 | 16 ±5 | 30 ±5 | 0.00027 | 0.00039 | 0.00048 | 0.00011 | 0.00061 | 0.00102 | 0.00046 |
| | 65 | 15 ±5 | 50 ±5 | 0.00050 | 0.00050 | 0.00037 | 0.00053 | 0.00068 | 0.00090 | 0.00015 |
| | 97 | 16 ±5 | 81 ±5 | 0.00033 | 0.00032 | 0.00039 | 0.00057 | 0.00018 | 0.00065 | -0.00006 |

Table J-6 (Continued) Cracked High-porosity Glass-bead Specimen – Shear Attenuation

| Saturation Condition | $P_c$, MPa | $P_f$, MPa | $P_d$, MPa | $1/Q_G$ | | | | | | |
|---|---|---|---|---|---|---|---|---|---|---|
| | | | | 0.01 Hz | 0.02 Hz | 0.05 Hz | 0.09 Hz | 0.16 Hz | 0.26 Hz | 0.78 Hz |
| Water saturation, decreasing $P_c$, $P_f \approx 15$ MPa | 97 | 16 ±5 | 81 ±5 | 0.00033 | 0.00032 | 0.00039 | 0.00057 | 0.00018 | 0.00065 | -0.00006 |
| | 80 | 16 ±5 | 64 ±5 | 0.00095 | 0.00064 | 0.00079 | 0.00115 | 0.00056 | 0.00112 | 0.00097 |
| | 55 | 14 ±5 | 41 ±5 | 0.00059 | 0.000793 | 0.000266 | 0.00067 | 0.000576 | 0.000418 | 0.00123 |
| | 38 | 13 ±5 | 25 ±5 | 0.00070 | 0.00059 | 0.00046 | 0.00050 | 0.00073 | 0.00081 | 0.00014 |
| | 33 | 12 ±4 | 21 ±4 | 0.00038 | 0.00028 | 0.00045 | 0.00035 | 0.00046 | -0.00002 | -0.00001 |
| | 27 | 12 ±4 | 15 ±4 | 0.00043 | 0.00027 | 0.000116 | 0.00026 | 8.64E-05 | 0.000402 | -0.00022 |
| | 22 | 11 ±4 | 11 ±4 | 0.00084 | 0.00094 | 0.00054 | 0.00092 | 0.00053 | 0.00097 | 0.00092 |

# Appendix K Ultrasonic-frequency (MHz) Mechanical Data

Table K-1 Uncracked Glass-rod Specimen

| Saturation Condition | $P_c$, MPa | $P_f$, MPa | $P_d$, MPa | $V_p$, m/s | $V_s$, m/s | $G$*, GPa | $K$, GPa | $E$, GPa | $v$ |
|---|---|---|---|---|---|---|---|---|---|
| Dry, increasing $P_c$ | 5 | 0 | 5 | 5761.96 | 3485.70 | 30.54 | 42.73 | 74.00 | 0.21 |
| | 10 | 0 | 10 | 5785.30 | 3496.68 | 30.74 | 43.15 | 74.52 | 0.21 |
| | 15 | 0 | 15 | 5792.00 | 3502.80 | 30.84 | 43.21 | 74.74 | 0.21 |
| | 20 | 0 | 20 | 5795.36 | 3506.49 | 30.91 | 43.22 | 74.87 | 0.21 |
| | 25 | 0 | 25 | 5805.46 | 3506.49 | 30.91 | 43.51 | 74.97 | 0.21 |
| | 30 | 0 | 30 | 5812.21 | 3511.42 | 30.99 | 43.59 | 75.17 | 0.21 |
| | 35 | 0 | 35 | 5805.46 | 3510.18 | 30.97 | 43.42 | 75.07 | 0.21 |
| | 40 | 0 | 40 | 5805.46 | 3510.18 | 30.97 | 43.42 | 75.07 | 0.21 |
| | 50 | 0 | 50 | 5805.46 | 3508.95 | 30.95 | 43.45 | 75.04 | 0.21 |
| | 60 | 0 | 60 | 5812.21 | 3508.95 | 30.95 | 43.65 | 75.10 | 0.21 |
| | 70 | 0 | 70 | 5812.21 | 3506.49 | 30.91 | 43.71 | 75.04 | 0.21 |
| | 80 | 0 | 80 | 5815.59 | 3506.49 | 30.91 | 43.81 | 75.07 | 0.21 |
| | 90 | 0 | 90 | 5825.76 | 3501.58 | 30.82 | 44.22 | 75.03 | 0.22 |
| | 100 | 0 | 100 | 5829.15 | 3505.26 | 30.89 | 44.23 | 75.16 | 0.22 |

Table K-1 (Continued) Uncracked Glass-rod Specimen

| Saturation Condition | $P_c$, MPa | $P_f$, MPa | $P_d$, MPa | $V_p$, m/s | $V_s$, m/s | $G$, GPa | $K$, GPa | $E$, GPa | $v$ |
|---|---|---|---|---|---|---|---|---|---|
| Dry, decreasing $P_c$ | 100 | 0 | 100 | 5829.15 | 3505.26 | 30.89 | 44.23 | 75.16 | 0.22 |
| | 90 | 0 | 90 | 5825.76 | 3504.03 | 30.86 | 44.16 | 75.10 | 0.22 |
| | 80 | 0 | 80 | 5818.98 | 3505.26 | 30.89 | 43.94 | 75.07 | 0.22 |
| | 70 | 0 | 70 | 5822.36 | 3507.72 | 30.93 | 43.98 | 75.17 | 0.22 |
| | 60 | 0 | 60 | 5815.59 | 3507.72 | 30.93 | 43.78 | 75.10 | 0.21 |
| | 50 | 0 | 50 | 5812.21 | 3508.95 | 30.95 | 43.65 | 75.10 | 0.21 |
| | 40 | 0 | 40 | 5812.21 | 3510.18 | 30.97 | 43.62 | 75.14 | 0.21 |
| | 30 | 0 | 30 | 5808.83 | 3508.95 | 30.95 | 43.55 | 75.07 | 0.21 |
| | 20 | 0 | 20 | 5812.21 | 3507.72 | 30.93 | 43.68 | 75.07 | 0.21 |
| | 10 | 0 | 10 | 5812.21 | 3497.90 | 30.76 | 43.91 | 74.80 | 0.22 |

$P_c$: confining pressure; $P_f$: pore-fluid pressure; $P_d$: differential pressure; $V_p$: P-wave velocity; $V_s$: S-wave velocity; $G$: shear modulus; $K$: bulk modulus; $E$: Young's modulus; $v$: Poisson's ratio.

*Elastic moduli are calculated from measured P- and S-wave velocities with Eq. (3.71) – (3.73).

Table K-2 Cracked Glass-rod Specimen

| Saturation Condition | $P_c$, MPa | $P_f$, MPa | $P_d$, MPa | $V_p$, m/s | $V_s$, m/s | $G$*, GPa | $K$, GPa | $E$, GPa | $v$ |
|---|---|---|---|---|---|---|---|---|---|
| Dry, increasing $P_c$ | 10 | 0 | 10 | 5585.16 | 3259.83 | 26.61 | 42.63 | 66.08 | 0.24 |
| | 15 | 0 | 15 | 5654.55 | 3295.23 | 27.19 | 43.81 | 67.59 | 0.24 |
| | 20 | 0 | 20 | 5673.77 | 3303.93 | 27.34 | 44.17 | 67.98 | 0.24 |
| | 25 | 0 | 25 | 5683.43 | 3309.39 | 27.43 | 44.32 | 68.21 | 0.24 |
| | 30 | 0 | 30 | 5689.89 | 3312.67 | 27.48 | 44.43 | 68.35 | 0.24 |
| | 35 | 0 | 35 | 5693.12 | 3313.77 | 27.50 | 44.50 | 68.40 | 0.24 |
| | 40 | 0 | 40 | 5693.12 | 3315.96 | 27.53 | 44.45 | 68.47 | 0.24 |
| | 50 | 0 | 50 | 5693.12 | 3320.36 | 27.61 | 44.35 | 68.59 | 0.24 |
| | 60 | 0 | 60 | 5699.60 | 3322.56 | 27.64 | 44.49 | 68.70 | 0.24 |
| | 70 | 0 | 70 | 5699.60 | 3324.77 | 27.68 | 44.44 | 68.77 | 0.24 |
| | 80 | 0 | 80 | 5706.10 | 3328.08 | 27.74 | 44.55 | 68.91 | 0.24 |
| | 90 | 0 | 90 | 5712.61 | 3330.30 | 27.77 | 44.69 | 69.02 | 0.24 |
| | 100 | 0 | 100 | 5722.40 | 3335.84 | 27.87 | 44.85 | 69.25 | 0.24 |

Table K-2 (Continued) Cracked Glass-rod Specimen

| Saturation Condition | $P_c$, MPa | $P_f$, MPa | $P_d$, MPa | $V_p$, m/s | $V_s$, m/s | $G$, GPa | $K$, GPa | $E$, GPa | $v$ |
|---|---|---|---|---|---|---|---|---|---|
| Dry, decreasing $P_c$ | 100 | 0 | 100 | 5722.40 | 3335.84 | 27.87 | 44.85 | 69.25 | 0.24 |
| | 90 | 0 | 90 | 5712.61 | 3334.73 | 27.85 | 44.59 | 69.15 | 0.24 |
| | 80 | 0 | 80 | 5712.61 | 3334.73 | 27.85 | 44.59 | 69.15 | 0.24 |
| | 70 | 0 | 70 | 5712.61 | 3335.84 | 27.87 | 44.57 | 69.18 | 0.24 |
| | 60 | 0 | 60 | 5709.35 | 3334.73 | 27.85 | 44.50 | 69.12 | 0.24 |
| | 50 | 0 | 50 | 5702.85 | 3333.62 | 27.83 | 44.34 | 69.04 | 0.24 |
| | 40 | 0 | 40 | 5702.85 | 3331.40 | 27.79 | 44.39 | 68.98 | 0.24 |
| | 30 | 0 | 30 | 5699.60 | 3328.08 | 27.74 | 44.37 | 68.86 | 0.24 |
| | 20 | 0 | 20 | 5696.36 | 3321.46 | 27.63 | 44.42 | 68.65 | 0.24 |
| | 10 | 0 | 10 | 5641.80 | 3294.14 | 27.17 | 43.48 | 67.46 | 0.24 |

Table K-2 (Continued) Cracked Glass-rod Specimen

| Saturation Condition | $P_c$, MPa | $P_f$, MPa | $P_d$, MPa | $V_p$, m/s | $V_s$, m/s | $G$, GPa | $K$, GPa | $E$, GPa | $v$ |
|---|---|---|---|---|---|---|---|---|---|
| Argon saturation, increasing $P_c$, $P_f$ = 10 MPa | 20 | 10 | 10 | 5683.43 | 3313.77 | 27.50 | 44.23 | 68.35 | 0.24 |
| | 25 | 10 | 15 | 5689.89 | 3320.36 | 27.61 | 44.27 | 68.58 | 0.24 |
| | 30 | 10 | 20 | 5693.12 | 3323.66 | 27.67 | 44.29 | 68.70 | 0.24 |
| | 35 | 10 | 25 | 5699.60 | 3326.98 | 27.72 | 44.40 | 68.84 | 0.24 |
| | 40 | 10 | 30 | 5702.85 | 3329.19 | 27.76 | 44.45 | 68.93 | 0.24 |
| | 45 | 10 | 35 | 5706.10 | 3329.19 | 27.76 | 44.54 | 68.96 | 0.24 |
| | 50 | 10 | 40 | 5699.60 | 3330.30 | 27.78 | 44.33 | 68.94 | 0.24 |
| | 60 | 10 | 50 | 5702.85 | 3332.51 | 27.82 | 44.37 | 69.03 | 0.24 |
| | 70 | 10 | 60 | 5712.61 | 3335.84 | 27.87 | 44.58 | 69.20 | 0.24 |
| | 80 | 10 | 70 | 5719.13 | 3336.95 | 27.89 | 44.74 | 69.28 | 0.24 |
| | 90 | 10 | 80 | 5725.67 | 3341.41 | 27.97 | 44.83 | 69.45 | 0.24 |
| | 100 | 10 | 90 | 5728.95 | 3343.64 | 28.00 | 44.87 | 69.54 | 0.24 |

Table K-2 (Continued) Cracked Glass-rod Specimen

| Saturation Condition | $P_c$, MPa | $P_f$, MPa | $P_d$, MPa | $V_p$, m/s | $V_s$, m/s | $G$, GPa | $K$, GPa | $E$, GPa | $v$ |
|---|---|---|---|---|---|---|---|---|---|
| Argon saturation, decreasing $P_c$, $P_f$ = 10 MPa | 100 | 10 | 90 | 5728.95 | 3343.64 | 28.00 | 44.87 | 69.54 | 0.24 |
| | 90 | 10 | 80 | 5715.87 | 3343.64 | 28.00 | 44.50 | 69.44 | 0.24 |
| | 80 | 10 | 70 | 5722.40 | 3343.64 | 28.00 | 44.68 | 69.49 | 0.24 |
| | 70 | 10 | 60 | 5715.87 | 3342.52 | 27.98 | 44.52 | 69.41 | 0.24 |
| | 60 | 10 | 50 | 5715.87 | 3341.41 | 27.97 | 44.55 | 69.38 | 0.24 |
| | 50 | 10 | 40 | 5706.10 | 3341.41 | 27.97 | 44.27 | 69.30 | 0.24 |
| | 40 | 10 | 30 | 5709.35 | 3339.18 | 27.93 | 44.41 | 69.27 | 0.24 |
| | 30 | 10 | 20 | 5706.10 | 3334.73 | 27.85 | 44.42 | 69.11 | 0.24 |
| | 20 | 10 | 10 | 5699.60 | 3325.87 | 27.71 | 44.43 | 68.81 | 0.24 |

Table K-2 (Continued) Cracked Glass-rod Specimen

| Saturation Condition | $P_c$, MPa | $P_f$, MPa | $P_d$, MPa | $V_p$, m/s | $V_s$, m/s | $G$, GPa | $K$, GPa | $E$, GPa | $v$ |
|---|---|---|---|---|---|---|---|---|---|
| Argon saturation, increasing $P_c$, $P_f$ = 20 MPa | 30 | 20 | 10 | 5709.35 | 3330.30 | 27.79 | 44.62 | 69.03 | 0.24 |
| | 35 | 20 | 15 | 5709.35 | 3333.62 | 27.84 | 44.54 | 69.13 | 0.24 |
| | 40 | 20 | 20 | 5709.35 | 3338.07 | 27.92 | 44.45 | 69.25 | 0.24 |
| | 45 | 20 | 25 | 5715.87 | 3340.29 | 27.95 | 44.58 | 69.36 | 0.24 |
| | 50 | 20 | 30 | 5725.67 | 3343.64 | 28.01 | 44.79 | 69.53 | 0.24 |
| | 55 | 20 | 35 | 5719.13 | 3345.87 | 28.05 | 44.55 | 69.55 | 0.24 |
| | 60 | 20 | 40 | 5722.40 | 3348.11 | 28.09 | 44.59 | 69.64 | 0.24 |
| | 70 | 20 | 50 | 5722.40 | 3351.47 | 28.14 | 44.52 | 69.73 | 0.24 |
| | 80 | 20 | 60 | 5742.09 | 3364.99 | 28.37 | 44.78 | 70.27 | 0.24 |
| | 90 | 20 | 70 | 5745.38 | 3368.38 | 28.43 | 44.80 | 70.39 | 0.24 |
| | 100 | 20 | 80 | 5751.98 | 3374.06 | 28.52 | 44.86 | 70.60 | 0.24 |

Table K-2 (Continued) Cracked Glass-rod Specimen

| Saturation Condition | $P_c$, MPa | $P_f$, MPa | $P_d$, MPa | $V_p$, m/s | $V_s$, m/s | $G$, GPa | $K$, GPa | $E$, GPa | $v$ |
|---|---|---|---|---|---|---|---|---|---|
| Argon saturation, decreasing $P_c$, $P_f$ = 20 MPa | 100 | 20 | 80 | 5751.98 | 3374.06 | 28.52 | 44.86 | 70.60 | 0.24 |
| | 90 | 20 | 70 | 5742.09 | 3368.38 | 28.43 | 44.71 | 70.36 | 0.24 |
| | 80 | 20 | 60 | 5735.51 | 3364.99 | 28.37 | 44.59 | 70.22 | 0.24 |
| | 70 | 20 | 50 | 5732.23 | 3362.73 | 28.33 | 44.55 | 70.13 | 0.24 |
| | 60 | 20 | 40 | 5725.67 | 3360.47 | 28.29 | 44.41 | 70.01 | 0.24 |
| | 50 | 20 | 30 | 5722.40 | 3354.84 | 28.20 | 44.44 | 69.83 | 0.24 |
| | 40 | 20 | 20 | 5728.95 | 3349.23 | 28.10 | 44.76 | 69.72 | 0.24 |
| | 30 | 20 | 10 | 5719.13 | 3338.07 | 27.92 | 44.73 | 69.33 | 0.24 |

Table K-2 (Continued) Cracked Glass-rod Specimen

| Saturation Condition | $P_c$, MPa | $P_f$, MPa | $P_d$, MPa | $V_p$, m/s | $V_s$, m/s | $G$, GPa | $K$, GPa | $E$, GPa | $v$ |
|---|---|---|---|---|---|---|---|---|---|
| Water saturation, increasing $P_c$, $P_f$ = 10 MPa | 20 | 10 | 10 | 5709.35 | 3342.52 | 28.02 | 44.39 | 69.44 | 0.24 |
| | 25 | 10 | 15 | 5706.10 | 3345.87 | 28.07 | 44.22 | 69.51 | 0.24 |
| | 30 | 10 | 20 | 5709.35 | 3349.23 | 28.13 | 44.24 | 69.63 | 0.24 |
| | 35 | 10 | 25 | 5715.87 | 3351.47 | 28.17 | 44.37 | 69.74 | 0.24 |
| | 40 | 10 | 30 | 5715.87 | 3354.84 | 28.22 | 44.30 | 69.84 | 0.24 |
| | 45 | 10 | 35 | 5719.13 | 3353.72 | 28.20 | 44.42 | 69.83 | 0.24 |
| | 50 | 10 | 40 | 5722.40 | 3355.97 | 28.24 | 44.46 | 69.92 | 0.24 |
| | 60 | 10 | 50 | 5719.13 | 3362.73 | 28.36 | 44.21 | 70.09 | 0.24 |
| | 70 | 10 | 60 | 5728.95 | 3366.12 | 28.41 | 44.42 | 70.26 | 0.24 |
| | 80 | 10 | 70 | 5728.95 | 3368.38 | 28.45 | 44.37 | 70.32 | 0.24 |
| | 90 | 10 | 80 | 5738.80 | 3372.92 | 28.53 | 44.55 | 70.53 | 0.24 |
| | 100 | 10 | 90 | 5745.38 | 3376.33 | 28.59 | 44.66 | 70.68 | 0.24 |

Table K-2 (Continued) Cracked Glass-rod Specimen

| Saturation Condition | $P_c$, MPa | $P_f$, MPa | $P_d$, MPa | $V_p$, m/s | $V_s$, m/s | $G$, GPa | $K$, GPa | $E$, GPa | $v$ |
|---|---|---|---|---|---|---|---|---|---|
| Water saturation, decreasing $P_c$, $P_f$ = 10 MPa | 100 | 10 | 90 | 5745.38 | 3376.33 | 28.59 | 44.66 | 70.68 | 0.24 |
| | 90 | 10 | 80 | 5732.23 | 3374.06 | 28.55 | 44.33 | 70.51 | 0.23 |
| | 80 | 10 | 70 | 5732.23 | 3371.78 | 28.51 | 44.39 | 70.45 | 0.24 |
| | 70 | 10 | 60 | 5728.95 | 3370.65 | 28.49 | 44.32 | 70.39 | 0.24 |
| | 60 | 10 | 50 | 5725.67 | 3368.38 | 28.45 | 44.27 | 70.30 | 0.24 |
| | 50 | 10 | 40 | 5719.13 | 3366.12 | 28.41 | 44.14 | 70.18 | 0.23 |
| | 40 | 10 | 30 | 5722.40 | 3361.60 | 28.34 | 44.33 | 70.08 | 0.24 |
| | 30 | 10 | 20 | 5719.13 | 3355.97 | 28.24 | 44.36 | 69.90 | 0.24 |
| | 20 | 10 | 10 | 5719.13 | 3346.99 | 28.09 | 44.57 | 69.64 | 0.24 |

Table K-2 (Continued) Cracked Glass-rod Specimen

| Saturation Condition | $P_c$, MPa | $P_f$, MPa | $P_d$, MPa | $V_p$, m/s | $V_s$, m/s | $G$, GPa | $K$, GPa | $E$, GPa | $v$ |
|---|---|---|---|---|---|---|---|---|---|
| Water saturation, increasing $P_c$, $P_f$ = 20 MPa | 30 | 20 | 10 | 5722.40 | 3353.72 | 28.20 | 44.51 | 69.86 | 0.24 |
| | 35 | 20 | 15 | 5725.67 | 3355.97 | 28.24 | 44.55 | 69.95 | 0.24 |
| | 40 | 20 | 20 | 5722.40 | 3358.22 | 28.28 | 44.41 | 69.98 | 0.24 |
| | 45 | 20 | 25 | 5732.23 | 3361.60 | 28.34 | 44.61 | 70.16 | 0.24 |
| | 50 | 20 | 30 | 5732.23 | 3366.12 | 28.41 | 44.51 | 70.29 | 0.24 |
| | 55 | 20 | 35 | 5732.23 | 3366.12 | 28.41 | 44.51 | 70.29 | 0.24 |
| | 60 | 20 | 40 | 5732.23 | 3368.38 | 28.45 | 44.46 | 70.35 | 0.24 |
| | 70 | 20 | 50 | 5738.80 | 3371.78 | 28.51 | 44.57 | 70.50 | 0.24 |
| | 80 | 20 | 60 | 5745.38 | 3376.33 | 28.59 | 44.66 | 70.68 | 0.24 |
| | 90 | 20 | 70 | 5745.38 | 3377.47 | 28.61 | 44.64 | 70.71 | 0.24 |
| | 100 | 20 | 80 | 5751.98 | 3383.18 | 28.70 | 44.70 | 70.93 | 0.24 |

Table K-2 (Continued) Cracked Glass-rod Specimen

| Saturation Condition | $P_c$, MPa | $P_f$, MPa | $P_d$, MPa | $V_p$, m/s | $V_s$, m/s | $G$, GPa | $K$, GPa | $E$, GPa | $v$ |
|---|---|---|---|---|---|---|---|---|---|
| Water saturation, decreasing $P_c$, $P_f$ = 20 MPa | 100 | 20 | 80 | 5751.98 | 3383.18 | 28.70 | 44.70 | 70.93 | 0.24 |
| | 90 | 20 | 70 | 5742.09 | 3378.61 | 28.62 | 44.51 | 70.72 | 0.24 |
| | 80 | 20 | 60 | 5742.09 | 3378.61 | 28.62 | 44.51 | 70.72 | 0.24 |
| | 70 | 20 | 50 | 5738.80 | 3376.33 | 28.59 | 44.47 | 70.63 | 0.24 |
| | 60 | 20 | 40 | 5735.51 | 3375.19 | 28.57 | 44.40 | 70.57 | 0.24 |
| | 50 | 20 | 30 | 5735.51 | 3371.78 | 28.51 | 44.48 | 70.47 | 0.24 |
| | 40 | 20 | 20 | 5735.51 | 3366.12 | 28.41 | 44.61 | 70.31 | 0.24 |
| | 30 | 20 | 10 | 5732.23 | 3355.97 | 28.24 | 44.74 | 70.00 | 0.24 |

$P_c$: confining pressure; $P_f$: pore-fluid pressure; $P_d$: differential pressure; $V_p$: P-wave velocity; $V_s$: S-wave velocity; $G$: shear modulus; $K$: bulk modulus; $E$: Young's modulus; $v$: Poisson's ratio.

*Elastic moduli are calculated from measured P- and S-wave velocities with Eq. (3.71) – (3.73). The density of the fluid-saturated specimen is assumed to be pressure independent.

Table K-3 Uncracked Low-porosity Glass-bead Specimen

| Saturation Condition | $P_c$, MPa | $P_f$, MPa | $P_d$, MPa | $V_p$, m/s | $V_s$, m/s | $G$*, GPa | $K$, GPa | $E$, GPa | $v$ |
|---|---|---|---|---|---|---|---|---|---|
| Dry, increasing $P_c$ | 10 | 0 | 10 | 5635.17 | 3450.74 | 29.06 | 38.74 | 69.74 | 0.20 |
| | 20 | 0 | 20 | 5657.50 | 3459.10 | 29.20 | 39.17 | 70.16 | 0.20 |
| | 30 | 0 | 30 | 5667.12 | 3463.89 | 29.28 | 39.33 | 70.37 | 0.20 |
| | 40 | 0 | 40 | 5680.00 | 3468.70 | 29.36 | 39.58 | 70.62 | 0.20 |
| | 50 | 0 | 50 | 5696.18 | 3469.91 | 29.38 | 40.00 | 70.80 | 0.20 |
| | 60 | 0 | 60 | 5705.94 | 3474.73 | 29.46 | 40.16 | 71.02 | 0.21 |
| | 70 | 0 | 70 | 5712.46 | 3478.36 | 29.52 | 40.26 | 71.17 | 0.21 |
| | 80 | 0 | 80 | 5722.27 | 3480.78 | 29.56 | 40.48 | 71.33 | 0.21 |
| | 90 | 0 | 90 | 5728.83 | 3481.99 | 29.58 | 40.64 | 71.42 | 0.21 |
| | 100 | 0 | 100 | 5735.40 | 3484.42 | 29.63 | 40.77 | 71.55 | 0.21 |

Table K-3 (Continued) Uncracked Low-porosity Glass-bead Specimen

| Saturation Condition | $P_c$, MPa | $P_f$, MPa | $P_d$, MPa | $V_p$, m/s | $V_s$, m/s | $G$, GPa | $K$, GPa | $E$, GPa | $v$ |
|---|---|---|---|---|---|---|---|---|---|
| Dry, decreasing $P_c$ | 100 | 0 | 100 | 5735.40 | 3484.42 | 29.63 | 40.77 | 71.55 | 0.21 |
| | 90 | 0 | 90 | 5732.11 | 3483.21 | 29.61 | 40.70 | 71.48 | 0.21 |
| | 80 | 0 | 80 | 5725.54 | 3481.99 | 29.58 | 40.55 | 71.39 | 0.21 |
| | 70 | 0 | 70 | 5722.27 | 3479.57 | 29.54 | 40.51 | 71.30 | 0.21 |
| | 60 | 0 | 60 | 5715.72 | 3477.15 | 29.50 | 40.38 | 71.17 | 0.21 |
| | 50 | 0 | 50 | 5712.46 | 3472.32 | 29.42 | 40.40 | 71.02 | 0.21 |
| | 40 | 0 | 40 | 5702.68 | 3469.91 | 29.38 | 40.18 | 70.87 | 0.21 |
| | 30 | 0 | 30 | 5692.94 | 3466.30 | 29.32 | 39.99 | 70.68 | 0.21 |
| | 20 | 0 | 20 | 5680.00 | 3462.69 | 29.26 | 39.71 | 70.47 | 0.20 |
| | 10 | 0 | 10 | 5667.12 | 3453.13 | 29.10 | 39.57 | 70.11 | 0.20 |

$P_c$: confining pressure; $P_f$: pore-fluid pressure; $P_d$: differential pressure; $V_p$: P-wave velocity; $V_s$: S-wave velocity; $G$: shear modulus; $K$: bulk modulus; $E$: Young's modulus; $v$: Poisson's ratio.

*Elastic moduli are calculated from measured P- and S-wave velocities with Eq. (3.71) – (3.73).

Table K-4 Cracked Low-porosity Glass-bead Specimen

| Saturation Condition | $P_c$, MPa | $P_f$, MPa | $P_d$, MPa | $V_p$, m/s | $V_s$, m/s | $G$*, GPa | $K$, GPa | $E$, GPa | $v$ |
|---|---|---|---|---|---|---|---|---|---|
| Dry, increasing $P_c$ | 10 | 0 | 10 | 5472.83 | 3325.51 | 27.07 | 37.23 | 65.37 | 0.21 |
| | 20 | 0 | 20 | 5668.06 | 3430.36 | 28.81 | 40.24 | 69.77 | 0.21 |
| | 30 | 0 | 30 | 5684.16 | 3451.66 | 29.17 | 40.21 | 70.46 | 0.21 |
| | 40 | 0 | 40 | 5697.10 | 3462.40 | 29.35 | 40.33 | 70.85 | 0.21 |
| | 50 | 0 | 50 | 5710.10 | 3467.20 | 29.43 | 40.58 | 71.10 | 0.21 |
| | 60 | 0 | 60 | 5719.89 | 3473.21 | 29.53 | 40.72 | 71.35 | 0.21 |
| | 70 | 0 | 70 | 5726.43 | 3476.83 | 29.59 | 40.82 | 71.50 | 0.21 |
| | 80 | 0 | 80 | 5732.99 | 3480.46 | 29.65 | 40.92 | 71.66 | 0.21 |
| | 90 | 0 | 90 | 5739.56 | 3481.67 | 29.68 | 41.08 | 71.75 | 0.21 |
| | 100 | 0 | 100 | 5742.86 | 3484.09 | 29.72 | 41.12 | 71.84 | 0.21 |

Table K-4 (Continued) Cracked Low-porosity Glass-bead Specimen

| Saturation Condition | $P_c$, MPa | $P_f$, MPa | $P_d$, MPa | $V_p$, m/s | $V_s$, m/s | $G$, GPa | $K$, GPa | $E$, GPa | $v$ |
|---|---|---|---|---|---|---|---|---|---|
| Dry, decreasing $P_c$ | 100 | 0 | 100 | 5742.86 | 3484.09 | 29.72 | 41.12 | 71.84 | 0.21 |
| | 90 | 0 | 90 | 5739.56 | 3482.88 | 29.70 | 41.05 | 71.78 | 0.21 |
| | 80 | 0 | 80 | 5732.99 | 3481.67 | 29.68 | 40.89 | 71.69 | 0.21 |
| | 70 | 0 | 70 | 5732.99 | 3478.04 | 29.61 | 40.98 | 71.59 | 0.21 |
| | 60 | 0 | 60 | 5726.43 | 3475.63 | 29.57 | 40.85 | 71.47 | 0.21 |
| | 50 | 0 | 50 | 5716.62 | 3468.40 | 29.45 | 40.74 | 71.19 | 0.21 |
| | 40 | 0 | 40 | 5710.10 | 3462.40 | 29.35 | 40.69 | 70.98 | 0.21 |
| | 30 | 0 | 30 | 5693.86 | 3452.85 | 29.19 | 40.45 | 70.58 | 0.21 |
| | 20 | 0 | 20 | 5680.93 | 3436.25 | 28.91 | 40.46 | 70.04 | 0.21 |
| | 10 | 0 | 10 | 5530.28 | 3344.40 | 27.38 | 38.36 | 66.36 | 0.21 |

Table K-4 (Continued) Cracked Low-porosity Glass-bead Specimen

| Saturation Condition | $P_c$, MPa | $P_f$, MPa | $P_d$, MPa | $V_p$, m/s | $V_s$, m/s | $G$, GPa | $K$, GPa | $E$, GPa | $v$ |
|---|---|---|---|---|---|---|---|---|---|
| Argon saturation, increasing $P_c$, $P_f$ = 10 MPa | 20 | 10 | 10 | 5700.34 | 3444.53 | 29.08 | 40.87 | 70.52 | 0.21 |
| | 30 | 10 | 20 | 5713.36 | 3460.01 | 29.35 | 40.89 | 71.04 | 0.21 |
| | 40 | 10 | 30 | 5713.36 | 3468.40 | 29.49 | 40.70 | 71.26 | 0.21 |
| | 50 | 10 | 40 | 5723.16 | 3474.42 | 29.59 | 40.84 | 71.50 | 0.21 |
| | 60 | 10 | 50 | 5729.71 | 3476.83 | 29.63 | 40.97 | 71.63 | 0.21 |
| | 70 | 10 | 60 | 5739.56 | 3480.46 | 29.69 | 41.16 | 71.81 | 0.21 |
| | 80 | 10 | 70 | 5742.86 | 3482.88 | 29.74 | 41.20 | 71.91 | 0.21 |
| | 90 | 10 | 80 | 5749.45 | 3485.31 | 29.78 | 41.33 | 72.03 | 0.21 |
| | 100 | 10 | 90 | 5752.76 | 3487.74 | 29.82 | 41.37 | 72.12 | 0.21 |

Table K-4 (Continued) Cracked Low-porosity Glass-bead Specimen

| Saturation Condition | $P_c$, MPa | $P_f$, MPa | $P_d$, MPa | $V_p$, m/s | $V_s$, m/s | $G$, GPa | $K$, GPa | $E$, GPa | $v$ |
|---|---|---|---|---|---|---|---|---|---|
| Argon saturation, decreasing $P_c$, $P_f$ = 10 MPa | 100 | 10 | 90 | 5752.76 | 3487.74 | 29.82 | 41.37 | 72.12 | 0.21 |
| | 90 | 10 | 80 | 5746.15 | 3485.31 | 29.78 | 41.24 | 72.00 | 0.21 |
| | 80 | 10 | 70 | 5746.15 | 3482.88 | 29.74 | 41.29 | 71.94 | 0.21 |
| | 70 | 10 | 60 | 5742.86 | 3481.67 | 29.71 | 41.23 | 71.87 | 0.21 |
| | 60 | 10 | 50 | 5739.56 | 3476.83 | 29.63 | 41.24 | 71.72 | 0.21 |
| | 50 | 10 | 40 | 5729.71 | 3472.01 | 29.55 | 41.07 | 71.50 | 0.21 |
| | 40 | 10 | 30 | 5723.16 | 3466.00 | 29.45 | 41.03 | 71.29 | 0.21 |
| | 30 | 10 | 20 | 5710.10 | 3458.81 | 29.33 | 40.82 | 70.98 | 0.21 |
| | 20 | 10 | 10 | 5703.59 | 3439.79 | 29.00 | 41.07 | 70.43 | 0.21 |

Table K-4 (Continued) Cracked Low-porosity Glass-bead Specimen

| Saturation Condition | $P_c$, MPa | $P_f$, MPa | $P_d$, MPa | $V_p$, m/s | $V_s$, m/s | $G$, GPa | $K$, GPa | $E$, GPa | $v$ |
|---|---|---|---|---|---|---|---|---|---|
| Argon saturation, increasing $P_c$, $P_f$ =20 MPa | 30 | 20 | 10 | 5719.89 | 3467.20 | 29.51 | 40.97 | 71.39 | 0.21 |
| | 40 | 20 | 20 | 5732.99 | 3472.01 | 29.59 | 41.22 | 71.63 | 0.21 |
| | 50 | 20 | 30 | 5732.99 | 3476.83 | 29.67 | 41.12 | 71.76 | 0.21 |
| | 60 | 20 | 40 | 5739.56 | 3481.67 | 29.76 | 41.19 | 71.94 | 0.21 |
| | 70 | 20 | 50 | 5746.15 | 3481.67 | 29.76 | 41.38 | 72.01 | 0.21 |
| | 80 | 20 | 60 | 5752.76 | 3486.52 | 29.84 | 41.45 | 72.19 | 0.21 |
| | 90 | 20 | 70 | 5756.07 | 3487.74 | 29.86 | 41.52 | 72.26 | 0.21 |
| | 100 | 20 | 80 | 5759.38 | 3490.17 | 29.90 | 41.56 | 72.35 | 0.21 |

Table K-4 (Continued) Cracked Low-porosity Glass-bead Specimen

| Saturation Condition | $P_c$, MPa | $P_f$, MPa | $P_d$, MPa | $V_p$, m/s | $V_s$, m/s | $G$, GPa | $K$, GPa | $E$, GPa | $v$ |
|---|---|---|---|---|---|---|---|---|---|
| Argon saturation, decreasing $P_c$, $P_f$=20 MPa, | 100 | 20 | 80 | 5759.38 | 3490.17 | 29.90 | 41.56 | 72.35 | 0.21 |
| | 90 | 20 | 70 | 5756.07 | 3486.52 | 29.84 | 41.55 | 72.23 | 0.21 |
| | 80 | 20 | 60 | 5756.07 | 3486.52 | 29.84 | 41.55 | 72.23 | 0.21 |
| | 70 | 20 | 50 | 5749.45 | 3481.67 | 29.76 | 41.47 | 72.04 | 0.21 |
| | 60 | 20 | 40 | 5746.15 | 3479.25 | 29.71 | 41.43 | 71.94 | 0.21 |
| | 50 | 20 | 30 | 5736.28 | 3474.42 | 29.63 | 41.26 | 71.73 | 0.21 |
| | 40 | 20 | 20 | 5726.43 | 3469.60 | 29.55 | 41.10 | 71.51 | 0.21 |
| | 30 | 20 | 10 | 5723.16 | 3460.01 | 29.39 | 41.22 | 71.23 | 0.21 |

Table K-4 (Continued) Cracked Low-porosity Glass-bead Specimen

| Saturation Condition | $P_c$, MPa | $P_f$, MPa | $P_d$, MPa | $V_p$, m/s | $V_s$, m/s | $G$, GPa | $K$, GPa | $E$, GPa | $v$ |
|---|---|---|---|---|---|---|---|---|---|
| Water saturation, increasing $P_c$, $P_f$ =20 MPa | 30 | 20 | 10 | 5726.43 | 3472.01 | 29.74 | 41.24 | 71.93 | 0.21 |
| | 40 | 20 | 20 | 5732.99 | 3476.83 | 29.82 | 41.32 | 72.11 | 0.21 |
| | 50 | 20 | 30 | 5736.28 | 3481.67 | 29.90 | 41.30 | 72.27 | 0.21 |
| | 60 | 20 | 40 | 5742.86 | 3486.52 | 29.99 | 41.38 | 72.46 | 0.21 |
| | 70 | 20 | 50 | 5749.45 | 3487.74 | 30.01 | 41.54 | 72.55 | 0.21 |
| | 80 | 20 | 60 | 5752.76 | 3491.38 | 30.07 | 41.55 | 72.68 | 0.21 |
| | 90 | 20 | 70 | 5756.07 | 3493.82 | 30.11 | 41.58 | 72.77 | 0.21 |
| | 100 | 20 | 80 | 5762.69 | 3496.26 | 30.16 | 41.72 | 72.90 | 0.21 |

Table K-4 (Continued) Cracked Low-porosity Glass-bead Specimen

| Saturation Condition | $P_c$, MPa | $P_f$, MPa | $P_d$, MPa | $V_p$, m/s | $V_s$, m/s | $G$, GPa | $K$, GPa | $E$, GPa | $v$ |
|---|---|---|---|---|---|---|---|---|---|
| Water saturation, decreasing $P_c$, $P_f$ =20 MPa, | 100 | 20 | 80 | 5762.69 | 3496.26 | 30.16 | 41.72 | 72.90 | 0.21 |
| | 90 | 20 | 70 | 5756.07 | 3490.17 | 30.05 | 41.67 | 72.68 | 0.21 |
| | 80 | 20 | 60 | 5756.07 | 3490.17 | 30.05 | 41.67 | 72.68 | 0.21 |
| | 70 | 20 | 50 | 5752.76 | 3486.52 | 29.99 | 41.66 | 72.55 | 0.21 |
| | 60 | 20 | 40 | 5749.45 | 3484.09 | 29.95 | 41.62 | 72.46 | 0.21 |
| | 50 | 20 | 30 | 5742.86 | 3479.25 | 29.86 | 41.54 | 72.27 | 0.21 |
| | 40 | 20 | 20 | 5732.99 | 3475.63 | 29.80 | 41.35 | 72.08 | 0.21 |
| | 30 | 20 | 10 | 5726.43 | 3464.80 | 29.61 | 41.41 | 71.74 | 0.21 |

Table K-4 (Continued) Cracked Low-porosity Glass-bead Specimen

| Saturation Condition | $P_c$, MPa | $P_f$, MPa | $P_d$, MPa | $V_p$, m/s | $V_s$, m/s | $G$, GPa | $K$, GPa | $E$, GPa | $v$ |
|---|---|---|---|---|---|---|---|---|---|
| Water saturation, $P_c$ =50 MPa, decreasing $P_f$ | 50 | 40 | 10 | 5756.07 | 3488.95 | 30.03 | 41.70 | 72.65 | 0.21 |
| | 50 | 30 | 20 | 5749.45 | 3485.31 | 29.97 | 41.59 | 72.49 | 0.21 |
| | 50 | 20 | 30 | 5736.28 | 3482.88 | 29.92 | 41.27 | 72.30 | 0.21 |
| | 50 | 10 | 40 | 5732.99 | 3481.67 | 29.90 | 41.21 | 72.24 | 0.21 |
| | 50 | 0 | 50 | 5726.43 | 3476.83 | 29.82 | 41.13 | 72.05 | 0.21 |
| Water saturation, $P_c$ =50 MPa, increasing $P_f$ | 50 | 0 | 50 | 5726.43 | 3476.83 | 29.82 | 41.13 | 72.05 | 0.21 |
| | 50 | 10 | 40 | 5726.43 | 3472.01 | 29.74 | 41.24 | 71.93 | 0.21 |
| | 50 | 20 | 30 | 5732.99 | 3474.42 | 29.78 | 41.37 | 72.05 | 0.21 |
| | 50 | 30 | 20 | 5739.56 | 3479.25 | 29.86 | 41.45 | 72.24 | 0.21 |
| | 50 | 40 | 10 | 5752.76 | 3479.25 | 29.86 | 41.82 | 72.36 | 0.21 |

$P_c$: confining pressure; $P_f$: pore-fluid pressure; $P_d$: differential pressure; $V_p$: P-wave velocity; $V_s$: S-wave velocity; $G$: shear modulus; $K$: bulk modulus; $E$: Young's modulus; $v$: Poisson's ratio.

*Elastic moduli are calculated from measured P- and S-wave velocities with Eq. (3.71) – (3.73). The density of the fluid-saturated specimen is assumed to be pressure independent.

Table K-5 Uncracked High-porosity Glass-bead Specimen

| Saturation Condition | $P_c$, MPa | $P_f$, MPa | $P_d$, MPa | $V_p$, m/s | $V_s$, m/s | $G^*$, GPa | $K$, GPa | $E$, GPa | $v$ |
|---|---|---|---|---|---|---|---|---|---|
| Dry, increasing $P_c$ | 5 | 0 | 5 | 5524.31 | 3433.72 | 28.61 | 35.91 | 67.82 | 0.19 |
| | 10 | 0 | 10 | 5539.61 | 3446.74 | 28.83 | 36.03 | 68.28 | 0.18 |
| | 15 | 0 | 15 | 5555.00 | 3453.89 | 28.95 | 36.28 | 68.60 | 0.18 |
| | 20 | 0 | 20 | 5561.18 | 3457.47 | 29.01 | 36.37 | 68.75 | 0.18 |
| | 25 | 0 | 25 | 5570.47 | 3458.66 | 29.03 | 36.60 | 68.87 | 0.19 |
| | 30 | 0 | 30 | 5570.47 | 3462.26 | 29.09 | 36.51 | 68.96 | 0.19 |
| | 35 | 0 | 35 | 5573.58 | 3461.06 | 29.07 | 36.63 | 68.96 | 0.19 |
| | 40 | 0 | 40 | 5576.69 | 3462.26 | 29.09 | 36.68 | 69.02 | 0.19 |
| | 50 | 0 | 50 | 5586.03 | 3463.46 | 29.11 | 36.91 | 69.15 | 0.19 |
| | 60 | 0 | 60 | 5598.54 | 3467.06 | 29.17 | 37.17 | 69.36 | 0.19 |
| | 70 | 0 | 70 | 5611.11 | 3469.47 | 29.21 | 37.46 | 69.55 | 0.19 |
| | 80 | 0 | 80 | 5620.57 | 3473.08 | 29.27 | 37.63 | 69.73 | 0.19 |
| | 90 | 0 | 90 | 5639.59 | 3475.50 | 29.31 | 38.10 | 69.99 | 0.19 |
| | 100 | 0 | 100 | 5645.96 | 3480.33 | 29.39 | 38.16 | 70.17 | 0.19 |

Table K-5 (Continued) Uncracked High-porosity Glass-bead Specimen

| Saturation Condition | $P_c$, MPa | $P_f$, MPa | $P_d$, MPa | $V_p$, m/s | $V_s$, m/s | $G$, GPa | $K$, GPa | $E$, GPa | $v$ |
|---|---|---|---|---|---|---|---|---|---|
| Dry, decreasing $P_c$ | 100 | 0 | 100 | 5645.96 | 3480.33 | 29.39 | 38.16 | 70.17 | 0.19 |
| | 90 | 0 | 90 | 5639.59 | 3477.91 | 29.35 | 38.04 | 70.04 | 0.19 |
| | 80 | 0 | 80 | 5630.07 | 3477.91 | 29.35 | 37.78 | 69.95 | 0.19 |
| | 70 | 0 | 70 | 5623.73 | 3475.50 | 29.31 | 37.66 | 69.82 | 0.19 |
| | 60 | 0 | 60 | 5614.26 | 3471.88 | 29.25 | 37.49 | 69.64 | 0.19 |
| | 50 | 0 | 50 | 5601.68 | 3467.06 | 29.17 | 37.25 | 69.40 | 0.19 |
| | 40 | 0 | 40 | 5592.28 | 3467.06 | 29.17 | 37.00 | 69.30 | 0.19 |
| | 30 | 0 | 30 | 5586.03 | 3464.66 | 29.13 | 36.88 | 69.18 | 0.19 |
| | 20 | 0 | 20 | 5579.80 | 3459.86 | 29.05 | 36.82 | 69.00 | 0.19 |
| | 10 | 0 | 10 | 5573.58 | 3451.50 | 28.91 | 36.84 | 68.74 | 0.19 |

$P_c$: confining pressure; $P_f$: pore-fluid pressure; $P_d$: differential pressure; $V_p$: P-wave velocity; $V_s$: S-wave velocity; $G$: shear modulus; $K$: bulk modulus; $E$: Young's modulus; $v$: Poisson's ratio.

*Elastic moduli are calculated from measured P- and S-wave velocities with Eq. (3.71) – (3.73).

Table K-6 Cracked High-porosity Glass-bead Specimen

| Saturation Condition | $P_c$, MPa | $P_f$, MPa | $P_d$, MPa | $V_p$, m/s | $V_s$, m/s | $G$*, GPa | $K$, GPa | $E$, GPa | $v$ |
|---|---|---|---|---|---|---|---|---|---|
| Dry, increasing $P_c$ | 10 | 0 | 10 | 5117.91 | 3287.44 | 26.09 | 28.45 | 59.95 | 0.15 |
| | 15 | 0 | 15 | 5302.44 | 3366.00 | 27.35 | 31.41 | 63.60 | 0.16 |
| | 20 | 0 | 20 | 5373.67 | 3395.72 | 27.84 | 32.60 | 65.01 | 0.17 |
| | 25 | 0 | 25 | 5420.27 | 3408.45 | 28.05 | 33.53 | 65.80 | 0.17 |
| | 30 | 0 | 30 | 5440.91 | 3423.62 | 28.30 | 33.74 | 66.34 | 0.17 |
| | 35 | 0 | 35 | 5461.71 | 3431.85 | 28.43 | 34.11 | 66.75 | 0.17 |
| | 40 | 0 | 40 | 5479.67 | 3436.56 | 28.51 | 34.48 | 67.05 | 0.18 |
| | 50 | 0 | 50 | 5503.80 | 3447.23 | 28.69 | 34.88 | 67.55 | 0.18 |
| | 60 | 0 | 60 | 5525.08 | 3454.37 | 28.81 | 35.29 | 67.94 | 0.18 |
| | 70 | 0 | 70 | 5540.39 | 3459.15 | 28.89 | 35.59 | 68.21 | 0.18 |
| | 80 | 0 | 80 | 5555.78 | 3463.94 | 28.97 | 35.89 | 68.48 | 0.18 |
| | 90 | 0 | 90 | 5568.15 | 3466.34 | 29.01 | 36.17 | 68.67 | 0.18 |
| | 100 | 0 | 100 | 5577.47 | 3473.57 | 29.13 | 36.26 | 68.93 | 0.18 |

Table K-6 (Continued) Cracked High-porosity Glass-bead Specimen

| Saturation Condition | $P_c$, MPa | $P_f$, MPa | $P_d$, MPa | $V_p$, m/s | $V_s$, m/s | $G$, GPa | $K$, GPa | $E$, GPa | $v$ |
|---|---|---|---|---|---|---|---|---|---|
| Dry, decreasing $P_c$ | 100 | 0 | 100 | 5577.47 | 3473.57 | 29.13 | 36.26 | 68.93 | 0.18 |
| | 90 | 0 | 90 | 5574.36 | 3472.36 | 29.11 | 36.21 | 68.87 | 0.18 |
| | 80 | 0 | 80 | 5571.25 | 3472.36 | 29.11 | 36.12 | 68.84 | 0.18 |
| | 70 | 0 | 70 | 5555.78 | 3467.55 | 29.03 | 35.81 | 68.56 | 0.18 |
| | 60 | 0 | 60 | 5546.53 | 3462.74 | 28.95 | 35.67 | 68.35 | 0.18 |
| | 50 | 0 | 50 | 5528.14 | 3455.56 | 28.83 | 35.34 | 68.00 | 0.18 |
| | 40 | 0 | 40 | 5497.75 | 3446.04 | 28.67 | 34.74 | 67.45 | 0.18 |
| | 30 | 0 | 30 | 5461.71 | 3429.49 | 28.39 | 34.16 | 66.70 | 0.17 |
| | 20 | 0 | 20 | 5402.70 | 3401.50 | 27.93 | 33.23 | 65.46 | 0.17 |
| | 10 | 0 | 10 | 5192.32 | 3303.73 | 26.35 | 29.95 | 61.13 | 0.16 |

Table K-6 (Continued) Cracked High-porosity Glass-bead Specimen

| Saturation Condition | $P_c$, MPa | $P_f$, MPa | $P_d$, MPa | $V_p$, m/s | $V_s$, m/s | $G$, GPa | $K$, GPa | $E$, GPa | $v$ |
|---|---|---|---|---|---|---|---|---|---|
| Argon saturation, increasing $P_c$, $P_f$ =10 MPa | 20 | 10 | 10 | 5426.15 | 3395.72 | 27.95 | 34.10 | 65.85 | 0.18 |
| | 25 | 10 | 15 | 5452.78 | 3415.44 | 28.27 | 34.37 | 66.57 | 0.18 |
| | 30 | 10 | 20 | 5476.67 | 3425.97 | 28.45 | 34.77 | 67.06 | 0.18 |
| | 35 | 10 | 25 | 5500.77 | 3435.38 | 28.60 | 35.20 | 67.52 | 0.18 |
| | 40 | 10 | 30 | 5518.98 | 3444.85 | 28.76 | 35.48 | 67.93 | 0.18 |
| | 45 | 10 | 35 | 5525.08 | 3448.41 | 28.82 | 35.56 | 68.07 | 0.18 |
| | 50 | 10 | 40 | 5534.26 | 3453.18 | 28.90 | 35.70 | 68.28 | 0.18 |
| | 60 | 10 | 50 | 5549.61 | 3461.54 | 29.04 | 35.92 | 68.63 | 0.18 |
| | 70 | 10 | 60 | 5565.05 | 3467.55 | 29.14 | 36.21 | 68.93 | 0.18 |
| | 80 | 10 | 70 | 5577.47 | 3469.95 | 29.18 | 36.49 | 69.12 | 0.18 |
| | 90 | 10 | 80 | 5586.82 | 3473.57 | 29.24 | 36.66 | 69.30 | 0.18 |
| | 100 | 10 | 90 | 5596.19 | 3474.77 | 29.26 | 36.89 | 69.43 | 0.19 |

Table K-6 (Continued) Cracked High-porosity Glass-bead Specimen

| Saturation Condition | $P_c$, MPa | $P_f$, MPa | $P_d$, MPa | $V_p$, m/s | $V_s$, m/s | $G$, GPa | $K$, GPa | $E$, GPa | $v$ |
|---|---|---|---|---|---|---|---|---|---|
| Argon saturation, decreasing $P_c$, $P_f$ =10 MPa | 100 | 10 | 90 | 5596.19 | 3474.77 | 29.26 | 36.89 | 69.43 | 0.19 |
| | 90 | 10 | 80 | 5586.82 | 3475.98 | 29.28 | 36.61 | 69.36 | 0.18 |
| | 80 | 10 | 70 | 5586.82 | 3474.77 | 29.26 | 36.63 | 69.33 | 0.18 |
| | 70 | 10 | 60 | 5574.36 | 3471.16 | 29.20 | 36.38 | 69.12 | 0.18 |
| | 60 | 10 | 50 | 5561.96 | 3465.14 | 29.10 | 36.18 | 68.85 | 0.18 |
| | 50 | 10 | 40 | 5546.53 | 3460.35 | 29.02 | 35.87 | 68.57 | 0.18 |
| | 40 | 10 | 30 | 5528.14 | 3448.41 | 28.82 | 35.64 | 68.11 | 0.18 |
| | 30 | 10 | 20 | 5494.73 | 3430.67 | 28.53 | 35.14 | 67.35 | 0.18 |
| | 20 | 10 | 10 | 5429.10 | 3387.67 | 27.82 | 34.35 | 65.71 | 0.18 |

Table K-6 (Continued) Cracked High-porosity Glass-bead Specimen

| Saturation Condition | $P_c$, MPa | $P_f$, MPa | $P_d$, MPa | $V_p$, m/s | $V_s$, m/s | $G$, GPa | $K$, GPa | $E$, GPa | $v$ |
|---|---|---|---|---|---|---|---|---|---|
| Argon saturation, increasing $P_c$, $P_f$ =20 MPa | 30 | 20 | 10 | 5491.71 | 3413.11 | 28.35 | 35.60 | 67.22 | 0.19 |
| | 35 | 20 | 15 | 5509.86 | 3427.14 | 28.59 | 35.77 | 67.72 | 0.18 |
| | 40 | 20 | 20 | 5525.08 | 3440.11 | 28.80 | 35.89 | 68.18 | 0.18 |
| | 45 | 20 | 25 | 5540.39 | 3448.41 | 28.94 | 36.12 | 68.53 | 0.18 |
| | 50 | 20 | 30 | 5552.69 | 3456.76 | 29.08 | 36.27 | 68.85 | 0.18 |
| | 55 | 20 | 35 | 5561.96 | 3460.35 | 29.14 | 36.44 | 69.03 | 0.18 |
| | 60 | 20 | 40 | 5565.05 | 3462.74 | 29.18 | 36.47 | 69.11 | 0.18 |
| | 70 | 20 | 50 | 5580.58 | 3469.95 | 29.31 | 36.72 | 69.45 | 0.18 |
| | 80 | 20 | 60 | 5593.06 | 3474.77 | 29.39 | 36.96 | 69.69 | 0.19 |
| | 90 | 20 | 70 | 5602.46 | 3477.19 | 29.43 | 37.16 | 69.85 | 0.19 |
| | 100 | 20 | 80 | 5608.75 | 3480.82 | 29.49 | 37.25 | 70.00 | 0.19 |

Table K-6 (Continued) Cracked High-porosity Glass-bead Specimen

| Saturation Condition | $P_c$, MPa | $P_f$, MPa | $P_d$, MPa | $V_p$, m/s | $V_s$, m/s | $G$, GPa | $K$, GPa | $E$, GPa | $v$ |
|---|---|---|---|---|---|---|---|---|---|
| Argon saturation, decreasing $P_c$, $P_f$ =20 MPa | 100 | 20 | 80 | 5608.75 | 3480.82 | 29.49 | 37.25 | 70.00 | 0.19 |
| | 90 | 20 | 70 | 5602.46 | 3478.40 | 29.45 | 37.13 | 69.87 | 0.19 |
| | 80 | 20 | 60 | 5599.33 | 3477.19 | 29.43 | 37.07 | 69.81 | 0.19 |
| | 70 | 20 | 50 | 5586.82 | 3472.36 | 29.35 | 36.84 | 69.57 | 0.19 |
| | 60 | 20 | 40 | 5574.36 | 3467.55 | 29.27 | 36.61 | 69.32 | 0.18 |
| | 50 | 20 | 30 | 5565.05 | 3460.35 | 29.14 | 36.52 | 69.06 | 0.18 |
| | 40 | 20 | 20 | 5540.39 | 3443.66 | 28.86 | 36.23 | 68.42 | 0.19 |
| | 30 | 20 | 10 | 5494.73 | 3411.94 | 28.33 | 35.71 | 67.22 | 0.19 |

Table K-6 (Continued) Cracked High-porosity Glass-bead Specimen

| Saturation Condition | $P_c$, MPa | $P_f$, MPa | $P_d$, MPa | $V_p$, m/s | $V_s$, m/s | $G$, GPa | $K$, GPa | $E$, GPa | $v$ |
|---|---|---|---|---|---|---|---|---|---|
| Water saturation, increasing $P_c$, $P_f$ =10 MPa | 20 | 10 | 10 | 5509.86 | 3406.13 | 28.66 | 36.78 | 68.24 | 0.19 |
| | 25 | 10 | 15 | 5525.08 | 3425.97 | 28.99 | 36.74 | 68.86 | 0.19 |
| | 30 | 10 | 20 | 5537.32 | 3440.11 | 29.23 | 36.76 | 69.32 | 0.19 |
| | 35 | 10 | 25 | 5552.69 | 3449.60 | 29.39 | 36.96 | 69.70 | 0.19 |
| | 40 | 10 | 30 | 5561.96 | 3455.56 | 29.49 | 37.08 | 69.94 | 0.19 |
| | 45 | 10 | 35 | 5571.25 | 3462.74 | 29.62 | 37.18 | 70.20 | 0.19 |
| | 50 | 10 | 40 | 5577.47 | 3467.55 | 29.70 | 37.24 | 70.38 | 0.18 |
| | 60 | 10 | 50 | 5586.82 | 3471.16 | 29.76 | 37.41 | 70.57 | 0.19 |
| | 70 | 10 | 60 | 5596.19 | 3478.40 | 29.88 | 37.51 | 70.84 | 0.19 |
| | 80 | 10 | 70 | 5608.75 | 3480.82 | 29.93 | 37.80 | 71.03 | 0.19 |
| | 90 | 10 | 80 | 5618.20 | 3485.67 | 30.01 | 37.95 | 71.25 | 0.19 |
| | 100 | 10 | 90 | 5624.52 | 3484.46 | 29.99 | 38.15 | 71.29 | 0.19 |

Table K-6 (Continued) Cracked High-porosity Glass-bead Specimen

| Saturation Condition | $P_c$, MPa | $P_f$, MPa | $P_d$, MPa | $V_p$, m/s | $V_s$, m/s | $G$, GPa | $K$, GPa | $E$, GPa | $v$ |
|---|---|---|---|---|---|---|---|---|---|
| Water saturation, decreasing $P_c$, $P_f$ =10 MPa | 100 | 10 | 90 | 5624.52 | 3484.46 | 29.99 | 38.15 | 71.29 | 0.19 |
| | 90 | 10 | 80 | 5618.20 | 3485.67 | 30.01 | 37.95 | 71.25 | 0.19 |
| | 80 | 10 | 70 | 5611.90 | 3484.46 | 29.99 | 37.80 | 71.15 | 0.19 |
| | 70 | 10 | 60 | 5599.33 | 3480.82 | 29.93 | 37.54 | 70.93 | 0.19 |
| | 60 | 10 | 50 | 5593.06 | 3477.19 | 29.86 | 37.45 | 70.78 | 0.18 |
| | 50 | 10 | 40 | 5580.58 | 3469.95 | 29.74 | 37.27 | 70.47 | 0.18 |
| | 40 | 10 | 30 | 5565.05 | 3460.35 | 29.57 | 37.06 | 70.08 | 0.18 |
| | 30 | 10 | 20 | 5552.69 | 3443.66 | 29.29 | 37.10 | 69.56 | 0.19 |
| | 20 | 10 | 10 | 5531.19 | 3408.45 | 28.69 | 37.31 | 68.52 | 0.19 |

Table K-6 (Continued) Cracked High-porosity Glass-bead Specimen

| Saturation Condition | $P_c$, MPa | $P_f$, MPa | $P_d$, MPa | $V_p$, m/s | $V_s$, m/s | $G$, GPa | $K$, GPa | $E$, GPa | $v$ |
|---|---|---|---|---|---|---|---|---|---|
| Water saturation, increasing $P_c$, $P_f$ =15 MPa | 25 | 15 | 10 | 5525.08 | 3423.62 | 28.95 | 36.80 | 68.81 | 0.19 |
| | 30 | 15 | 15 | 5537.32 | 3437.74 | 29.19 | 36.81 | 69.26 | 0.19 |
| | 35 | 15 | 20 | 5549.61 | 3448.41 | 29.37 | 36.91 | 69.64 | 0.19 |
| | 40 | 15 | 25 | 5561.96 | 3453.18 | 29.45 | 37.14 | 69.88 | 0.19 |
| | 45 | 15 | 30 | 5571.25 | 3463.94 | 29.64 | 37.15 | 70.23 | 0.18 |
| | 50 | 15 | 35 | 5577.47 | 3465.14 | 29.66 | 37.29 | 70.33 | 0.19 |
| | 55 | 15 | 40 | 5580.58 | 3471.16 | 29.76 | 37.24 | 70.50 | 0.18 |
| | 65 | 15 | 50 | 5589.94 | 3477.19 | 29.86 | 37.36 | 70.74 | 0.18 |
| | 75 | 15 | 60 | 5602.46 | 3479.61 | 29.90 | 37.65 | 70.93 | 0.19 |
| | 85 | 15 | 70 | 5615.05 | 3484.46 | 29.99 | 37.89 | 71.18 | 0.19 |
| | 95 | 15 | 80 | 5624.52 | 3486.89 | 30.03 | 38.10 | 71.34 | 0.19 |

Table K-6 (Continued) Cracked High-porosity Glass-bead Specimen

| Saturation Condition | $P_c$, MPa | $P_f$, MPa | $P_d$, MPa | $V_p$, m/s | $V_s$, m/s | $G$, GPa | $K$, GPa | $E$, GPa | $v$ |
|---|---|---|---|---|---|---|---|---|---|
| Water saturation, decreasing $P_c$, $P_f$ =15 MPa | 95 | 15 | 80 | 5624.52 | 3486.89 | 30.03 | 38.10 | 71.34 | 0.19 |
| | 85 | 15 | 70 | 5611.90 | 3484.46 | 29.99 | 37.80 | 71.15 | 0.19 |
| | 75 | 15 | 60 | 5608.75 | 3479.61 | 29.90 | 37.83 | 71.00 | 0.19 |
| | 65 | 15 | 50 | 5596.19 | 3477.19 | 29.86 | 37.53 | 70.81 | 0.19 |
| | 55 | 15 | 40 | 5583.70 | 3472.36 | 29.78 | 37.30 | 70.56 | 0.18 |
| | 45 | 15 | 30 | 5574.36 | 3461.54 | 29.60 | 37.29 | 70.21 | 0.19 |
| | 35 | 15 | 20 | 5558.87 | 3450.79 | 29.41 | 37.11 | 69.79 | 0.19 |
| | 25 | 15 | 10 | 5540.39 | 3422.45 | 28.93 | 37.24 | 68.94 | 0.19 |

$P_c$: confining pressure; $P_f$: pore-fluid pressure; $P_d$: differential pressure; $V_p$: P-wave velocity; $V_s$: S-wave velocity; $G$: shear modulus; $K$: bulk modulus; $E$: Young's modulus; $v$: Poisson's ratio.

*Elastic moduli are calculated from measured P- and S-wave velocities with Eq. (3.71) – (3.73). The density of the fluid-saturated specimen is assumed to be pressure independent.

# Appendix L Strain Gauge Data

Table L-1 Cacked Glass-rod Specimen

| Confining Pressure, MPa | Axial Strain, % | Circumferential Strain, % |
|---|---|---|
| 0.1 | 0.000 | 0.000 |
| 5 | 0.045 | 0.004 |
| 10 | 0.055 | 0.008 |
| 15 | 0.061 | 0.013 |
| 20 | 0.066 | 0.017 |
| 25 | 0.070 | 0.021 |
| 30 | 0.075 | 0.025 |
| 35 | 0.079 | 0.030 |
| 40 | 0.082 | 0.034 |
| 50 | 0.090 | 0.043 |
| 60 | 0.098 | 0.051 |
| 70 | 0.106 | 0.058 |
| 80 | 0.114 | 0.067 |
| 90 | 0.122 | 0.076 |
| 100 | 0.130 | 0.085 |
| 90 | 0.121 | 0.075 |
| 80 | 0.113 | 0.068 |
| 70 | 0.106 | 0.060 |
| 60 | 0.097 | 0.051 |
| 50 | 0.090 | 0.043 |
| 40 | 0.082 | 0.034 |
| 30 | 0.073 | 0.025 |
| 20 | 0.065 | 0.016 |
| 10 | 0.055 | 0.007 |
| 0.1 | 0.006 | 0.000 |

Table L-2 Uncracked Low-porosity Glass-bead Specimen

| Confining Pressure, MPa | Axial Strain, % |
|---|---|
| 0 | 0.000 |
| 10 | 0.004 |
| 20 | 0.013 |
| 30 | 0.023 |
| 40 | 0.030 |
| 50 | 0.038 |
| 60 | 0.047 |
| 70 | 0.053 |
| 80 | 0.059 |
| 90 | 0.064 |
| 100 | 0.069 |

Table L-3 Cacked High-Porosity Glass-bead Specimen

| Confining Pressure, MPa | Axial Strain, % |
|---|---|
| 0.1 | 0.000 |
| 5 | 0.021 |
| 10 | 0.032 |
| 15 | 0.039 |
| 20 | 0.045 |
| 25 | 0.050 |
| 30 | 0.056 |
| 35 | 0.062 |
| 40 | 0.067 |
| 50 | 0.076 |
| 60 | 0.088 |
| 70 | 0.097 |
| 80 | 0.108 |
| 90 | 0.117 |
| 100 | 0.127 |
| 90 | 0.116 |
| 80 | 0.108 |
| 70 | 0.098 |
| 60 | 0.088 |
| 50 | 0.079 |
| 40 | 0.070 |
| 30 | 0.060 |
| 20 | 0.049 |
| 10 | 0.036 |
| 0.1 | 0.004 |

# Appendix M Intermediate-frequency (kHz) Mechanical Data

Table M-1 Uncracked Glass-rod Specimen

| | Confining Pressure, MPa | Pore-fluid Pressure, MPa | Differential Pressure, MPa | $f_G$, Hz | $G$, GPa | $1/(2Q_G)$, % | $f_E$, Hz | $E$, GPa | $1/(2Q_E)$, % |
|---|---|---|---|---|---|---|---|---|---|
| Dry, increasing $P_c$ | 0.3 | - | 0.3 | 1247.5 | 12.85 | 0.637 | 1660.0 | 18.61 | 1.845 |
| | 0.6 | | 0.6 | 1403.1 | 20.23 | 0.465 | 1984.4 | 32.37 | 2.339 |
| | 1.6 | | 1.6 | 1483.8 | 26.37 | 0.144 | 2262.5 | 54.47 | 1.220 |
| | 3.2 | | 3.2 | 1501.3 | 28.07 | 0.184 | 2319.0 | 61.15 | 0.877 |
| | 4.8 | | 4.8 | 1509.3 | 28.89 | 0.150 | 2348.0 | 64.96 | 0.753 |
| | 6.4 | | 6.4 | 1513.5 | 29.30 | 0.134 | 2367.5 | 67.86 | 0.603 |
| | 8.0 | | 8.0 | 1516.8 | 29.66 | 0.144 | 2383.5 | 70.30 | 0.491 |
| | 9.6 | | 9.6 | 1518.2 | 29.81 | 0.107 | 2394.0 | 71.94 | 0.417 |
| | 11.2 | | 11.2 | 1519.5 | 29.95 | 0.142 | 2404.5 | 73.61 | 0.513 |
| | 12.8 | | 12.8 | 1520.5 | 30.07 | 0.153 | 2397.5 | 72.48 | 0.298 |
| | 14.4 | | 14.4 | 1521.0 | 30.12 | 0.182 | 2402.0 | 73.17 | 0.230 |
| | 16.0 | | 16.0 | 1521.5 | 30.18 | 0.185 | 2403.0 | 73.34 | 0.146 |
| | 17.6 | | 17.6 | 1522.0 | 30.24 | 0.185 | 2404.5 | 73.58 | 0.114 |
| | 19.2 | | 19.2 | 1523.2 | 30.37 | 0.252 | 2405.0 | 73.68 | 0.128 |
| | 20.8 | | 20.8 | 1523.2 | 30.37 | 0.214 | 2406.5 | 73.92 | 0.161 |
| | 22.4 | | 22.4 | 1523.5 | 30.40 | 0.171 | 2402.0 | 73.27 | (1.055)* |
| | 24.0 | | 24.0 | 1523.5 | 30.40 | 0.149 | 2403.5 | 73.46 | 0.114 |

Table M-1 (Continued) Uncracked Glass-rod Specimen

| Saturation Condition | Confining Pressure, MPa | Pore-fluid Pressure, MPa | Differential Pressure, MPa | $f_G$, Hz | $G$, GPa | $1/(2Q_G)$, % | $f_E$, Hz | $E$, GPa | $1/(2Q_E)$, % |
|---|---|---|---|---|---|---|---|---|---|
| Dry, decreasing $P_c$ | 24.0 | - | 24.0 | 1523.5 | 30.40 | 0.149 | 2403.5 | 73.46 | 0.114 |
| | 22.4 | | 22.4 | 1523.8 | 30.45 | 0.223 | 2403.5 | 73.45 | (1.026) |
| | 19.2 | | 19.2 | 1523.5 | 30.45 | 0.143 | 2405.5 | 73.81 | 0.107 |
| | 16.0 | | 16.0 | 1523.0 | 30.42 | 0.191 | 2403.5 | 73.54 | 0.193 |
| | 12.8 | | 12.8 | 1520.5 | 30.12 | 0.193 | 2390.0 | 71.24 | 0.521 |
| | 9.6 | | 9.6 | 1516.5 | 29.69 | 0.163 | 2376.0 | 69.06 | 0.803 |
| | 6.4 | | 6.4 | 1507.3 | 28.65 | 0.142 | 2341.0 | 64.01 | 1.053 |
| | 3.2 | | 3.2 | 1484.5 | 26.41 | 0.134 | 2278.5 | 56.21 | 1.507 |
| | 1.6 | | 1.6 | 1454.0 | 23.82 | 0.147 | 2234.4 | 51.45 | 1.783 |
| | 0.6 | | 0.6 | 1359.4 | 17.71 | 0.341 | 2178.1 | 45.72 | 2.278 |

$f_G$: torsional resonance frequency; $G$: shear modulus after the correction for interfacial effect; $1/(2Q_G)$: shear attenuation; $f_E$: extensional resonance frequency; $E$: Young's modulus after the correction for interfacial effect; $1/(2Q_E)$: extensional attenuation.

*Attenuation value in parentheses is affected by interference, hence less trustable.

Table M-2 Cracked Glass-rod Specimen

| Saturation Condition | Confining Pressure, MPa | Pore-fluid Pressure, MPa | Differential Pressure, MPa | $f_G$, Hz | $G$, GPa | $1/(2Q_G)$, % | $f_E$, Hz | $E$, GPa | $1/(2Q_E)$, % |
|---|---|---|---|---|---|---|---|---|---|
| Dry, increasing $P_c$ | 1.6 | - | 1.6 | 1143.8 | 13.72 | 0.891 | 1468.8 | 32.38 | 0.965 |
| | 3.2 | | 3.2 | 1306.3 | 17.48 | 0.608 | 1825.0 | 37.02 | 0.740 |
| | 4.8 | | 4.8 | 1390.6 | 20.94 | 0.481 | 2025.0 | 43.42 | 0.560 |
| | 6.4 | | 6.4 | 1435.0 | 23.46 | 0.351 | 2145.0 | 49.03 | 0.608 |
| | 8.0 | | 8.0 | 1462.5 | 25.24 | 0.506 | 2217.5 | 53.04 | 0.415 |
| | 9.6 | | 9.6 | 1477.0 | 26.31 | 0.297 | 2265.0 | 56.32 | 0.274 |
| | 11.2 | | 11.2 | 1488.0 | 27.16 | 0.264 | 2298.5 | 58.45 | 0.234 |
| | 12.8 | | 12.8 | 1495.5 | 27.76 | 0.184 | 2322.0 | 62.54 | 0.182 |
| | 14.4 | | 14.4 | 1500.5 | 28.20 | 0.145 | 2338.5 | 63.98 | 0.149 |
| | 16.0 | | 16.0 | 1504.0 | 28.51 | 0.116 | 2350.5 | 65.48 | 0.133 |
| | 17.6 | | 17.6 | 1506.5 | 28.71 | 0.116 | 2359.5 | 66.52 | 0.098 |
| | 19.2 | | 19.2 | 1508.5 | 28.79 | 0.103 | 2367.5 | 67.57 | 0.134 |
| | 20.8 | | 20.8 | 1509.8 | 28.91 | 0.101 | 2374.5 | 68.36 | (0.513)* |
| | 22.4 | | 22.4 | 1510.7 | 28.98 | 0.098 | 2372.0 | 68.75 | 0.160 |
| | 24.0 | | 24.0 | 1511.8 | 29.10 | 0.098 | 2376.0 | 69.08 | 0.125 |

Table M-2 (Continued) Cracked Glass-rod Specimen

| Saturation Condition | Confining Pressure, MPa | Pore-fluid Pressure, MPa | Differential Pressure, MPa | $f_G$, Hz | $G$, GPa | $1/(2Q_G)$, % | $f_E$, Hz | $E$, GPa | $1/(2Q_E)$, % |
|---|---|---|---|---|---|---|---|---|---|
| Dry, decreasing $P_c$ | 24.0 | - | 24.0 | 1512.5 | 29.16 | 0.081 | 2378.0 | 69.35 | 0.104 |
| | 22.4 | | 22.4 | 1511.8 | 29.16 | 0.087 | 2373.0 | 68.88 | 0.208 |
| | 19.2 | | 19.2 | 1509.5 | 28.92 | 0.117 | 2367.5 | 67.64 | 0.157 |
| | 16.0 | | 16.0 | 1505.5 | 28.70 | 0.256 | 2350.0 | 65.40 | 0.220 |
| | 12.8 | | 12.8 | 1497.8 | 28.05 | 0.201 | 2323.0 | 62.67 | 0.326 |
| | 9.6 | | 9.6 | 1483.0 | 26.83 | 0.272 | 2269.5 | 56.78 | 0.504 |
| | 6.4 | | 6.4 | 1449.0 | 24.49 | 0.429 | 2157.0 | 50.02 | 0.803 |
| | 3.2 | | 3.2 | 1337.5 | 18.90 | 1.064 | 1850.0 | 38.02 | 1.511 |
| | 1.6 | | 1.6 | 1175.0 | 14.56 | 1.549 | 1493.8 | 32.96 | 1.881 |

Table M-2 (Continued) Cracked Glass-rod Specimen

| Saturation Condition | Confining Pressure, MPa | Pore-fluid Pressure, MPa | Differential Pressure, MPa | $f_G$, Hz | $G$, GPa | $1/(2Q_G)$, % | $f_E$, Hz | $E$, GPa | $1/(2Q_E)$, % |
|---|---|---|---|---|---|---|---|---|---|
| Nitrogen saturation, increasing $P_c$, $P_f$ = 3.1 MPa | 4.7 | 3.1 | 1.6 | 1181.3 | 14.75 | 2.865 | 1631.3 | 36.86 | 3.674 |
| | 6.3 | 3.1 | 3.2 | 1331.3 | 18.60 | 1.534 | 1934.4 | 42.17 | 1.912 |
| | 7.9 | 3.1 | 4.8 | 1409.4 | 22.14 | 0.908 | 2106.3 | 48.98 | 1.117 |
| | 9.5 | 3.1 | 6.4 | 1445.0 | 24.21 | 0.617 | 2195.0 | 53.34 | 0.747 |
| | 11.1 | 3.1 | 8.0 | 1467.5 | 25.64 | 0.442 | 2250.6 | 56.39 | 0.543 |
| | 12.7 | 3.1 | 9.6 | 1482.0 | 26.75 | 0.319 | 2288.5 | 58.92 | 0.408 |
| | 14.3 | 3.1 | 11.2 | 1491.0 | 27.44 | 0.209 | 2314.0 | 60.39 | 0.292 |
| | 15.9 | 3.1 | 12.8 | 1497.0 | 27.91 | 0.187 | 2332.0 | 63.81 | 0.255 |
| | 17.5 | 3.1 | 14.4 | 1502.0 | 28.35 | 0.167 | 2346.5 | 65.09 | 0.210 |
| | 19.1 | 3.1 | 16.0 | 1505.0 | 28.61 | 0.141 | 2357.5 | 66.45 | 0.226 |
| | 20.7 | 3.1 | 17.6 | 1507.5 | 28.82 | 0.119 | 2367.0 | 67.65 | (1.237) |
| | 22.3 | 3.1 | 19.2 | 1509.5 | 28.89 | 0.103 | 2367.0 | 67.59 | 0.189 |
| | 24.0 | 3.1 | 20.8 | 1510.5 | 28.99 | 0.103 | 2372.5 | 68.09 | 0.130 |
| | 25.6 | 3.1 | 22.4 | 1512.0 | 29.11 | 0.098 | 2377.5 | 69.49 | 0.125 |
| | 27.2 | 3.1 | 24.0 | 1512.5 | 29.17 | 0.087 | 2378.5 | 69.45 | 0.145 |

Table M-2 (Continued) Cracked Glass-rod Specimen

| Saturation Condition | Confining Pressure, MPa | Pore-fluid Pressure, MPa | Differential Pressure, MPa | $f_G$, Hz | $G$, GPa | $1/(2Q_G)$, % | $f_E$, Hz | $E$, GPa | $1/(2Q_E)$, % |
|---|---|---|---|---|---|---|---|---|---|
| Nitrogen saturation, decreasing $P_c$, $P_f$ = 3.1 MPa | 27.2 | 3.1 | 24.0 | 1512.5 | 29.17 | 0.087 | 2378.5 | 69.45 | 0.145 |
| | 25.6 | 3.1 | 22.4 | 1512.2 | 29.17 | 0.107 | 2377.0 | 69.48 | 0.138 |
| | 22.3 | 3.1 | 19.2 | 1510.3 | 29.03 | 0.109 | 2367.5 | 67.67 | 0.233 |
| | 19.1 | 3.1 | 16.0 | 1506.3 | 28.79 | 0.198 | 2359.0 | 66.74 | 0.247 |
| | 15.9 | 3.1 | 12.8 | 1500.0 | 28.26 | 0.210 | 2335.4 | 64.32 | 0.313 |
| | 12.7 | 3.1 | 9.6 | 1486.8 | 27.19 | 0.314 | 2294.0 | 59.57 | 0.550 |
| | 9.5 | 3.1 | 6.4 | 1456.3 | 25.09 | 0.648 | 2209.4 | 54.67 | 0.971 |
| | 6.3 | 3.1 | 3.2 | 1359.4 | 20.01 | 1.756 | 1971.9 | 44.15 | 2.015 |
| | 4.7 | 3.1 | 1.6 | 1212.5 | 15.69 | 3.077 | 1669.0 | 38.01 | 3.529 |

Table M-2 (Continued) Cracked Glass-rod Specimen

| Saturation Condition | Confining Pressure, MPa | Pore-fluid Pressure, MPa | Differential Pressure, MPa | $f_G$, Hz | $G$, GPa | $1/(2Q_G)$, % | $f_E$, Hz | $E$, GPa | $1/(2Q_E)$, % |
|---|---|---|---|---|---|---|---|---|---|
| Water saturation, increasing $P_c$, $P_f$ = 3.2 MPa | 4.8 | 3.2 | 1.6 | 1348.0 | 21.09 | 3.841 | 2232.0 | 68.41 | 4.596 |
| | 6.4 | 3.2 | 3.2 | 1428.0 | 24.17 | 1.634 | 2304.0 | 70.80 | 2.045 |
| | 8.0 | 3.2 | 4.8 | 1456.0 | 25.47 | 0.888 | 2332.0 | 70.84 | 1.459 |
| | 9.6 | 3.2 | 6.4 | 1472.0 | 26.38 | 0.581 | 2340.0 | 69.19 | (1.834) |
| | 11.2 | 3.2 | 8.0 | 1483.5 | 27.03 | 0.423 | 2354.5 | 68.86 | 0.675 |
| | 12.8 | 3.2 | 9.6 | 1491.5 | 27.63 | 0.357 | 2364.0 | 68.62 | 0.487 |
| | 14.4 | 3.2 | 11.2 | 1497.0 | 28.03 | 0.280 | 2371.5 | 68.09 | 0.428 |
| | 16.0 | 3.2 | 12.8 | 1501.0 | 28.31 | 0.248 | 2376.0 | 69.94 | 0.399 |
| | 17.6 | 3.2 | 14.4 | 1504.5 | 28.61 | 0.223 | 2380.5 | 69.96 | 0.304 |
| | 19.2 | 3.2 | 16.0 | 1506.3 | 28.73 | 0.165 | 2383.5 | 70.26 | 0.263 |
| | 20.8 | 3.2 | 17.6 | 1508.3 | 28.90 | 0.147 | 2387.0 | 70.58 | 0.358 |
| | 22.4 | 3.2 | 19.2 | 1509.3 | 28.86 | 0.133 | 2382.5 | 69.87 | 0.359 |
| | 24.0 | 3.2 | 20.8 | 1510.5 | 28.99 | 0.112 | 2386.0 | 70.13 | 0.221 |
| | 25.6 | 3.2 | 22.4 | 1511.0 | 29.01 | 0.123 | 2387.5 | 70.99 | 0.209 |
| | 27.2 | 3.2 | 24.0 | 1512.0 | 29.12 | 0.126 | 2387.5 | 70.81 | 0.312 |

Table M-2 (Continued) Cracked Glass-rod Specimen

| Saturation Condition | Confining Pressure, MPa | Pore-fluid Pressure, MPa | Differential Pressure, MPa | $f_G$, Hz | $G$, GPa | $1/(2Q_G)$, % | $f_E$, Hz | $E$, GPa | $1/(2Q_E)$, % |
|---|---|---|---|---|---|---|---|---|---|
| Water saturation, decreasing $P_c$, $P_f$ = 3.2 MPa | 27.2 | 3.2 | 24.0 | 1512.0 | 29.12 | 0.126 | 2387.5 | 70.81 | 0.312 |
| | 25.6 | 3.2 | 22.4 | 1512.0 | 29.12 | 0.121 | 2388.0 | 71.09 | 0.194 |
| | 22.4 | 3.2 | 19.2 | 1510.3 | 29.02 | 0.164 | 2383.0 | 69.97 | 0.387 |
| | 19.2 | 3.2 | 16.0 | 1508.0 | 28.96 | 0.172 | 2385.0 | 70.50 | 0.277 |
| | 16.0 | 3.2 | 12.8 | 1504.0 | 28.66 | 0.209 | 2380.0 | 70.63 | 0.389 |
| | 12.8 | 3.2 | 9.6 | 1495.8 | 28.11 | 0.280 | 2367.5 | 69.18 | 0.536 |
| | 9.6 | 3.2 | 6.4 | 1480.0 | 27.07 | 0.431 | 2359.5 | 71.92 | 1.067 |
| | 6.4 | 3.2 | 3.2 | 1440.0 | 25.04 | 1.378 | 2312.0 | 71.93 | 1.969 |
| | 4.8 | 3.2 | 1.6 | 1384.0 | 23.05 | 4.216 | 2260.0 | 71.85 | 4.918 |

$f_G$: torsional resonance frequency; $G$: shear modulus after the correction for interfacial effect; $1/(2Q_G)$: shear attenuation; $f_E$: extensional resonance frequency; $E$: Young's modulus after the correction for interfacial effect; $1/(2Q_E)$: extensional attenuation.

*Attenuation value in parentheses is affected by interference, hence less trustable.

# Appendix N Change in Elastic Moduli Induced by Fluid Saturation

Table N-1 Glass-rod Specimen

| Differential Pressure, MPa | Saturant | ΔG, % | | | | | | | | | ΔE, % | | |
|---|---|---|---|---|---|---|---|---|---|---|---|---|---|
| | | 0.01 Hz | 0.02 Hz | 0.05 Hz | 0.09 Hz | 0.16 Hz | 0.26 Hz | 0.78 Hz | $1.5\times10^3$ Hz | $10^6$ Hz | $10^{-1}$ Hz | $2.3\times10^3$ Hz | $10^6$ Hz |
| 10 MPa | Argon or Nitrogen | -0.4 | -0.3 | -0.4 | -0.1 | -0.4 | -0.1 | 0.0 | 1.5 | 2.7 | - | 4.8 | 2.7 |
| | Water | 3.8 | 4.1 | 3.9 | 3.9 | 3.8 | 4.0 | 3.7 | 4.9 | 4.3 | - | 21.8 | 4.1 |
| 15 MPa | Argon or Nitrogen | -0.1 | -0.2 | -0.3 | -0.3 | -0.2 | -0.1 | -0.4 | 0.5 | 1.6 | - | 1.7 | 1.5 |
| | Water | 1.6 | 1.8 | 1.7 | 1.8 | 1.8 | 1.8 | 2.5 | 1.5 | 3.2 | - | 9.3 | 2.8 |

ΔG: percentage change in shear modulus; ΔE: percentage change in Young's modulus.

Table N-1 (Continued) Glass-rod Specimen

| Differential Pressure, MPa | Saturant | ΔG, % | | | | | | | | | ΔE, % | | |
|---|---|---|---|---|---|---|---|---|---|---|---|---|---|
| | | 0.01 Hz | 0.02 Hz | 0.05 Hz | 0.09 Hz | 0.16 Hz | 0.26 Hz | 0.78 Hz | $1.5\times10^3$ Hz | $10^6$ Hz | $10^{-1}$ Hz | $2.3\times10^3$ Hz | $10^6$ Hz |
| 20 MPa | Argon or Nitrogen | -0.4 | -0.2 | -0.1 | -0.1 | 0.1 | 0.0 | 0.1 | 0.4 | 1.0 | - | 0.0 | 0.9 |
| | Water | 1.1 | 1.6 | 1.6 | 1.6 | 1.8 | 1.6 | 1.8 | 0.3 | 2.6 | - | 3.4 | 2.1 |
| 25 MPa | Argon or Nitrogen | -0.1 | -0.5 | -0.2 | -0.1 | -0.1 | 0.0 | -0.1 | 0.1 | 1.1 | - | 0.3 | 0.9 |
| | Water | 1.1 | 1.2 | 1.5 | 1.3 | 1.4 | 1.4 | 2.0 | 0.0 | 2.7 | - | 2.3 | 2.3 |

ΔG: percentage change in shear modulus; ΔE: percentage change in Young's modulus.

Table N-2 Low-porosity Glass-bead Specimen

| Differential Pressure, MPa | Saturant | ΔG, % | | | | | | | | ΔE, % | |
|---|---|---|---|---|---|---|---|---|---|---|---|
| | | 0.01 Hz | 0.02 Hz | 0.05 Hz | 0.09 Hz | 0.16 Hz | 0.26 Hz | 0.78 Hz | $10^6$ Hz | $10^{-1}$ Hz | $10^6$ Hz |
| 10 MPa | Argon | 3.5 | 3.4 | 3.5 | 3.6 | 3.4 | 3.6 | 4.0 | 6.7 | 22.8 | 7.0 |
| | Water | 2.8 | 2.7 | 2.9 | 3.0 | 2.5 | 3.2 | 2.5 | 9.0 | 35.7 | 9.1 |
| 20 MPa | Argon | 1.0 | 0.9 | 0.5 | 1.1 | 0.6 | 0.6 | 0.9 | 1.7 | 6.2 | 1.6 |
| | Water | - | - | - | - | - | - | - | 3.3 | - | 3.1 |

ΔG: percentage change in shear modulus; ΔE: percentage change in Young's modulus.

Table N-2 (Continued) Low-porosity Glass-bead Specimen

| Differential Pressure, MPa | Saturant | ΔG, % | | | | | | | | ΔE, % | |
|---|---|---|---|---|---|---|---|---|---|---|---|
| | | 0.01 Hz | 0.02 Hz | 0.05 Hz | 0.09 Hz | 0.16 Hz | 0.26 Hz | 0.78 Hz | $10^6$ Hz | $10^{-1}$ Hz | $10^6$ Hz |
| 30 MPa | Argon | - | - | - | - | - | - | - | 1.0 | - | 1.1 |
| | Water | 1.9 | 1.8 | 1.8 | 2.1 | 1.6 | 1.7 | 2.2 | 2.4 | 7.2 | 2.5 |
| 50 MPa | Argon | 0.0 | 0.1 | 0.1 | -0.1 | -0.3 | 0.4 | -0.4 | 0.7 | 1.3 | 0.7 |
| | Water | - | - | - | - | - | - | - | 1.9 | - | 2.0 |

ΔG: percentage change in shear modulus; ΔE: percentage change in Young's modulus.

Table N-3 High-porosity Glass-bead Specimen

| Differential Pressure, MPa | Saturant | ΔG, % | | | | | | | | ΔE, % | |
|---|---|---|---|---|---|---|---|---|---|---|---|
| | | 0.01 Hz | 0.02 Hz | 0.05 Hz | 0.09 Hz | 0.16 Hz | 0.26 Hz | 0.78 Hz | $10^6$ Hz | $10^{-1}$ Hz | $10^6$ Hz |
| 10 MPa | Argon | -1.3 | -1.4 | -1.6 | -1.3 | -1.7 | -1.4 | -1.7 | 6.3 | 1.6 | 8.7 |
| | Water | 0.7 | 0.3 | 0.2 | 0.8 | 0.4 | 0.5 | 0.4 | 9.4 | 15.2 | 13.0 |
| 20 MPa | Argon | -1.5 | -1.5 | -1.4 | -1.4 | -1.3 | -1.0 | -1.0 | 2.2 | -6.0 | 3.0 |
| | Water | -1.6 | -1.5 | -1.4 | -1.3 | -1.4 | -1.1 | -1.2 | 4.9 | 2.1 | 6.5 |

ΔG: percentage change in shear modulus; ΔE: percentage change in Young's modulus.

Table N-3 (Continued) High-porosity Glass-bead Specimen

| Differential Pressure, MPa | Saturant | ΔG, % | | | | | | | | ΔE, % | |
|---|---|---|---|---|---|---|---|---|---|---|---|
| | | 0.01 Hz | 0.02 Hz | 0.05 Hz | 0.09 Hz | 0.16 Hz | 0.26 Hz | 0.78 Hz | $10^6$ Hz | $10^{-1}$ Hz | $10^6$ Hz |
| 30 MPa | Argon | -0.9 | -0.9 | -0.8 | -0.9 | -1.1 | -0.4 | -1.0 | 1.6 | -6.5 | 2.2 |
| | Water | -1.5 | -1.7 | -1.4 | -1.6 | -1.6 | -1.4 | -1.6 | 4.2 | -3.6 | 5.2 |
| 50 MPa | Argon | -0.5 | -1.3 | -0.7 | -0.5 | -0.3 | -0.3 | 0.0 | 1.1 | -7.7 | 1.4 |
| | Water | -0.8 | -1.8 | -1.1 | -1.1 | -1.2 | -1.2 | -0.8 | 3.7 | -4.2 | 4.3 |

ΔG: percentage change in shear modulus; ΔE: percentage change in Young's modulus.